Novel Structural Characterization Method for Mesoporous Carbon–Ceramic Composites towards Their Applications for Energy Storage and Conversion

メソポーラスカーボン–セラミックス複合体の新規構造評価法の開発とエネルギー貯蔵・変換材料への応用

by

Yosuke Ishii

石井　陽祐

Department of Materials Science and Engineering,
Graduate School of Engineering,
Nagoya Institute of Technology, Japan

January, 2014

Abstract

Porous materials, such as activated carbons, silica gels, and zeolites, are industrially important resources. The porous materials are widely used such as catalyst, catalysts-supports, adsorbents, separators, and electric double-layer capacitor electrodes. In this dissertation, a novel structure characterization method was proposed for mesoporous materials having ordered cylindrical nanopores. In addition, electrical energy storage and photoluminescence properties of various types of mesoporous carbon-ceramic composite materials were studied.

In Chapter 2, the XRD-based structural characterization method developed in the present study was described. Using this method, mesopore-diameter and density of frame-work structure can also be determined from powder XRD pattern, in addition to the previously determined structural symmetry and pore-to-pore distance (i.e. unit-cell constant *a*). It was demonstrated that this XRD analysis can be performed even for samples immersed in water. This means that the XRD method has great potential for *in situ* experiments that cannot be performed by electron microscopy or gas-adsorption / desorption isotherm analysis methods. The XRD method does not require any special measurement environment or pretreatment.

By analyzing N_2 adsortption / desorption isotherms and XRD data, structural changes of various types of mesoporous materials associated with various heat-treatments were discussed in Chapter 3. It was found that the mesoporous carbon has superior thermal stability compared to the mesoporous SiO_2 samples and mesoporous carbon–SiO_2 composite. Although ordered pore structure of mesoporous SiO_2 samples were collapsed below 1000 °C treatment, the structure of mesoporous carbon was maintained even after the 2000 °C treatment. Electrochemical energy storage properties of the heat-treated mesoporous carbons were studied in Chapter 4. The mesoporous carbon electrode processed at 1200 °C showed good electrode properties for EDLC and LIB application. It was expected that micropores in the carbon-framework could be used as effective ion-storage sites.

In Chapter 5, lithium-ion storage properties of mesoporous carbon–TiO_2 composites

(MCTs) were investigated. The MCT electrode synthesized at 600 °C showed good electrode performance even at high current-density conditions. This superior electrode performance seems to come from TiO_2(B) crystals in the composite. In order to elucidate lithium-ion storage mechanisms of the TiO_2(B) phase, an *in situ* XRD observation during galvanostatic charge / discharge cycling was performed. Reversible structural changes of TiO_2(B) during lithium-ion insertion / extraction were successfully observed in the present investigation. Although two-steps of two-phase equilibrium reactions and a following solid-solution-type lithium insertion reaction occurs at charge / discharge cycling, its crystal structure was almost maintained in contrast to well-known anatase-type TiO_2 electrodes. The manner of unique structural changes, and ideal ion-diffusion pathway of TiO_2(B) crystals seem to play an important role for the good rate-performance and cyclability of the MCT electrodes.

In Chapter 6, photoluminescence properties of oxidized mesoporous carbon–SiO_2 composites (oxMCSs) were investigated. Even though the oxMCSs do not contains any transition-metal or rare-earth elements, the composites showed strong visible-white-light under 365 nm UV-light exposure. The shapes of photoluminescence spectra were close to the spectrum of sun-light, and the spectra of oxMCSs covered almost entire visible-range (400–800 nm). It was found that the color of luminescence can be varied with changing preparation conditions such as carbonization temperature, oxidation temperature, and duration of oxidation-treatment. Although detailed luminescence mechanisms have not been elucidated yet, carbon-fragments in the composites seem to play an important role for luminescence. In order to discuss a possibility of carbon-fragment based luminescence in the oxMCSs, nano-sized graphene (graphene nano-fragments) were prepared by using pentacenes as a precursor (Chapter 7). By optimizing preparation methods, polymerized pentacene molecules, which would be regard as graphene nano-fragment, were obtained up to octamer. First principle calculations revealed that such polymerized pentacene molecules have a unique electronic-structure. The obtained nano-fragments showed strong visible-luminescence under UV-irradiation, and the luminescence color was changed with synthetic condition.

The results shown in Chapter 3 to Chapter 7 indicate that the mesoporous

carbon-ceramic composites have hopeful-potential for energy storage and conversion applications.

Acknowledgments

The studies presented in this thesis have been carried out under the direction of Professor Shinji Kawasaki at Department of Materials Science and Engineering, Graduate School of Engineering, Nagoya Institute of Technology. The author would like to express his gratitude to all people related in this study for their dedicated supports.

The author wishes to express his sincerest gratitude to Professor Shinji Kawasaki for his kind guidance, valuable suggestions, vigorous discussions, and warm encouragement throughout this work.

The author also thanks to Professor Yukari Ishikawa and her research group at Japan Fine Ceramics Center (JFCC), for meaningful discussions and experimental supports for photoluminescence study.

The author expresses his appreciation for Professor Shigeru Okamoto at Nagoya Institute of Technology, and Professor Akio Ohta at Kanazawa University for their support in small-angle X-ray diffraction (XRD) measurements.

The author is grateful to Professor Fujio Okino at Shinshu University for heat-treatment experiments using high-temperature furnace.

The author wish to express his thanks to Mr. Hidenori Kato and Mr. Masashige Takatori at Kurogane Kasei Co. Ltd. for providing high-purity pentacene sample, and valuable discussion for its polymerization reaction.

The author also thanks to Professor Masamichi Yoshimura at Toyota Technological Institute for scanning tunneling microscopy (STM) observations.

The author expresses gratitude to Professor Akihiro Yoshino at Nagoya Institute of Technology for helpful discussion on ^{29}Si solid-state nuclear magnetic resonance (NMR) measurements.

The author expresses his appreciation to Professor Norihiro Shida at Nagoya Institute of Technology for setting up the Gaussian software.

In the present work, synchrotron XRD measurements were performed using beam line BL-18C at the Photon Factory (PF) in the High Energy Accelerator Research Organization (KEK). The author thanks to all of the beam line staff for their experimental supports and maintenance of equipment.

The author is sincerely obliged to all of the members in Shinji Kawasaki's laboratory for valuable comments, discussions, and advices on this study. Especially, the author thanks to Mr. Yusuke Kanamori, Mr. Takehiro Kawashita, and Mr. Koki Okamura for their dedicated discussion and experimental support for the synthesis and characterizations of mesoporous materials. The author also would like to express his sincere gratitude to Mr. Tomohiro Sakashita, Mr. Yusuke Okai, and Mr. Hayong Song for their kind support for the polymerization experiments of pentacene. The author also wishes to express his thanks to Mr. Tomohiro Matsushita for meaningful discussion about sodium-ion battery. The author also thanks to Mr. Masashi Hirose for his support on the development of an electrochemical cell used for *in situ* synchrotron XRD experiment. The author also thanks to Mr. Atsushi Iwata, Mr. Masashi Hirose, Mr. Tsuyoshi Inoue, Mr. Koki Okamura, Mr. Tomohiro Matsushita, Ms. Ayar Al-zubaidi, Mr. Yoshiki Nishiwaki, Mr. Hayong Song, and Mr. Masato Tsutsui for their committed experimental support in synchrotron X-ray diffraction experiments. In addition, the author obliged to Ms. Ayar Al-zubaidi for her valuable and kind guidance on my English. Furthermore, the author thanks to Ms. Sumi Sato for her assistance for the laboratory's office works.

The author is sincerely grateful to Japan Society for the Promotion of Science (JSPS) for financial support (Research Fellowship for Young Scientists, DC2) from April 2012 to March 2014.

Finally, the author expresses his deep appreciation to his family, especially his parents, Hiromi Ishii and Satoko Ishii, and his brother Masahiro Ishii for their constant assistances and encouragements.

Yosuke Ishii

January, 2014

Contents

List of Figures

List of Tables

Chapter 1

General Introduction

1.1 Ordered Mesoporous Materials

1.1.1 Overview

Porous materials, such as activated carbons, silica gels, and zeolites, are industrially important resources. The porous materials are widely used such as catalysts, catalysts-supports, adsorbents, and separators. It is well known that the properties of porous materials are highly depending on their pore-size, and pore-alignment. According to the IUPAC's recommendation, porous materials are classified into three categories based on their pore-diameter d: microporous materials ($d < 2$ nm), mesoporous materials (2 nm$< d <$ 50 nm), and macroporous materials (50 nm$< d$) as shown in Figure 1-1.

Ever since the discovery of surfactant-template synthesis methods, ordered mesoporous materials have generated tremendous interest.[1)] Because of their unique and controllable nanostructure, ordered mesoporous materials are expected to be used in various fields of application, such as catalysts,[2–5)] adsorbents,[5,6)] drug derivery,[7,8)] sensors,[8,9)] and in energy conversion and storage.[10–12)] Vigorous researches are still performed in the present day.

1.1.2 Synthesis

In 1992, Mobil's researchers report a synthesis procedure for a mesoporous SiO_2 called MCM-41.[13)] The MCM-41 material has hexagonally-aligned uniform cylindrical-pores with about 2 nm in diameter. In the MCM-41 synthesis, well-aligned cylindrical micelles consisting of a surfactant (Cetyl trimethyl ammonium bromide, CTAB) were used as a mesopore-template.

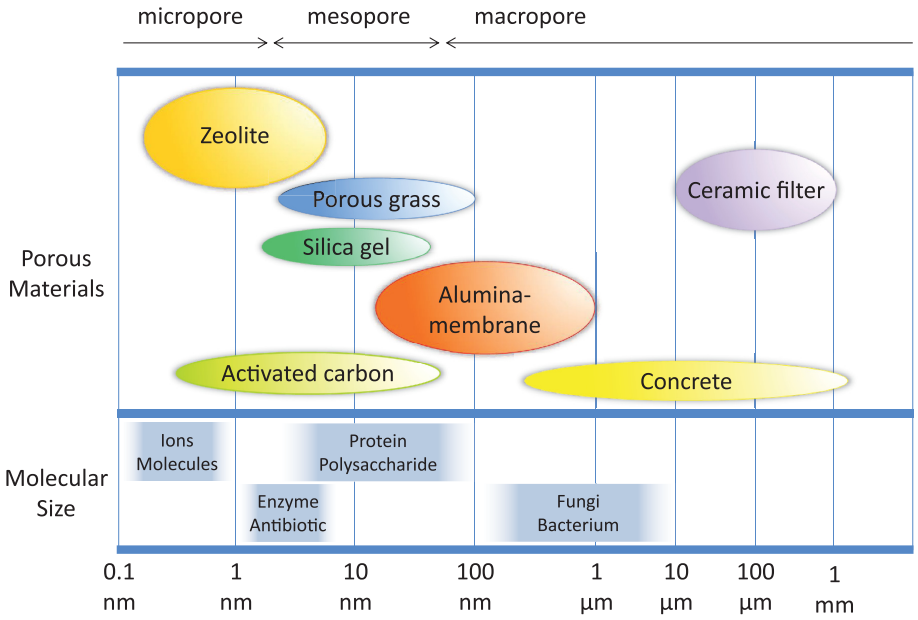

Figure 1-1 Porous Materials.

By performing sol-gel polymerizations of silica-precursor at the micelle surfaces, an ordered SiO_2–micelle composite is obtained. The surfactant micelles, which used as a template of mesopores, are easily removed by extraction or calcination process.

By changing the size of surfactant molecules, the size of mesopores are easily controlled. Furthermore, in addition to the commonly known MCM-41 type silicas, various kinds of mesoporous materials with different structural symmetries[14–22] and framework compositions[23–29] have been synthesized over the last twenty years.

In addition to the mesoporous ceramics prepared by the sol-gel reaction of inorganic precursors, mesoporous materials having organic-framework are also synthesized by using thermosetting polymers as structural backbones. Furthermore, by carbonizing the mesoporous polymers, mesoporous carbons are also obtained. In addition to the simple mesoporous materials having single framework-component, more complicated "mesoporous composites" are also prepared. For example, Liu *et al.* reported a mesoporous carbon–SiO_2 composite synthesized by a novel procedure called "triconstituent co-assembly method" in 2006.[30] By performing post-oxidation or post-etching treatment, unique mesoporous carbon and mesoporous SiO_2 are obtained from the carbon–SiO2 composite, as illustrated in Figrue 1-2.

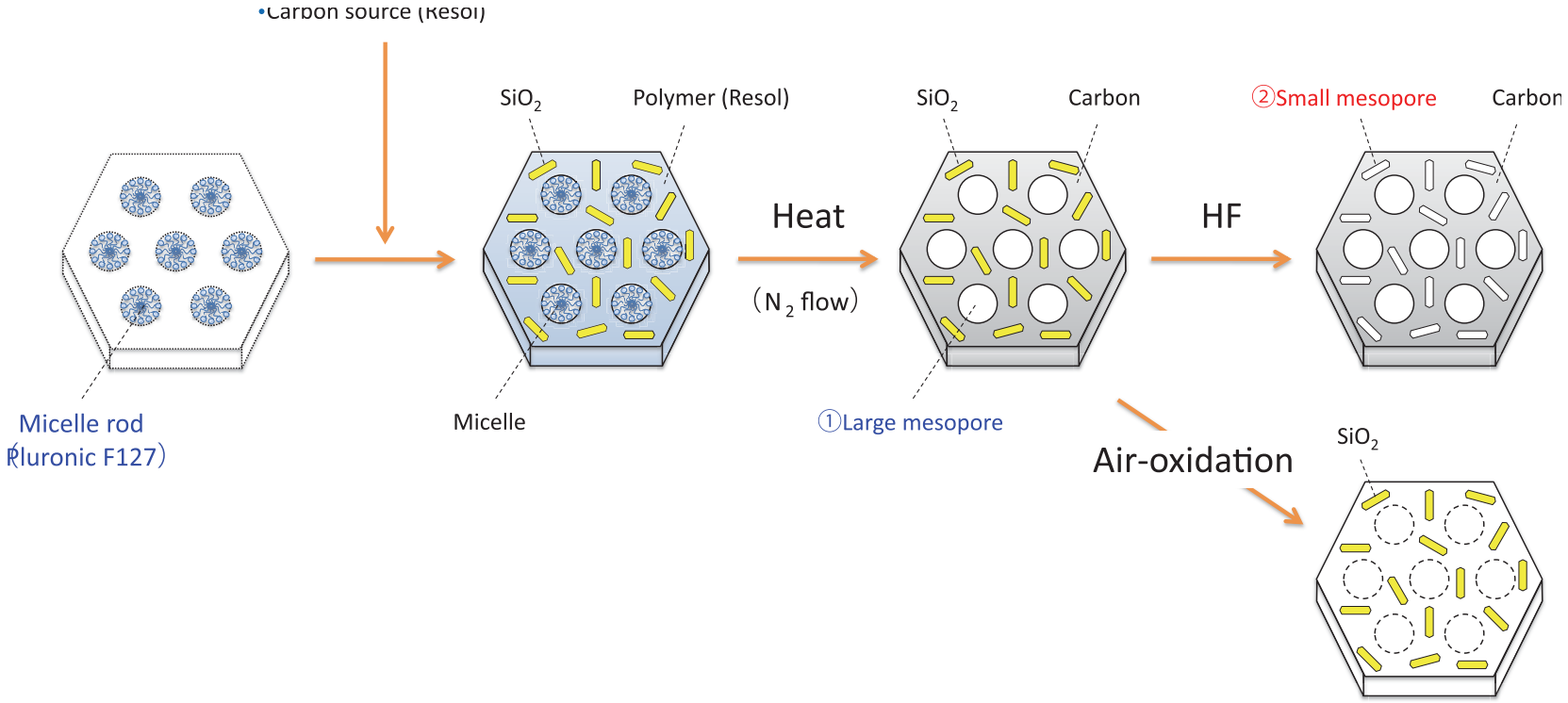

Figure 1-2 Synthesis scheme of ordered mesoporous polymer–SiO_2 composite, mesoporous carbon, and mesoporous SiO_2, by the triconstituent co-assembly method.

1.1.3 Structural Characterization

Needless to say, the structural characterization of ordered mesoporous materials is essential in researching their applications. Direct observations using transmission electron microscope (TEM) or scanning electron microscope (SEM), gas adsorption / desorption isotherm analysis, and small-angle powder X-ray diffraction (XRD) are commonly used structural characterization methods for ordered mesoporous materials.

Of these techniques, TEM observation is the most direct and most commonly used method. In addition to the normal 2D transmission micrographs, 3D structural images can also be obtained using a recently developed electron tomography technique.[14–21] However, specialized experience is required for exact analysis because TEM images are strongly affected by various experimental conditions, such as focus settings, sample thickness, and electromagnetic lens aberrations.[31] Furthermore, the TEM method is unsuitable for statistical analysis, because the images contain only local information from a selected area. SEM method is also used for structural observation of mesopore-structure in recent years. With increasing resolution of SEM equipment, small mesopores less than 10 nm in diameter can be observed. Compare to the TEM, SEM images are less affected by experimental conditions, and their images can intuitively be understood. However, the SEM images give us only surface-information. Furthermore, the SEM method is also unsuitable for statistical analysis.

On the other hand, the gas adsorption-desorption method provides bulk pore structure information. Specific surface areas estimated by the Brunauer–Emmett–Teller (BET) method[32] and pore-size distributions calculated by the Barrett–Joyner–Halenda (BJH) method[33] are often employ structural information obtained from gas adsorption-desorption isotherm analysis. In addition to these classical methods, more sophisticated analysis such as non-localized density functional theory simulation (NLDFT)[34–37] and grand canonical Monte Carlo calculations (GCMC)[38–40] have also been used in recent years. However, structure parameters obtained by the gas adsorption-desorption methods are strongly dependent on their calculation models. Moreover, structural ordering cannot be determined by gas

adsorption-desorption methods alone.

Small-angle powder XRD is often used to counter this disadvantage of the gas adsorption-desorption methods. From the XRD peak positions, structural symmetry and the distances between adjacent pores have been determined. However, quantitative discussions of XRD peak intensities have not often been reported.

1.2 Electrochemical Energy Storage

1.2.1 Lithium-ion Battey

1.2.1.1 Overview

Lithium-ion batteries (LIBs) have the highest energy density compared to other commercialized rechargeable batteries such as lead-acid-, nickel-cadmium, and nickel-metal hydride-batteries as shown in Figure 1-3. Ever since the initial commercialization by Sony in 1991, the market for LIBs has been rapidly grown with exploding demands for portable electronic devices such as cell-phones, digital cameras, and laptop computers. In recent years, the LIBs are also received a lot of attention as a power source for electric vehicles (EVs),renewable energy storage, and smart grid applications.

LIBs consists cathode, anode, separator, and organic electrolyte. As schematically illustrated in Figure 1-4, Li-ions in LIBs move from the anode to cathode during discharge, and from the cathode to anode during charge. In the most typical LIB cell, lithium cobaltate ($LiCoO_2$) and graphite (C) are used as cathode and anode materials, respectively. In this cell, the reaction schemes are expressed as follows:

$$\text{(cathode)} \quad 2Li_{0.5}CoO_2 + Li^+ + e^- \rightleftarrows 2LiCoO_2$$

$$\text{(anode)} \quad LiC_6 \rightleftarrows C_6 + Li^+ + e^-$$

$$\text{(total)} \quad 2Li_{0.5}CoO_2 + LiC_6 \rightleftarrows 2LiCoO_2 + C_6$$

where, right-arrows and left-arrows represent discharge and charge reactions, respectively. Since graphite can store Li-ions up to LiC_6, theoretical capacity of the graphite anode is

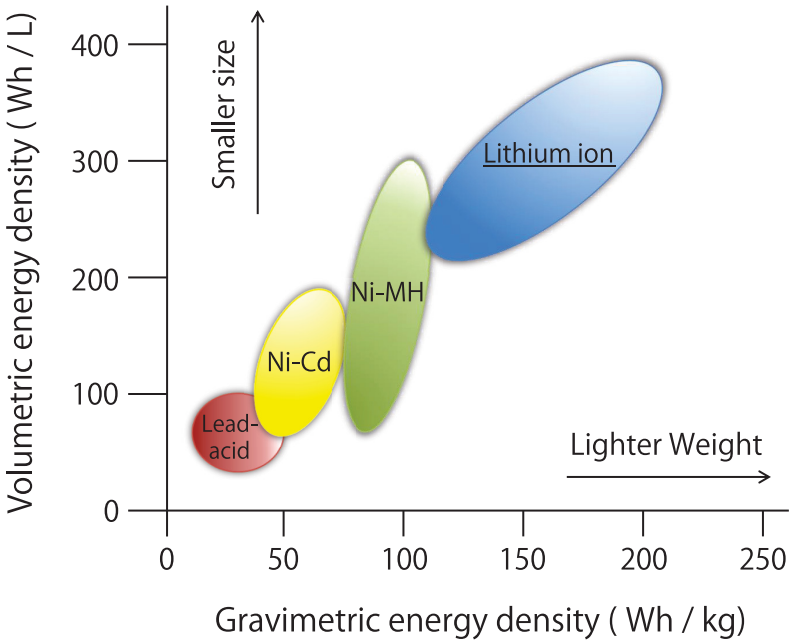

Figure 1-3 Energy densities of commercialized rechargeable batteries.

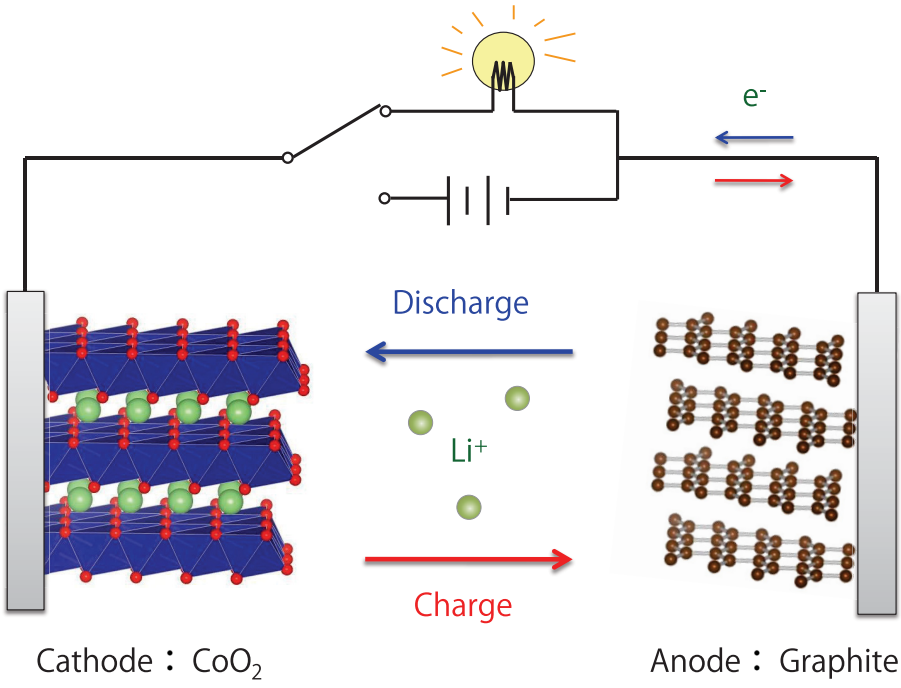

Figure 1-4 Schematical illustration of lithium-ion battery cell.

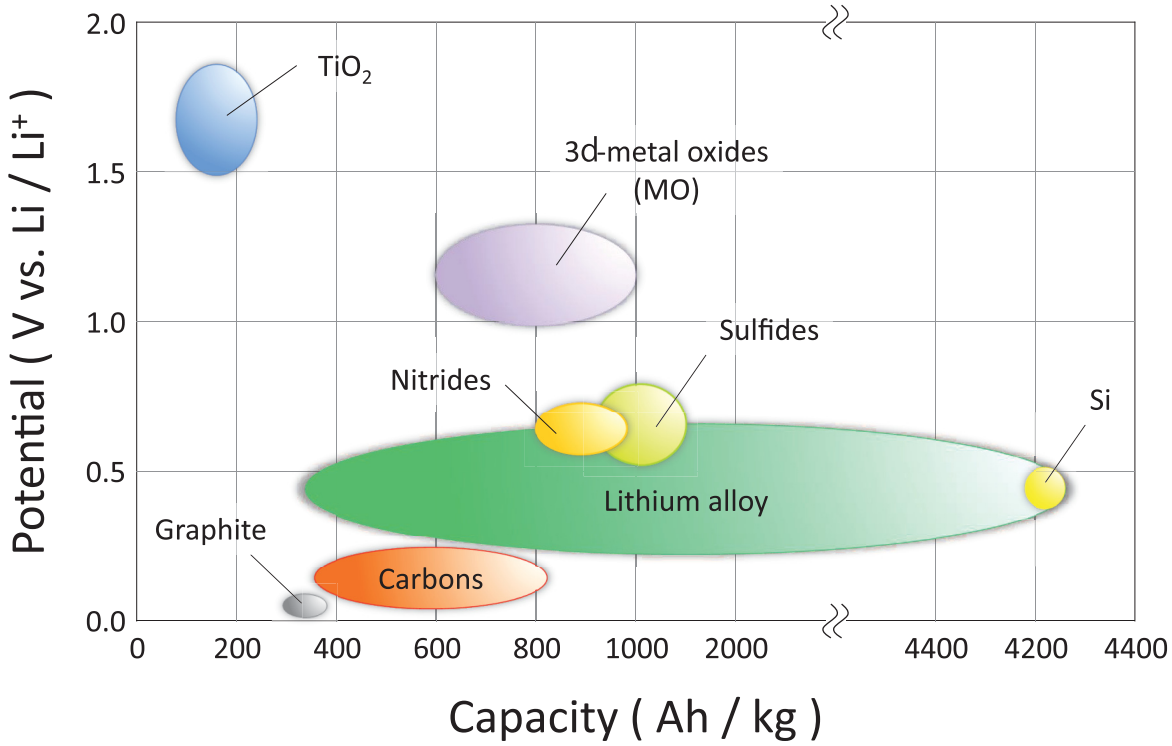

Figure 1-5 Anode materials for lithium-ion batteries.

calculated to be 372 mAh g^{-1}. On the other hand, $LiCoO_2$ cathode release Li-ions until the electrode becomes $Li_{0.5}CoO_2$ composition, [i] and theoretical capacity of the $LiCoO_2$ cathode is calculated to be 137 mAh g^{-1}. In this combination, the cell-voltage is 3.6 V.

As shown in Figure 1-5, various types of materials have been studied as anode-material for LIBs. From a fundamental viewpoint, anode material having larger lithium storage capacity and lower lithium insertion/extraction voltages are better anode material. However, other parameters such as safety, costs, cycleability, coulombic efficiency, and power density are also important factors for practical applications. Since the demands for the batteries are highly depend on its application field, we cannot easily define which material is the most excellent anode. Material selection with considering its advantages and disadvantages should be important. In following contents, the author would like to introduce carbons and TiO_2 as anode active materials for LIBs.

[i] Actually, $LiCoO_2$ is able to release Li-ions until Li_0CoO_2 composition. However, such a highly delithiated state is unfavorable due to poor-cycling performance.

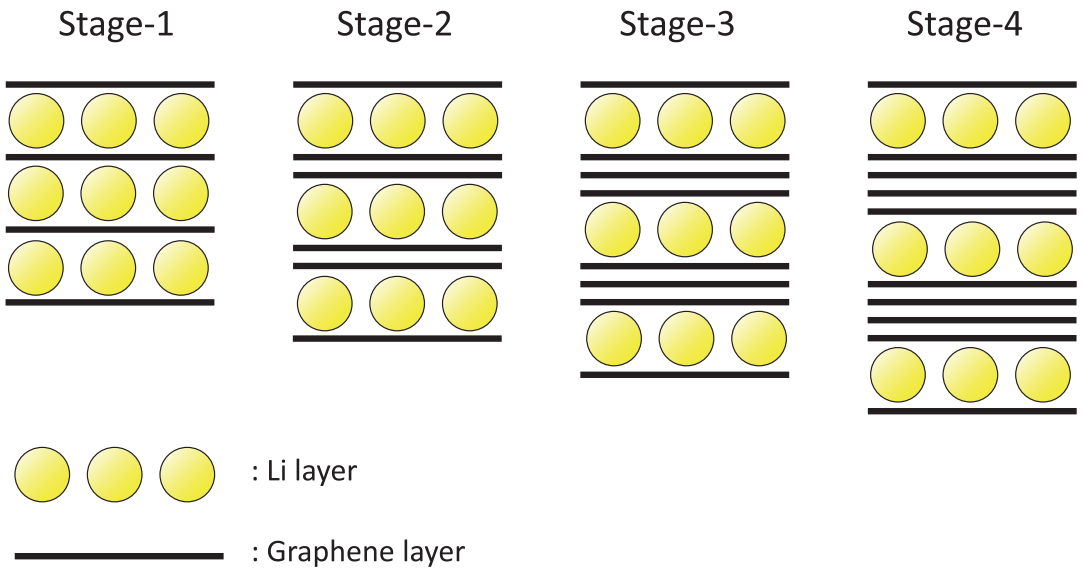

Figure 1-6 Schematic illustrations of lithium-intercalated graphite.

1.2.1.2 Carbon Anodes

High crystallinity graphite is the most commonly used anode material for LIBs. In the case of graphite electrode, lithium-insertion/extraction reactions occurs at < 0.25 V vs. Li/Li^+, and shows reversible capacity of 300–370 mAh g^{-1} under typical operating conditions. At the first charge process, irreversible reactions occurs under 1 V vs. Li/Li^+. This irreversible reaction is attributed to electrolyte-decompositions at the graphite surfaces. The decomposed electrolytes forms lithium-conductive but electron-insulating passivation films, called SEI (solid-electrolyte interphase), on the graphite surface. At the graphite electrode, Li-ions are stored between stacked graphene layers, and forms graphite-intercalation compounds (GIC) as illustrated in Figure 1-6. The lithium intercalation process on graphite was well-studied by using XRD and Raman-spectroscopy, and revealed that the graphite can store Li-ions up to stage-1 structure (LiC_6). The structure of GIC is gradually changed with stepwise two-phase equilibrium reactions during lithium-insertion and extraction process.[41,42)]

Non-crystalline carbons have also been studied as Li-storing anode material. Generally, the non-crystalline carbons are divided into “hard-carbons” and “soft-carbons”

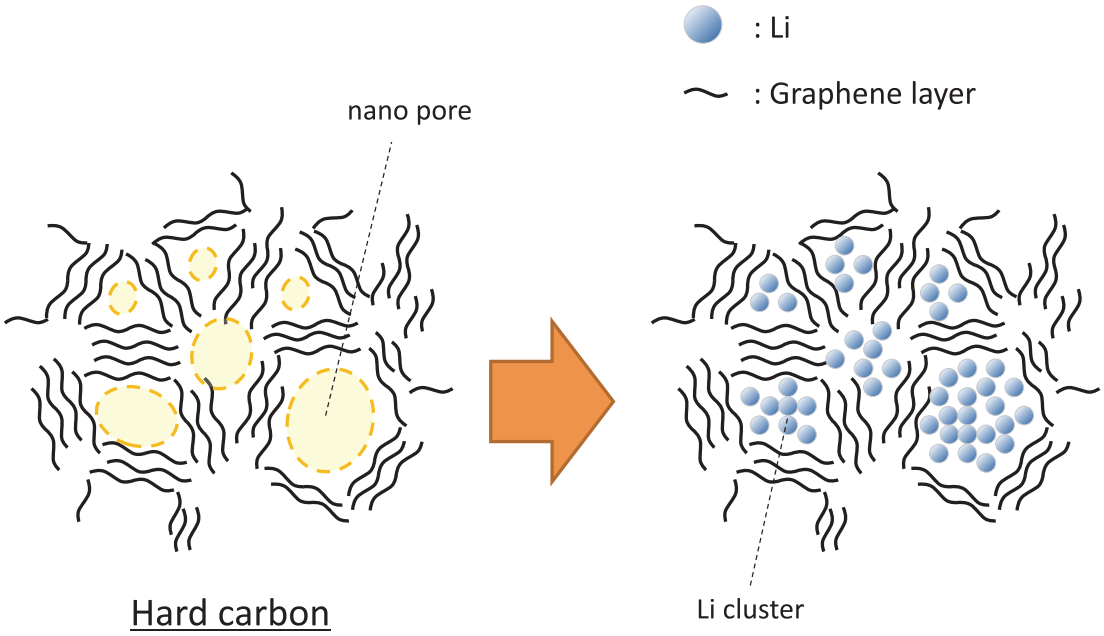

Figure 1-7 Li clusters formed in hard-carbon electrodes.

according to their ease of graphitization accompanied by heat-treatments. Due to their superior properties of low-cost, high-capacity and small-volume expansion associated with Li-insertion / extraction, hard-carbon anodes are expected to be used for large-scale LIBs. As shown in "carbons" in Figure 1-5, lithium-storage capacities of hard-carbons are much larger than graphite. Such a high-capacity of hard-carbons seems to be explained by their unique ion-storage sites. According to the previous reports using ^{7}Li solid-state nuclear magnetic resonance spectroscopy (NMR), in addition to the normal ionic lithium-ions, semi-metallic Li clusters are also observed in fully-lithiated hard-carbon electrodes. The observed Li-clusters seem to be stored in nanopores of hard-carbons as illustrated in Figure 1-7. However, the detailed relationships between nanopore-structure and Li-clustering are still unexplained. Furthermore, hard-carbon anodes have some problems: irreversible capacities at the first cycle are much larger than graphite electrode, and large-hysteresis are observed in their charge-discharge profiles. Such problems cause significant energy-loss, and need to be overcome.

1.2.1.3 TiO_2 Anodes

In commonly used LIBs, graphite is used as an anode material. However, the lithium storage potential of graphite (0.1 V vs. Li/Li^+) is close to that of lithium plating. This fact is unfavorable for applications that require high-power operation because the formation of lithium metal dendrites at contingent overcharged states tends to occur in high-speed charge–discharge operations, thereby causing internal short circuit in the battery. In addition, the formation of a solid electrolyte interface (SEI) on the graphite electrodes leads to irreversible energy consumption in the battery system. Therefore, new types of anode material are strongly desired. Because of its advantages in terms of cost, environmental friendly, and rate capability, titanium dioxide (TiO_2) has been attracted much attention as an anode material. Since the lithium storage potential of TiO_2 (> 1.5 V vs. Li/Li^+) is thoroughly high compared with lithium plating potential, the risk of dendrites formation is negligible.

Anatase, Rutile, and Brookite are well-known TiO_2 polymorphous. As shown in Figure 1-8, all TiO_2 crystals consists TiO_6 octahedron, but their manners of connection and spatial configuration are different in each polymorphous. In these polymorphous, lithium-storage properties of anatase and rutile have been well-studied due to their easy synthesis procedure. Anatase-type TiO_2 can stably store Li-ions up to $Li_{0.5}TiO_2$ composition, and its theoretical capacity is calculated to be 168 mAh g^{-1}. Detailed structural and electrical changes during Li insertion / extraction process have been experimentally investigated by using XRD, neutron diffraction, Raman spectroscopy, NMR, and X-ray absorption fine structure (XAFS) measurements.[43,44] On the other hand, lithium storage capacity of bulk rutile electrodes is very poor (Li_xTiO_2, $x < 0.1$), probably due to remarkably low diffusion rate of Li-ions in *ab*-plane ($D_{ab} = 10^{-15}$ cm^2 s^{-1}).[45] However, recent studies showed that Li-storage capacity of rutile electrodes can dramatically be increased by designing its nanostructure.[45,46] For example, mesoporous rutile-TiO_2 electrode showed very high reversible capacity about 185 mAh g^{-1}.[46]

In the researches of TiO_2 anodes, TiO_2(B) phase attracts a great deal of attention

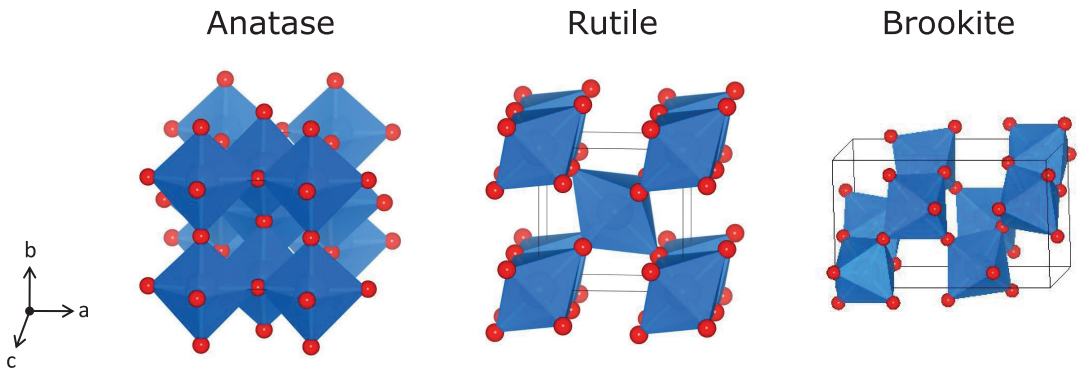

Figure 1-8 Crystal structures of (left) anatase, (center) rutile, and (right) brookite. Oxygen and titanium atoms are shownin red and blue, respectively.

in recent years. Here TiO_2(B) is one of TiO_2 polymorphous discovered by Marchand *et al*. in 1980.[47] As shown in Figure 1-9, TiO_2(B) is also consists TiO_6 octahedron like anatase, rutile and brookite, but the density of TiO_2(B) is much smaller than other TiO_2 polymorphous. Compared to other TiO_2 polymorphous, which has a similar operating voltage (about 1.55 V vs. Li/Li^+), but the TiO_2(B) presents a higher capacity up to 335 mAh g^{-1}. TiO_2(B) is also have attract attentions due to its high-speed lithium insertion/extraction reaction called pseudocapacitive behavior. Therefore, extensive studies of the TiO_2(B) polymorph have been performed in recent years.[48–53] However, detailed lithium storage mechanisms in TiO_2(B) has still not been thoroughly investigated.

1.2.2 Sodium-ion Battey

As mentioned in section 1.2.1.1, the market for LIBs has been rapidly grown. However, lithium resources are confirmed to be unevenly distributed in South America at the present time. The cost of the lithium raw materials has roughly doubled from the first commercialization in 1991 to the present[54], and it would still increases with dissemination of EVs equipped with large-scale LIBs. Therefore, development of alternative rechargeable batteries is required. In this context, sodium-ion batteries (SIBs) should be one of the most promising candidates, because there is no doubt that the sodium resources are inexhaustible and unlimited everywhere

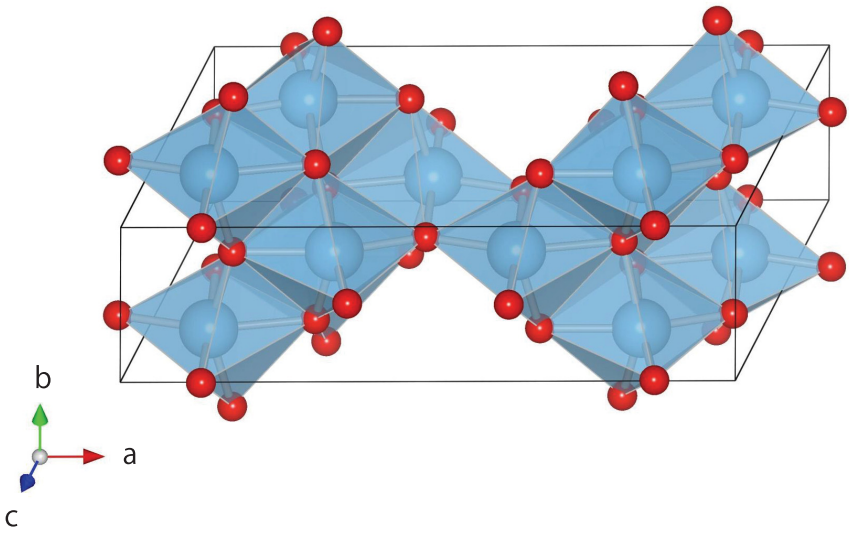

Figure 1-9 Crystal structure of TiO_2(B). Oxygen and titanium atoms are shownin red and blue, respectively.

around the world. The electrochemical equivalent and standard potential of sodium are the most advantageous as post lithium battery.[54,55] However, exploration of new anode materials is required for SIBs, because the graphite, which is commonly used anode in LIB systems, cannot form low-stage intercalation compounds (i.e. sodium-storage capacity of graphite is low) probably due to larger ion-size of sodium compared to that of lithium. Therefore, other ion-storing strategies which are different from intercalation, is required for SIB anode. In this context, ion-clustering storage at hard-carbon materials should be effective. Therefore, extensive studies are performed for hard-carbon electrodes as anode material for SIB. [54,55]

1.2.3 Electric Double-layer Capacitor

Electric double-layer capacitor (EDLC) is electrochemical systems that are used as energy storage devices. Scientifically, the expression EDLC is used to describe the accumulation of charge on the interface of a charged electrode and a surrounding electrolyte. While a classical dielectric capacitor consists of two parallel surfaces where accumulation of two opposite charges occurs as the results of applied electric potential, an EDLC consists of one “real” surface of electronically conducting material (metal, semiconductor, carbon material) and a

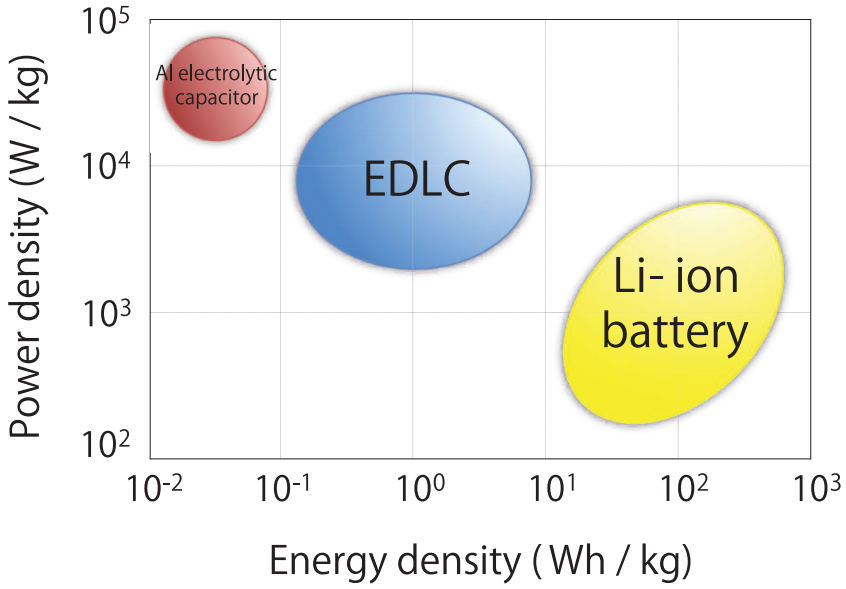

Figure 1-10 Energy density vs. power density plot (Ragone plot) of energy storage devices.

second "virtual" surface that is the inner interfacial limit of the conducting electrolyte solution phase. The double layer distribution of charges is established across this interfacial region. EDLC in its simplest configuration consists of two electrodes immersed into electrolyte and separated by an ion-conduction but electron-insulating membrane. Upon the application of a potential to one of the electrodes the ions of the opposite sign travel from the bulk of the electrolyte and accumulate on its surface in a quantity proportional to the applied voltage, forming a so-called electrical double layer. This double layer consists of an electrical space charge from the electrode side and an ion space charge from the electrolyte side.[56)]

Since physical charge storage remains the dominant mechanism in EDLCs, they are capable of fast delivery of stored charge without any limitation caused by the electrochemical kinetics found in batteries. They are therefore characterized by very high power density and long cycle life, which makes them particularly useful for high power applications. In applications that require high energy and high power delivery, EDLCs can be used to complement the lithium ion rechargeable batteries, which provide high energy density but low power density (see Figure 1-10). On the other hand, the major drawback of EDLCs is their lower energy density, which is bound by the available surface area for ion adsorption, resulting in less energy stored per unit mass compared to that of rechargeable batteries.

1.3 Luminescent Materials

In the field of lighting and display application, the development of white-light sources, possessing high luminous intensity and high efficiency, has aroused great interest.[57] In particular, because of their low energy consumption, light-emitting diodes (LEDs) have attracted a great deal of attention.[58–60] Currently, two types of modules are commonly used to generate LED-based white light: multi-chip type and single-chip type. The multi-chip type consists of individual red, green, and blue (RGB) LEDs; white light is produced by the combination of these three colors. Due to such sophisticated system, the products should be expensive. On the other hand, the single-chip type uses phosphor materials to convert the monochromatic light of a blue or ultraviolet (UV) LED to a broad white-light spectrum as shown in Figure 1-11. For example, due to their high luminous efficacy, a combination of a blue LED and Ce^{3+}-doped yttrium aluminum garnet (Ce^{3+}:YAG) yellow phosphor has been widely used for various applications.[59] However, the commonly available phosphors used with LEDs include expensive and/or environmentally toxic metals such as transition metals and rare-earth elements.[61,62] Furthermore, the color rendering performance of Ce^{3+}:YAG based pseudo-white LED system is not enough. Although the problem of color rendering performance becomes negligible owing to recently developed SiAlON or $CaAlSiN_3$ phosphors, the inorganic phosphors still contain expensive rare-earth elements as luminescent centers. Therefore, a class of stable, efficient, and inexpensive phosphor materialsthat provide a high color rendering performance with less toxicity are strongly desired.

1.4 Nanographene

Since the groundbreaking report by Geim *et al.* in 2004[63], graphene, which is a single layer of graphite, has attracted much attention.[64–67] With its unique physical and electronic structure, graphene is expected to be used in next-generation electronic devices,[68] sensors,[69–72] transparent electrodes,[73,74] and energy storage devices.[75–78] Although graphene samples

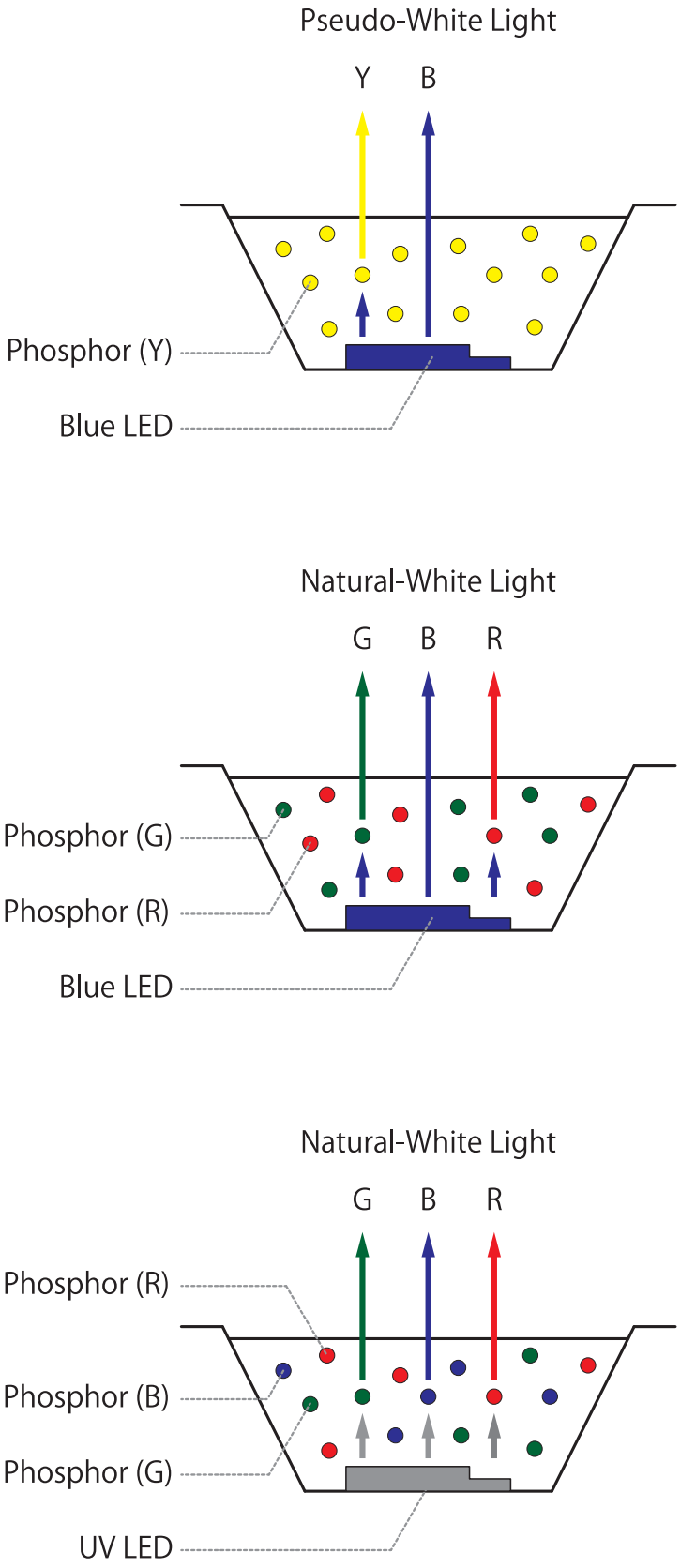

Figure 1-11 Structures of white LEDs using phosphor materials.

prepared by the mechanical cleaving method proposed by Geim *et al*.[63] have a significant advantage in terms of quality, the quantity of samples obtained by this method is considerably limited. Therefore, in recent years, enormous effort has been invested to synthesize large amounts of graphene. High-quality single- and few-layered graphene sheets have been successfully grown by the decomposition of silicon carbide,[79–82] chemical vapor deposition on single and polycrystal transition metals,[83,84] and pulsed laser deposition.[85,86] However, controlling graphene morphology (size and edge structure) with these top-down methods is still a challenge. Because theoretical studies have predicted that the electronic and magnetic properties of graphenes are greatly affected by their size and edge structure,[87–91] control of their morphology is essential for graphene applications.

To this end, chemical syntheses based on the bottom-up strategy should be a promising approach because we can control graphene morphology by designing appropriate precursors. For example, Simpson et al. reported the synthesis route for a $C_{222}H_{42}$ molecule with 91 benzene rings using the cyclodehydrogenation reaction of a $C_{222}H_{150}$ polyphenylene dendritic precursor.[92] Although this approach could be used for large-scale production of graphene-like molecules of a defined structure, such an organic synthetic route requires many stepwise reactions.

Another bottom-up approach for graphene synthesis is using direct dehydrogenation reaction of commonly available polycyclic aromatic hydrocarbon (PAH) precursors. For example, Talyzin *et al*. recently reported the thermal polymerization of coronene ($C_{24}H_{12}$) molecules.[93] However, the exact molecular size and structure of the polymerized products were not well determined probably because of the large variety of product molecules. Because coronene has an isotropic zigzag edge structure, we cannot control growth direction and morphology. A promising method for controlling graphene morphology with PAH precursors is a template method that uses single-walled carbon nanotubes (SWCNTs) as a reactor.[94–97] Long-length and width-defined graphene nanoribbons (GNRs) can be synthesized by this method. However, the extraction of GNRs from SWCNTs is still a difficult task. To synthesize GNRs without using a structural template, we should use PAH precursors with

an anisotropic edge structure. Recently, Cai *et al*. reported a method of fabricating GNRs from PAH molecules having -Br groups at the zigzag edge.[98] Here, the -Br groups were used as structural directing milestones for graphene growth. Moreover, some of the acenes (PAH molecules composed of linearly fused benzene rings) seem to polymerize in a definite direction without any special functional groups. For instance, a fusing reaction of pentacene ($C_{22}H_{14}$) molecules was reported by Roberson *et al*.[99] By heating pentacenes under inert gas flow, a dehydrogenation condensation reaction occurs at the zigzag edge and a mixture of a pentacene dimer (peripentacene) and trimer (trisperipentacene) can be obtained.

1.5 Objectives and Outline of This Thesis

As mentioned in Section 1.1.2, various types of mesoporous materials having ordered frame-work structure can be synthesized by recent technologies. The author thought that by changing or modifying their framework compositions, mesoporous carbon–ceramic composites would be used for various types of application fields. Since the advancement of the energy storage and conversion technology is an essential approach to overcome the global warming issue that the world is currently facing, various types of mesoporous carbon–ceramic composites were designed and synthesized to develop superior electrochemical energy storage and conversion materials in this study.

Since the characterizations of structure of mesopore is essential task in the researche fields of mesoporous materials, the author proposed novel structural characterization method using small-angle powder X-ray diffraction (XRD) in Chapter 2. In addition to the previously determined structural symmetry and pore-to-pore distance, diameter of mesopores and their density of frame-work can also be determined by using this method. Furthermore, the method was applied for structure analysis of mesoporous materials heat-treated at various temperatures. Thermal-stability of mesoporous SiO_2, mesoporous carbon–SiO_2, and mesoporous carbon were discussed in Chapter 3.

For energy-storage application, electrochemical energy-storage properties of mesoporous carbons and mesoporous carbon–TiO_2 composites were discussed in Chapters 4

and 5, respectively, in while, photo-energy conversion (Photoluminescence) properties of oxidized mesoporous carbon–SiO_2 composites were studied in Chapter 6. In the carbon–SiO_2 composites, carbon-fragments seems to play an important role for luminescence. In order to discuss the possibility of carbon-fragment based luminescence, graphene nano-fragments were synthesized and characterized in Chapter 7.

These results showed that the mesoporous carbon–ceramic composites have hopeful-potential for energy storage and conversion applications.

Chapter 2

Structure Determination of Ordered Mesoporous Materials using X-ray Diffraction

2.1 Introduction

As mentioned in Section 1.1.3, structure analysis based on XRD peak positions is a commonly used method for ordered mesoporous materials. From the XRD peak positions, structural symmetry and the distances between adjacent mesopores have been determined. On the other hand, quantitative discussions of XRD peak intensities have not often been reported. According to the previous reports[100–103], mesopore diameter seems to also be estimated by the analysis of XRD peak intensities, in addition to the commonly determined structural symmetry and pore-to-pore distances. Since XRD data provide direct structural information without any semi-empirical parameters or assumptions which required for gas adsorption / desorption method, the XRD-based method shold be valuable for ordered mesoporous materials. In addition, the author believe that the XRD method has great potential for various kinds of *in situ* experiments (*in situ* observatoin under high-pressure, high-temperature, in solution etc.), because the XRD method does not require any special measurement-environments or pretreatments unlike electron microscopy or gas-adsorption methods. Therefore, the author focused on the XRD method in this study.

In 1994, B. P. Feuston *et al*. reported model structures for MCM-41 silica materials obtained from molecular dynamics (MD) simulations.[100] In their report, XRD pattern simulations were also performed using optimized atomic coordination obtained from the MD calculations. They mentioned that the XRD peak intensities are highly dependent on mesopore diameter and unit cell size. However, no general relationship between XRD peak intensity and

mesopore diameter was discussed in their paper. Furthermore, XRD pattern calculation based on MD optimization is not suitable for routine analysis, because the MD simulation requires significant computational expense. Owing to the dramatic improvements of computational technology, the problem of calculation cost is gradually fading out in recent years. However, the MD-based method is still not easy to use, because the method requires sophisticated skill and knowledge to perform molecular calculation. Fortunately, such an elaborate MD simulation process may be not indispensable for XRD pattern calculation. W. Schmidt demonstrated that reasonable XRD pattern simulation can be performed even without optimization of the atomic position in the model structure.[103] This means that the detailed atomic coordination does not have a significant effect on XRD pattern calculation for ordered mesoporous materials. In the meantime, M. Impéror-Clerc *et al*. demonstrated an XRD pattern simulation for SBA-15 silica materials using a simpler structural model.[101] In their paper, the solid framework structure (amorphous silica region) was approximated by a uniform electron density matrix instead of by exact atomic configurations. According to their theory, the XRD peak intensity of hkl lines (I_{hkl}) are calculated from a unit cell form factor ($F(q)$) as follows:

$$I_{hkl} = K M_{hkl} \frac{|F(q_{hkl})|^2}{q_{hkl}^2} \tag{2-1}$$

where K is a scaling factor used to adjust the peak intensities to match the experimentally observed intensities, M_{hkl} is a multiplicity factor for the hkl line, q_{hkl} is the magnitude of the scattering vector for the hkl line (here, q_{hkl} is calculated using Bragg's law), and $1/q_{hkl}^2$ is the Lorentz factor for powder diffraction. The form factor was calculated from a Fourier transform of the electron density distribution in the unit cell. Similar uniform electron density matrix model was also adapted for MCM-41 silica materials by L. A. Solovyov *et al*.[102] However, the author believe that the XRD pattern calculation using equation 2-1 may be problematic because the range of pore ordering (i.e., coherent length, crystallite size) was not precisely considered. XRD pattern calculation based on the equation 2-1 would be correct only for infinitely-ordered mesopore samples. Since the XRD peak width, which is indicative of crystallite size, of mesoporous materials is usually broad (i.e., crystallites are small), such an infinitely-ordered pore description may be unreasonable.

Therefore, the author would like to propose a modified XRD calculation model for ordered mesoporous materials in this section. In this model, the degree of interference between unit cells (i.e., crystallite size effect) was treated by convoluting the unit cell form factor function with a Laue-type interference function. In order to test the validity of our method, various types of ordered mesoporous samples having 2D-hexagonal symmetry were synthesized, and their XRD patterns were compared with theoretically calculated patterns.

2.2 Experimental Methods

2.2.1 Sample Preparation

2.2.1.1 Synthesis of SBA-15 Mesoporous SiO_2

SBA-15 mesoporous SiO_2 was synthesized as reported by Zhao *et al.*[104] In this procedure, we used tetraethoxysilane (TEOS) as a SiO_2 precursor, and triblock copolymer Pluronic P123 ($HO(CH_2CH_2O)_{20}(CH_2CH(CH_3)O)_{70}(CH_2CH_2O)_{20}H$; BASF) as a structure directing template. First, 4.0 g of Pluronic P123 was dissolved in a solution of 30 g of water and 120 g of 0.2 M HCl aqueous solution, and stirred at 60 °C for 30 min. Then, 8.5 g of TEOS was added to the solution. After stirring the mixture for 10 min, it was kept at 35 °C for 20 h without stirring. Then, the mixture was aged at 80 °C for 72 h. The generated solid product was filtered, washed with water and ethanol, and dried in an oven at 140 °C for 4 h. To remove the Pluronic P123 template, the sample was heated in an electric furnace at 550 °C for 4 h under air. In order to avoid mesostructure collapse, the heating and cooling rates were fixed at 5 °C min^{-1}. After the heat treatment, the obtained mesoporous SiO_2 was ground into a fine powder with an agate mortar. For convenience, the obtained product was designated as MS1 in this chapter.

2.2.1.2 Synthesis of MCM-41 Mesoporous SiO_2

MCM-41 mesoporous SiO_2 fiber samples were synthesized using tetrabutoxysilane (TBOS) as a SiO_2 precursor, and cetyltrimethylammonium bromide (CTAB) as a structure directing template.[105] First, 2.25 g of CTAB was dissolved in a solution of 32.5 g of water and 125 g of 5 M HCl aqueous solution, and stirred at room temperature for 30 min. Then, 2.7 g of TBOS was dripped into the solution, and kept at 50 °C for 10 days without stirring. The resultant solid fibers were filtered, washed with water and ethanol, and dried in an oven at 80 °C for 12 h. The obtained mesoporous SiO_2 was ground into a fine powder with an agate mortar. In order to remove the CTAB template, two types of post-treatments were performed for the as-synthesized samples: one was a solvent extraction method, and the other was a combustion method. In the solvent extraction method, the as-synthesized SiO_2 was refluxed with ethanol in a Soxhlet extractor for 30 h. After the extraction, the sample was dried in an oven at 80 °C for 12 h. The obtained product was designated as MS2. On the other hand, in the combustion method, the as-synthesized SiO_2 was heated in an electric furnace under O_2 flow (50 ccm) at 500 °C for 5 h. The heating and cooling rates were fixed at 5 °C min^{-1} to avoid mesostructure collapse. The obtained product was designated as MS3.

2.2.1.3 Synthesis of Resol

The phenol-formaldehyde resin (resol) used as a carbon source was prepared by following procedure. First, 0.61 g of phenol (65 mmol) was mixed with 1.3 mL of 20 wt.% NaOH aqueous solution, and stirred at 50 °C for 10 min. Then, 10.5 g of formalin (35–38 wt.% formaldehyde; 120–130 mmol) was slowly added in the solution. After further stirring at 70 °C for 1 h, the mixture was cooled to room temperature and neutralized with HCl aqueous solution to stop the polymerization reaction. Then, in order to remove unreacted phenol and formaldehyde, vacuum evaporation was performed with rotary evaporator below 50 °C. The obtained resol was diluted with ethanol to obtain 20 wt.% solution. The resol's ethanolic solution was kept at about 0 °C at least 3 days to precipitate NaCl generated at the neutralization

step. The NaCl precipitation was removed by decantation before use.

2.2.1.4 Synthesis of Mesoporous Carbon–SiO_2 Composite

The mesoporous carbon–SiO_2 composite sample was synthesized using the triconstituent co-assembly method proposed by Liu *et al.*[30] In this procedure, we used phenol-formaldehyde resin (resol) as a carbon source, TEOS as a SiO_2 precursor, and triblock copolymer Pluronic F127 ($HO(CH_2CH_2O)_{106}(CH_2CH(CH_3)O)_{70}(CH_2CH_2O)_{106}H$; BASF) as a structure directing template. First, 0.5 g of Pluronic F127 was dissolved in a solution of 32.0 g of ethanol and 4.0 g of 0.2 M HCl aqueous solution, and stirred for 15 min. Then 8.0 g of TEOS and 20.0 g of 20 wt.% resol's ethanolic solution (synthesis procedure is described in Section 2.2.1.3) was added in the solution. After stirring the mixture for 2 h, it was transferred into polytetrafluoroethylene (PTFE) dishes. The dishes were maintained at 40 °C for 24 h to evaporate ethanol. Subsequently they were kept at 100 °C for 24 h to attain thermo-polymerization. The polymerized product was carbonized by heating in an electric furnace under N_2 flow (30 ccm) at 900 °C for 1 h following elimination of Pluronic F127 by heating at 400 °C for 2 h. The heating and cooling rates were fixed at 1 °C min^{-1} to avoid mesostructure collapse. After the carbonization, obtained mesoporous carbon–SiO_2 composite was ground into a fine powder with an agate mortar. The obtained product was designated as MCS.

2.2.2 Structural Characterization

The nanostructures of the obtained samples were observed using a JEOL JEM-z2500 transmission electron microscope operated at 200 kV. The removal of surfactant molecules used as a structure directing template was confirmed by thermogravimetric (TG) analysis using a Shimadzu TGA-50 instrument. The TG analysis also determined the carbon / SiO_2 ratio of the MCS sample. Nitrogen adsorption / desorption isotherms at 77 K were measured using a Shimadzu Gemini 2375 instrument. Prior to the isotherm measurements, the samples were heat treated at 200 °C under vacuum (< 3 Pa) for at least 1 h to remove adsorbed

moisture. The specific surface areas (S_{BET}) were estimated using the Brunauer–Emmett–Teller (BET) method[32] and the adsorption data in the relative pressure (P / P_0) range from 0.05 to 0.16. The total pore volumes (V_{total}) were calculated using the Gurvich rule at $P / P_0 = 0.97$. The α_s-plot method was used to estimate the micropore (V_{micro}) and mesopore (V_{meso}) volumes. In the α_s analysis, adsorption isotherm data for the LiChrospher Si-1000 SiO_2 reported by Jaroniec *et al.*[106] was used as the reference adsorbent. The pore-size distributions were calculated based on an analysis of the adsorption branch of the isotherms using the Barrett–Joyner–Halenda (BJH) method.[33] In the BJH calculation, the Kelvin radius (r_K) and statistical film thickness of the N_2 adsorbed layer (t) were estimated using the Kelvin equation (equation 2-2) and the Halsey equation (equation 2-3), respectively.

$$r_K = -\frac{2\gamma V_L}{RT \ln (P/P_0)} \tag{2-2}$$

$$t = 3.54 \left[-\frac{5}{\ln (P/P_0)} \right]^{1/3} \tag{2-3}$$

where r_K is expressed in Å, γ is the surface tension of the liquid N_2 (8.88×10^{-3} J m^{-2}), V_L is the molar volume of the liquid N_2 (3.468×10^{25} Å^3 mol^{-1}), R is the ideal gas constant (8.8314×10^{20} J Å^2 K^{-1} mol^{-1} m^{-2}), and T is the absolute temperature of adsorption (77 K). t is expressed in Å. In this paper, the primary mesopore diameter determined by the BJH method is designated as D_{BJH}. Since the traditional BJH method tends to underestimate mesopore diameter,[34, 107] a modified BJH method proposed by Kruk, Jaroniec, and Sayari (BJH–KJS method[107]) was also used in this study. In the BJH-KJS calculation, a modified Kelvin equation developed for N_2 adsorption on SiO_2 samples with cylindrical mesopores (equation 2-4), and a Harkins–Jura type equation (equation 2-5) were used to calculate r_K and t, respectively.

$$r_K = -\frac{2\gamma V_L}{RT \ln (P/P_0)} + 3 \tag{2-4}$$

$$t = \left[\frac{60.65}{0.03071 - \log (P/P_0)} \right]^{0.3968} \tag{2-5}$$

The primary mesopore diameter estimated by the KJS method is designated as D_{KJS} in this paper.

Powder XRD measurements were carried out using a Rigaku Nano-Viewer diffractometer, equipped with a two dimensional (2D) imaging plate detector (Rigaku R-AXIS IV^{++}), using Cu Kα radiation (λ = 1.54 Å) as an incident beam. The XRD measurements were performed in transmission geometry as shown in Figure 2-1. Camera Length was set to 700 mm. Lindemann glass capillary tubes (Hilgenberg; ϕ = 0.5 mm) were used as a sample container, and the typical exposure time was 30 min. For MCM-41 (MS2 and MS3) samples, XRD measurements using synchrotron radiation were also performed to obtain high-quality diffraction patterns. The synchrotron XRD measurements were performed using beam line BL-18C at the Photon Factory (PF) in the High Energy Accelerator Research Organization (KEK), Tsukuba, Japan. The synchrotron radiation beams emitted from an electron storage ring operated at 2.5 GeV were monochromatized by a Si(111) double-crystal monochromator and collimated by a pinhole collimator 100 μm in diameter. The incident X-ray wavelength for these measurements was λ = 0.613 Å. Each diffraction pattern was collected using a 2D imaging plate detector (Fujifilm; 200 mm × 250 mm) located 500 mm behind the sample position. GE Healthcare Typhoon FLA7000 imaging plate reader was used to digital conversion. The typical exposure time was 5 min. Lindemann glass capillary tubes (Hilgenberg; ϕ = 1.0 mm) were used as a sample container. Prior to the measurements, the incident X-ray wavelength and the distance from the sample to the imaging plate detector were calibrated using the XRD peaks of a CeO_2 powder by the double cassette method.[108] Prior to further analysis, the obtained XRD intensities $I_{\mathrm{obs}}(2\theta)$ were corrected for polarization factor $p(2\theta)$, geometric factor for the 2D flat plate detector $G(2\theta) = \cos^3 2\theta$,[109] dark current noise of the detector I_{dark}, transmission factor, and background scattering from a blank capillary and air $I_{\mathrm{back}}(2\theta)$ as follows:

$$I_{\mathrm{corr}}(2\theta) = \frac{1}{p(2\theta)\,G(2\theta)} \left\{ \frac{I_0}{I_{\mathrm{s}}} \left[I_{\mathrm{obs}}(2\theta) - I_{\mathrm{dark}} \right] - \frac{I_0}{I_{\mathrm{b}}} \left[I_{\mathrm{back}}(2\theta) - I_{\mathrm{dark}} \right] \right\} \qquad (2\text{-}6)$$

where $I_{\mathrm{corr}}(2\theta)$, I_0, I_{s}, and I_{b} are the corrected XRD intensity, incident X-ray intensity, X-ray intensity after transmission through the sample, and X-ray intensity after transmission through the blank capillary, respectively. All XRD measurements were performed at room temperature.

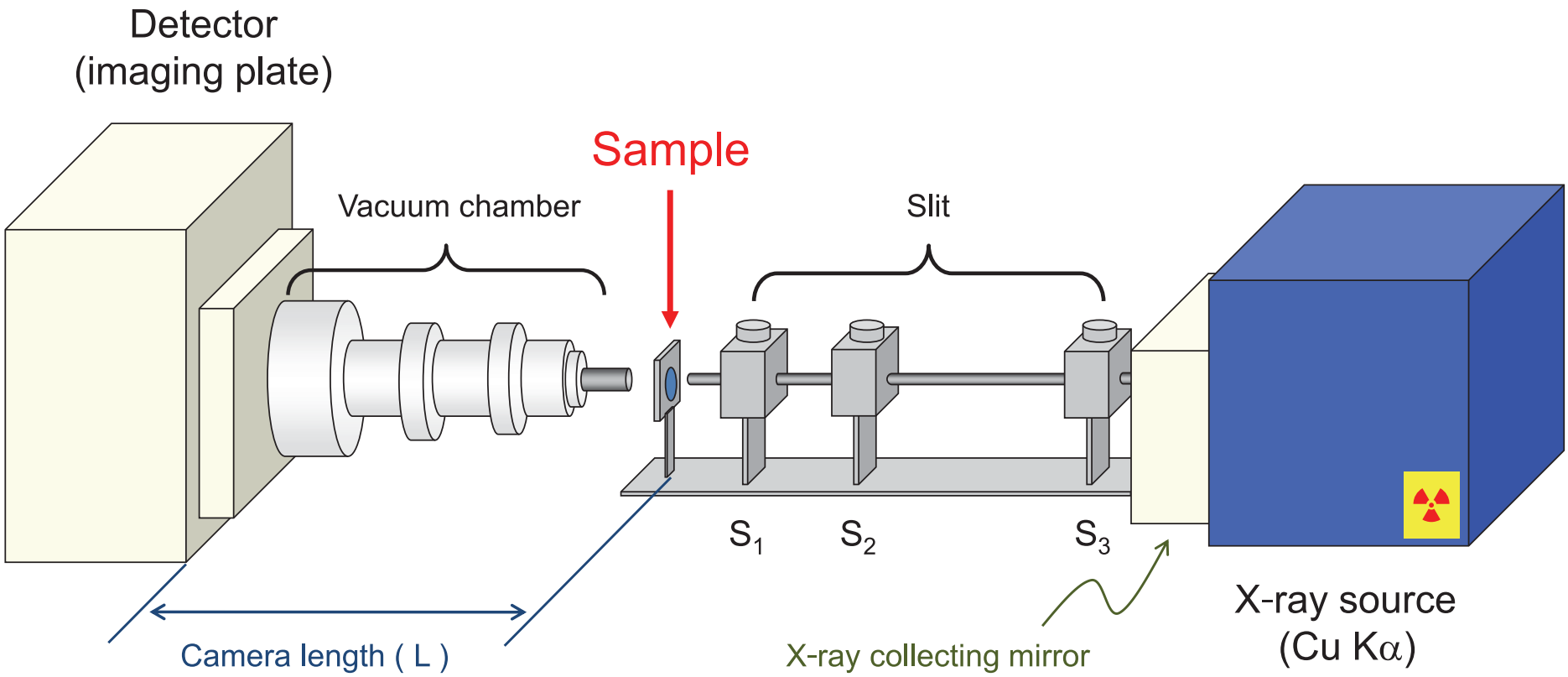

Figure 2-1 Block diagrarn of small-angle XRD diffractometer.

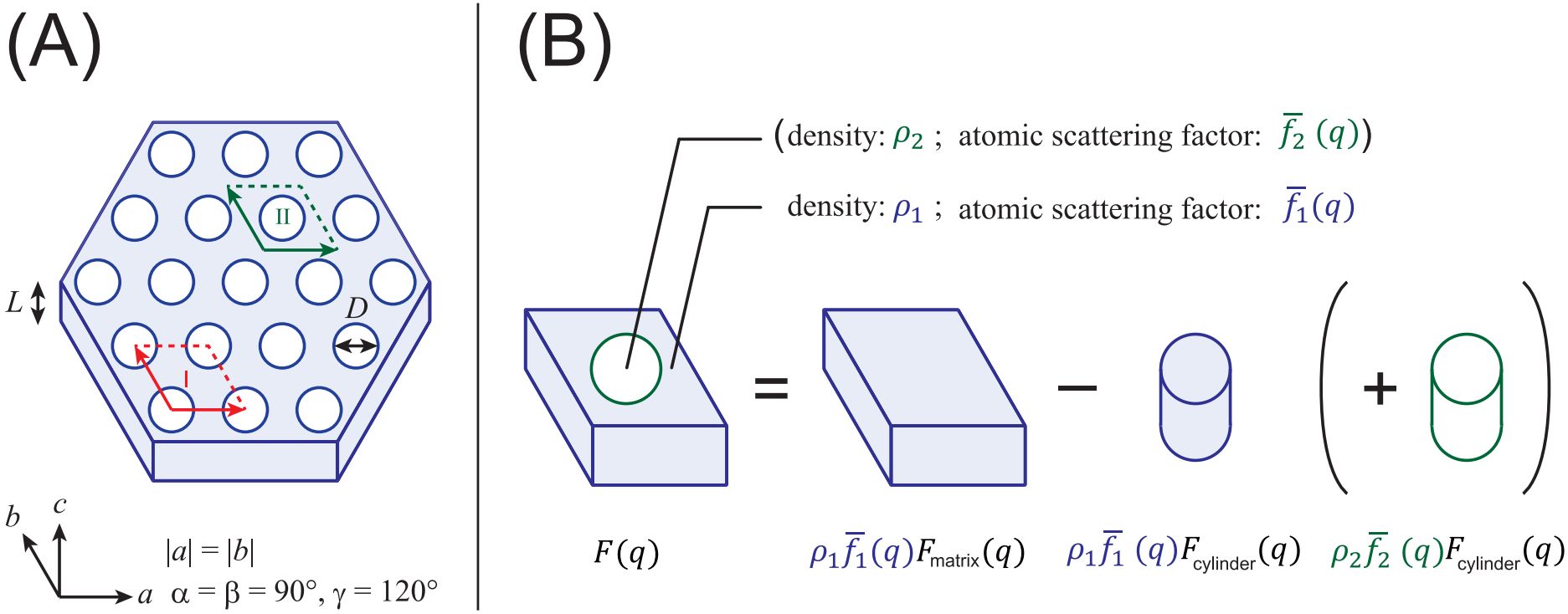

Figure 2-2 (A) Schismatic structure of the ordered mesoporous material examined in this study. Cylindrical mesopores (diameter: $D = 2R$, length: L) are 2D hexagonally aligned, and form an ordered crystalline nanostructure. The structural backbone (wall region) consists of a uniform amorphous matrix (density: ρ_1). (B) Calculation scheme of the unit cell form factor ($F(q)$).

2.3 Theoretical Basis

2.3.1 Theoretical XRD Pattern for Ordered Mesoporous Materials with 2D-Hexagonal Symmetry

In this section, theoretically derivation of powder X-ray diffraction patterns of ordered mesoporous materials with 2D-alingned cylindrical pores are performed. Here, the author assume the structure model shown schematically in Figure 2-2(A). In this model, empty cylindrical mesopores (radius: R; length: L) are hexagonally aligned in a uniform amorphous matrix (density: ρ_1; average atomic X-ray scattering factor: $\overline{f_1}(q)$).

The diffraction intensity from a non-oriented powder crystalline sample, $I(q)$, would be calculated using a unit cell form factor $F(q)$ in the following manner:

$$I\left(q\right) \propto \left|F\left(q\right)\right|^2 L\left(q\right) \sum_{h,\,k,\,l} M_{hkl} G_{hkl}\left(q\right) \tag{2-7}$$

where q is the magnitude of the scattering vector ($q = 4\pi \sin\theta \,/\, \lambda$), θ is the scattering angle, λ is the X-ray wavelength, $L(q)$ is the Lorentz factor for powder diffraction ($L = 1 \,/\, (\sin^2\theta \cos\theta)$), M_{hkl} is the multiplicity factor of the hkl diffraction line, and $G_{hkl}(q)$ is the Laue function representing the interference between unit cells. Since the exact form of the Laue function is not appropriate for numerical calculations, $G_{hkl}(q)$ was approximated by a pseudo Voigt function in this study. The pseudo Voigt function G'_{hkl} is the sum of a Gaussian profile and a Lorenz profile, and can be expressed as

$$G'_{hkl}\left(q\right) = \eta \frac{2}{w}\sqrt{\frac{\ln 2}{\pi}} \exp\left[-4\ln 2\left(\frac{q - q_{hkl}}{w}\right)^2\right] + \left(1-\eta\right)\frac{2}{\pi w}\left[1 + 4\left(\frac{q - q_{hkl}}{w}\right)^2\right]^{-1} \tag{2-8}$$

where w is the full-width-at-half-maximum (FWHM), η is the Gaussian/Lorenz ratio, and q_{hkl} is the scattering vector at the Bragg's angles of the hkl line. Note that such pseudo Voigt type peak profile functions are often used in Rietveld refinements for powder XRD analysis. In the meantime, for 2D-hexagonally aligned mesoporous materials, only $l = 0$ (i.e. $hk0$) diffraction lines are observed. Therefore, diffraction indices are represented by two digits in

the following parts. In this time, the scattering vector at the Bragg's angles of the hk line q_{hk} can be expressed as

$$q_{hk} = \frac{4\pi}{a}\sqrt{\frac{h^2 + hk + k^2}{3}} \tag{2-9}$$

where a is a unit cell lattice constant that represents the interval of adjacent mesopore centers. The multiplicity factors of $h0$, hh, and hk ($h \neq k$, $k \neq 0$) diffraction peaks become 6, 6, and 12, respectively.

The form factor $F(q)$ can be calculated on the basis of the structure model shown in Figure 2-2(A). In this study, we considered a shifted unit cell (indicated by II in Figure 2-2(A)), instead of the commonly used version (indicated by I in Figure 2-2(A)). As shown in Figure 2-2(B), $F(q)$ may be expressed as follows:

$$F(q) = \rho_1 \overline{f_1}(q) F_{\text{matrix}} - \rho_1 \overline{f_1}(q) F_{\text{cylinder}}(q) \tag{2-10}$$

where $F_{\text{matrix}}(q)$ and $F_{\text{cylinder}}(q)$ represent structure factors of the uniform matrix and of the cylinder (radius: R, length: L), respectively. The structure factors could be calculated from a Fourier transform of the atomic (or more principally electron density) distribution. Since the Fourier transform of a constant value, that representing the uniform matrix, becomes a delta function $\delta(q)$, the $F_{\text{matrix}}(q)$ terms would be replaced by zero, except for in the $q = 0$ case. Therefore, equation 2-10 can be rewritten as

$$F(q) = -\rho_1 \overline{f_1}(q) F_{\text{cylinder}}(q) \tag{2-11}$$

Taking mesoporous SiO_2 as an example, $\overline{f_1}(q)$ may be expressed as

$$\overline{f_1}(q) = \frac{1}{3} f_{\text{Si}}(q) + \frac{2}{3} f_{\text{O}}(q) \tag{2-12}$$

where $f_{\text{Si}}(q)$ and $f_{\text{O}}(q)$ represent the atomic scattering factors of Si and O, respectively. Although practical values of atomic scattering factors have been tabulated in the International Tables for Crystallography,[110] the $\overline{f_a}(q)$ term would be ignored in practical calculations since the atomic scattering factors of light atoms (such as Si, O, and C) are approximately constant

in the small-angle region. In the meantime, $F_{\text{cylinder}}(q)$ would be expressed as follows:

$$F_{\text{cylinder}}(\boldsymbol{q}) = \int \exp(-i\boldsymbol{q}\cdot\boldsymbol{r})\,\mathrm{d}\boldsymbol{v} \tag{2-13}$$

$$= \int_{z=-L/2}^{L/2}\int_{r=0}^{R}\int_{\phi=0}^{2\pi} r\exp(-i\boldsymbol{q}\cdot\boldsymbol{r})\,\mathrm{d}\phi\mathrm{d}r\mathrm{d}z \tag{2-14}$$

where $\boldsymbol{r}(z;\ r;\ \phi)$ is the positional vector in the cylinder. In a cylindrical coordinate system (see Figure 2-3), $\boldsymbol{q}$ and $\boldsymbol{r}$ may be represented as follows:

$$\boldsymbol{q} = \begin{pmatrix} q_{\perp} \\ 0 \\ q_{\parallel} \end{pmatrix} \tag{2-15}$$

$$\boldsymbol{r} = \begin{pmatrix} r\cos\phi \\ r\sin\phi \\ z \end{pmatrix} \tag{2-16}$$

where, $q_{\perp}$ is the $\boldsymbol{q}$ component perpendicular to the direction of cylindrical axis (c axis in Figure 2-2(A)), and $q_{\parallel}$ is the $\boldsymbol{q}$ component parallel to the direction of cylindrical axis. In this case, $\boldsymbol{q}\cdot\boldsymbol{r}$ is expressed as "$q_{\perp}r\cos\phi + zq_{\parallel}$". Thus, equation 2-14 is rewritten as follows:

$$F_{\text{cylinder}}(\boldsymbol{q}) = \int_{z=-L/2}^{L/2}\int_{r=0}^{R}\int_{\phi=0}^{2\pi} r\exp\left[-i\left(q_{\perp}r\cos\phi + zq_{\parallel}\right)\right]\mathrm{d}\phi\mathrm{d}r\mathrm{d}z \tag{2-17}$$

$$= \left[\int_{r=0}^{R}\int_{\phi=0}^{2\pi} r\exp(-iq_{\perp}r\cos\phi)\,\mathrm{d}\phi\mathrm{d}r\right]\left[\int_{z=-L/2}^{L/2}\exp(-izq_{\parallel})\,\mathrm{d}z\right] \tag{2-18}$$

The radial component $F_{\perp}(q_{\perp})$, written in the left side bracket in equation 2-18, becomes as follows:

$$F_{\perp}(q_{\perp}) = \int_{r=0}^{R}\int_{\phi=0}^{2\pi} r\exp(-iq_{\perp}r\cos\phi)\,\mathrm{d}\phi\mathrm{d}r \tag{2-19}$$

$$= \int_{r=0}^{R} r\left[\int_{\phi=0}^{2\pi}\exp(-iq_{\perp}r\cos\phi)\,\mathrm{d}\phi\right]\mathrm{d}r \tag{2-20}$$

$$= \int_{r=0}^{R} 2\pi r J_0(q_{\perp}r)\,\mathrm{d}r \tag{2-21}$$

$$= \int_{t=0}^{q_{\perp}R}\frac{2\pi t}{q_{\perp}^2}\mathrm{d}t\Bigg|_{t=q_{\perp}R} \tag{2-22}$$

$$= 2\pi R^2\frac{J_1(q_{\perp}R)}{q_{\perp}R} \tag{2-23}$$

where, J_0 is the 0th order Bessel function of the first kind, J_1 is the 1st order Bessel function of the first kind. At the step between equations 2-20 to 2-21, the following mathematical relations were used:

$$J_0(\xi) = \frac{1}{2\pi}\int_{\eta=0}^{2\pi} \exp\left(i\xi\cos\eta\right) \mathrm{d}\eta \tag{2-24}$$

$$J_0\left(-\xi\right) = J_0\left(\xi\right) \tag{2-25}$$

Furthermore, the following equation was also used at the step between equations 2-22 to 2-23.

$$\frac{\mathrm{d}}{\mathrm{d}t}\left[tJ_1\left(t\right)\right] = tJ_0\left(t\right) \tag{2-26}$$

On the other hand, the axial component $F_{\|}(q_{\|})$, written in the right side bracket in equation 2-18, becomes as follows:

$$F_{\|}\left(q_{\|}\right) = \int_{z=-L/2}^{L/2} \exp\left(-izq_{\|}\right) \mathrm{d}z \tag{2-27}$$

$$= \int_{u=iq_{\|}L/2}^{-iq_{\|}L/2} -\frac{1}{iq_{\|}} \exp(u)\mathrm{d}u\Bigg|_{u=-izq_{\|}} \tag{2-28}$$

$$= -\frac{1}{iq_{\|}}\left\{\exp\left(-\frac{iq_{\|}L}{2}\right) - \exp\left(\frac{iq_{\|}L}{2}\right)\right\} \tag{2-29}$$

$$= -\frac{1}{iq_{\|}}\left\{\left[\cos\left(-\frac{iq_{\|}L}{2}\right) + i\sin\left(-\frac{iq_{\|}L}{2}\right)\right] - \left[\cos\left(\frac{iq_{\|}L}{2}\right) - i\sin\left(\frac{iq_{\|}L}{2}\right)\right]\right\} \tag{2-30}$$

$$= -\frac{1}{iq_{\|}}\left\{\left[\cos\left(\frac{iq_{\|}L}{2}\right) - i\sin\left(\frac{iq_{\|}L}{2}\right)\right] - \left[\cos\left(\frac{iq_{\|}L}{2}\right) + i\sin\left(\frac{iq_{\|}L}{2}\right)\right]\right\} \tag{2-31}$$

$$= -\frac{1}{iq_{\|}}\left[-2i\sin\left(\frac{q_{\|}L}{2}\right)\right] \tag{2-32}$$

$$= \frac{\sin\left(q_{\|}L/2\right)}{q_{\|}L/2} \tag{2-33}$$

Therefore, equation 2-18 becomes the following expression:

$$F_{\text{cylinder}}\left(\boldsymbol{q}\right) = F_{\text{cylinder}}\left(q_{\perp},\, q_{\|}\right) = 2\pi R^2 \frac{J_1\left(q_{\perp}R\right)}{q_{\perp}R}\frac{\sin\left(q_{\|}L/2\right)}{q_{\|}L/2} \tag{2-34}$$

Because most mesoporous materials have very large L values, the term "$\sin(q_{\|}L\,/\,2)\,/\,(q_{\|}L\,/\,2)$" behaves like a delta function, $\delta(q_{\|})$. This means that diffraction peaks can be observed only when $q_{\|} \approx 0$ (i.e. $|q| \approx q_{\perp}$). This is consistent with the well-known

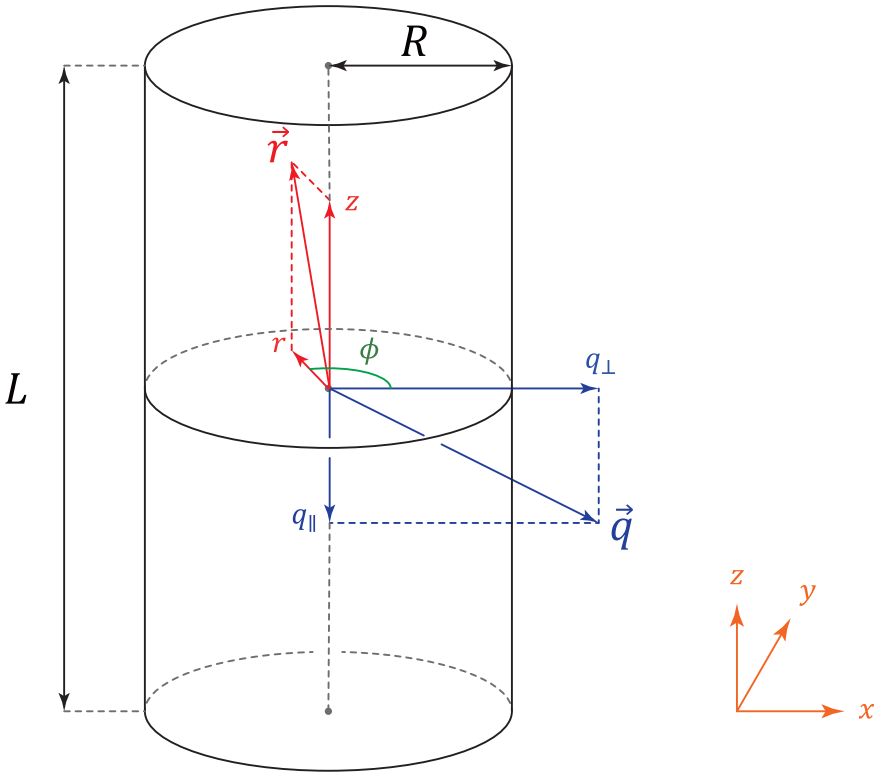

Figure 2-3 Cylindrical coordinate system used to calculate the form factor of cylindrical pore F_{cylinder}. R: pore radius; L: pore length; $\boldsymbol{q}$: X-ray scattering vector; $\boldsymbol{r}$: positional vector in cylindrical pore; $q_\perp$: $\boldsymbol{q}$ component perpendicular to the direction of cylindrical axis; $q_\parallel$: $\boldsymbol{q}$ component parallel to the direction of cylindrical axis; r: $\boldsymbol{r}$ component perpendicular to the direction of cylindrical axis; z: $\boldsymbol{r}$ component parallel to the direction of cylindrical axis; ϕ: angle between $q_\perp$ and r.

experimental axiom that only $l = 0$ diffraction lines are observed in 2D-hexagonal mesoporous materials. In this case, equation 2-34 can be further simplified to the following expression:

$$F_{\text{cylinder}}(q) = 2\pi R \frac{J_1(qR)}{q} \tag{2-35}$$

Because the mesopore channels in real materials are not perfectly oriented, and their positions fluctuate as illustrated in Figure 2-4, additional terms are required for practical XRD pattern fitting. In this work, in order to consider the fluctuation of mesopore positions (Figure 2-4(B)), equation 2-7 was multiplied by the Debye–Waller factor ($D(q;\ \sigma) = \exp(-\sigma^2 q^2 / 2)$; σ: mean-square displacement), assuming a Gaussian displacement of pore center positions. The detail of this treatment will be discussed in Section 2.3.2.1. In addition to

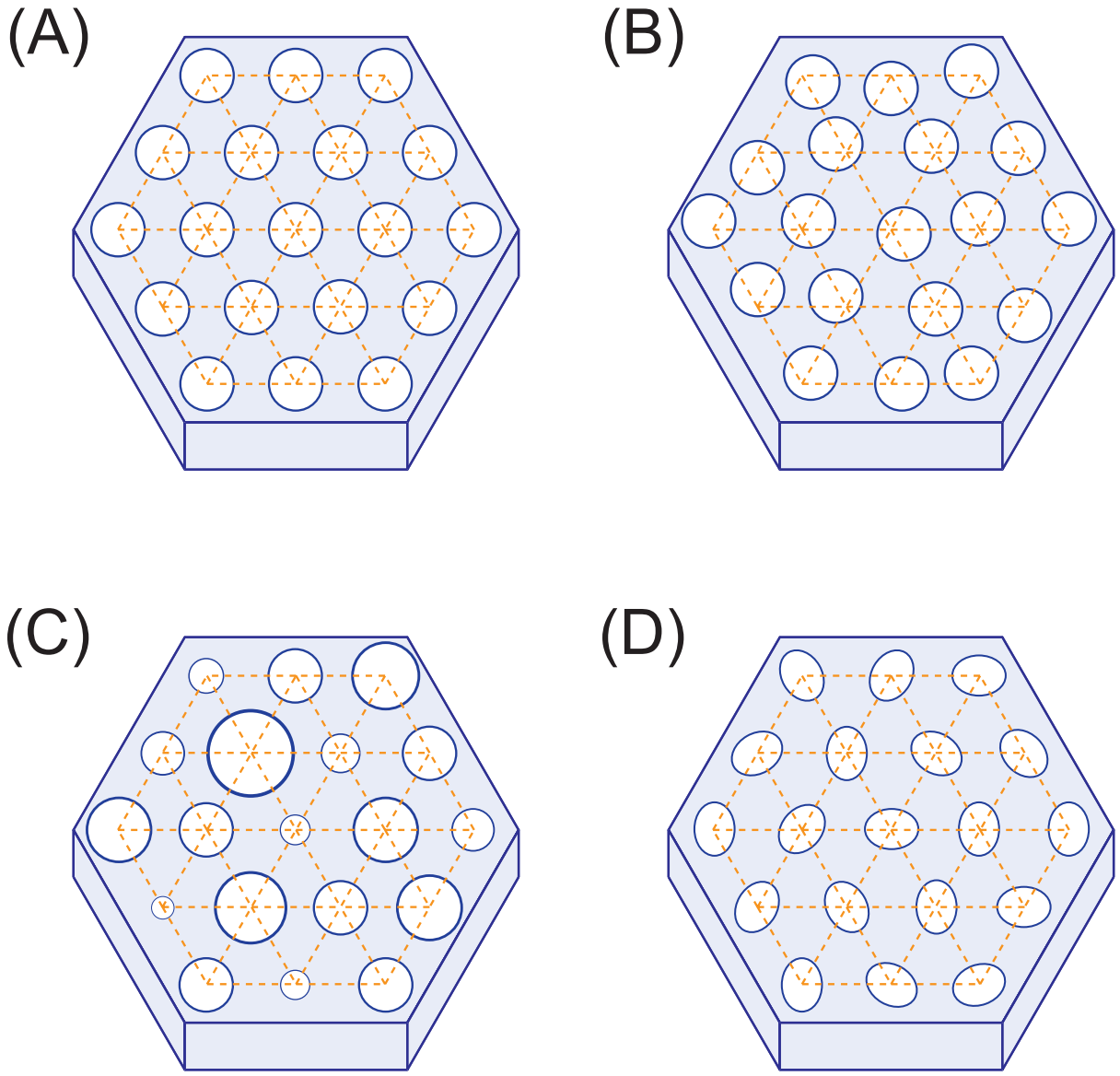

Figure 2-4 Schematic representations of the fluctuations: (B) mesopore positions, (C) mesopore radius, and (D) mesopore structure. (A) represent ideal fluctuation-less structure.

the fluctuation in pore position, (i) fluctuation in pore radius *R* as illustrated in Figure 2-4(C), and (ii) deformation of pore structure as illustrated in Figure 2-4(D) would also be considered as described in Sections 2.3.2.2 and 2.3.2.3. Since the mesoporous samples used in this study have very narrow pore-size distributions and well-formed circular pore-cross-sections, the factors (i) and (ii) were not considered in the following discussions.

Thus, theoretical XRD patterns of ordered mesoporous materials with 2D-hexagonal

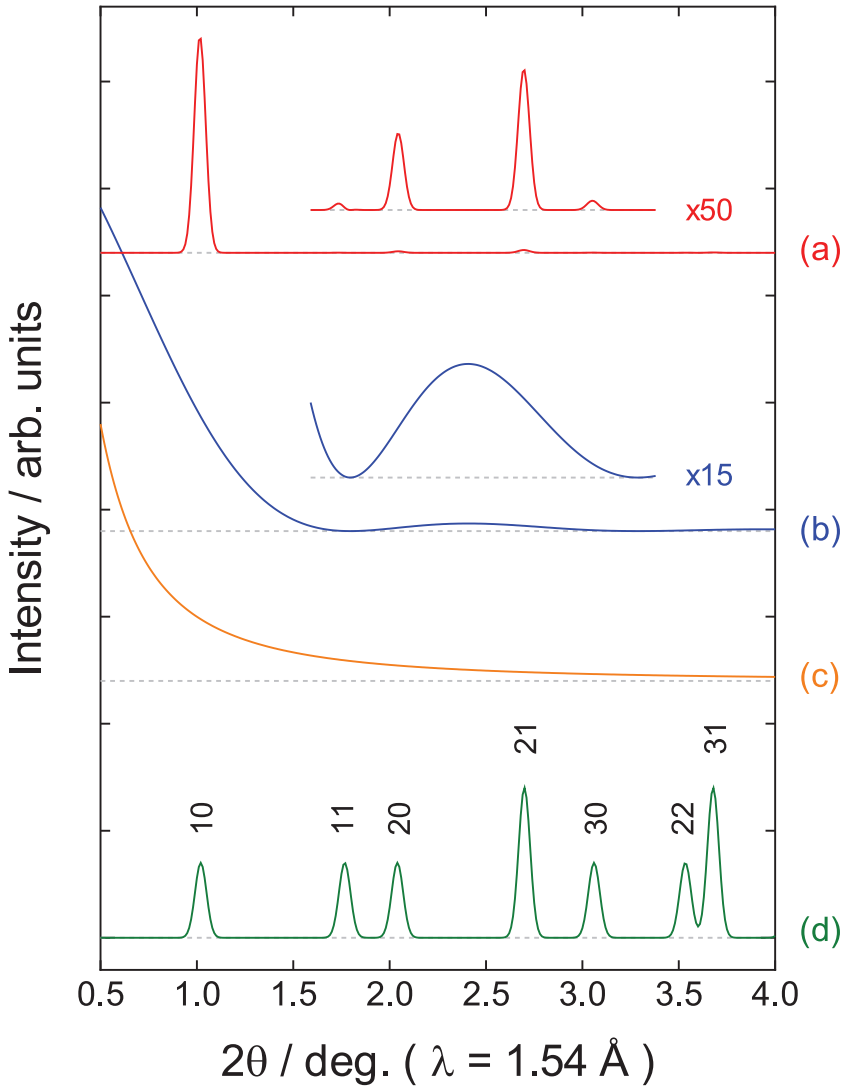

Figure 2-5 (a) Theoretical XRD pattern of an ordered mesoporous material with 2D-hexagonal symmetry (a = 10.0 nm, R = 3.0 nm). The theoretical XRD profile was calculated by multiplying (b) the squared unit cell form factor $|F(q)|^2 \propto |RJ_1(qR) / q|^2$, (c) Lorentz factor $L(q)$, and (d) the sum of the peak functions ($\sum M_{hk} G_{hk}(q)$).

symmetry can be calculated by the following equation:

$$I(q) = s \left| \rho \overline{f_a}(q) \frac{RJ_1(qR)}{q} \right|^2 L(q) D(q;\ \sigma) \sum_{h,\,k} M_{hk} G_{hk}(q;\ a;\ w;\ \eta) \qquad (2\text{-}36)$$

where s is a scaling factor. For example, the theoretical XRD pattern of a mesoporous SiO_2 sample (a = 11.0 nm, R = 3.0 nm) would be calculated as shown in Figure 2-5.

2.3.2 Effects of Fluctuation and Deformation of Mesopore Structure for XRD pattern

2.3.2.1 Fluctuation in Pore Positions

In Section 2.3.1, the term of "crystal structure factor (interference between unit cells)" was treated as a summation of the Laue functions. However, in order to consider the effects of fluctuation in pore positions (Figure 2-4(B)), another expression using a crystal structure factor $F_{\mathrm{crystal}}(\boldsymbol{q})$ is required. For the ordered mesoporous materials with 2D-hexagonal symmetry, crystal structure factor $F_{\mathrm{crystal}}(\boldsymbol{q})$ is expressed using the form factor of cylindrical mesopore $F_{\mathrm{cylinder}}(q)$ (see equation 2-35) as follow:

$$F_{\mathrm{crystal}}(\boldsymbol{q}) = \sum_{n} F_{\mathrm{cylinder}}(q) \exp\left(-i\boldsymbol{q} \cdot \boldsymbol{R}'_n\right) \tag{2-37}$$

where, $\boldsymbol{R}'_n$ is a positional vector for nth unit cell (i.e. positional vector for nth cylindrical mesopore).

The effects of fluctuation is considered by replacing the vector $\boldsymbol{R}'_n$ with $(\boldsymbol{R}_n + \boldsymbol{u}_n)$, where $\boldsymbol{R}_n$ and $\boldsymbol{u}_n$ are positional vector for ideal nth mesopore position, and displacement vector for nth mesopore from $\boldsymbol{R}_n$, respectively. In this time, diffraction intensity from a crystallite $I(\boldsymbol{q})$ is expressed as:

$$I(\boldsymbol{q}) = \left|F_{\mathrm{crystal}}(\boldsymbol{q})\right|^2 \tag{2-38}$$

$$= F_{\mathrm{crystal}}(\boldsymbol{q})\, F_{\mathrm{crystal}}(\boldsymbol{q})^* \tag{2-39}$$

$$= \left\{\sum_{m} F_{\mathrm{cylinder}}(q) \exp\left[-i\boldsymbol{q} \cdot (\boldsymbol{R}_m + \boldsymbol{u}_m)\right]\right\} \left\{\sum_{n} F_{\mathrm{cylinder}}(q)^* \exp\left[i\boldsymbol{q} \cdot (\boldsymbol{R}_n + \boldsymbol{u}_n)\right]\right\} \tag{2-40}$$

$$= \sum_{m}\sum_{n} F_{\mathrm{cylinder}}(q)\, F_{\mathrm{cylinder}}(q)^* \exp\left[-i\boldsymbol{q} \cdot (\boldsymbol{R}_m - \boldsymbol{R}_n)\right] \exp\left[-i\boldsymbol{q} \cdot (\boldsymbol{u}_m - \boldsymbol{u}_n)\right] \tag{2-41}$$

In the practical experiment of powder diffraction, we observe "averaged intensity" of mesoporous crystallites. Therefore, we shold consider averaged value of equation 2-41 as

follow:

$$\langle I(\boldsymbol{q})\rangle = \sum_m \sum_n F_{\text{cylinder}}(q)\, F_{\text{cylinder}}(q)^* \exp\left[-i\boldsymbol{q}\cdot(\boldsymbol{R}_m - \boldsymbol{R}_n)\right] \langle \exp\left[-i\boldsymbol{q}\cdot(\boldsymbol{u}_m - \boldsymbol{u}_n)\right]\rangle \tag{2-42}$$

Since $\boldsymbol{q}$ is parallel to $\boldsymbol{u}_m$ and $\boldsymbol{u}_n$, [ii] the term "$\langle \exp\left[-i\boldsymbol{q}\cdot(\boldsymbol{u}_m - \boldsymbol{u}_n)\right]\rangle$" can be rewritten as "$\langle \exp\left[-iq\,(u_m - u_n)\right]\rangle$".

In the meantime, the term "$\langle \exp\left[-iq\,(u_m - u_n)\right]\rangle$" is further simplified by using the Baker–Hausdorff's theorem. According to the theorem, if a variable x follows a Gaussian distribution, following equation is obtained:

$$\langle \exp(ix)\rangle = \exp\left(-\frac{1}{2}\langle x^2\rangle\right) \tag{2-43}$$

By using equation 2-43, the term "$\langle \exp\left[-iq\,(u_m - u_n)\right]\rangle$" becomes as follows:

$$\langle \exp\left[-iq\,(u_m - u_n)\right]\rangle = \exp\left[-\frac{1}{2}\langle q^2(u_m - u_n)^2\rangle\right] \tag{2-44}$$

$$= \exp\left[-\frac{1}{2}q^2\langle (u_m - u_n)^2\rangle\right] \tag{2-45}$$

$$= \exp\left(-\frac{1}{2}q^2\langle u_m^2\rangle\right) \exp\left(q^2\langle u_m u_n\rangle\right) \exp\left(-\frac{1}{2}q^2\langle u_n^2\rangle\right) \tag{2-46}$$

Because of translational symmetry, the value of $\langle u_m^2\rangle$ is equal to $\langle u_n^2\rangle$. For convenience, these terms are denoted as σ. Furthermore, $\exp\left(-q^2\sigma^2/2\right)$ is designated as $D(q;\sigma)$ in the following parts. Here note that $D(q;\sigma)$ is generally called Debye–Waller factor. By translating "$\exp\left(q^2\langle u_m u_n\rangle\right)$" into "$1 + \left[\exp\left(q^2\langle u_m u_n\rangle\right) - 1\right]$", equation 2-42 becomes:

$$\begin{aligned}\langle I(\boldsymbol{q})\rangle = &\sum_m \sum_n F_{\text{cylinder}}(q)\, D(q;\sigma)\, F_{\text{cylinder}}(q)^*\, D(q;\sigma)^* \exp\left[-i\boldsymbol{q}\cdot(\boldsymbol{R}_m - \boldsymbol{R}_n)\right] \\ &+ \sum_m \sum_n F_{\text{cylinder}}(q)\, D(q;\sigma)\, F_{\text{cylinder}}(q)^*\, D(q;\sigma)^* \exp\left[-i\boldsymbol{q}\cdot(\boldsymbol{R}_m - \boldsymbol{R}_n)\right] \\ &\times \left[\exp\left(q^2\langle u_m u_n\rangle\right) - 1\right] \end{aligned} \tag{2-47}$$

$$\begin{aligned}= &\left|F_{\text{cylinder}}(q)\, D(q;\sigma)\right|^2 \sum_m \sum_n \exp\left[-i\boldsymbol{q}\cdot(\boldsymbol{R}_m - \boldsymbol{R}_n)\right] \\ &+ \left|F_{\text{cylinder}}(q)\, D(q;\sigma)\right|^2 \sum_m \sum_n \exp\left[-i\boldsymbol{q}\cdot(\boldsymbol{R}_m - \boldsymbol{R}_n)\right] \left[\exp\left(q^2\langle u_m u_n\rangle\right) - 1\right] \end{aligned} \tag{2-48}$$

[ii] As mentioned in Section 2.3.1, only $hk0$ diffractions are observed for 2D-Hexagonal mesoporous materials. Since the displacement is considered in a-b plane, $\boldsymbol{q}$ becomes parallel to $\boldsymbol{u}_m$ and $\boldsymbol{u}_n$.

Since we consider random displacement in pore position, the $\langle u_m u_n \rangle$ part in equation 2-48 become 0, and the second term in equation 2-48 should be ignored. By using Laue function, the first term in equation 2-48 is rewritten as:

$$\langle I(\boldsymbol{q}) \rangle = \left| F_{\text{cylinder}}(q)\, D(q;\sigma) \right|^2 \sum_{h,\,k} M_{hk} G_{hk}(q) \tag{2-49}$$

This means that, the fluctuation in pore position can be treated by using $D(q;\sigma)$. This equation means that, peak intensity at high-angler diffraction are gradually damped with increasing the degree of fluctuation. Note that peak width is not affected by the $D(q;\sigma)$ value.

2.3.2.2 Fluctuation in Pore Radius

In the XRD calculation, fluctuation in pore radius (Figure 2-4(C)) would be considered by modifying the structure factor term in equation 2-7. When the pore-size distribution function is expressed as $P(R)$, effective structure factor might be calculated as:

$$|F(q)|^2 = \int_{R=0}^{\infty} P(R)\, F_{\text{cylinder}}(q;\ R)^2\, \mathrm{d}R \tag{2-50}$$

In the case of uniform pore radius system, $F_{\text{cylinder}}(q;\ R)^2$ is damped oscillation function as shown in Figure 2-5(b). In this case, the oscillation feature is changed with R value. On the other hand, in the case of non-uniform pore-size (i.e. fluctuated pore radius) system, such a unique oscillation manner of dependence on R gradually disappears with increasing the width of pore-size distribution.

2.3.2.3 Deformation of Pore Structure

Deformation of pore structure would also be considered by modifying the structure factor term. For example, if pore cross-sections deformed from circular to elliptic shape, the structure factor of circular cylinder (equation 2-34) is replaced by that of the elliptical cylinder. Here we assume an elliptical cylinder with length L, and with cross-section semi axis εR and R. In a cylindrical

coordinate system, scattering vector $\boldsymbol{q}$ and positional vector $\boldsymbol{r}$ may be represented as follows:

$$\boldsymbol{q} = \begin{pmatrix} q_\perp \cos(\psi + \phi) \\ q_\perp \sin(\psi + \phi) \\ q_\parallel \end{pmatrix} \tag{2-51}$$

$$\boldsymbol{r} = \begin{pmatrix} \varepsilon r \cos\phi \\ r \sin\phi \\ z \end{pmatrix} \tag{2-52}$$

where, $q_\perp$ is the $\boldsymbol{q}$ component perpendicular to the direction of cylindrical axis, $q_\parallel$ is the $\boldsymbol{q}$ component parallel to the direction of cylindrical axis, and ψ is the angle between $q_\perp$ and cross-section semi axis εR. In this case, $\boldsymbol{q} \cdot \boldsymbol{r}$ is expressed as "$q_\perp r\sqrt{\sin^2\phi + \varepsilon\cos^2\phi}\,\cos\psi + zq_\parallel$". Thus, the structure factor of elliptical cylinder $F_{\text{elliptical}}(\boldsymbol{q})$ may be calculated as follow:

$$F_{\text{elliptical}}(\boldsymbol{q}) = \int \exp(-i\boldsymbol{q}\cdot\boldsymbol{r})\,\mathrm{d}\boldsymbol{v} \tag{2-53}$$

$$= \int_{z=-L/2}^{L/2}\int_{r=0}^{R}\int_{\phi=0}^{2\pi} \varepsilon r \exp\left[-i\left(q_\perp r\sqrt{\sin^2\phi + \varepsilon\cos^2\phi}\,\cos\psi + zq_\parallel\right)\right]\mathrm{d}\phi\mathrm{d}r\mathrm{d}z \tag{2-54}$$

If the deformation directions of mesopores are not correlated with each other (Figure 2-4(D) case), "orientation-averaged structure factor $\left\langle F_{\text{elliptical}}(q)\right\rangle$" should be considered. In this case, equation 2-54 is modified as follows:

$$\left\langle F_{\text{elliptical}}(q)\right\rangle = \frac{1}{2\pi}\int_{\psi=0}^{2\pi} F_{\text{elliptical}}(\boldsymbol{q})\mathrm{d}\psi \tag{2-55}$$

$$= \left\{\int_{\psi=0}^{2\pi}\int_{r=0}^{R}\int_{\phi=0}^{2\pi} \varepsilon r \exp\left[-i\left(q_\perp r\sqrt{\sin^2\phi + \varepsilon\cos^2\phi}\,\cos\psi\right)\right]\mathrm{d}\phi\mathrm{d}r\mathrm{d}\psi\right\}$$

$$\times\left\{\int_{z=-L/2}^{L/2}\exp(-izq_\parallel)\,\mathrm{d}z\right\} \tag{2-56}$$

$$= \left[\varepsilon R\int_{\phi=0}^{2\pi}\frac{J_1(q_\perp R\omega)}{q_\perp\omega}\mathrm{d}\phi\right]\left[\frac{\sin(q_\parallel L/2)}{q_\parallel L/2}\right] \tag{2-57}$$

where,

$$\omega = \sqrt{\sin^2\phi + \varepsilon^2\cos^2\phi} \tag{2-58}$$

As discussed in the circular cylinder case (Section 2.3.1), the term "$\sin(q_\parallel L/2)\,/\,(q_\parallel L/2)$" can be ignored in practical calculations. Therefore, orientation-averaged structure factor of

elliptical cylinder can be calculated using following equation:

$$\left\langle F_{\text{elliptical}}(q) \right\rangle = \varepsilon R \int_{\phi=0}^{2\pi} \frac{J_1(qR\omega)}{q\omega} \mathrm{d}\phi \tag{2-59}$$

Note that since the integration in equation 2-59 cannot be performed analytically, numerical integration is required in practical calculation.

2.3.3 Relationship between Lattice Constant and Mesopore Diameter

Although theoretical XRD patterns of ordered mesoporous materials can be calculated using equation 2-36, the relationship between mesopore structure and the XRD pattern may be difficult to understand because the equation contains many parameters. In this section, we derive a more practical expression that represents the relationship between structural features (mesopore diameter D and lattice constant a) and XRD peak intensities. As discussed in Section 2.3.1, the diffraction intensity at the hk Bragg's angle q_{hk}, I_{hk} is expressed as follows:

$$I_{hk} \propto M_{hk} \left| \rho \overline{f_a}(q_{hk}) \frac{RJ_1(q_{hk}R)}{q_{hk}} \right|^2 L(q_{hk}) D(q_{hk};\, \sigma) \tag{2-60}$$

Therefore, the peak intensity ratio of hk to $h'k'$ can be written

$$\frac{I_{hk}}{I_{h'k'}} = \frac{M_{hk}}{M_{h'k'}} \frac{J_1(q_{hk}R)^2}{J_1(q_{h'k'}R)^2} \frac{L(q_{hk})}{L(q_{h'k'})} \frac{D(q_{hk};\, \sigma)}{D(q_{h'k'};\, \sigma)} \tag{2-61}$$

In the meantime, Lorentz factor L at scattering angle θ is expressed as:

$$L = \frac{1}{\sin^2\theta \cos\theta} = \frac{2}{\sin 2\theta \sin\theta} \tag{2-62}$$

In the small 2θ region, "$\sin 2\theta$" in equation 2-62 would be approximated by "$2\sin\theta$". In this time, the Lorentz factor becomes:

$$L \simeq \left(\frac{1}{\sin\theta} \right)^2 \tag{2-63}$$

In the case of 2D-hexagonal mesoporous samples, $\sin\theta$ at the hk diffraction line ($\sin\theta_{hk}$) is expressed by using the incident X-ray wavelength λ, unit cell lattice constant a, and Miller's

indices hk, as follow:

$$\sin\theta_{hk} = \frac{\lambda}{4\pi} q_{hk} = \frac{\lambda}{a}\sqrt{\frac{h^2 + hk + k^2}{3}} \tag{2-64}$$

From equations 2-63 and 2-64, the Lorentz factor at the hk diffraction line L_{hk} may be expressed as:

$$L_{hk} \simeq \frac{3a^2}{\lambda^2 \left(h^2 + hk + k^2\right)} \tag{2-65}$$

Therefore, the term "$L(q_{hk})$ / $L(q_{h'k'})$" in equation 2-61 may be expressed as

$$\frac{L\left(q_{hk}\right)}{L\left(q_{h'k'}\right)} = \frac{h'^2 + h'k' + k'^2}{h^2 + hk + k^2} \tag{2-66}$$

in the small-angle region. From equation 2-9, $q_{hk}R$ becomes:

$$q_{hk}R = 2\pi\gamma\sqrt{\frac{h^2 + hk + k^2}{3}} \tag{2-67}$$

where γ is the mesopore diameter normalized by a ($\gamma = 2R / a = D / a$). Therefore, if we can assume that the fluctuation of mesopore position is negligible, equation 2-61 can be rewritten as:

$$\frac{I_{hk}}{I_{h'k'}} = \frac{M_{hk}}{M_{h'k'}} \frac{J_1\left(2\pi\gamma\sqrt{g/3}\right)^2}{J_1\left(2\pi\gamma\sqrt{g'/3}\right)^2} \frac{g'}{g} \tag{2-68}$$

$$g = h^2 + hk + k^2 \tag{2-69}$$

$$g' = h'^2 + h'k' + k'^2 \tag{2-70}$$

Equation 2-68 indicates that the relative diffraction intensities at the Bragg's angles are essentially determined only by the γ (= D / a) value. Figure 2-6 shows the relationship between γ and the diffraction peak intensities. In this graph, the intensity of the 10 diffraction line was normalized to 1. Since the unit cell lattice constant a is directly determined from the peak positions, the mesopore diameter D can be estimated from the γ value determined by analysis of the diffraction intensity using Figure 2-6.

Note that if the fluctuation of mesopore position (Debye–Waller factor) is not negligible, the diffraction peak intensities will decrease with increasing q value. We should

also note that I_{hk} (diffraction intensity at q_{hk}) is not proportional to the peak area of the hk line A_{hk}, because the exact shapes of the diffraction peaks are modulated by the $F(q)$ shape. The difference between I_{hk} and A_{hk} becomes non-negligible when the diffraction peaks are broad. Therefore, pattern fitting using equation 2-36 is required for a rigorous structure assessment.

2.4 Results and Discussion

2.4.1 Structural Characterization of Obtained Materials using Commonly-used Procedures

First, we characterized the nanostructure of the obtained samples using commonly used procedures. Figure 2-7(A, B) shows TEM images of the MS1 sample. Hexagonally aligned straight channel pores were clearly observed. Similar porous structures were observed in the other samples (MS2, MS3, and MCS) used in this study. Nitrogen adsorption / desorption isotherms are shown in Figure 2-8(A). In the MS1 and MCS samples, clear hysteresis loops appeared. Their isotherm shapes were classified as type IV, according to the International Union of Pure and Applied Chemistry (IUPAC) definition.[111] On the other hand, no hysteresis loops were observed in MS2 or MS3 samples, probably due to their narrow mesopore diameters, which were close to the micropore range (< 2 nm). Such a lack of hysteresis loops feature is often reported for small pore-size MCM-41 type materials.[112–114] In the adsorption branch of the isotherms, rapid increases of adsorbed volume, which is characteristic of capillary condensation within mesopores, occurred around $P / P_0 = 0.67$ (MS1), 0.32 (MS2), 0.28 (MS3), and 0.61 (MCS). Such a sharp increase indicates a high uniformity of the mesopores. The narrow distributions of mesopore diameter were confirmed by pore size distribution curves calculated using the BJH method, as shown in Figure 2-8(B).

Figure 2-9 show powder XRD patterns of the obtained samples. As illustrated in the figures, more than 4 diffraction peaks were observed in all samples, and these peaks could be indexed to a 2D-hexagonal symmetry (*p6mm*). The observed diffraction peak positions and the peak intensity ratio of MS1 were quite different from those of MS2. Meanwhile, although

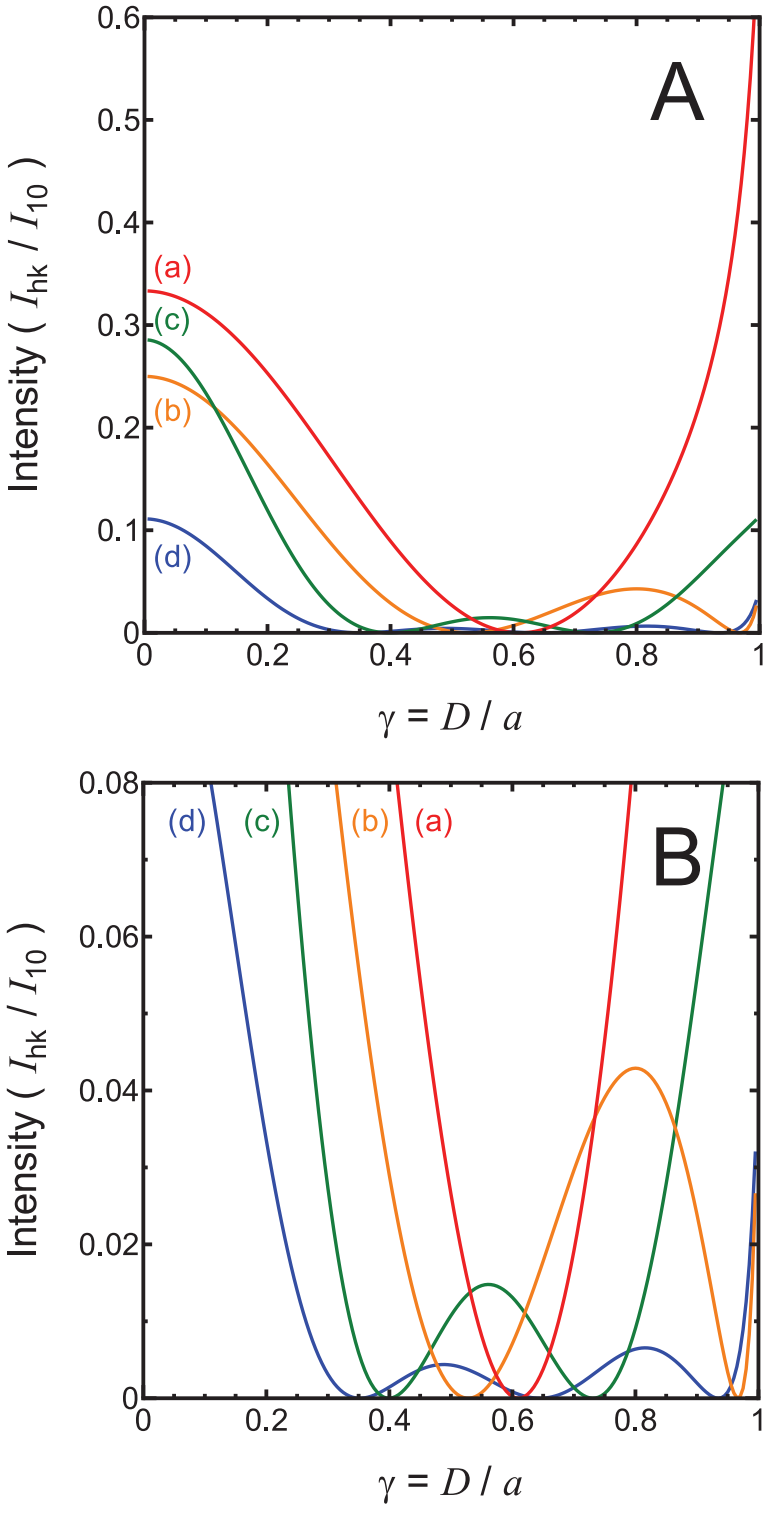

Figure 2-6 Diffraction intensities of (a) 11, (b) 20, (c) 21, and (d) 30 peaks calculated using equation 2-68. The peak intensity of the 100 diffraction peak was set to 1. (B) is a magnified view of (A).

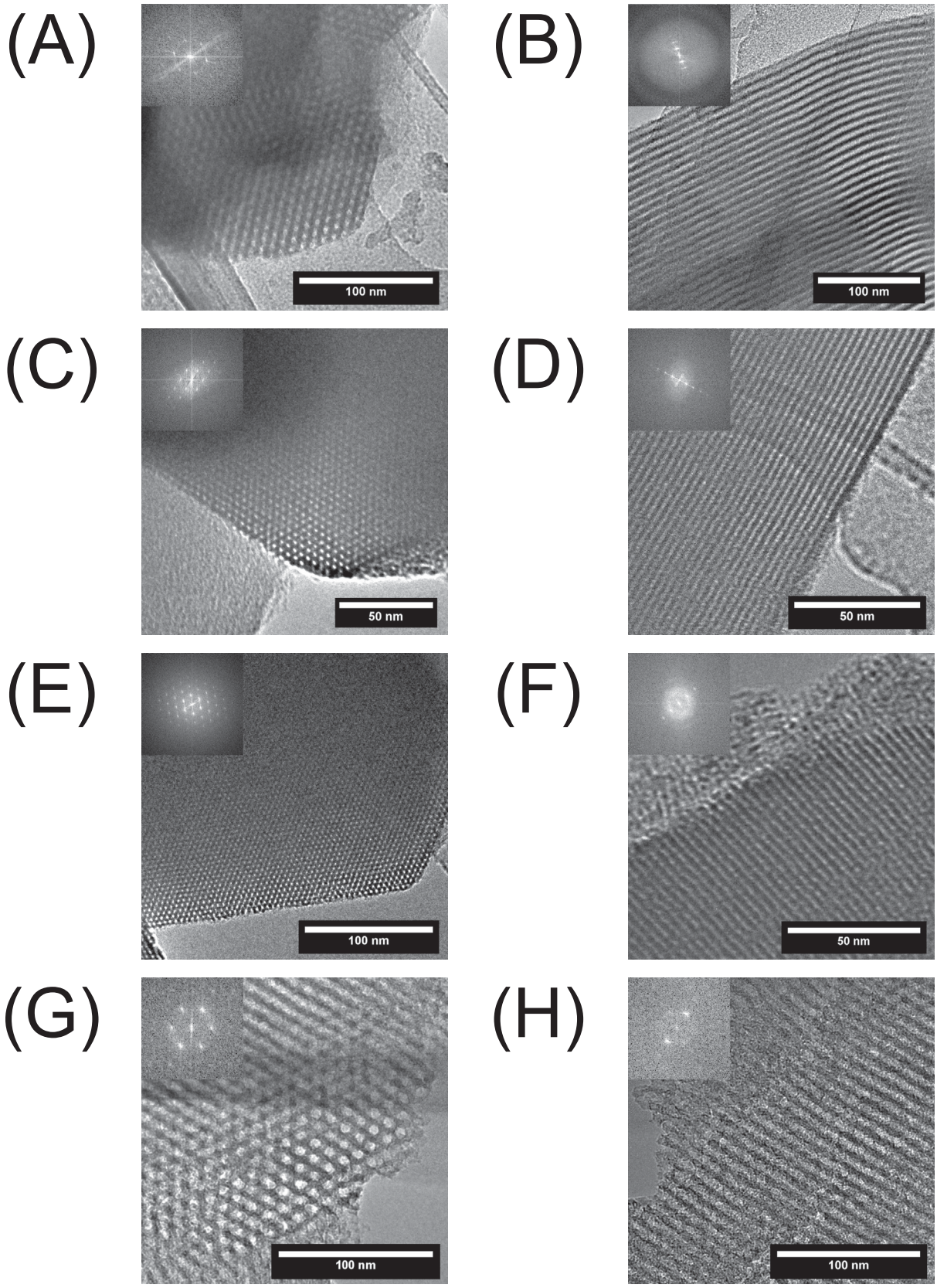

Figure 2-7 TEM photographs and corresponding fast Fourier transform (FFT) images of (A, B) MS1, (C, D) MS2, (E, F) MS3, and (G, H) MCS. (A, C, E, G): parallel and (B, D, F, H): perpendicular to the channel pore axis.

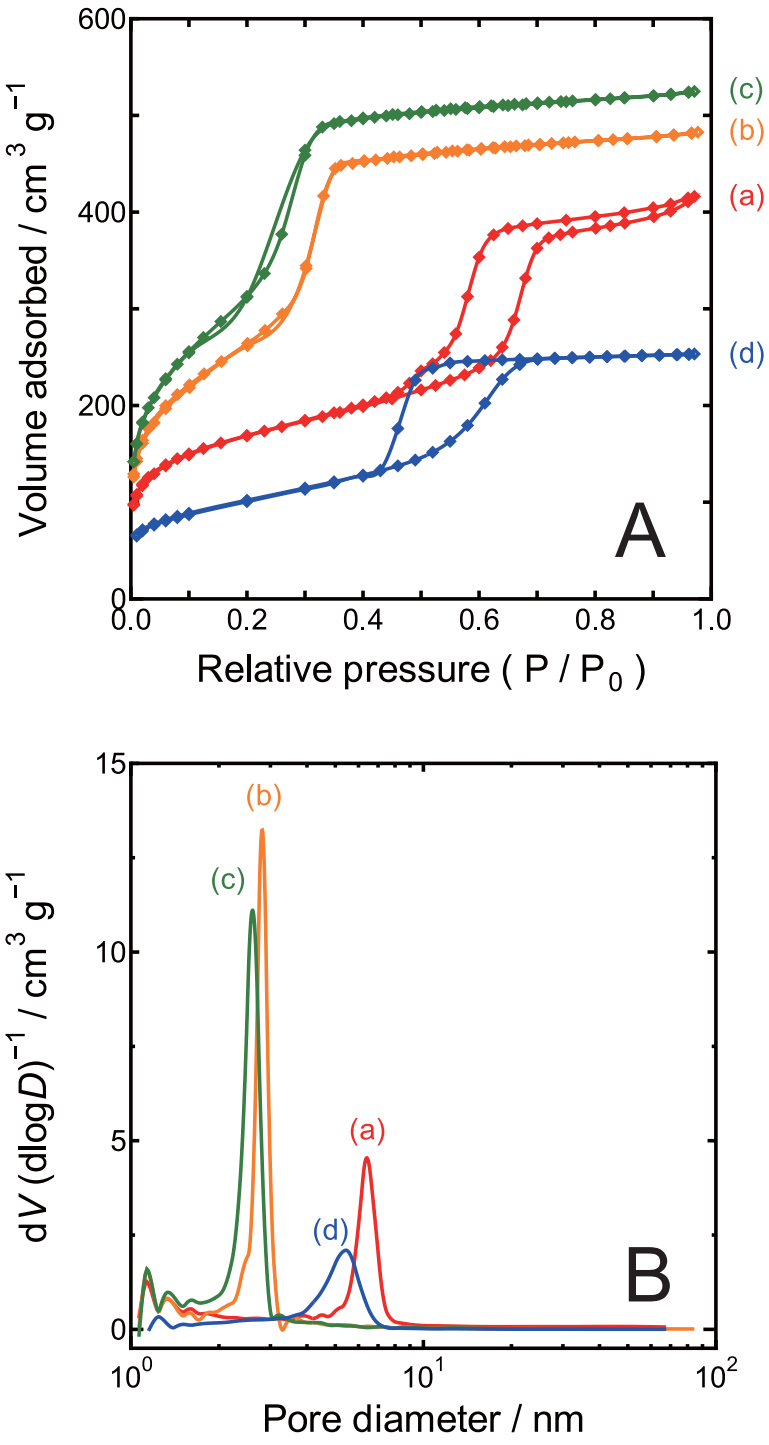

Figure 2-8 (A) N_2 adsorption / desorption isotherms of (a) MS1, (b) MS2, (c) MS3, and (d) MCS. (B) BJH pore size distribution curves of (a) MS1, (b) MS2, (c) MS3, and (d) MCS.

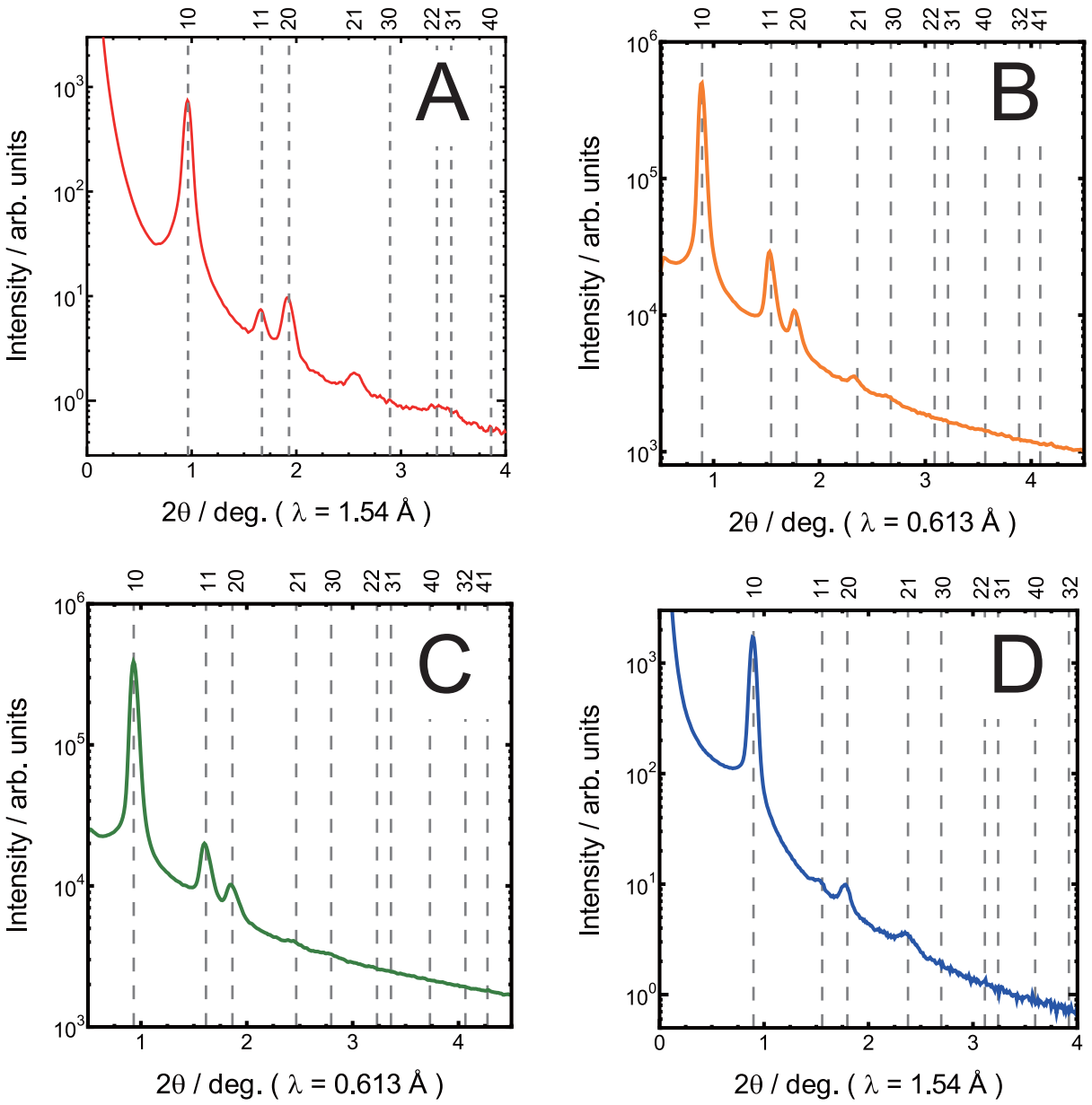

Figure 2-9 XRD patterns of (A) MS1, (B) MS2, (C) MS3, and (D) MCS.

the peak intensity ratios of MS2 were close to those of MS3, the peak positions of MS2 were located at lower angles than those of MS3. The relationship between mesopore structure and the XRD pattern will be discussed later in this section. Lattice constant (a) values of MS1, MS2, MS3, and MCS, estimated from the positions of 10 diffraction peaks, were 10.62 nm, 4.56 nm, 4.33 nm, and 11.42 nm, respectively.

According to previous reports, the mesopore diameter (denoted here as D_{geo}) could be roughly estimated from the unit cell lattice constant a and mesopore volume V_{meso} using a

simple geometrical calculation, assuming a pore wall density ρ.[107,115–117] Since the existence of micropores was confirmed by α_s-plot analysis (see Figure 2-10), we used the following equation instead of the previously proposed one.

$$D_{geo} = \left\{ \frac{2\sqrt{3}\rho V_{meso}}{\pi \left[1 + \rho \left(V_{meso} + V_{micro}\right)\right]} \right\}^{1/2} a \tag{2-71}$$

where V_{micro} is the micropore volume, and the densities of SiO_2 and C were assumed to $\rho = 2.2$ g cm^{-3} and $\rho = 1.8$ g cm^{-3}, respectively. In this equation, we assumed that all of the micropores are homogeneously dispersed in the wall region located between aligned mesopore channels. Equation 2-71 becomes equivalent to the equations presented in previous reports[107,115–117] by replacing the term "($V_{meso} + V_{micro}$)" with "V_{meso}". The obtained structural parameters are summarized in Table 2-1. The D_{KJS} values were very close to D_{geo}, except for the MCS sample. The mismatch between D_{KJS} and D_{geo} in MCS may arise from roughness of the mesopore structure. As shown in the TEM photographs (Figure 2-7) and pore size distribution curve (Figure 2-8(B)), the structural roughness of the MCS sample was much higher than in other samples. In addition to the structural roughness, the differences in surface chemistry between SiO_2 and C may also have affected the pore size estimation, because such differences are not properly considered in the BJH or KJS calculations in this study. The V_{micro} value of the MCS may also have a problem, because α_s-analysis should also be affected by the surface properties. Here we note that the BJH or KJS method has a potential to accommodate surface properties through the selection of the statistical film thickness for an appropriate surface type. However, the accommodation is hard for the MCS due to its complicated chemical composition. In contrast to the gas adsorption / desorption methods, such information of pore-surface is not required for the XRD analysis method.

2.4.2 Structural Determination in Ordered Mesoporous Materials using XRD Method which Developed in This Study

In this section, we will discuss the details of the XRD analysis. As mentioned in Section 2.3.3, the structure parameter γ that represents the size ratio between the lattice constant a and

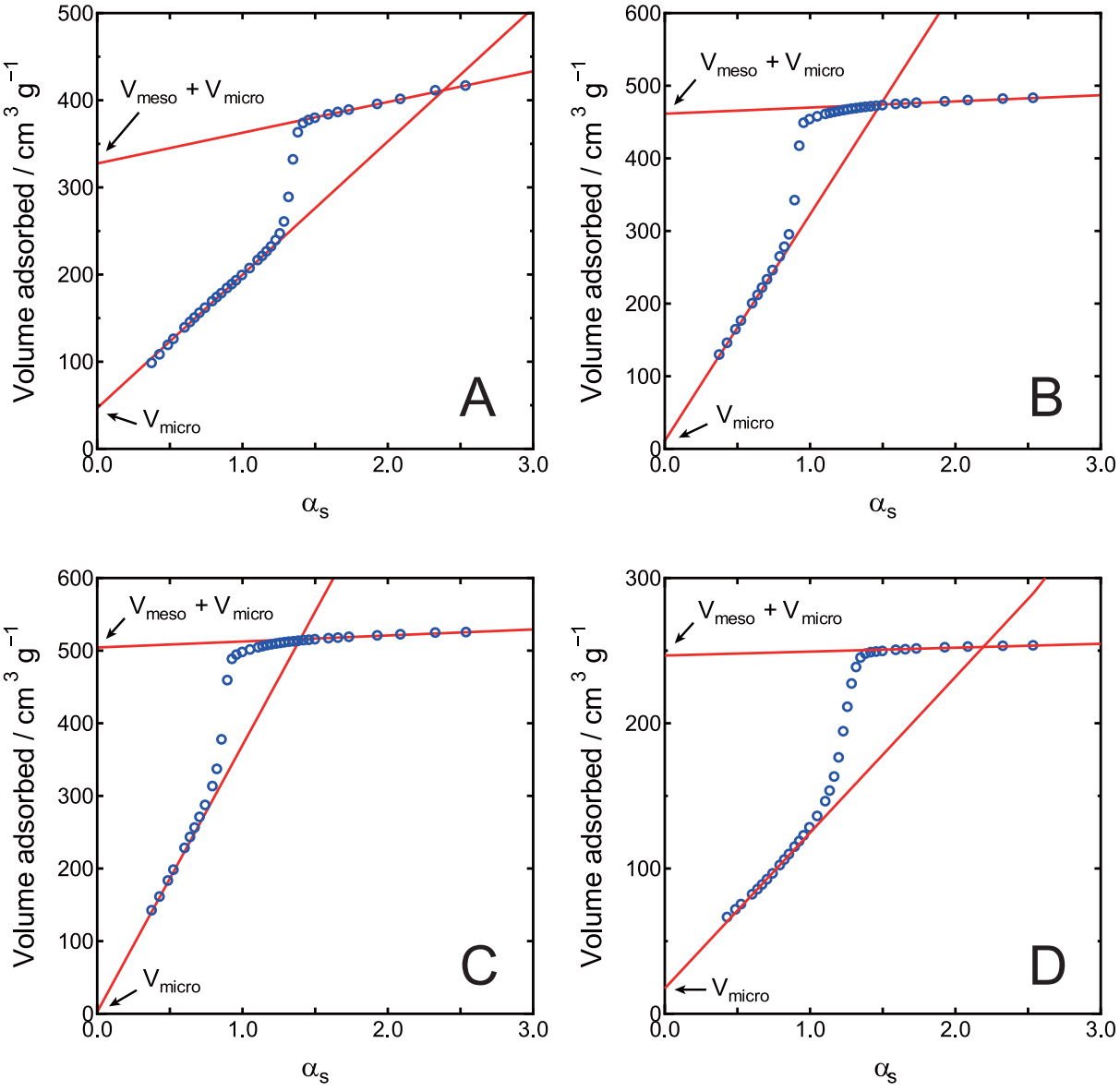

Figure 2-10 α_s-plot of (A) MS1, (B) MS2, (C) MS3, and (D) MCS.

the mesopore diameter D can essentially be estimated from the XRD peak intensities using Figure 2-6. For example, for the MS1 sample, the following relationships were observed in Figure 2-9: (A) $I_{11} < I_{20}$, (B) $I_{20} > I_{21}$, (C) $I_{21} > I_{30}$. In order to satisfy requirement (A), the γ value should be somewhere between 0.58 and 0.73. Furthermore, $0.62 < \gamma$ and $\gamma < 0.70$ are also required to satisfy (B) and (C), respectively. Therefore, the γ value of MS1 was estimated to be $0.62 < \gamma < 0.70$ (6.6 nm$< D <$ 7.4 nm). In order to narrow down the estimation range of γ, XRD pattern fittings were performed. Equation 2-36 was used as a model function, and the modified Levenberg-Marquardt method was adopted as a

Table 2-1 Structural parameters of the obtained materials.[a]

	a_{10} (nm)	S_{BET} ($m^2\ g^{-1}$)	V_{total} ($cm^3\ g^{-1}$)	V_{meso} ($cm^3\ g^{-1}$)	V_{micro} ($cm^3\ g^{-1}$)	D_{BJH} (nm)	D_{KJS} (nm)	D_{geo} (nm)
MS1	10.62	596	0.64	0.43	0.07	6.4	7.3	7.5
MS2	4.56	962	0.75	0.70	0.02	2.8	3.6	3.7
MS3	4.33	1156	0.81	0.78	0.00	2.6	3.4	3.6
MCS[b]	11.42	365	0.39	0.35	0.03	5.4	6.3	7.6

[a] a_{10}: lattice constant estimated from apparent position of 10 XRD peak; S_{BET}: specific surface area estimated by the BET method; V_{total}: total pore volume; V_{meso}: primary mesopore volume; V_{micro}: micropore volume; D_{BJH}: primary mesopore diameter estimated by the BJH method; D_{KJS}: primary mesopore diameter estimated by the KJS method; D_{geo}: mesopore diameter estimated by geometrical relationship shown in equation 2-71.

[b] $C : SiO_2$ weight ratio estimated by thermogravimetric analysis was 37.5 : 62.5.

nonlinear least squares fitting algorithm. The obtained structure parameters are summarized in Table 2-2. Simulated XRD patterns calculated from the structural parameters obtained by the fitting are shown in Figure 2-11. As shown in Figure 2-11, the simulated patterns well reproduced the experimentally observed patterns. Mesopore diameters determined by the XRD method (D_{XRD}) were close to D_{KJS}, and were larger than D_{BJH} in all samples. According to previous reports, the traditional BJH method tends to underestimate mesopore diameter.[34, 107] Our XRD analysis data support this underestimation of the BJH method, without making any semi-empirical assumptions. Furthermore, as shown in Table 2-2, the σ value of the MCS sample was larger than those of MS1, MS2, and MS3. This is probably a result of the abovementioned structural roughness of MCS.

By comparing Tables 2-1 and 2-2, we found that the values of a_{Fit} were smaller than a_{10} in all samples. This means that the observed peak positions were somewhat different from those simply predicted by Bragg's law. This difference seems to arise from the shape of the form factor term ($|F(q)|^2$) in equation 2-7. The author found that $|F(q)|^2$ always monotonically

Table 2-2 Structural parameters determined by least-suquare fittings of XRD patterns.[a]

	a_{Fit} (nm)	D_{XRD} (nm)	σ (nm)	γ (= $D_{\mathrm{XRD}}/a_{\mathrm{Fit}}$) (-)
MS1	10.555(1)	6.95(6)	0.72(2)	0.66
MS2	4.526(2)	3.60(7)	0.39(2)	0.79
MS3	4.292(3)	3.38(9)	0.40(2)	0.79
MCS	11.359(2)	6.98(16)	1.04(2)	0.61

[a] a_{Fit}: lattice constant; D_{XRD}: primary mesopore diameter; σ: mean-square displacement of mesopore position.

decreases near the Bragg's 10 diffraction angle, independent of a and R. Therefore, the net shape of the 10 peak profile (the convolution of $|F(q)|^2$ and $G_{10}(q)$) should be downshifted relative to the pure $G_{10}(q)$ peak, which was located at the Bragg's angle. The modulation becomes conspicuous with increasing diffraction peak width. In addition to the 10 peak, other peak positions are also modulated by the shape of $|F(q)|^2$. As shown in Figure 2-12, the degrees of peak modulations are different with γ. A similar modulation of XRD peak positions has been reported for single-walled carbon nanotube (SWCNT) bundles.[118] (Note that individual SWCNTs are generally aggregated due to van der Waals interactions to form a 2D-hexgonally aligned crystal structure called a bundle. The XRD pattern of SWCNTs can be calculated based on equation 2-7 by replacing the form factor with $F(q) = 2\pi R f_{\mathrm{C}}(q) J_0(qR)$, where J_0 is the 0th order Bessel function of the first kind, $f_{\mathrm{C}}(q)$ is the X-ray scattering factor of the carbon atom, and R is the tube diameter.)

2.4.3 Estimation of Framework-Density using XRD Method

Thus far, we have discussed the XRD patterns of mesoporous materials measured in the dry state. Let us broaden our scope to include wet conditions. For SWCNTs, it is well known that the XRD pattern of a water-immersed sample is completely different from that of a dry sample.[119] For example, the I_{10}/I_{11} ratio of a water-immersed SWCNT is much smaller

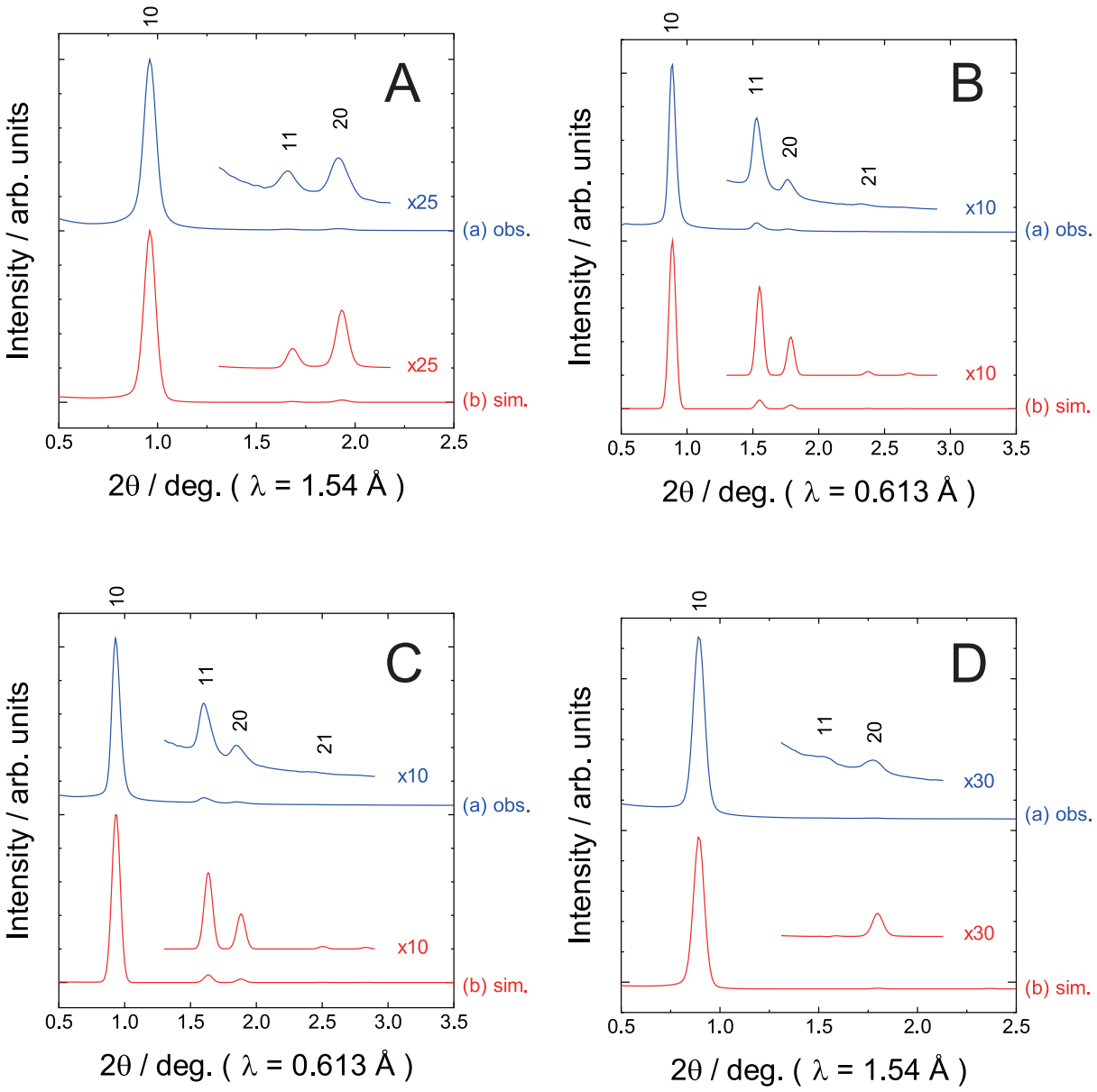

Figure 2-11 Comparison between (a) observed and (b) simulated XRD patterns of (A) MS1, (B) MS2, (C) MS3, and (D) MCS.

than that of a dry SWCNT. However, for mesoporous materials, the peak intensity ratio of a water-immersed sample was similar to that of a dry sample. Although the XRD peak intensity ratio was the same, the absolute intensity of a water-immersed wet mesoporous sample was much smaller than that of a dry sample. It was found that the pore wall density can be estimated from the difference in XRD intensity between dry and wet samples. The XRD patterns of wet mesoporous samples can be calculated by modifying the unit cell form factor used in equation 2-10. Assuming that all mesopores are homogeneously filled with water (density: ρ_2;

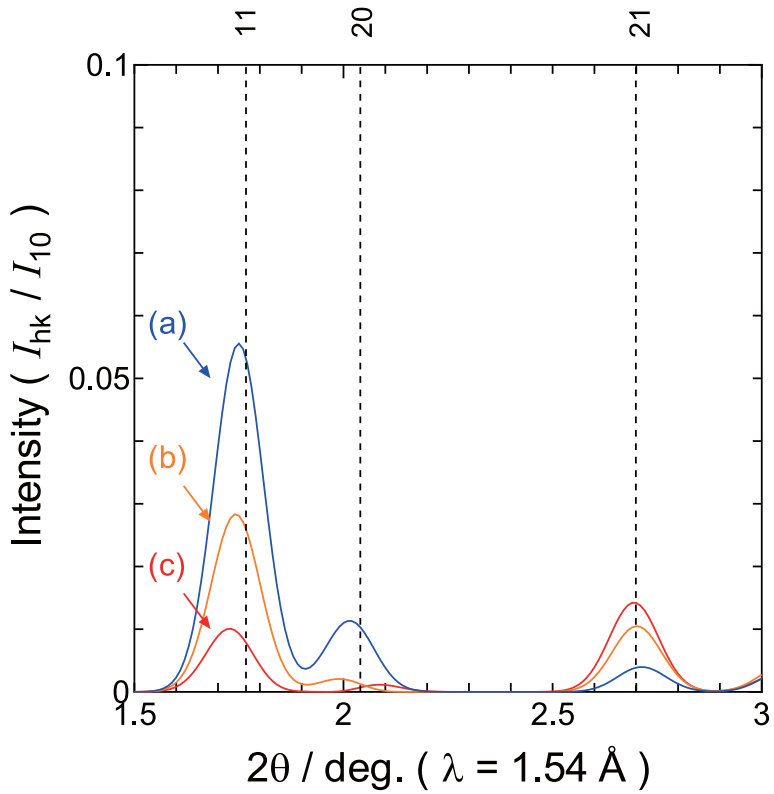

Figure 2-12 Theoretical XRD patens of ordered mesoporous materials with 2D-hexagonal symmetry: (a) $\gamma = 0.45$ ($a = 10.0$ nm; $D = 4.5$ nm), (b) $\gamma = 0.50$ ($a = 10.0$ nm; $D = 5.0$ nm), and (c) $\gamma = 0.55$ ($a = 10.0$ nm; $D = 5.5$ nm). The positions of Bragg's angles are shown with dashed-lines.

average atomic X-ray scattering factor: $\overline{f_2}(q)$), $F(q)$ may be expressed as follows, except for the $q = 0$ case:

$$F(q) = \rho_1 \overline{f_1}(q) F_{\text{matrix}}(q) - \rho_1 \overline{f_1}(q) F_{\text{cylinder}}(q) + \rho_2 \overline{f_2}(q) F_{\text{cylinder}}(q) \tag{2-72}$$

$$= \left[\rho_2 \overline{f_2}(q) - \rho_1 \overline{f_1}(q)\right] F_{\text{cylinder}}(q) \tag{2-73}$$

Since the observed XRD intensity is proportional to $|F(q)|^2$, the intensity ratio between dry and wet samples can be expressed as follows:

$$\frac{I_{\text{wet}}}{I_{\text{dry}}} = \left| 1 - \frac{\rho_2 \overline{f_2}(q)}{\rho_1 \overline{f_1}(q)} \right|^2 \tag{2-74}$$

where I_{wet} and I_{dry} are the XRD intensities of wet and dry samples, respectively. Taking MS3 as an example, the experimentally observed $I_{\text{wet}} / I_{\text{dry}}$ was 0.258 (see Figure 2-13). Assuming that the density of water in the mesopores is similar to the bulk density ($\rho_2 = 1.00$ g cm^{-3}),

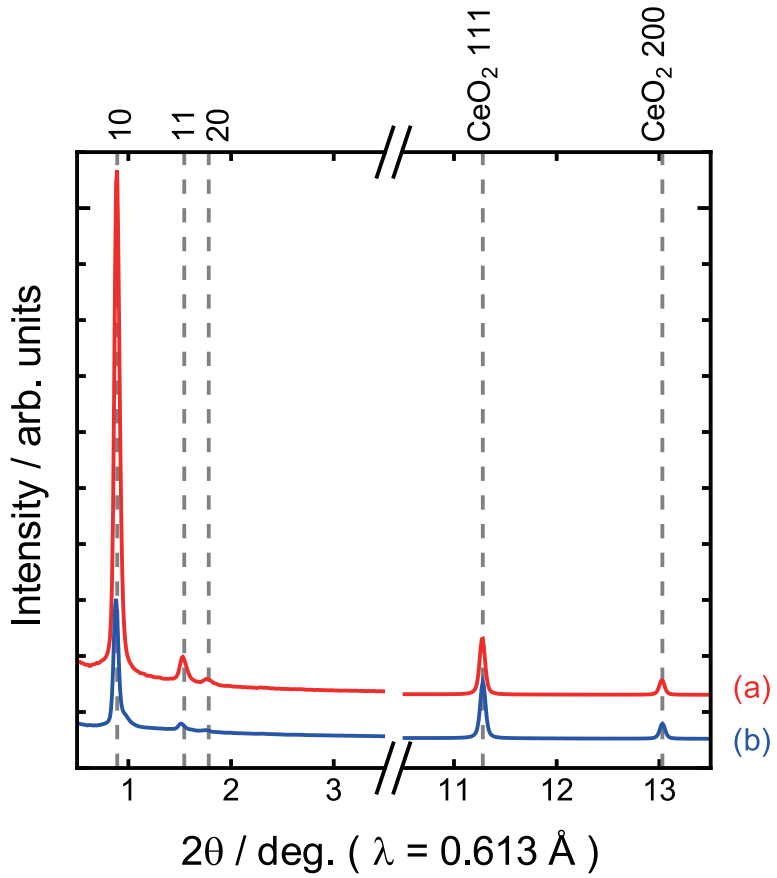

Figure 2-13 XRD patterns of (a) dry and (b) water-immersed MS3. Diffraction peaks of CeO_2 powder used as internal intensity standard (The weight ratio of MS3 : CeO_2 was 2 : 1) also shown.

ρ_1 was calculated to be 2.26 g cm^{-3}. This value is reasonable for amorphous SiO_2 (about 2.2 g cm^{-3}).[115,120] However, we should note that there is no assurance that the density of water confined in the mesopore is similar to the bulk density, because there are reports discussing the abnormal physical properties of molecules confined within nanospaces.[119,121–129] Further research is required to examine the exact density of water in mesopores. Normally, such a research would be difficult because we have to distinguish confined water from bulk one. However, I expect that our XRD method might be useful to probe the density of liquids confined in mesopore, because the XRD peak intensity of mesoporous samples are selectively affected by the densities of confined liquids. By comparing XRD intensities of ordered mesoporous samples immersed in various kinds of liquids, the densities of the liquids confined in mesopores would be evaluated.

2.5 Summary

In this study, the author derived theoretical XRD patterns of ordered mesoporous materials with 2D-hexagonal symmetry ($p6mm$). In order to test the validity of our theory, various types of mesoporous samples with different pore sizes and chemical compositions were synthesized, and their XRD patterns were compared with theoretically calculations. The theoretically calculated XRD patterns agreed well with experimentally observed patterns. We found that the exact XRD peak positions were modulated by the form factor $|F(q)|^2$, and were different from the positions calculated using Bragg's law. By analyzing the XRD peak intensities carefully, we successfully determined mesopore diameter and unit cell lattice spacing without support from other methods such as TEM or N_2 adsorption-desorption analysis. We also found that the XRD analysis can be adopted for water-immersed wet samples, and that the density of the pore wall can be estimated from the difference between XRD intensities of dry and wet samples.

Chapter 3

Structural Changes of Ordered Mesoporous Materials by Heat Treatment

3.1 Introduction

As mentioned in Section 1.1.1, ordered mesoporous materials are expected to be used as catalysts, adsorbents, filter, etc. In some industrial application field, stability under extreme conditions such as high-pressure and high-temperature should be required. However, thermal stability of mesoporous materials has not often been studied, except for a few reports for mesoporous silicas. Therefore, thermal stability of ordered mesoporous materials having various kinds of framework compositions were compared in this chapter. In the analysis of structural changes, the XRD method developed in Chapter 2 was partly used in this chapter.

3.2 Experimental Methods

3.2.1 Sample Preparation

3.2.1.1 Synthesis of Mesoporous SiO_2

Two types of mesoporous SiO_2 samples (MS1 and MS2) were prepared as mentioned in Sections 2.2.1.1 and 2.2.1.2. In this chapter, the obtained as-made MS1 and MS2 were designated as MS1-AM and MS2-AM, respectively.

3.2.1.2 Synthesis of Mesoporous Carbon–SiO_2 Composite

Mesoporous carbon–SiO_2 composite (MCS) was synthesized by triconstituent co-assembly method as described in Section 2.2.1.4. For convenience, the obtained as-made MCS was designated as MCS-AM, in this chapter.

3.2.1.3 Synthesis of Mesoporous Carbon

Mesoporous Carbon (MC) was prepared by hydrofluoric acid (HF) etching treatment of the mesoporous carbon-SiO_2 (MCS) sample. For typical process, about 0.5 g of the MCS-AM sample was stirred in 20 mL of 10 wt.% HF's ethanolic solution at least 12 h at room temperature. By this treatment, SiO_2 nano-particles in the MCS's framework structure are selectively removed. After the HF-treatment, remained solid (MC) was filtered, and washed with ethanol and water until the pH of the filtrate becomes >5. The recovered MCs were dried in an oven at 80 °C at least 12 h. The obtained product was designated as MC-AM in this chapter.

3.2.2 Heat Treatment

The as-made samples (MS1-AM, MS2-AM, MCS-AM, and MC-AM) were heated to the target temperature at a constant rate of 5 °C min^{-1} and maintained at the temperature for 2 h under Ar flow (50ccm). The obtained products were designated as *X*-*T*, where *X* and *T* represent type of mesoporous material and target temperature of the heat-treatment, respectively. For example, "MC-1200" means mesoporous carbon heat-treated at 1200 °C.

3.2.3 Structural Characterization

The obtained mesoporous materials were characterized by transmission electron microscope (TEM) observation, Nitrogen adsorption / desorption isotherms analysis, and powder X-ray diffraction (XRD) as mentioned in Section 2.2.2.

Table 3-1 Structural parameters of heat-treated mesoporous SiO_2 (MS1) samples.[a]

	S_{BET} ($cm^2\ g^{-1}$)	V_{total} ($cm^3\ g^{-1}$)	D_{KJS} (nm)	a_{10} (nm)
MS1-AM	696	0.77	7.3	10.6
MS1-600	566	0.64	7.3	10.5
MS1-700	673	0.79	7.3	10.5
MS1-800	457	0.57	6.9	10.2
MS1-900	315	0.42	6.8	9.9
MS1-1000	73	0.09	4.4	8.9
MS1-1200	23	0.03	—	—

[a] S_{BET}: specific surface area estimated by the BET method; V_{total}: total pore volume; D_{KJS}: primary mesopore diameter estimated by the KJS method; a_{10}: lattice constant estimated from apparent position of 10 XRD peak;

Table 3-2 Structural parameters of heat-treated mesoporous SiO_2 (MS2) samples.[a]

	S_{BET} ($cm^2\ g^{-1}$)	V_{total} ($cm^3\ g^{-1}$)	D_{KJS} (nm)	a_{10} (nm)
MS2-AM	1073	1.01	3.7	4.9
MS2-400	1041	0.77	3.5	4.7
MS2-500	1095	0.81	3.5	4.5
MS2-600	1102	0.65	3.3	4.3
MS2-700	1048	0.62	3.0	4.2
MS2-800	943	0.55	2.9	4.1
MS2-900	471	0.26	—	3.9
MS2-1000	7	0.01	—	—

[a] S_{BET}: specific surface area estimated by the BET method; V_{total}: total pore volume; D_{KJS}: primary mesopore diameter estimated by the KJS method; a_{10}: lattice constant estimated from apparent position of 10 XRD peak;

3.3 Results and Discussion

3.3.0.1 Mesoporous SiO_2 (MS1 and MS2)

Pore size distribution curves and small-angle XRD patterns of MS1s are shown in Figures 3-1 and 3-2, respectively. The structural parameters of the MS1s obtained by the XRD and N_2 adsorption isotherm data are summarized in Table 3-1. As shown in Figure 3-2, peak positions of MS1 were gradually shifted toward high-angler side with increasing heat-treatment temperature. The high-angler shifts of peak positions indicate that the pore-to-pore distance (unit cell size a) was gradually decreased with increasing heat-treatment temperature. As shown in Figure 3-1, the mesopore-diameter of MS1 was also decreased with increasing heat-treatment temperature. In the KJS analysis, existence of the mesopore was confirmed until 900 °C treatment, but the peak was suddenly disappeared after 1000 °C treatment. On the other hand, in the case of XRD data, diffraction peaks were still observed for the MS1-1000 sample, but the observed peak intensities in MS1-1000 were much smaller than that of the MS-900. These data clearly shows that mesopores of MS1 were rapidly destroyed between 900 °C and 1000 °C treatments. In the meantime, the width of diffraction peaks in MS1 were almost unchanged below 900 °C treatment. In contrast, the diffraction peak width of the MS1-1000 were much larger compared to MS-900. The increment of XRD peak width indicates a decrement of mesopore crystallite size, which gives information for the range of pore-ordering. This data also shows rapid structural deformation between 900 °C and 1000 °C treatments.

In the KJS analysis, peak widths of pore-size-distribution curves were almost unchanged until 900 °C treatment. Therefore, we can analyze the XRD data of MS1 until 900 °C treatment, without considering the effects of pore size distribution which discussed in Section 2.3.2.2. As discussed in Section 2.3.3, the ratio of peak intensities are depend on the γ value, that represent size ratio between mesopore-diameter D and pore-to-pore distance a. Since the ratio of 10, 11 and 20 diffraction intensities were almost constant under 900 °C

treatments, the structural shrinkage in mesopores and framework seems to occur with a similar manner. According to the N_2 adsorption and XRD data, about 7 % of shrinkage was observed between MS1-AM and MS1-900 samples.

In the next step, structural change of the MS2 was studied. Pore size distribution curves and small-angle XRD patterns of MS2s are shown in Figures 3-3 and 3-4, respectively. Structural parameters of the MS2 samples obtained from the XRD and N_2 adsorption isotherm analysis data are summarized in Table 3-2.

Although the shrinkage in mesopore diameter and inter-pore distance were also observed in MS2, the structural-changing behavior of MS2 seems somewhat different from MS1. As shown in Table 3-2, total volume V_{total} of MS2 was rapidly decreased between 800 °C and 900 °C treatments. Although 10 XRD diffraction peak was still observed, 11 and 20 peaks were not observed in MS2-900 sample. Furthermore, the 10 peak width of MS2-900 sample was rapidly increased compared to that of the MS2-800 sample. These data means that rapid structural deformation occurs for MS2 between 800 °C and 900 °C treatments. Differ from MS1, the relative peak intensities between 11 and 20 diffraction $I_{11}\,/\,I_{20}$ was gradually decreased with increasing heat-treatment temperature, especially above 600 °C treatments. According to the discussion performed in Section 2.3.3, such changes indicate a decrement of the γ value. In the case of MS2-AM sample, γ value was calculated to be 0.75. On the other hand, the gamma value of MS2-800 is calculated to be 0.72. This result means that the manner of shrinkage in mesopores were somewhat different from that in the framework-structure.

3.3.0.2 Mesoporous Carbon–SiO_2 Composite (MCS)

Pore size distribution curves and small-angle XRD patterns of MCSs are shown in Figures 3-5 and 3-6, respectively. Structural parameters of the MCS samples obtained from the XRD and N_2 adsorption isotherm data are summarized in Table 3-3.

Although a sharp peak was observed in KJS pore-size distribution curve in MCS-AM, the distribution rapidly spread above 1000 °C treatment. The pore volume V_{total} estimated from the N_2 adsorption data, also rapidly decreased at this temperature. As shown in Figure 3-6,

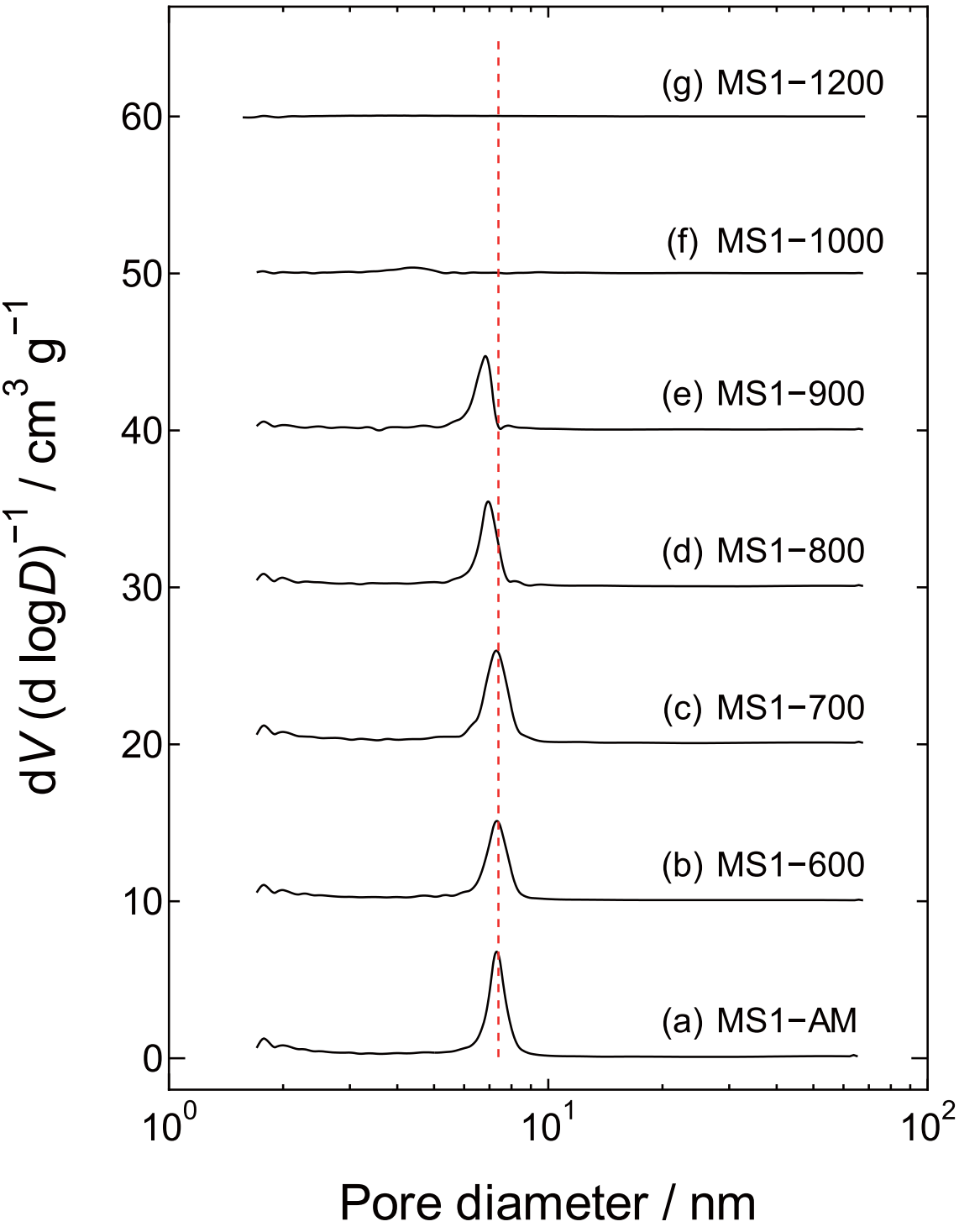

Figure 3-1 KJS pore size distributions of (a) MS1-AM, (b) MS1-600, (c) MS1-700, (d) MS1-800, (e) MS1-900, (f) MS1-1000, and (g) MS1-1200.

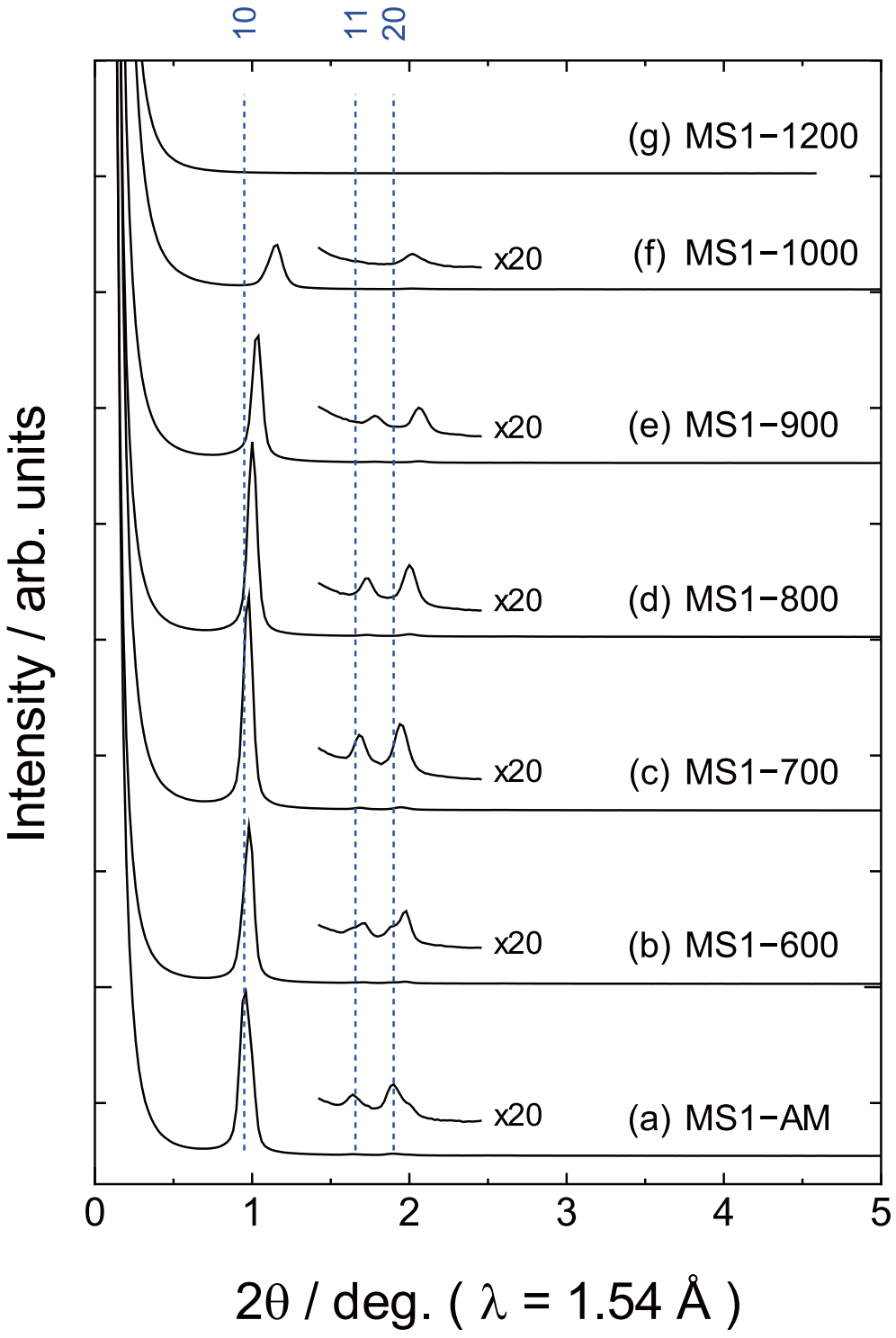

Figure 3-2 Small-angle X-ray diffraction patterns of (a) MS1-AM, (b) MS1-600, (c) MS1-700, (d) MS1-800, (e) MS1-900, (f) MS1-1000, and (g) MS1-1200.

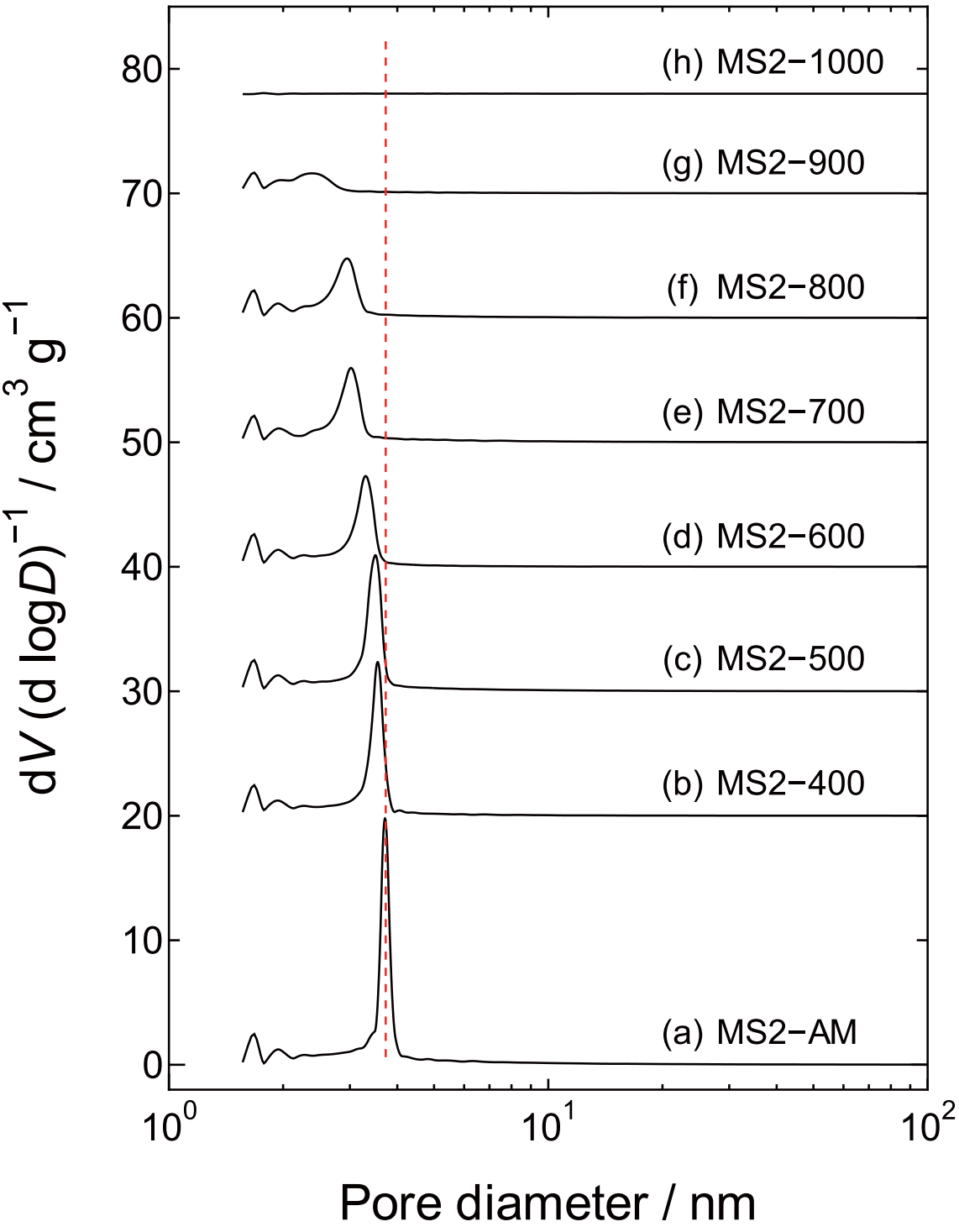

Figure 3-3 KJS pore size distributions of (a) MS2-AM, (b) MS2-400, (c) MS2-500, (d) MS2-600, (e) MS2-700, (f) MS2-800, (g) MS2-900, and (h) MS2-1000.

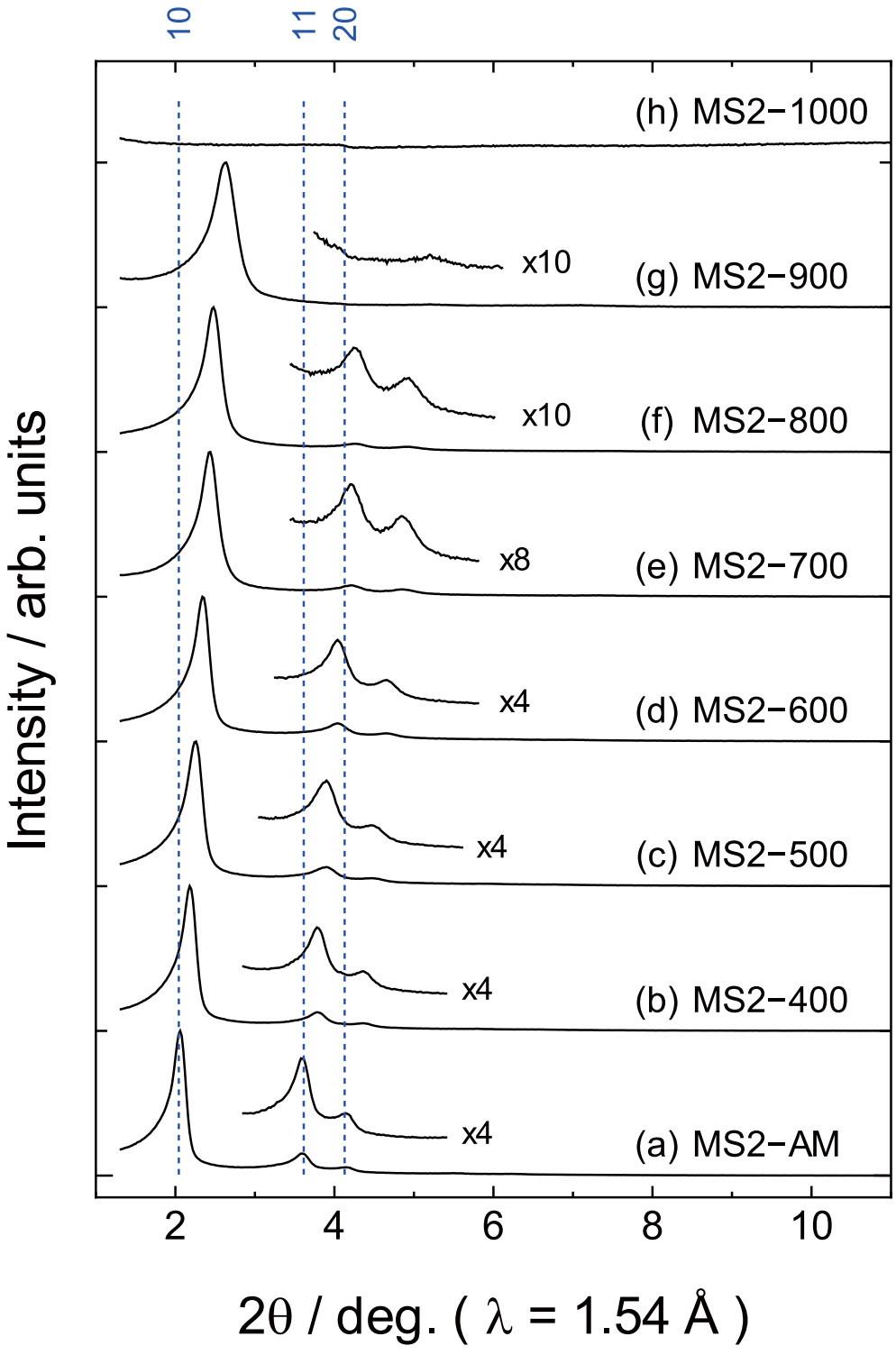

Figure 3-4 Small-angle X-ray diffraction patterns of (a) MS2-AM, (b) MS2-400, (c) MS2-500, (d) MS2-600, (e) MS2-700, (f) MS2-800, (g) MS2-900, and (h) MS2-1000.

Table 3-3 Structural parameters of heat-treated mesoporous carbon–SiO_2 (MCS) composites.[a]

	S_{BET} ($cm^2\ g^{-1}$)	V_{total} ($cm^3\ g^{-1}$)	D_{KJS} (nm)	a_{10} (nm)
MCS-AM	309	0.34	6.3	11.4
MCS-1000	302	0.26	5.6	10.9
MCS-1100	211	0.18	5.5	10.6
MCS-1200	234	0.20	5.1	10.5
MCS-1300	214	0.18	5.0	10.2
MCS-1400	173	0.14	5.0	10.1
MCS-1500	154	0.11	—	—
MCS-1600	78	0.23	—	—
MCS-1700	32	0.07	—	—

[a] S_{BET}: specific surface area estimated by the BET method; V_{total}: total pore volume; D_{KJS}: primary mesopore diameter estimated by the KJS method; a_{10}: lattice constant estimated from apparent position of 10 XRD peak;

10 diffraction peak was observed until 1500 °C treatment. However, higher-order peaks (11, 20 and 21) was disappeared even at 1000 °C treatment. As mentioned in Section 2.3.2.1, the vanishment of high-order peaks can be explained by displacement of the pore positions. These results are probably explained by the crystallization of SiO_2 particles encapsulated in their framework as follows: As seen in MS1 and MS2 case, structure of SiO_2 is rapidly changed at around 1000 °C, but since SiO_2 particles are well-dispersed in amorphous matrix, the mesostructure of MCS was not completely deformed by this crystallization. Therefore, the 10 diffraction peak was maintained even above 1000 °C. On the other hand, since the positions of mesopores are partially fluctuated due to this crystallization, high-order peaks disappeared by the Debye–Waller factor. Above 1600 °C treatment, the mesostructure of MCS was almost totally destroyed.

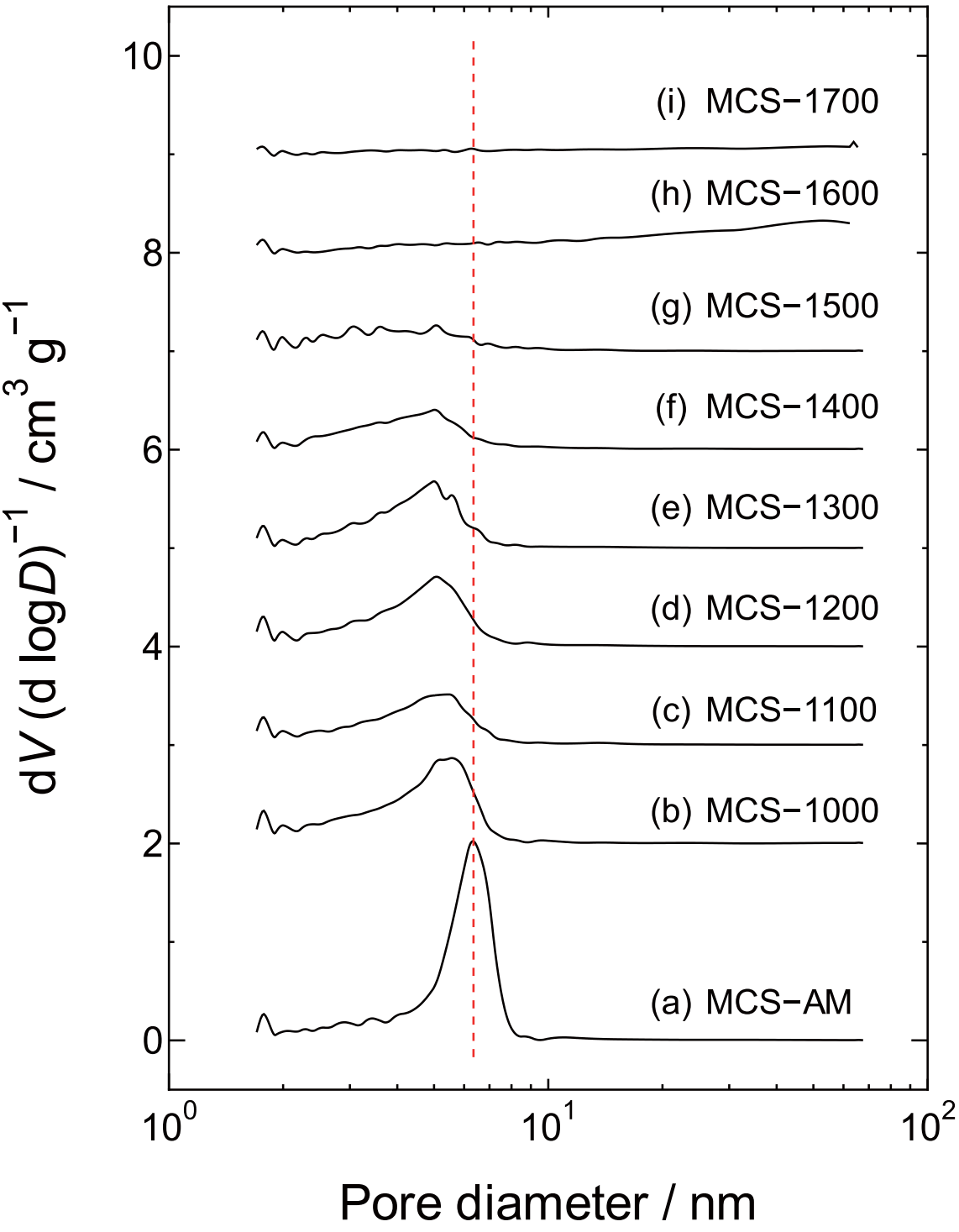

Figure 3-5 KJS pore size distributions of (a) MCS-AM, (b) MCS-1000, (c) MCS-1100, (d) MCS-1200, (e) MCS-1300, (f) MCS-1400, (g) MCS-1500, (h) MCS-1600, and (i) MCS-1700.

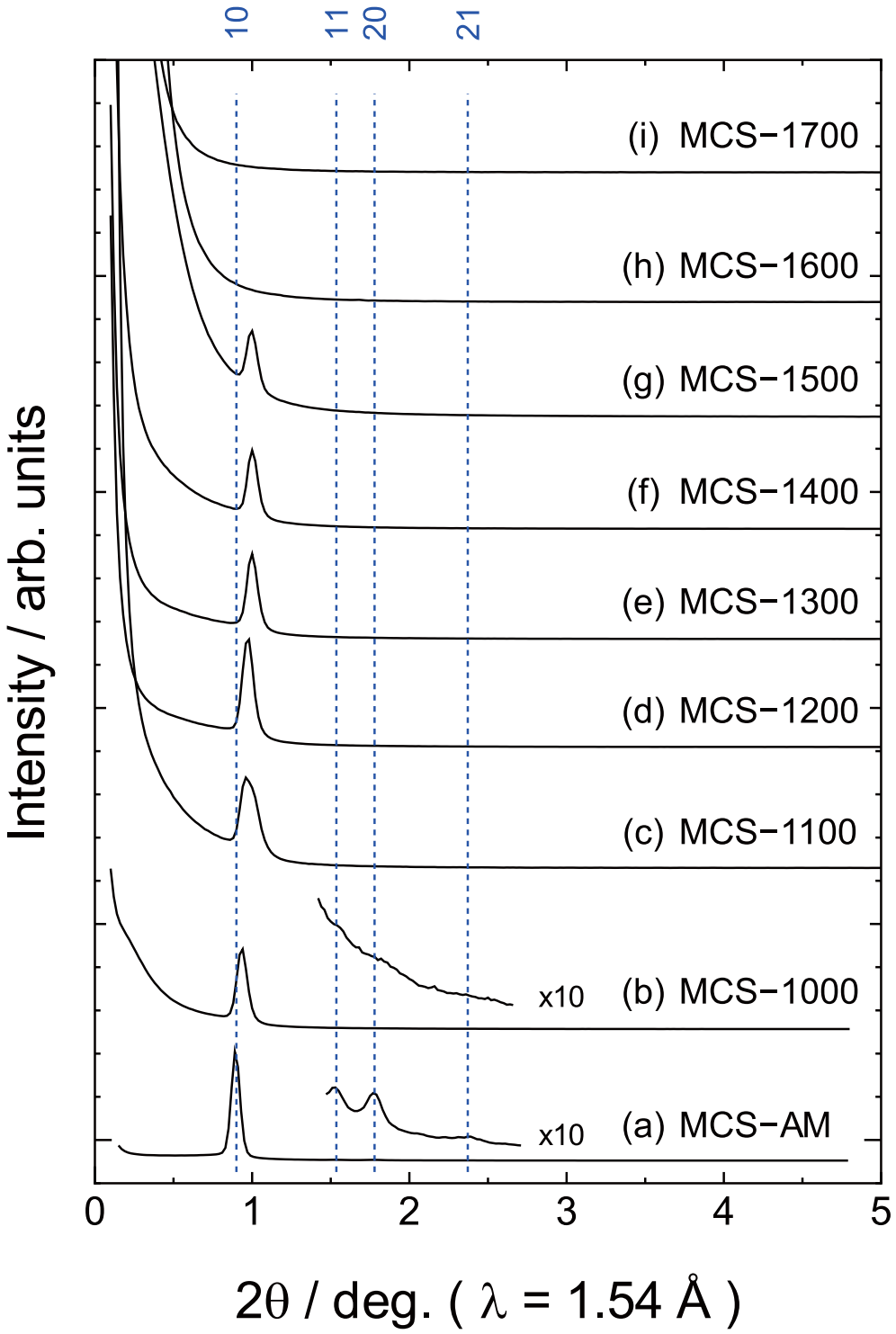

Figure 3-6 Small-angle X-ray diffraction patterns of (a) MCS-AM, (b) MCS-1000, (c) MCS-1100, (d) MCS-1200, (e) MCS-1300, (f) MCS-1400, (g) MCS-1500, (h) MCS-1600, and (i) MCS-1700.

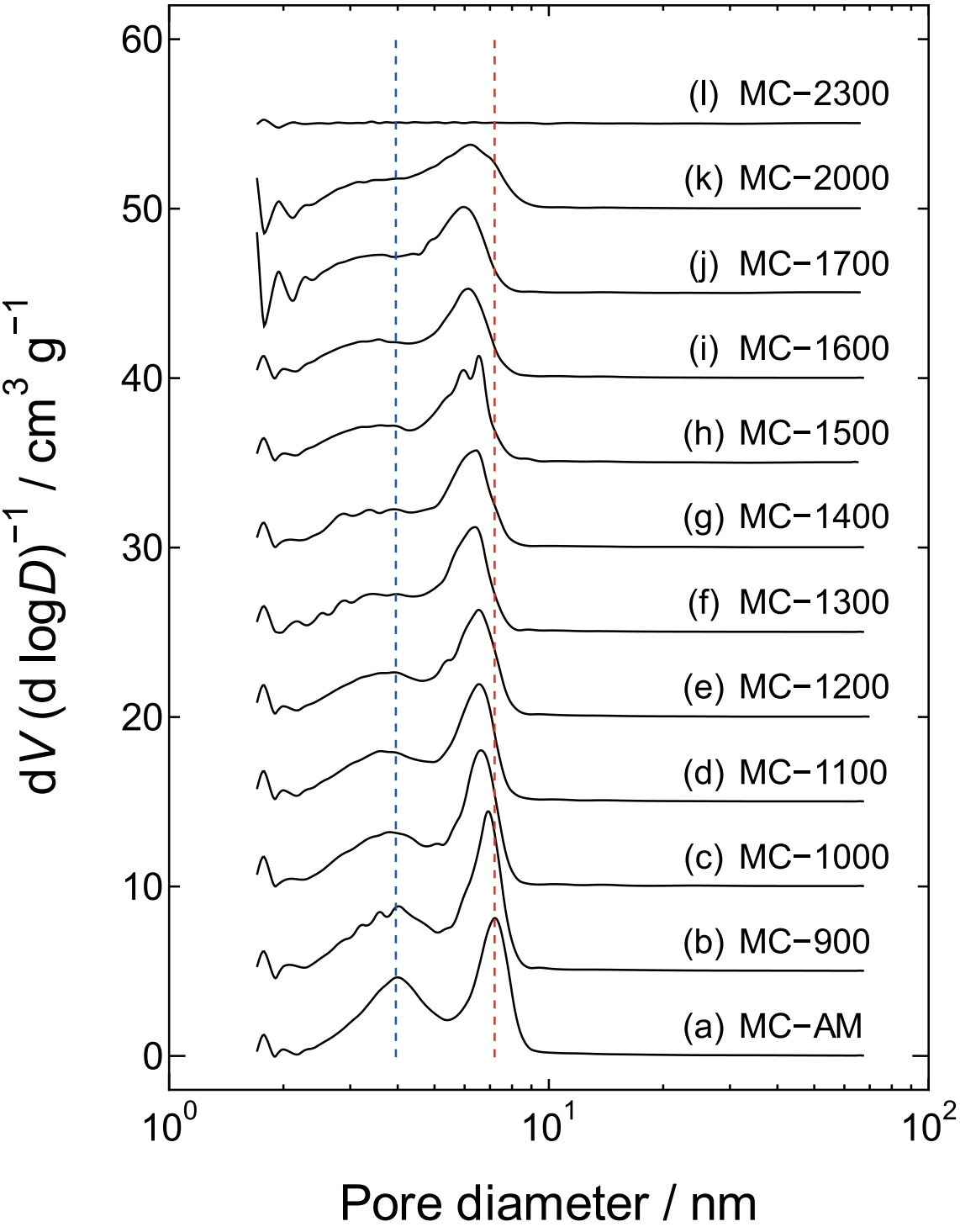

Figure 3-7 KJS pore size distributions of (a) MC-AM, (b) MC-900, (c) MC-1000, (d) MC-1100, (e) MC-1200, (f) MC-1300, (g) MC-1400, (h) MC-1500, (i) MC-1600, (j) MC-1700, (k) MC-2000, and (l) MS1-2300.

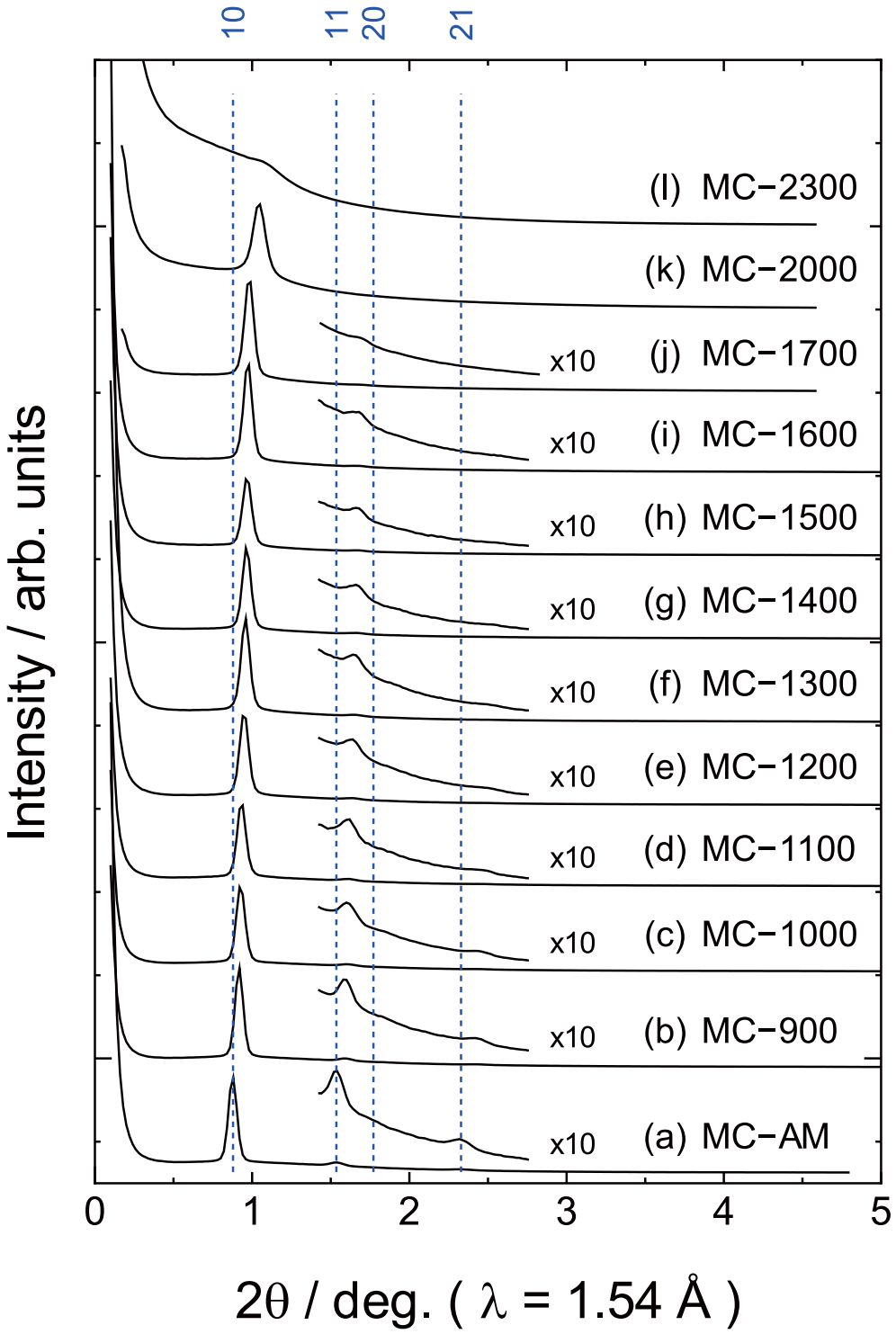

Figure 3-8 Small-angle X-ray diffraction patterns of (a) MC-AM, (b) MC-900, (c) MC-1000, (d) MC-1100, (e) MC-1200, (f) MC-1300, (g) MC-1400, (h) MC-1500, (i) MC-1600, (j) MC-1700, (k) MC-2000, and (l) MS1-2300.

Table 3-4 Structural parameters of heat-treated mesoporous carbon (MC) samples.[a]

	S_{BET} ($cm^2\ g^{-1}$)	V_{total} ($cm^3\ g^{-1}$)	D_{KJS} (nm)	a_{10} (nm)
MC-AM	1659	1.81	7.2	11.1
MC-900	1791	1.86	6.9	11.1
MC-1000	1815	1.77	6.6	11.0
MC-1100	1804	1.68	6.5	10.9
MC-1200	1766	1.63	6.5	10.7
MC-1300	1709	1.54	6.4	10.6
MC-1400	1727	1.53	6.4	10.5
MC-1500	1785	1.57	6.5	10.5
MC-1600	1728	1.49	6.1	10.5
MC-1700	1622	1.44	6.0	10.4
MC-2000	1121	1.13	6.2	9.8
MC-2300	33	0.06	—	—

[a] S_{BET}: specific surface area estimated by the BET method; V_{total}: total pore volume; D_{KJS}: primary mesopore diameter estimated by the KJS method; a_{10}: lattice constant estimated from apparent position of 10 XRD peak;

3.3.0.3 Mesoporous Carbon (MC)

Pore size distribution curves and small-angle XRD patterns of MCs are shown in Figures 3-7 and 3-8, respectively. Structural parameters of the MCS samples obtained by the XRD and N_2 adsorption isotherm data are summarized in Table 3-4.

In the case of MC, the existence of primary-mesopore originates from surfactant micelles was confirmed even after 2000 °C treatment (see Figure 3-7). As seen in Figure 3-8, the 10 diffraction peak was also maintained at this temperature. As observed in other samples, structural shrinkage accompanied by an increment of heating temperature was also confirmed

in the MCS. The intensity ratio of 11, 20, and 21 diffraction peaks was almost unchanged in all samples which have high-order diffraction peaks. This result means that structural shrinkage in primary-mesopore and framework-structure occurred in simultaneous manner like MS1 case. Above 1400 °C treatment, the high-order diffraction was gradually damped. Structural deformation seems to occur gradually from this temperature region. After 2300 °C treatment, these structural features were completely disappeared.

3.4 Summary

In this chapter, thermal stability of two-types of mesoporous SiO_2 samples (MS1 and MS2), a mesoporous carbon–SiO_2 (MCS), and a mesoporous carbon (MC) were studied. The MC showed superior thermal stability compared to MS1, MS2 and MCS. Although ordered pore structure of mesoporous SiO_2 samples were collapsed below 1000 °C treatment, the structure of MC was maintained even after 2000 °C treatment.

Chapter 4

Electrochemical Energy Storage Properties of Ordered Mesoporous Carbons

4.1 Introduction

Since their high-surface areas, and electric conductivity, mesoporous carbons (MCs) would be used as superior electrode materials for electric double-layer capacitor (EDLC). Furthermore, their amorphous-carbon framework may enable their usage as anode materials for lithium-ion battery (LIB) and sodium-ion battery (SIB). For these electrochemical applications, the ordered-mesoporous in MC electrodes would be used as an ideal ion-diffusion path.

In Chapter 3, it was found that the MCs, synthesized from a mesoporous carbon-SiO_2 composite (MCS), has good thermal stability up to about 2000 °C. The pore-to-pore distance (i.e. unit cell constant a) of MCs was gradually decreased with increasing heat-treatment temperature, probably due to thermally-induced crystallization of the framework structure. These results mean that we can control the crystallinity of amorphous carbon in mesoporous-framework with keeping its ordered nano-structure. Since the lithium- and sodium-ion storage properties of amorphous carbons should be affected by their crystallinity, the MCs processed by different heat-treatment temperatures are expected to show different electrochemical properties. However, for MCs, the relationships between electrode-properties and framework-crystallinity have not be experimentally investigated yet. Therefore, EDLC-, LIB-, and SIB-electrode properties of MC samples witch processed at different heat-treatment temperatures were investigated and compared in this chapter.

4.2 Experimental Methods

4.2.1 Sample Preparation

The MC samples processed by various heat-treatment temperatures were compared in this chapter. Preparation procedures of MCs are described in Sections 3.2.1.3 and 3.2.2. For comparison, a hard-carbon sample carbonized at 900 °C (RC-900), which is prepared from same carbon-source (resol) with MCs but lacks of ordered mesostracture, was also used in this chapter. The synthesis method of resol, and a heat-treatment procedure were mentioned in Sections 2.2.1.3 and 3.2.2, respectively.

4.2.2 EDLC Measurements

EDLC properties of MCs were characterized by galvanostatic charge-discharge tests and cyclic voltammetry using a three-electrode-type cell shown in Figure 4-1. The measurements were conducted using a potentiostat / galvanostat (HA-151, Hokuto Denko) controlled by a computerized system. The voltage window was set to −1.0–1.5 V vs. Ag / Ag^{+}. In the measurement, an activated carbon-fiber (ACF A-7, AD' ALL), a Ag / Ag^{+} electrode (BAS), and a propylene carbonate (PC) containing 1 mol L^{-1} triethylmethylammonium tetrafluoroborate (TEMA-BF_4) were used as the counter electrode, reference electrode, and electrolyte, respectively. Platinum-meshs were used as the current-correctors for working- and reference-electrodes. To prepare the working electrode, the MC samples (80 wt.%) were mixed with polytetrafluoroethylene (PTFE) binder (10 wt.%) and Ketjenblack carbon (10 wt.%) in appropriate quantities of 2-propanol. The mixture was formed into a sheet, and dried at 120 °C for at least 2 h in vacuum prior to use. Both the set-up of the cell and charge-discharge measurements were performed in an Ar-filled glove box to avoid air exposure and contamination. In order to imbue the electrodes sufficiently with the electrolyte solution, the assembled cells were kept in the glove box for at least 12 h before the measurements.

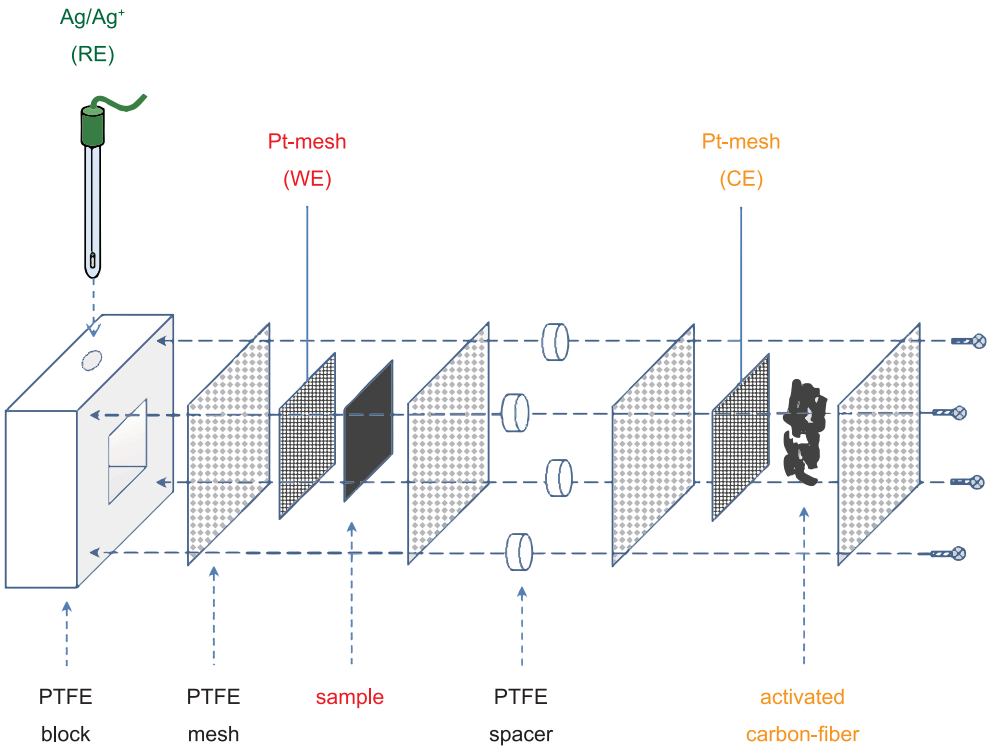

Figure 4-1 Structure of the three-electrode-type cell used for EDLC measurements.

4.2.3 LIB Measurements

Lithium-ion storage electrode properties of MCs were characterized by galvanostatic charge-discharge tests using a conventional two-electrode-type cell (Hohsen HSCell) shown in Figure 4-2. The measurements were conducted using a galvanostat (Toyo System TOSCAT-3200). The voltage window was set to 0.0–3.0 V vs. Li / Li^+. To prepare the working electrode, the MC samples (90 wt.%) were mixed with polyvinylidene difluoride (PVDF) binder (10 wt.%) in appropriate quantities of 1-methyl-2-pyrrolidone (NMP). Since the mesoporous carbon samples have electric conductivity, conductive agent was not used in this study. The obtained slurry was pasted onto a Cu foil and dried at 120 °C for at least 2 h in vacuum prior to use. A lithium foil (Aldrich) was used as the counter and quasi reference electrode. A mixture of ethylene carbonate (EC) and diethyl carbonate (DEC) solution (EC : DEC=1 : 1 in volume ratio) containing 1 mol L^{-1} $LiClO_4$ was used as the electrolyte. A porous polypropylene film (Celgard #2500) was used as a separator. Both the

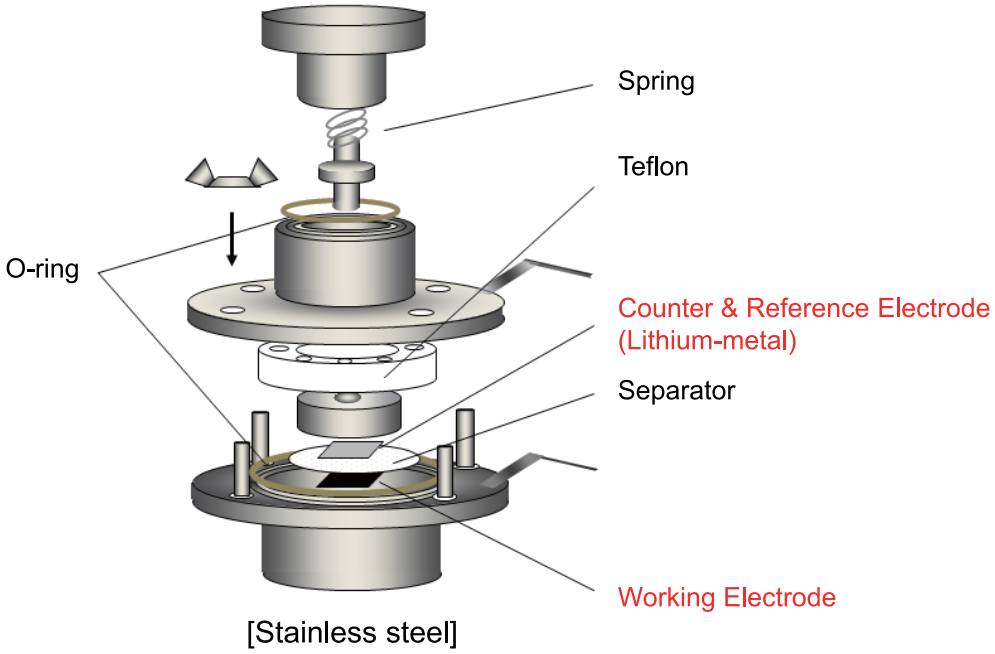

Figure 4-2 Structure of the two-electrode-type cell used for LIB and SIB measurements. (Hohsen HSCell)

set-up of the cell and charge-discharge measurements were performed in an Ar-filled glove box to avoid air exposure and contamination. In order to imbue the electrodes sufficiently with the electrolyte solution, the assembled cells were kept in the glove box for at least 24 h before the measurements.

4.2.4 SIB Measurements

Sodium-ion storage properties of MCs were characterized by galvanostatic charge-discharge tests using similar equipment and procedure described in Section 4.2.3, except for the types of counter-electrode, electrolyte, and range of voltage window. In the SIB measurements, a sodium foil (Aldrich) was used as the counter and quasi reference electrode. A propylene carbonate (PC) solution containing 1 mol L^{-1} $NaClO_4$ was used as the electrolyte. The voltage window was set to 0.0–3.0 V vs. Na / Na^+

4.3 Results and Discussion

4.3.1 EDLC Electrode Properties

Cyclic voltammograms (CVs) of MC-900, MC-1200, MC-1500, and MC-1700 electrodes are shown in Figure 4-3. Butterfly-shape CV curves were observed in the all electrodes. The voltage of the most constricted part in the CV curves were almost same value (about -100 mV vs. Ag/Ag^{+}) independent of the heat-treatment temperature. The value was almost matched with open-circuit voltage (OCV) of the MC electrode. According to previous EDLC reports, the type of adsorbed ions switches at the OCV: cation adsorption occurs below the OCV, and anion adsorption occurs above the OCV. Although cation used in this measurement ($TEMA^{+}$) was much larger than anion ($BF_4{}^{-}$), the shape of CV curves in cation-adsorption side and anion-adsorption side were quite symmetrical. This feature differs from microporous electrodes such as activated carbons.

The capacitance of EDLC electrodes can be estimated from the size of CV curves. The capacitance values estimated from the CV curves were well agreed with that estimated from the slope of galvanostatic charge/discharge curves shown in Figure 4-4. As shown in Figure 4-5, The MC electrodes showed good rate performance, probably due to their large mesopores. In the current study, the highest capacitance were obtained for the MC-1200 electrode (106 F g^{-1}).

As shown in Figures 4-3 and 4-4, the capacitance values of MC electrodes were changed with heat-treatment temperature. Since, the capacitance of EDLC electrode is essentially proportional to their surface areas which used as ion-adsorption sites, relationship between BET surface area and specific capacitance value of MC electrodes were compared. Figure 4-6 shows capacity value vs. BET surface area plot of the MC electrodes. In the case of MC-1400, MC-1500, MC-1600, and MC-1700 electrodes, the capacitance values were almost proportional to the BET surface areas. On the other hand, although capacitance values of MC-900, MC-1000, MC-1100, MC-1200, and MC-1300 were not promotional to the BET surface areas, they showed higher capacitance than MC-1400, MC-1500, MC-1600,

and MC-1700 electrodes. Since previous studies indicate that abnormal capacitance increment occurs in the carbon-micropores, the observed surface-area-independent high capacitance may be explained by the micropores in MC's framework. In fact, the existence of large amount of micropores in the MC-1200 sample was also be expected from the structural analysis data discussed in the Section 3.3.0.3: Although mesopore diameter D_{meso} is continuously decreased with increasing heat-treatment temperature, their BET surface areas S_{BET} was almost unchanged under 1200 °C treatment (see Table 3-4). This fact imply that the micropore volume of MC was gradually increased with increasing heat-treatment temperature under 1200 °C treatment. After the 1200 °C treatment, both S_{BET} and D_{meso} were continuously decreased with increasing heat-treatment temperature. This imply that the micropore volume was gradually decreased, above 1200 °C treatment. Therefore the MC electrode processed above 1400 °C would showed relatively low capacitance compare to the electrodes that heat-treated under 1300 °C.

4.3.2 LIB and SIB Electrode Properties

Figures 4-7 and 4-8 shows galvanostatic charge-discharge curves of MC electrodes. Although large hystereses were observed in charge-discharge curves, the MC electrodes showed very large reversible capacity in the LIB measurement. About 1200 mAh g^{-1} was observed in MC-1200 electrode.

As shown in Figure 4-9, the capacity of MC-900 electrode was much higher than non-mesoporous RC-900 electrode, especially at low current density conditions. On the other hand, in SIB measurement, the reversible capacitances of MC electrodes were smaller than RC-900 electrode (see Figure 4-10). According to the previous nuclear-magnetic resonance (NMR) spectroscopy and small-angle X-ray scattering (SAXS) studies, at least two-types of ion-storage sites are considered for hard-carbon electrodes: one is intercalation with misaligned graphene layer, and the other is ion-clustering at micropores.[54,55] In both Li and Na storage electrode, the former reaction occurs at relatively high voltage (0.4–1.2 V) and the latter storage occurs near metal-plating voltage (< 0.4 V). Figures 4-11 and 4-12 show magnified views of

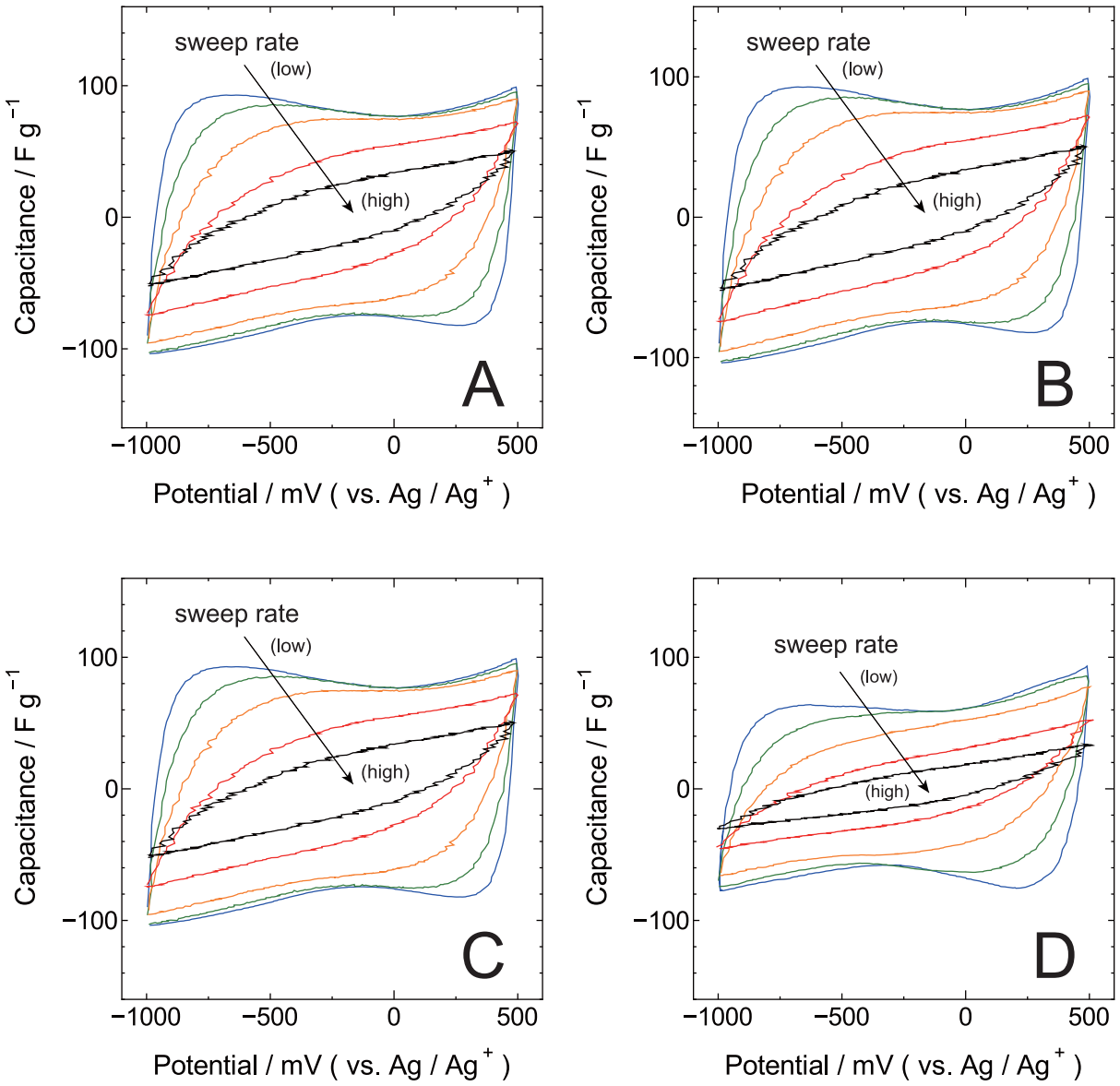

Figure 4-3 Cyclic voltammograms of (A) MC-900, (B) MC-1200, (C) MC-1500, and (D) MC-1700 electrodes. Sweep rates were set to 5 mV s^{-1} (blue line), 10 mV s^{-1} (green line), 20 mV s^{-1} (orange line), 50 mV s^{-1}, and 100 mV s^{-1} (black line).

galvanostatic charge / discharge curves at the 2nd cycle. In both LIB and SIB measurements, slope of discharge curves were changed at around 0.4 V. In the case of LIB cell, the discharge capacities at the 2nd cycle of MC-900, MC-1200, MC-1700, and RC-900 electrodes above 0.4 V were 318, 290, 149, and 107 mAh g^{-1}, respectively. On the other hand, the discharge capacity of MC-900, MC-1200, MC-1700, and RC-900 electrodes below 0.4 V were 783, 963, 262, and 166 mAh g^{-1}, respectively. Therefore, in the all carbon electrode, Li-storage

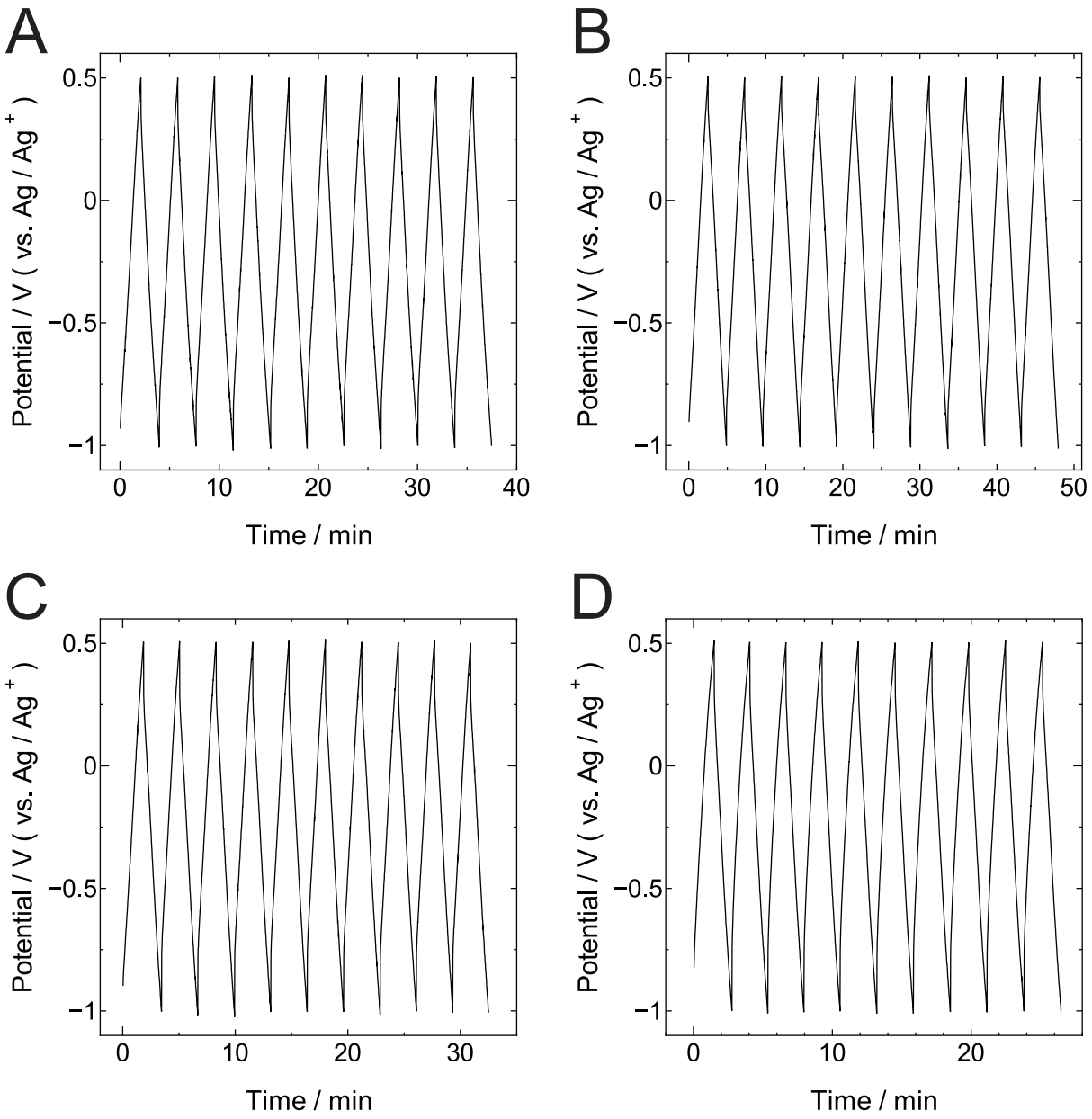

Figure 4-4 Galvanostatic charge-discharge curves of (A) MC-900, (B) MC-1200, (C) MC-1500, and (D) MC-1700 electrodes measured at 1000 mAh g^{-1}.

at < 0.4 V region, which probably attribute to Li-clustering in micropore, was more dominant compared the above 0.4 V region which intercalation into misaligned graphene-sheets occur. The MC-1200 electrode showed highest reversible capacity in those four electrodes. The high capacity of MC-1200 seems to come from its large micropore volume used as Li-ion clustering site. As mentioned in Section 4.3.1, the amount of micropores in MC-1200 electrode seems to be much higher than MC-900 and MC-1700 electrodes. Actually the MC-1200 electrode

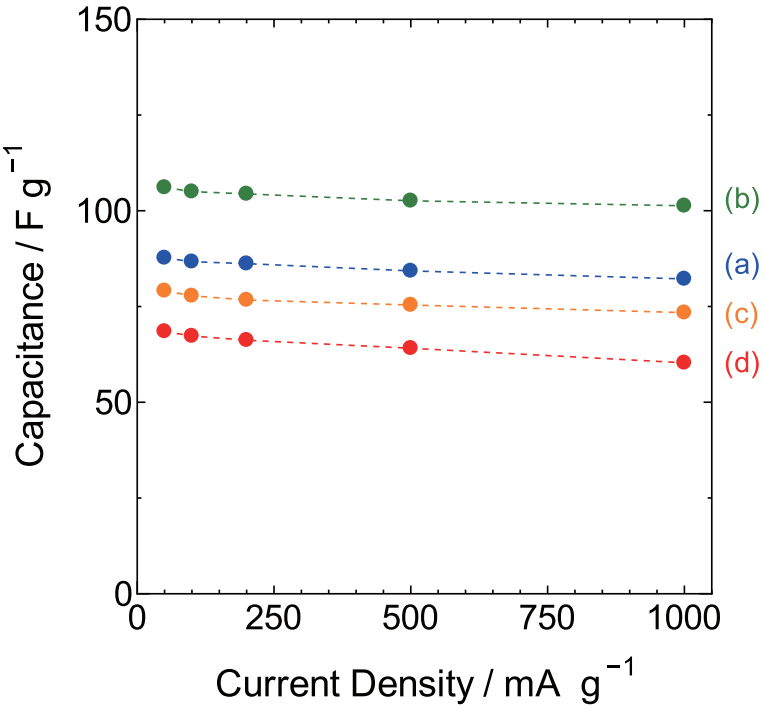

Figure 4-5 Current density vs. reversible capacity plot of (A) MC-900, (B) MC-1200, (C) MC-1500, and (D) MC-1700 EDLC electrodes.

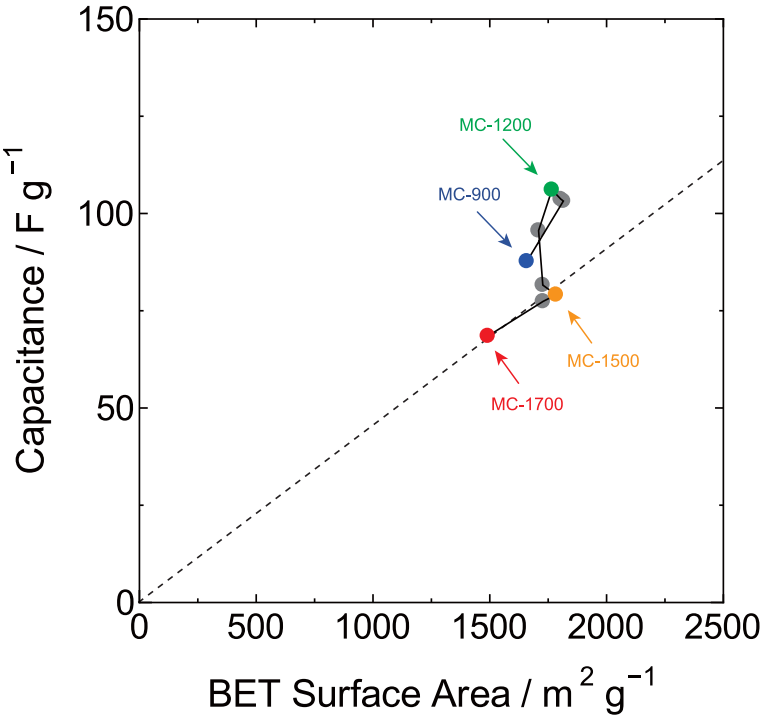

Figure 4-6 BET surface area vs. EDLC capacity plot. For the capacity calculation, galvanostatic charge-discharge data obtained at 50 mA g^{-1} were used.

showed largest discharge capacity at below 0.4 V region.Although large contribution below 0.4 V was also confirmed in in the case of SIB cell, absolute value of capacity were much lower than LIB case. Even in the case of MC-1200 electrode, the Na-storage at < 0.4 V region was only 56 mAh g^{-1}. According to the recently performed NMR study,[54] electric structure of Na-ion cluster in carbon micropores are completely different from that o Li-ion clusters. Such a difference may cause the difference in capacity between LIB and SIB. Anyway, introducing micropores into mesoporous carbon-framework seems to be effective for increasing capacity of alkaline-ion storing electrodes. Modification of micropore structure in mesoporous carbons should be required in the future work.

4.4 Summary

In this chapter, electrode properties of MC samples processed by different heat-treatment temperatures were compared. In the EDLC measurement, large capacitance (about 100 F g^{-1}) was obtained for MC-1200 electrode. In the LIB measurement, the MC-1200 electrode also showed good performance compared to the other MC electrodes. Although large hystereses were observed in charge-discharge curves, the MC electrodes showed very large reversible capacity up to about 1200 mAh g^{-1}. The cyclability and capacitance value of MC-900 electrode was much higher than that of nonporous RC-900 electrode. Unfortunately however, NIB electrode properties of MC electrode were much poor compared to LIB properties. Micropores in MCs seems to be used as important ion-storage site for EDLC and LIB electrode.

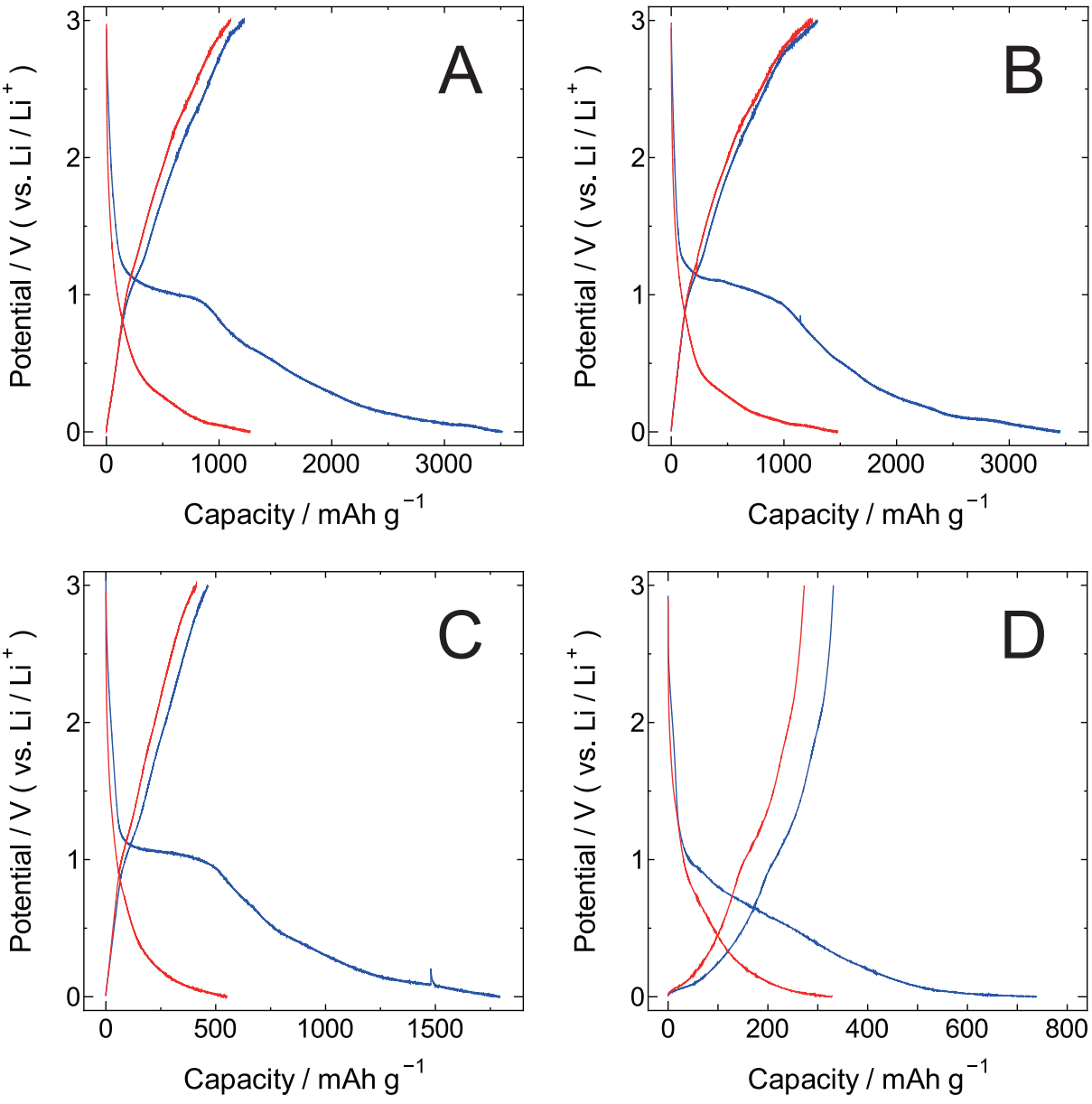

Figure 4-7 Lithium-ion storage properties of (A) MC-900, (B) MC-1200, (C) MC-1700, and (D) RC-900 electrodes. Galvanostatic charge-discharge curves measured at 25 mAh g^{-1} are shown. Charge-discharge curves at the first cycle and second cycle are shown in blue- and red-line, respectively.

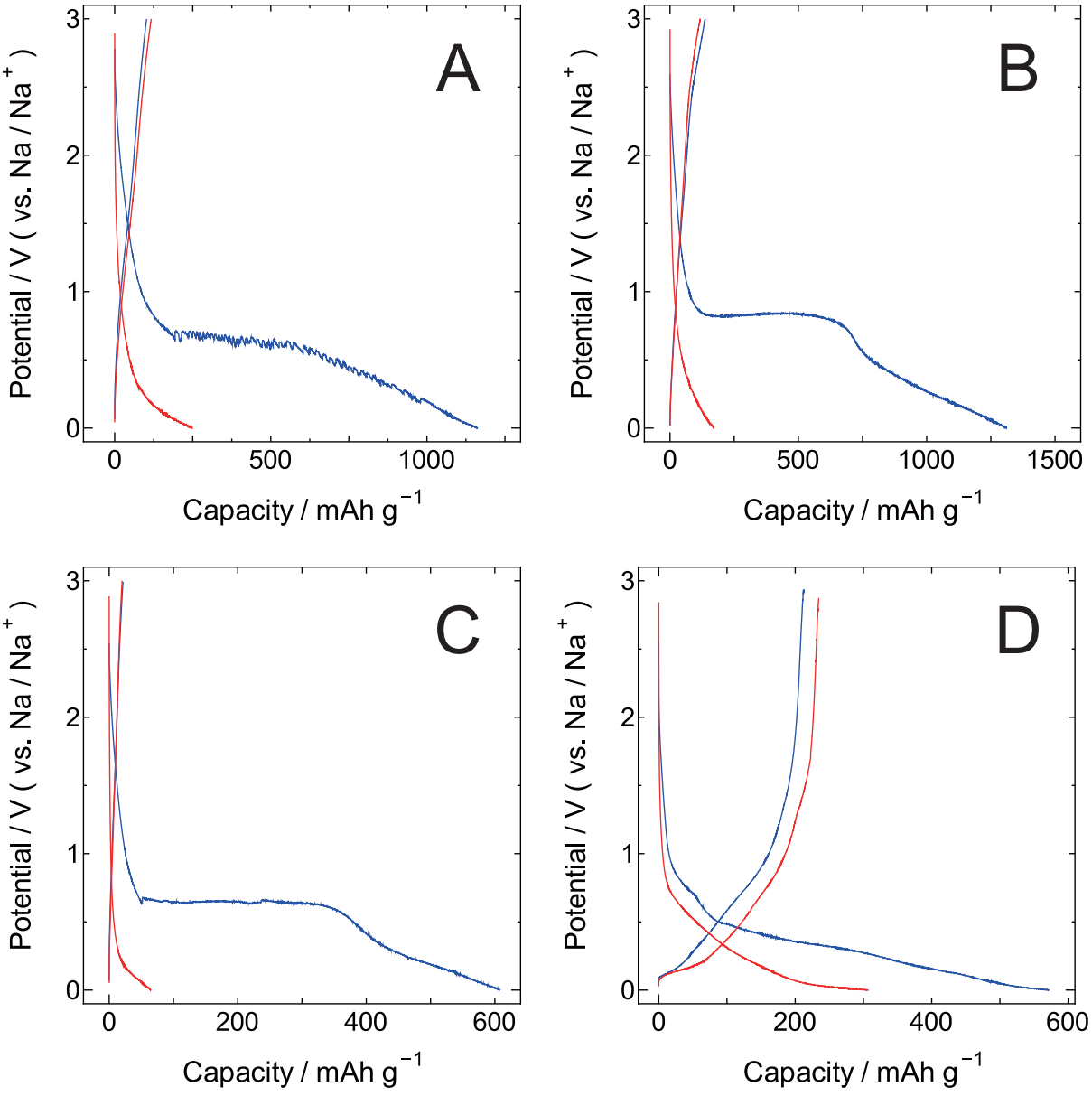

Figure 4-8 Sodium-ion storage properties of (A) MC-900, (B) MC-1200, (C) MC-1700, and (D) RC-900 electrodes. Galvanostatic charge-discharge curves measured at 25 mAh g^{-1} are shown. Charge-discharge curves at the first cycle and second cycle are shown in blue- and red-line, respectively.

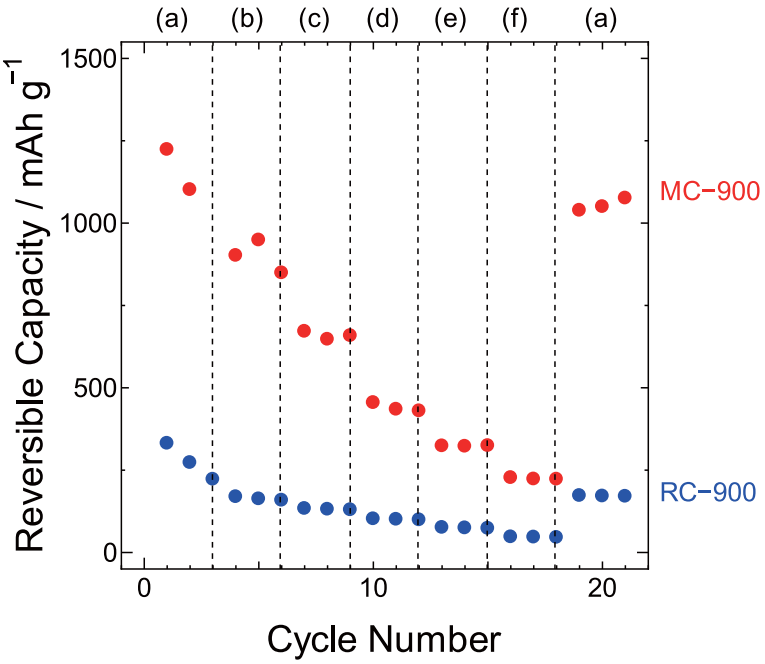

Figure 4-9 Cycling performance of MC-900 (red circles) and RC-900 (blue circles) LIB electrodes at different current densities of (a) 25, (b) 50, (c) 100, (d) 250, (e) 500 and (f) 1000 mA g^{-1}. The voltage window was set to 0.0–3.0 V vs. Li/Li^{+}.

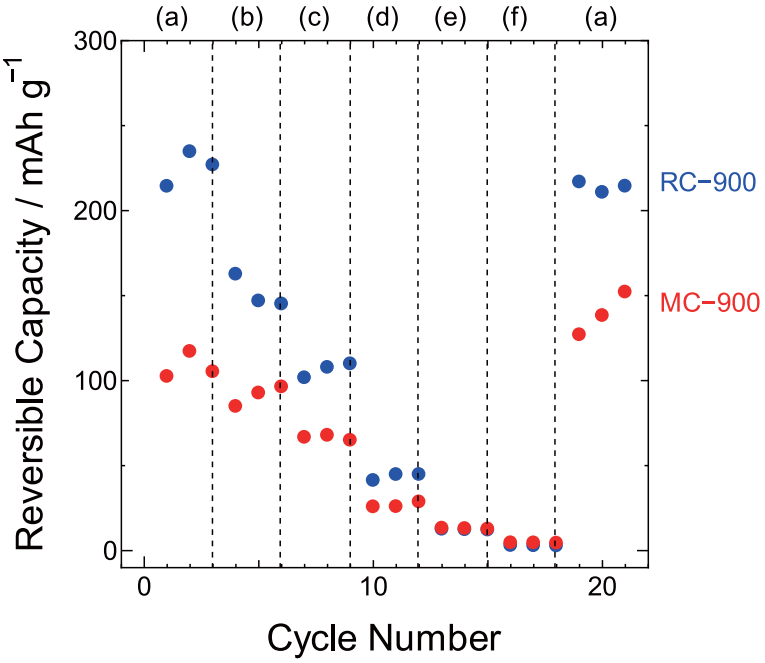

Figure 4-10 Cycling performance of MC-900 (red circles) and RC-900 (blue circles) SIB electrodes at different current densities of (a) 25, (b) 50, (c) 100, (d) 250, (e) 500 and (f) 1000 mA g^{-1}. The voltage window was set to 0.0–3.0 V vs. Na/Na^{+}.

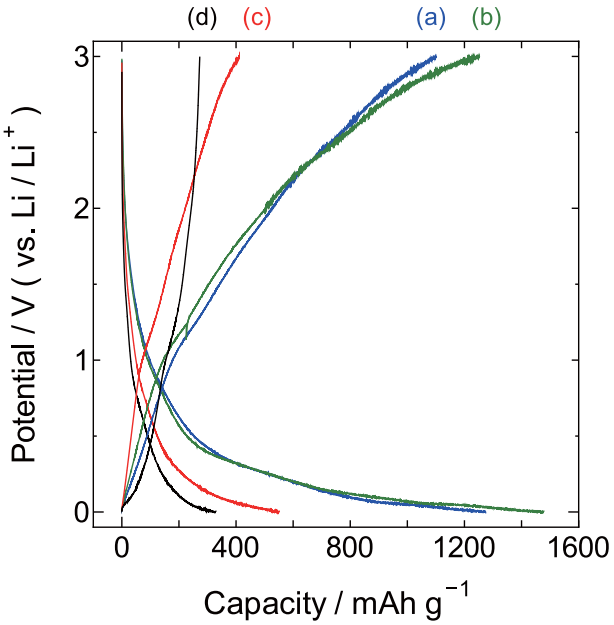

Figure 4-11 Galvanostatic charge-discharge curves at 2nd cylcle of (a, blue line) MC-900, (b, green line) MC-1200, (c, red line) MC-1700, and (d, black line) RC-900 LIB electrodes. Current density was set to 25 mA g^{-1}.

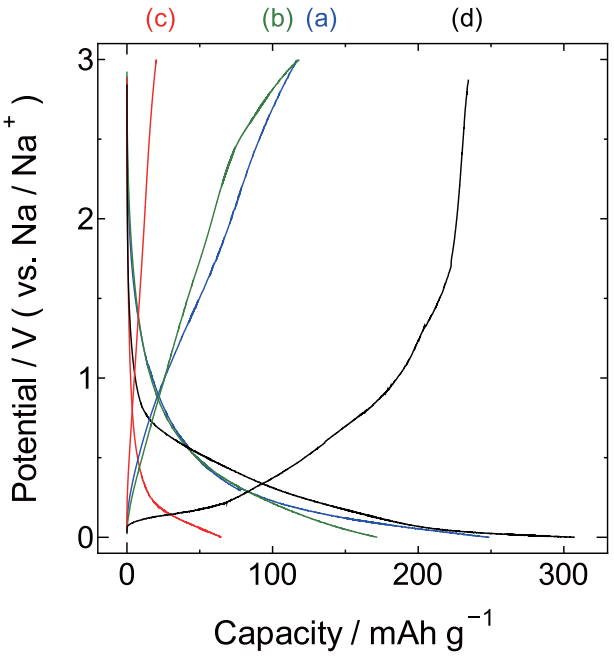

Figure 4-12 Galvanostatic charge-discharge curves at 2nd cylcle of (a, blue line) MC-900, (b, green line) MC-1200, (c, red line) MC-1700, and (d, black line) RC-900 SIB electrodes. Current density was set to 25 mA g^{-1}.

Chapter 5

Lithium Storage Properties of Ordered Mesoporous Carbon–TiO_2 Composites

5.1 Introduction

As mentioned in Section 1.2.1.3, TiO_2 is one of a promising candidate for electrochemical lithium storage material for high-power operation. So far, various types of TiO_2 samples such as nanoparticles,[45,130,131] hollow microspheres,[132–134] nanoribbon,[49] nanotubes,[135–140] nanowires,[48,50,53,141–143] and mesoporous types[46,51,144–153] have been synthesized and applied as lithium-ion battery electrodes. These studies have been showed that electrode performance can dramatically be improved by designing its nanostructure. However, a common disadvantage of such TiO_2 electrodes is their low electric conductivity.[154–156] Such a low electric-conductivity electrode induces decrease in capacity, especially during high power operations, because of ohmic loss. Compounding with carbon materials is a promising approach to overcome this problem. To date, various carbon–TiO_2 composite materials such as carbon-coated TiO_2,[52,157–159] carbon nanotubes–TiO_2 composites,[155,160] and graphene–TiO_2 composites,[161–164] have been reported. These carbon–TiO_2 composites have been showed superior charge-discharge performances especially at high rate conditions. In this context, the authur think that carbon–TiO_2 composite electrodes having ordered cylindrical mesopores, and consists of a homogeneous matrix of TiO_2 nanoparticles and amorphous carbon (i.e. mesoporous carbon–TiO_2 composites; MCTs) should show superior electrode performance; that is to say, carbon compensates the low electric conductivity of TiO_2, the cylinder mesopore would be used as conduction path for solvated lithium-ions, and its large surface areas increase solid-electrolyte interphase where Li insertion / extraction reaction occurs. Furthermore, small

grain size of TiO_2 crystal can reduce the solid-state lithium-ion diffusion length. Therefore, lithium storage properties of MCT electrodes were studied in this chapter.

By analyzing crystal structure of obtained MCTs, the author found that the MCTs seem to have two types of TiO_2 crystals: anatase and TiO_2(B). Here TiO_2(B) is a TiO_2 polymorph discovered by Marchand *et al.* in 1980.[47] The TiO_2(B) phase is different from the well-known brookite, rutile, and anatase phases. Compared to spinel $Li_4Ti_5O_{12}$ (theoretical capacity: 175 mAh g^{-1}), which has a similar operating voltage (about 1.55 V vs. Li/Li^+), but TiO_2(B) presents a higher theoretical capacity (335 mAh g^{-1}). Therefore, extensive studies of the TiO_2(B) polymorph have been performed in recent years.[48–53] So far, in case of anatase, the detailed lithium insertion mechanism has been elucidated by some groups.[43,165,166] On the other hand, lithium storage in TiO_2(B) has still not been thoroughly investigated. In order to discuss the different electrochemical properties of MCT electrode, an *in situ* XRD investigation during the galvanostatic charge-discharge test was also performed for a bulk TiO_2(B) sample in this study. In my best knowledge, this is the first report for *in situ* structural analysis for TiO_2(B) electrode.

5.2 Experimental Methods

5.2.1 Sample Preparation

5.2.1.1 Synthesis of Mesoporous Carbon–TiO_2 Composites

The mesoporous carbon–TiO_2 composite samples were synthesized using the triconstituent co-assembly method.[167] In this procedure, we used phenol-formaldehyde resin (resol) as a carbon source, titanium tetrachloride ($TiCl_4$) as a TiO_2 precursor, and triblock copolymer Pluronic F127 ($HO(CH_2CH_2O)_{106}(CH_2CH(CH_3)O)_{70}(CH_2CH_2O)_{106}H$; BASF) as a structure directing template. The typical synthesis procedure was as follows. First, 2.1 g of $TiCl_4$ was dissolved in a solution of 7.4 g of ethanol and 1.1 g of distillated water, and vigorously stirred for 30 min in an ice–water bath. Then, a mixtureof 4.5 g of Pluronic F127, 15.0 g ethanol,

and 1.5 g of distillated water was added to the solution, and continuously stirred for 1 h at room temperature. Next, 2.3 g of 20 wt.% resol's ethanolic solution (synthesis procedure is described in Section 2.2.1.3) was added to the mixture. After stirring the mixture for 10 min, it was transferred into Petri dishes. The polymerized product was carbonized by heating in an electric furnace under N_2 flow (30 ccm) at 500–800 °C for 1 h following elimination of Pluronic F127 by heating at 400 °C for 2 h. The heating and cooling rates were fixed at 1 °C min^{-1} to avoid mesostructure collapse. After the carbonization, obtained mesoporous carbon–TiO_2 composite was ground into a fine powder with an agate mortar. For convenience, the obtained composites were designated as MCT-x, where x represents the carbonization temperature (°C).

5.2.1.2 Synthesis of Bulk TiO_2(B)

For *in situ* XRD observation, bulk TiO_2(B) sample was prepared according to the method previously reported by Marchand *et al.*[47] First, KNO_3 and anatase-type TiO_2 (5 μm, 99.9%, Wako) powders (molar ratio 1 : 2) were well-mixed, and pelletized using a hydraulic press. The obtained pellets were calcined at 1000 °C for 12 h under air. The resulting white solid ($K_2Ti_4O_9$) was ground in an agate mortar and then ion-exchanged at 60 °C for three days in 0.45 mol L^{-1} HCl aqueous solution (250 mL HCl solution was used per 1.0 g $K_2Ti_4O_9$). In this procedure, the HCl solution was exchanged with a fresh one every 24 h to attain a fully ion-exchanged product. The filtered sample powder ($H_2Ti_4O_9 \cdot nH_2O$) was washed with distillated water and dried at 100 °C for 12 h. The dried powder was heated at 500 °C in air for 30 min to obtain the bulk TiO_2(B) phase.

5.2.2 Characterization

The nanostructures of the obtained samples were observed using a JEOL JEM-3010 transmission electron microscope (TEM) operated at 200 kV. The carbon / TiO_2 ratio of obtained MCT samples were determined by thermogravimetric (TG) and differential thermal analysis (DTA) using a Rigaku Thermoplus TG-8101D instrument. In the measurements, heating ratio was set to 5 °C min^{-1}. Nitrogen adsorption / desorption isotherms at 77 K were

measured using a Shimadzu Gemini 2375 instrument. Prior to the isotherm measurements, the samples were heat treated at 200 °C under vacuum (< 3 Pa) for at least 1 h to remove adsorbed moisture. The specific surface areas (S_{BET}) were estimated using the Brunauer–Emmett–Teller (BET) method[32] and the adsorption data in the relative pressure (P / P_0) range from 0.05 to 0.16. The total pore volumes (V_{total}) were calculated using the Gurvich rule at $P / P_0 = 0.97$. The microstructures of the obtained bulk TiO_2(B) sample was observed using a JEOL JSM-7001F scanning electron microscope (SEM) operated at 10 kV. Powder X-ray diffraction (XRD) measurements were carried out using a Rigaku Miniflex diffractometer, where Cu Kα radiation ($\lambda = 1.54$ Å) was used as an incident beam. Crystallite size of TiO_2 in MCTs were estimated by the Scherrer's formula:

$$D = \frac{K\lambda}{B\cos\theta} \tag{5-1}$$

where, D is crystallite size perpendicular to hkl plane used in the calclation, K is Scherrer's constant, B is peak width (full width at half maximum; FWHM) of the diffraction line [rad], λ is X-ray wavelength, and θ is Bragg's angle. B was calclated by following equaiton:

$$B = B_{obs} - b \tag{5-2}$$

where, B_{obs} is observed peak width, and b is peak broadening due to the diffractometer. In this study, b was calibrated by well-crystallized silicon sample. Raman spectra excited by a 532 nm laser diode were collected using a JASCO NRS-3300 spectrometer. The removal of K^+ ions in the single-phase TiO_2(B) sample was confirmed by elemental analysis data obtained by an energy dispersive X-ray (EDX) spectrometer equipped with the SEM.

5.2.3 Electrochemical Measurement

The electrochemical properties of the obtained materials were characterized by a galvanostatic charge-discharge test using a conventional two-electrode-type cell (Hohsen HSCell). The measurements were conducted using a galvanostat (HA-151, Hokuto Denko) controlled by a computerized system. The voltage window was set to 1.3–3.0 V vs. Li / Li^+. To prepare the working electrode, the TiO_2 sample (60 wt.%) and acetylene carbon black (30 wt.%) were

mixed with polyvinylidene difluoride (PVDF) binder (10 wt.%) in appropriate quantities of 1-methyl-2-pyrrolidone. The obtained slurry was pasted onto a Cu foil and dried at 120 °C for at least 2 h in vacuum prior to use. A lithium foil (Aldrich) was used as the counter and quasi reference electrode. A mixture of ethylene carbonate (EC) and diethyl carbonate (DEC) solution (EC : DEC=1 : 1 in volume ratio) containing 1 mol L^{-1} $LiClO_4$ was used as the electrolyte. A porous polypropylene film (Celgard #2500) was used as a separator. Both the set-up of the cell and charge-discharge measurements were performed in an Ar-filled glove box to avoid air exposure and contamination. In order to imbue the electrodes sufficiently with the electrolyte solution, the assembled cells were kept in the glove box for at least 24 h before the measurements.

5.2.4 *In Situ* XRD Observation

For the bulk TiO_2(B) sample, *in situ* synchrotron XRD investigation during a galvanostatic charge-discharge test was performed. The synchrotron XRD measurements were performed using beam line BL-18C at the Photon Factory (PF) in the High Energy Accelerator Research Organization (KEK), Tsukuba, Japan. The beam line configuration for the measurements is schematically shown in Figure 5-1(A). In this study, we used a specially designed two-electrode type configuration cell shown in Figure 5-1(B) was used for the measurements. In order to perform the experiments accurately and effectively, observation windows with high X-ray transmittance, high electrochemical stability, and low gas permeability are required for the cell. Therefore, we chose crystalline diamond plates (thickness: 500 μm) as the window material. The working electrode containing the TiO_2(B) sample was sandwiched between the diamond windows. The XRD patterns were sequentially collected with continuously operated galvanostatic charge-discharge cycle. In order to transmit the X-ray beams, a Cu mesh (ϕ = 0.11 mm, 100 mesh) was used as the current collector for working electrode in this experiment. Except for the current collector of the working electrode, the cell constitution was similar to that described in Section 5.2.2. The cell was assembled in an Ar-filled glove box. The experiments were conducted using synchrotron radiation beams emitted from an

electron storage ring operated at 2.5 GeV. The beams were monochromatized by a Si(111) double-crystal monochromator and collimated by a pinhole collimator 100 μm in diameter. The incident X-ray wavelength for these measurements was λ = 0.613 Å. Each diffraction pattern was collected using a 2D imaging plate detector (Fujifilm; 200 mm × 250 mm) located 165 mm behind the sample position. Fujifilm BAS2500 imaging plate reader was used to digital conversion. The typical exposure time were 20–30 min. Prior to the measurements, the incident X-ray wavelength and the distance from the sample to the imaging plate detector were calibrated using the XRD peaks of a CeO_2 powder by the double cassette method.[108] All XRD measurements were performed at room temperature. Prior to further analysis, the obtained XRD patterns were corrected for the influence of the Lorentz-polarization factor.[109] The Rietveld refinements were performed using RIETAN-FP software.[168]

5.3 Results and Discussion

In this chapter, the author will report two topics: (i) lithium-storage properties of the mesoporous carbon–TiO_2 composite electrodes, and (ii) *in situ* XRD observation of lithium intercalation process of pure TiO_2(B) electrode. Topic (i) will be discussed in the Sections of 5.3.1, 5.3.2, and 5.3.5. Topic (ii) will be discussed in the Sections of 5.3.3 and 5.3.4.

5.3.1 Structural Properties of Mesoporous Carbon–TiO_2 Composites

Figure 5-2 shows typical TEM image of MCT-600. Hexagonally aligned straight channel pores created by the removal of the cylindrical surfactant micelle were clearly observed. The diameter of the pore channel observed using TEM (about 5 nm) is in good agreement with the pore size determined by N_2 adsorption isotherm analysis shown in Figure 5-3(inset). The ordered mesostructures are also confirmed in the other samples, except for the MCT-800. The structural degradation at 800 °C treatment can be explained by the crystal growth of TiO_2 nanoparticles in the framework, because crystallite sizes of the anatase TiO_2 estimated from the XRD patterns

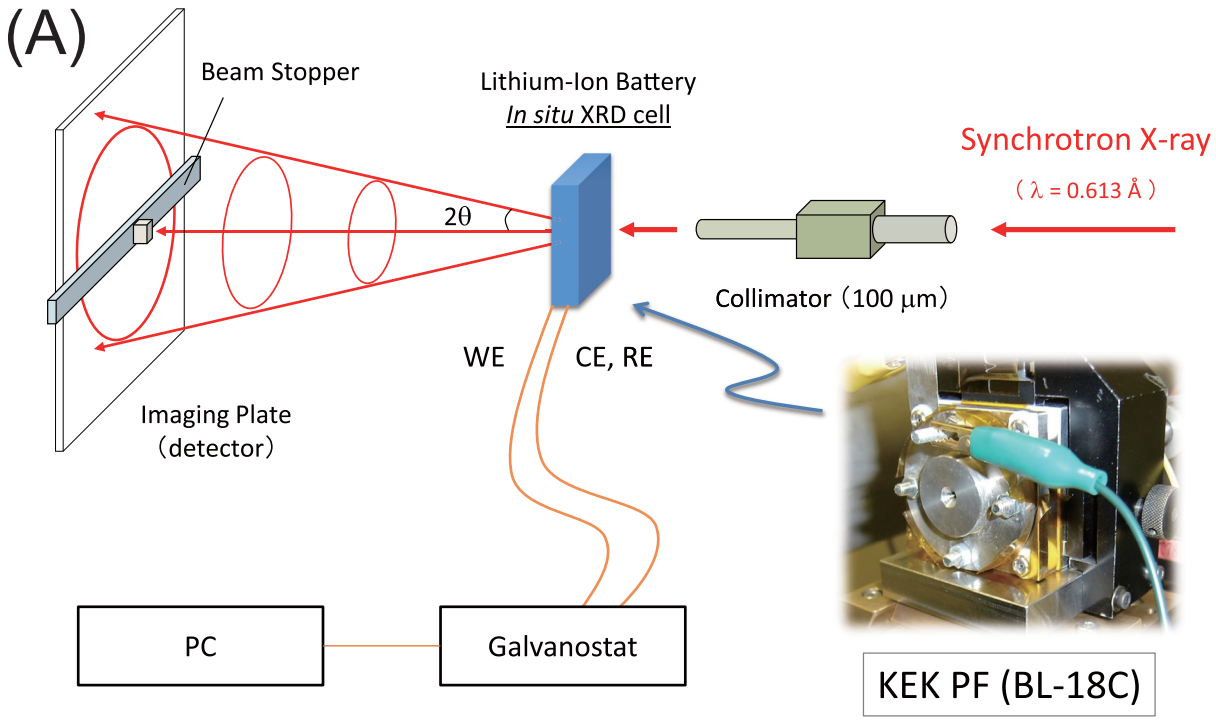

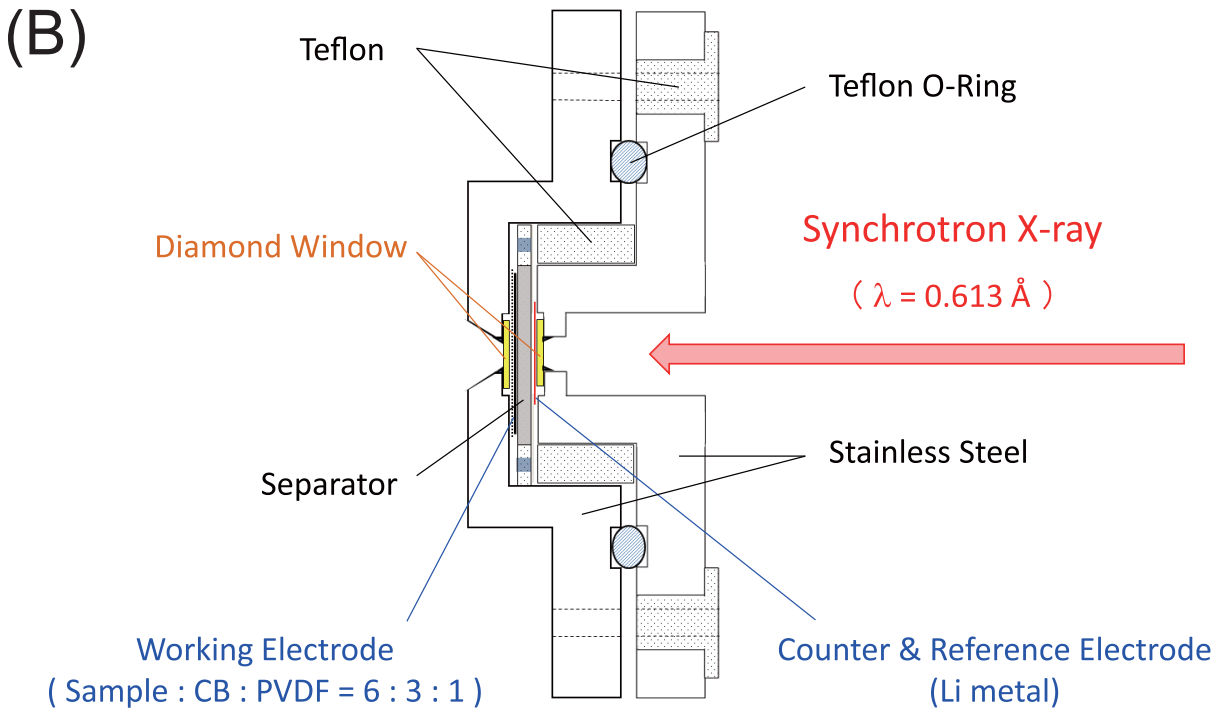

Figure 5-1 (A) Schematic of the beam line configuration for the *in situ* synchrotron XRD investigation. (B) Structure of the *in situ* XRD cell.

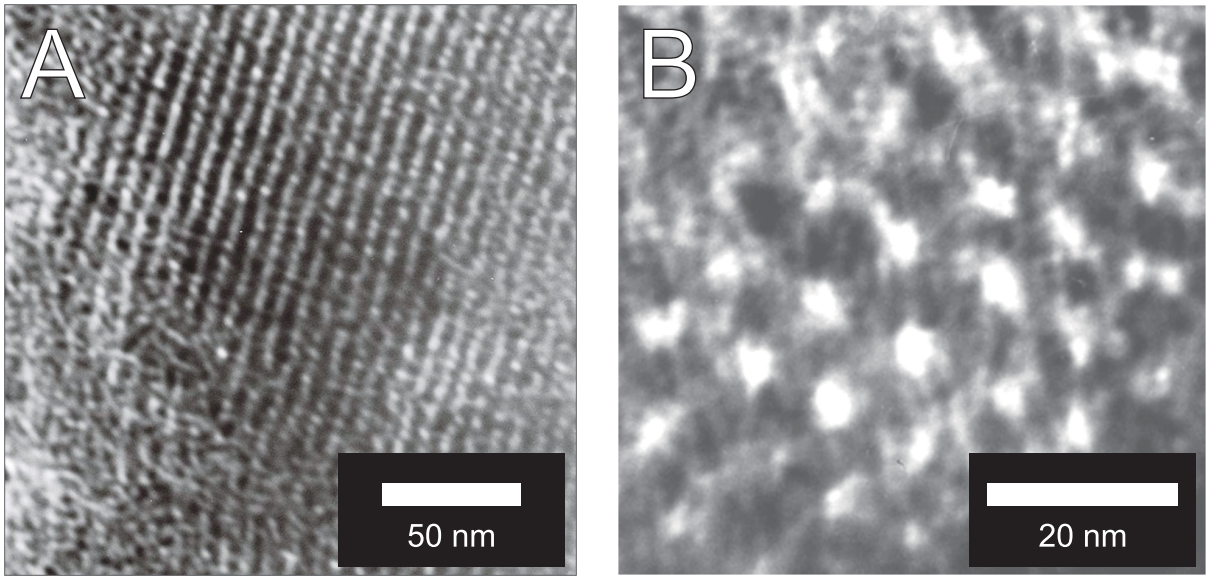

Figure 5-2 TEM photographs of MCT-600 observed (A) perpendicular and (B) parallel to the channel pore axis.

(Figure 5-4) are drastically increased between 700 °C and 800 °C treatment. TG/DTA curves of MCT-600 is shown in Figure 5-5. Rapid weight-loss and exoergic peak were observed at 300–400 °C. These peak are originate from a combustion reaction of amorphous carbon in the composite. C : TiO_2 weight ratio estimated by the TG cureve was about 3 : 7. By performing hydrofluoric acid (HF) etching treatment, TiO_2 component is selectively removed from the MCT composites. As shown in Figure 5-6(B), in addition to the 5 nm peak originated from the removal of the cylindrical surfactant micelle, new pore peak was appeared at around 2 nm after HF treatment. This result indicate that TiO_2 crystals are well-dispersed in the mesoporous framework. The obtained properties are summarized in Table 5-1.

Powder XRD patterns of the composites measured with conventional laboratory-scale equipment using Cu Kα radiation are shown in Figure 5-4. As shown in this figure, clear diffraction peaks are observed at around 2θ = 25, 38, 48, 55, 63, 69, and 75°. These positions are in good agreement with those in the diffraction pattern of the anatase TiO_2. Besides the anatase peaks, very small peaks are observed at around 2θ = 30, 44, and 58°. These peaks cannot be explained by the commonly known TiO_2 polymorphs such as rutile or brookite. In order to analyze the detailed crystal structure of the composites, we performed synchrotron

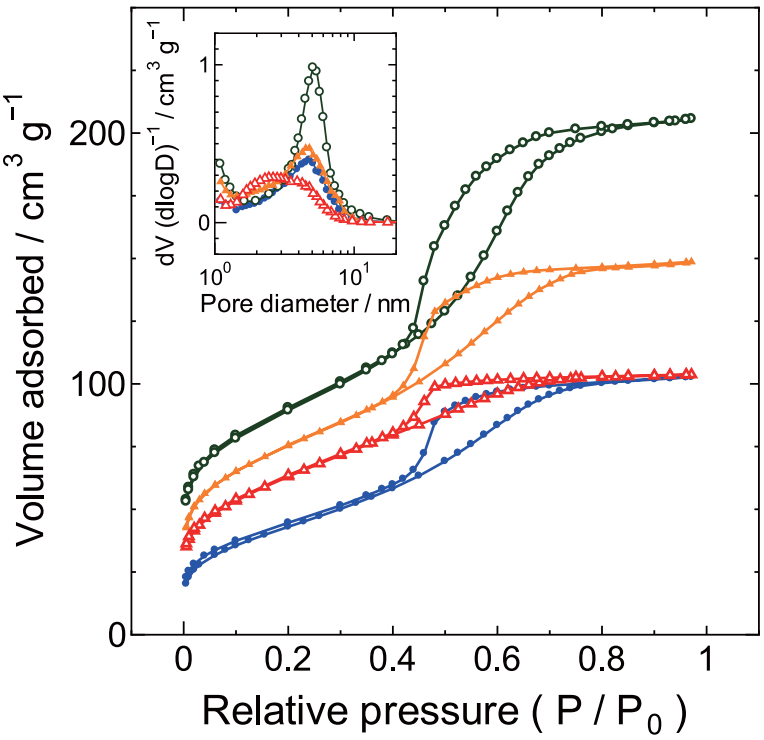

Figure 5-3 N_2 sorption-desorption isotherms of MCT-500 (closed green circles), MCT-600 (open orange circles), MCT-700 (closed red triangles), and MCT-800 (open blue triangles). The inset shows BJH pore size distributions calculated using the adsorption branch of the isotherm.

Table 5-1 Structural parameters of the mesoporous carbon–TiO_2 composites.[a]

	D_{BJH} (nm)	S_{BET} ($m^2\ g^{-1}$)	V_{total} ($m^3\ g^{-1}$)	D_A (nm)
MCT-500	4.8	158	0.17	7.4
MCT-600	5.1	309	0.30	9.7
MCT-700	4.8	263	0.22	10.6
MCT-800	2.4	224	0.15	17.7

[a] D_{BJH}: primary mesopore diameter estimated by the BJH method; S_{BET}: specific surface area estimated by the BET method; V_{total}: total pore volume; D_A: crystallite size of anatase estimated by the Scherrer's formula (equation 5-1).

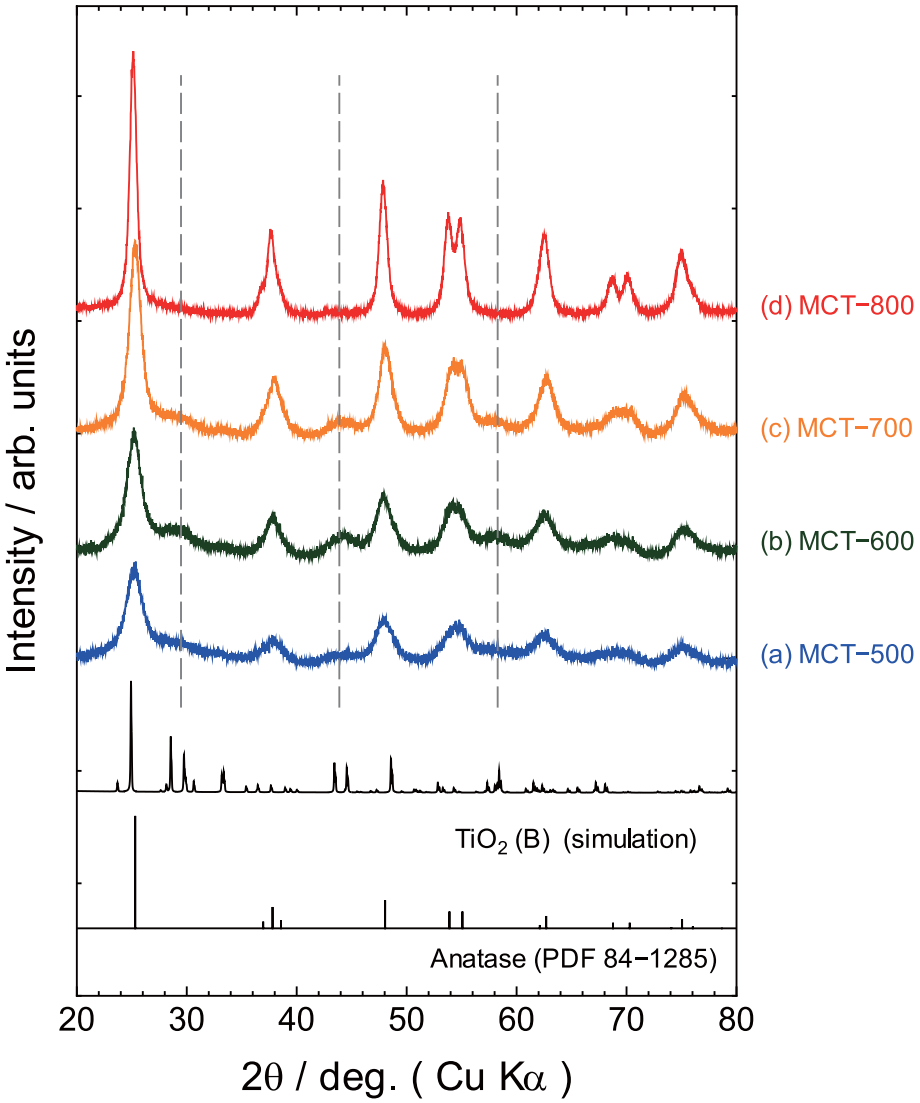

Figure 5-4 Powder XRD patterns of (a) MCT-500, (b) MCT-600, (c) MCT-700, and (d) MCT-800 electrodes. Cu Kα radiation (λ = 1.54 Å) was used as the incident beam.

powder XRD measurements. To eliminate the preferred orientation effect, the quartz capillary tubes containing the samples were continuously oscillated during the measurements. The observed XRD pattern of the MCT-600 electrode is shown in Figure 5-7. As shown in this figure, a highly resolved diffraction pattern was successively obtained. The most characteristic peak was located at around 2θ = 5.5°. The peak position was found to be in good agreement with the TiO_2(B) phase. The observed synchrotron XRD pattern of the MCT-600 electrode can be completely understood by a mixture of the anatase and TiO_2(B) phases. The amount of the TiO_2(B) phase in the composites is highly dependent on carbonization temperature. The

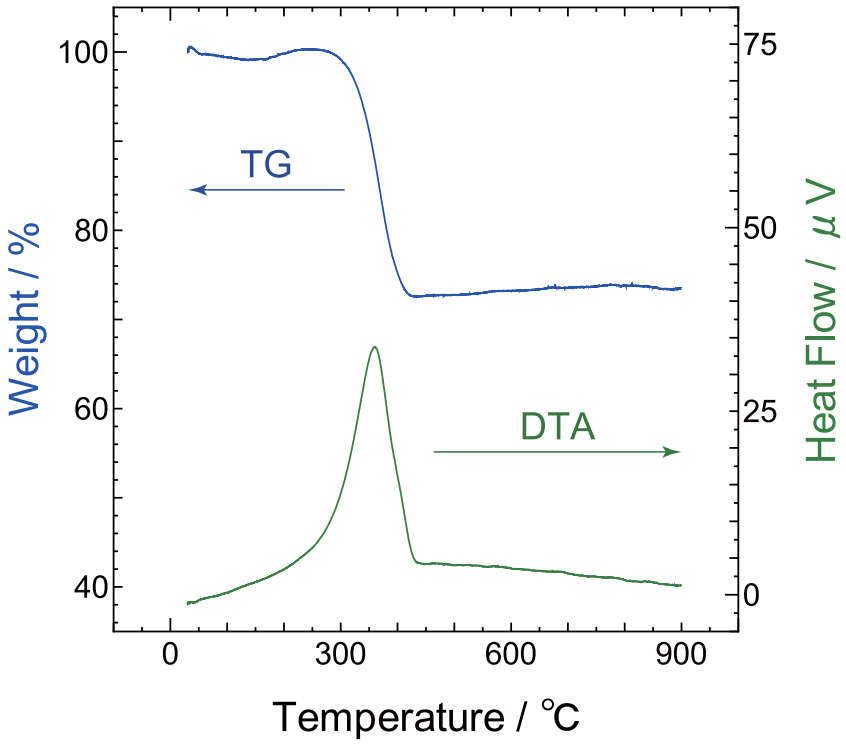

Figure 5-5 TG / DTA cureves of MCT-600.

diffraction feature of the TiO_2(B) phase can be observed at around 2θ = 30, 44, and 58° in Figure 5-4. These peaks gradually disappear as the treatment temperature increases, with exception of the the MCT-500 electrode. This result is related to the thermal stability of the TiO_2(B) phase. Since TiO_2(B) is metastable, the phase transition of TiO_2(B) to anatase occurs easily at high temperatures. On the other hand, the intensity of TiO_2(B) peaks for the MCT-500 electrode was weaker as compared to that of the MCT-600 electrode. Thus, the heat-treatment temperature of 500 °C might not be sufficient for the crystallization of the TiO_2(B) phase.

Although the formation mechanism of the TiO_2(B) phase in the composites is still unclear, we will discuss it in this section. In general, TiO_2(B) is synthesized using hydrothermal methods[47] or by the calcination of layered titanate ($H_2Ti_4O_9$).[169] However, the synthesis on the sol-gel method, as used in this study, is quite different from other classical methods. Recently, Kaper *et al.* reported a new synthesis root for a low-temperature sol-gel method using various surfactants and ionic liquids.[170,171] They pointed out that the formation efficiency of the TiO_2(B) phase is strongly affected by the selection of solvents and surfactants. They

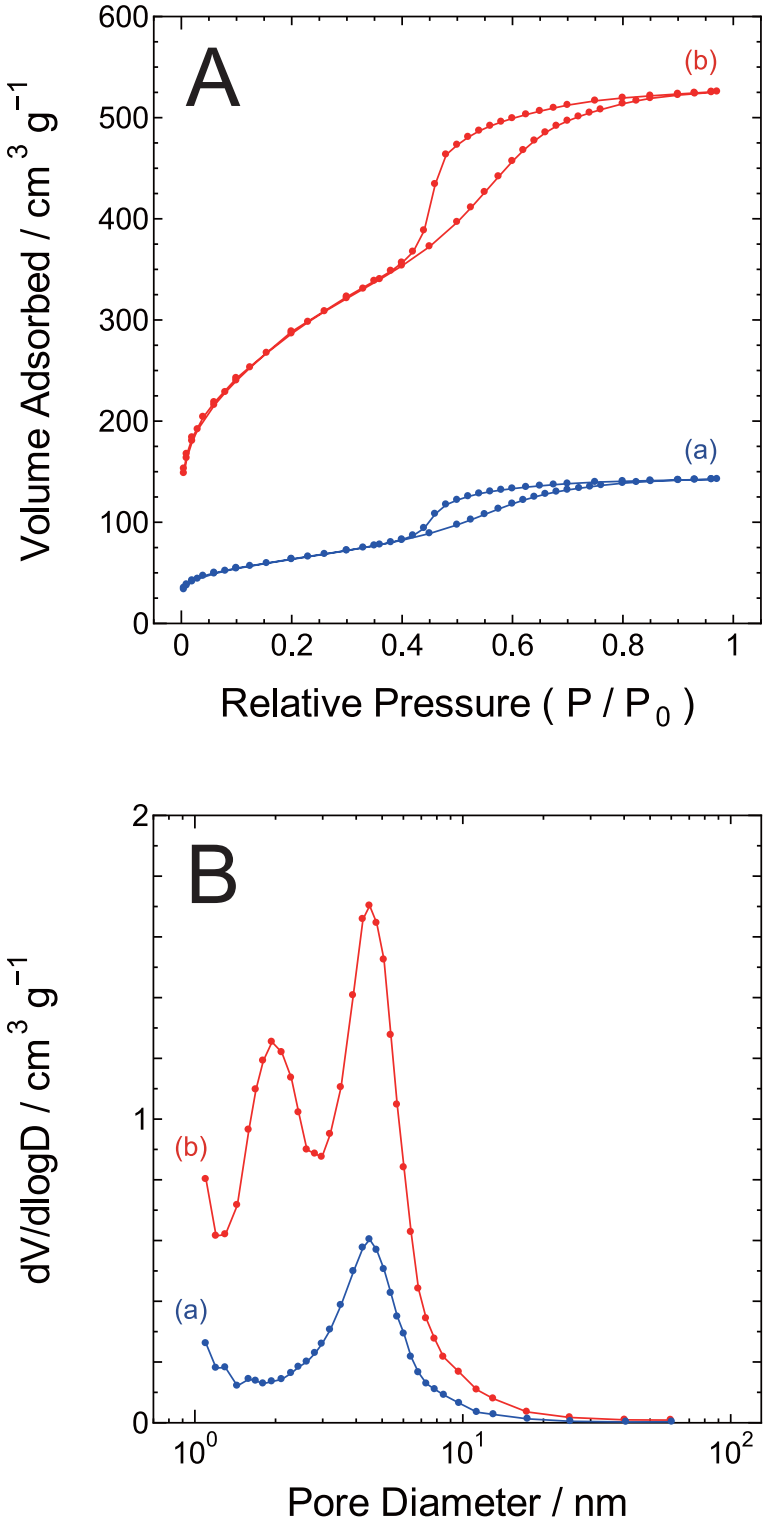

Figure 5-6 (A) N_2 sorption-desorption isotherms and (B) BJH pore size distributions calculated using the adsorption branch of the isotherm of (a) MCT-650 and (b) HF-treated (TiO_2-removed) MCT-650.

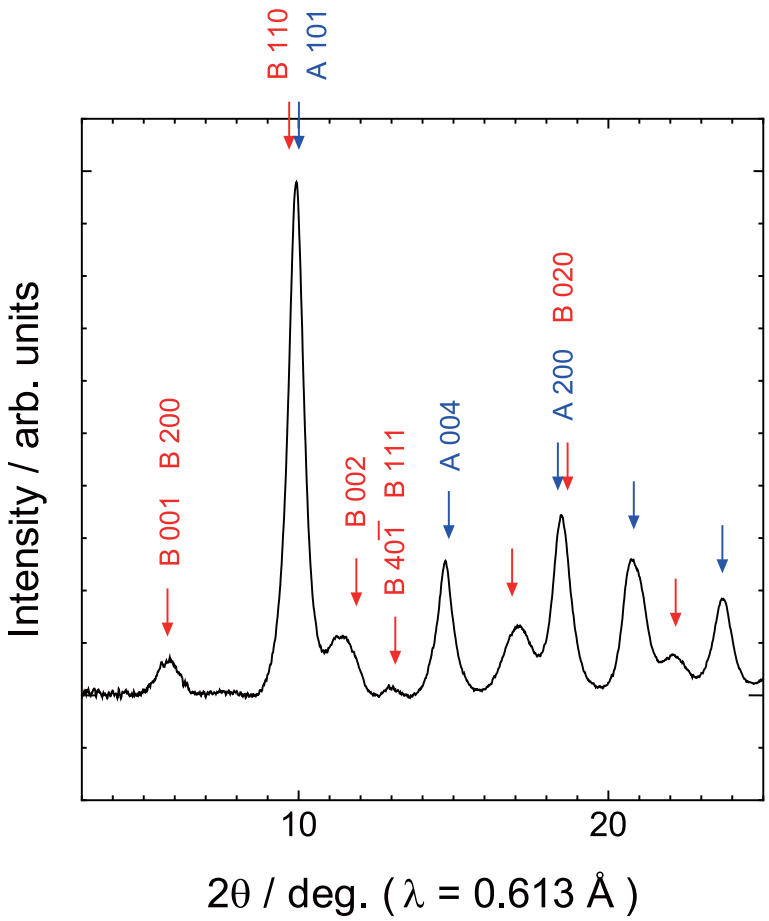

Figure 5-7 Powder XRD pattern of the MCT-600 electrode. Monochromatized synchrotron radiation beam (λ = 0.613 Å) was used as an incident X-ray. The sample was placed in a quartz capillary tube, and the tube was continuously oscillated during the measurements. Anatase and TiO_2(B) diffraction peaks are marked with A and B, respectively.

explained the reason for a peculiar charge distribution and polarization pattern created by the surfactant self-assembly. Although the combination of the surfactant and solvent used in the present study (Pluronic F127 and ethanol) was not studied in Kaper's report, these components might promote the generation of the TiO_2(B) phase in the composites. The carbon source of the composites (resol) might also affect it. On the other hand, the experimental results reported by Procházka *et al.* indicate that sol-gel processes starting from molecular TiO_2 precursors (e.g., $TiCl_4$) always provide mixtures of TiO_2(B) and anatase.[172] Thus, further studies are required to discuss the formation mechanism of the TiO_2(B) phase.

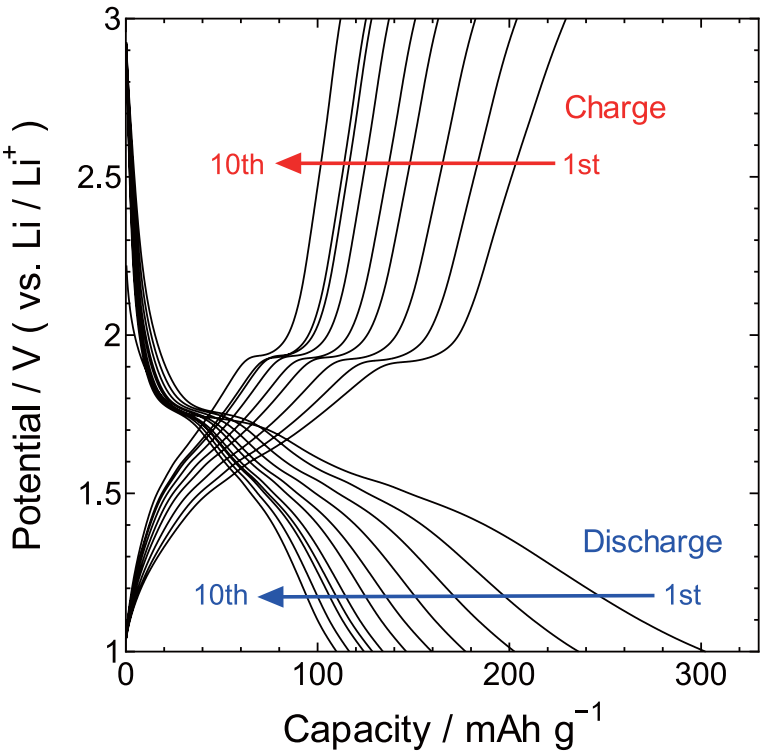

Figure 5-8 (A) Charge-discharge curves of MCT-600 electrode measured at a constant current density of 50 mA g^{-1}. The voltage window was set to 1.5–3.0 V vs. Li/Li^+. Profiles of the initial 10 cycles were shown in the graph. The abscissa is shown as the capacity value per TiO_2 mass.

5.3.2 Electrochemical Properties of Mesoporous Carbon–TiO_2 Composites

Figure 5-8 shows galvanostatic charge-discharge curves of MCT-600 electrode. In this measurement, the negative cut-off voltage was set to 1.0 V vs. Li/Li^+. As shown in the Figure, cycle performance was very poor. The reversible capacity of MCT-600 electrode was decreased about 49% in the initial 10 cycles. However, by changing the negative cut-off voltage from 1.0 to 1.3 V vs. Li/Li^+, cycle performance was dramatically improved (see Figure 5-9(A)). Similar improvement in cyclability were also observed in other MCT electrodes. Therefore, voltage window at the charge-discharge measurement was set to 1.3–3.0 V vs. Li/Li^+ in the following discussion.

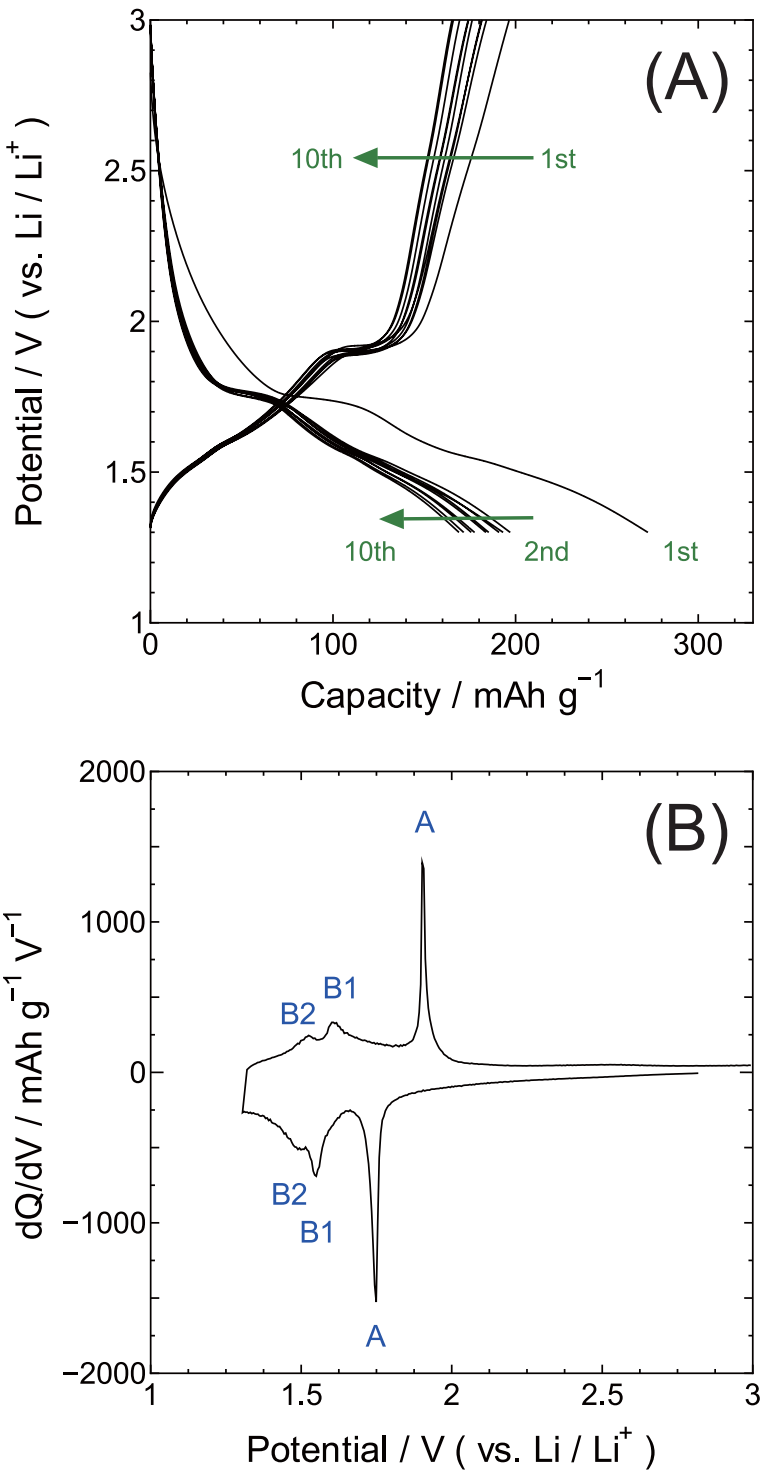

Figure 5-9 (A) Charge-discharge curves of MCT-600 electrode measured at a constant current density of 50 mA g^{-1}. Profiles of the initial 10 cycles were shown in the graph. The abscissa is shown as the capacity value per TiO_2 mass. (B) Derivation of galvanostatic charge-discharge curve of the MCT-600 electrode at the first cycle. The voltage window was set to 1.3–3.0 V vs. Li/Li^+.

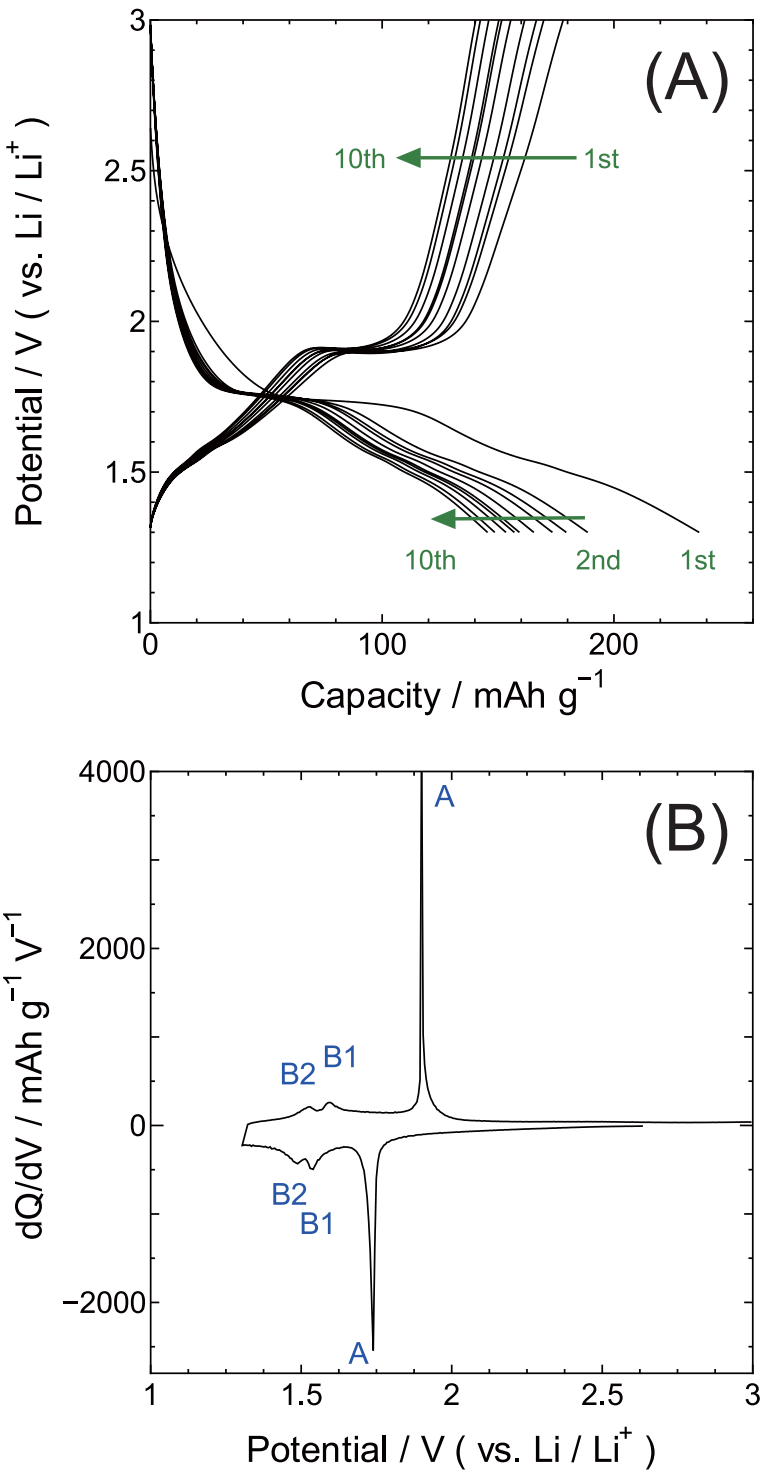

Figure 5-10 (A) Charge-discharge curves of MCT-700 electrode measured at a constant current density of 50 mA g^{-1}. Profiles of the initial 10 cycles were shown in the graph. The abscissa is shown as the capacity value per TiO_2 mass. (B) Derivation of galvanostatic charge-discharge curve of the MCT-700 electrode at the first cycle. The voltage window was set to 1.3–3.0 V vs. Li/Li^+.

The charge-discharge curves of the MCT-600 and MCT-700 electrodes measured at 1.3–3.0 V vs. Li/Li^+ range are shown in Figures 5-9(A) and 5-10(A), respectively. The reversible capacity in the first cycle of the MCT-600 electrode (197 mAh g^{-1}) was higher than that of the MCT-700 (178 mAh g^{-1}). Generally, electrodes having larger surface area show superior rate performance due to ion transport. Therefore, it is reasonable that the result of superior rate performance of the MCT-600 electrode than that of the MCT-700 electrode. On the other hand, in the lower rate condition, this surface effect becomes to be negligible. However, the reversible capacities and the shape of charge-discharge curves were different between MCT-600 and MCT-700 electrodes even in the low rate condition (50 mA g^{-1}; see Figures 5-9 and 5-10). This indicates that the different electrochemical performance between MCT-600 and MCT-700 cannot be explained only by the difference in the pore structure. Therefore, the author focused on the structural change in TiO_2(B) included in the composites.

Since lithium insertion into amorphous carbon (hard carbon) occurs at lower potential than 1 V vs. Li / Li^+, only lithium insertion into the TiO_2 phases were observed in the potential range of 1.3–3.0 V vs. Li / Li^+. As shown in Figures 5-9 and 5-10, the shapes of the charge-discharge curves of the MCT-600 and MCT-700 electrodes were found to be similar. The features of the discharge curves corresponding to the lithium insertion process can be divided into following three components:

I. Initial slope region (3.0–1.8 V vs. Li / Li^+).

II. Plateau region (1.8–1.7 V vs. Li / Li^+).

III. Large slope region (1.7–1.3 V vs. Li / Li^+).

Examining the curves carefully, the author found that region III is composed of two plateaux. This is further confirmed by the differential capacity plots shown in Figures 5-9(B) and 5-10(B).

Reversible charge-discharge processes were observed in all the three regions; however, overpotential (the difference of plateau potential between the Li insertion and extraction processes) differed from one region to another. The overpotential of the plateaux in region III was small (~50 mV), while that of the plateau in region II was much larger

(~250 mV). The plateau observed at around 1.75 V vs. Li / Li^+ (region II, peak A in Figures 5-9(B) and 5-10(B)) is explained as lithium insertion in the anatase phase.[43, 165, 166] On the other hand, the two pairs of plateaux observed in region III (peaks B1 and B2 in Figures 5-9(B) and 5-10(B)) can be explained by the TiO_2(B) phase. The lithium insertion potential of TiO_2(B) was in good agreement with the previous reports. The origin of region I is not clear, but many researchers have observed a similar feature in TiO_2(B)-containing systems.[48–53]

As shown in Figure 5-11, the cycle stability and rate performance of the MCT-600 electrode were superior to those of the MCT-700 electrode. As shown in Figures 5-12 and 5-13, the MCT-600 electrode showed good rate performance. This result seems to be related to the amount of the TiO_2(B) phase. As mentioned above, TiO_2(B) in the composites gradually decreased with increasing carbonization temperature. This fact is also confirmed in the charge-discharge curves shown in the Figures 5-9(A) and 5-10(A). On the discharge curve in the first cycle, the capacity of anatase (region II) in the MCT-600 and MCT-700 electrodes was about 50 and 70 mAh g^{-1}, respectively. Meanwhile, the capacity of TiO_2(B) (region III) in the MCT-600 and MCT-700 electrodes was about 150 and 120 mAh g^{-1}, respectively. The capacity of region I (which is probably related to the TiO_2(B) phase) in the MCT-600 was also larger than that of the MCT-700 electrode at the first discharge. Thus, relative capacity contribution of TiO_2(B) to anatase in the MCT-600 electrode was higher than that of the MCT-700 electrode. The coulombic efficiency at the first cycle was very poor for both MCT-600 and MCT-700 electrodes: 72% for MCT-600 and 75% for MCT-700. In both electrodes, the behavior of capacity loss in the first cycle of the TiO_2(B) phase (regions I and III) was similar to that of anatase (region II). In contrast, the capacity retention after the second cycle was quite different in each electrode. The reversible capacity of the MCT-700 electrode rapidly decreased with the cycles, whereas the capacity drop of MCT-600 was relatively negligible. The capacity loss of the MCT-700 electrode seems to be attributable to the anatase phase since the reversible capacity of region II clearly decreased with the cycles, in contrast to those of regions I and III.

In order to discuss the origin of the above mentioned difference between anatase and

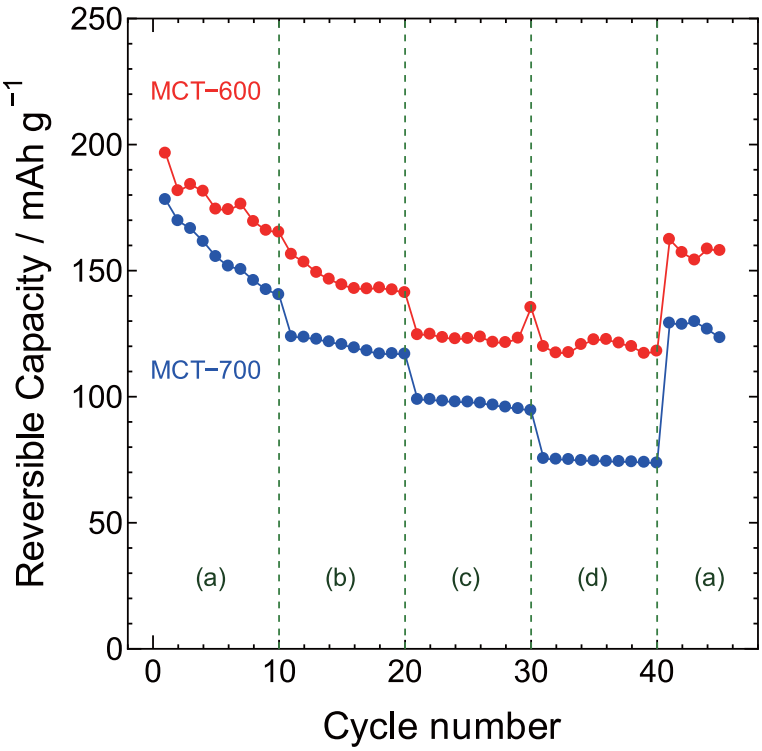

Figure 5-11 Cycling performance of MCT-600 (open red circles) and MCT-700 (closed blue circles) electrodes at different current densities of (a) 50, (b) 100, (c) 200, and (d) 400 mA g^{-1}. The voltage window was set to 1.3–3.0 V vs. Li/Li^+.

TiO_2(B) in the composites, a comparison of the lithium storage mechanism among their crystal phases is required. In this sense, *in situ* structural observation, especially that of an XRD study, should provide useful information. In the case of anatase, detailed structural change upon lithium insertion was elucidated by some groups.[43,165,166] On the other hand, lithium storage at TiO_2(B) has still not been thoroughly investigated. So far, the discussion of the lithium insertion mechanism in the TiO_2(B) phase has been conducted mainly on the basis of theoretical calculations.[173–175] To the best of our knowledge, an *ex situ* neutron diffraction investigation recently performed by Armstrong *et al.*[176] and an *ex situ* X-ray adsorption spectroscopy study performed by Okumura *et al.*[177] are the only experimental studies with regard to TiO_2(B) electrodes. Since the scattering factor of a lithium atom for neutrons is higher than that for X-rays, neutron diffraction is more suitable for the analysis of the lithium storage position in electrode materials than XRD. However, certain problems of neutron diffraction,

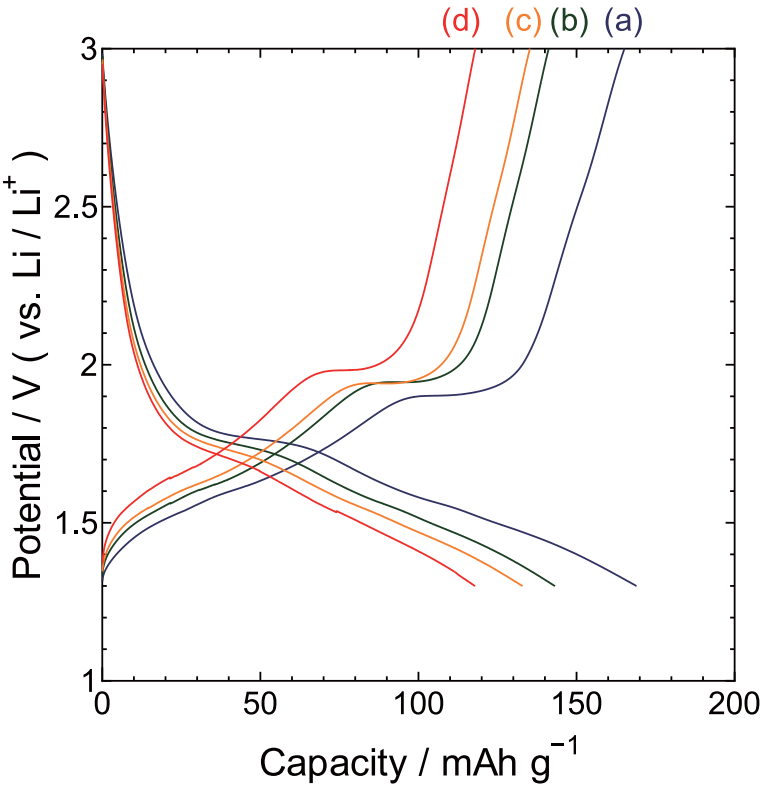

Figure 5-12 Charge-discharge curves of MCT-600 electrode at different current densities of (a) 50, (b) 100, (c) 200, (d) 400 and (e) 1000 mA g^{-1}. The voltage window was set to 1.3–3.0 V vs. Li/Li^+. 10th cycle data are shown in the graph.

such as restrictions of cell geometry and low beam flux, make it difficult to apply this technique to *in situ* measurement. Thus, the XRD method has a great advantage for analyzing continuous structural changes in electrode materials under controlling of electrode potential. Therefore, we attempted *in situ* structural investigation of a TiO_2(B) electrode using the XRD method. Since a high-brightness X-ray source is required for the measurements, we used a synchrotron radiation beam in this study. The *in situ* XRD investigation was carried out using a bulk TiO_2(B) sample, instead of carbon–TiO_2 composites. This is because the diffraction patterns of the carbon–TiO_2 composites are too complicated owing to their mixed phase and the feature of broad peaks makes it difficult to examine the detailed structural changes in the TiO_2(B) phase upon lithium insertion.

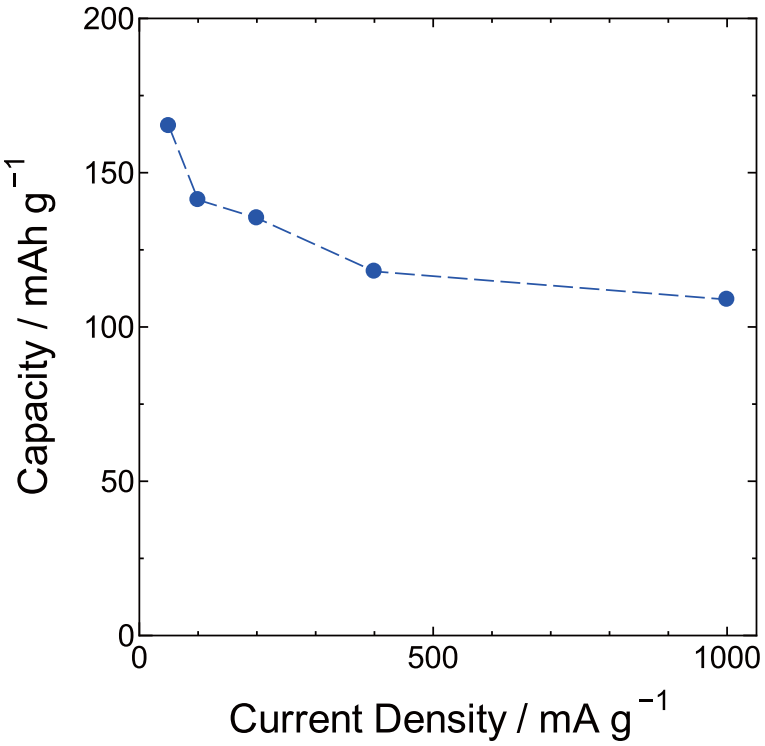

Figure 5-13 Current density vs. reversible capacity plot of the MCT-600 electrode. Corresponding charge-discharge curves are shown in Figure 5-12.

5.3.3 Characterization of Bulk TiO_2(B) Sample for *In Situ* Observation

Figure 5-14 represents the XRD pattern of the obtained bulk TiO_2(B) sample measured using Cu Kα radiation. All peaks were assigned to the TiO_2(B) phase. The Raman spectrum was also in good agreement with previously reported spectra of TiO_2(B) samples (Figure 5-15).[178] The low-intensity feature of the 144 cm^{-1} peak (originating from the anatase and TiO_2(B) phases, marked with black inverted triangle) compared with the 123 cm^{-1} peak (originating from the TiO_2(B) phase, marked with white inverted triangle) indicates small amount of anatase impurity in the sample.[178] The lattice parameters and the crystal structure obtained by Rietveld refinement of the XRD pattern (Figure 5-14) are shown in Table 5-2 and Figure 5-16, respectively. The pattern refinement indicated a preferred orientation parallel to the *b*-axis of TiO_2(B). This result can be understood by its rod-like morphology. As shown in the SEM

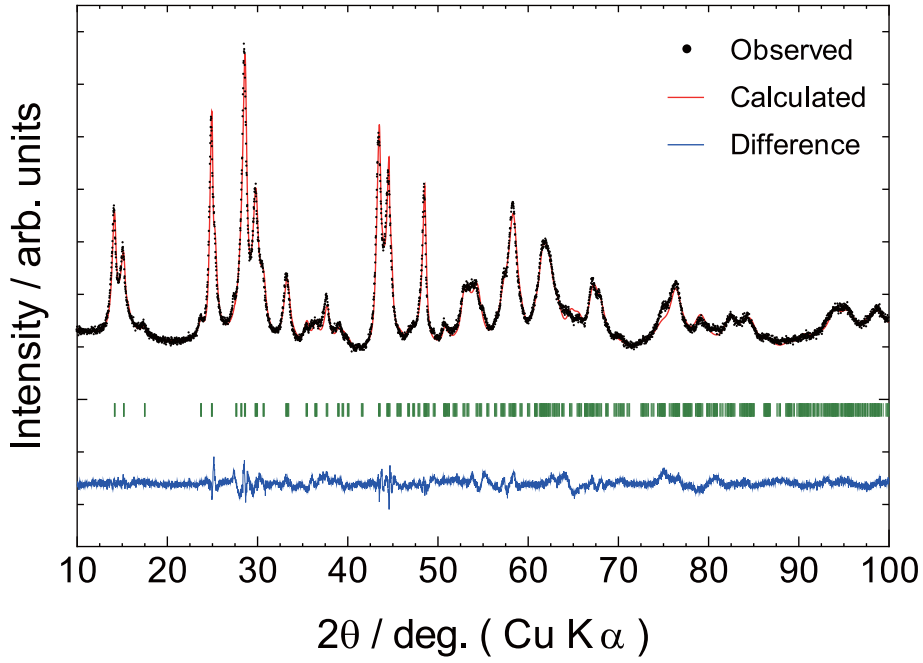

Figure 5-14 Powder XRD patterns of the obtained bulk TiO_2(B) sample. Cu Kα radiation (λ = 1.54 Å) was used as the incident beam.

image in Figure 5-17(A), rod-like crystals about 300 nm wide and 1-4 μm in length were clearly observed. Previous studies using high-resolution TEM showed that the direction of the long axis of the rods corresponds to that of the *b*-axis in the TiO_2(B) crystal.[176] The SEM-EDX spectrum of the obtained sample is shown in Figure 5-17(B).As shown in the figure, only Ti, O, and C elements were detected. This result shows that K^+ ions were sufficiently removed by the ion-exchange process.

The galvanostatic charge-discharge curve of the obtained TiO_2(B) sample is shown in Figure 5-18(A). In the discharge curve, two pairs of plateaux, which are characteristic features of the TiO_2(B) phase, were observed at around 1.5–1.6 V vs. Li / Li^+ (marked as B1 and B2 in Figure 5-18(B)) and were similar to those of the carbon–TiO_2 composites. In addition, another small plateau pair was observed at around 1.7–2.0 V vs. Li / Li^+ (marked as A in Figure 5-18(B)). This plateau may be attributed to the anatase phase. However, as mentioned above, anatase was not detected by XRD method. Since anatase was not detected even in the synchrotron XRD patterns, the *in situ* XRD observations were performed using this sample.

Table 5-2 Structural parameters of synthesized TiO_2(B), from the Rietveld refinement.

Space group: $C2/m$ (No. 12, unique axis b, monoclinic)

a = 12.2121(10) Å, b = 3.7555(1) Å, c = 6.5365(4) Å, β = 107.042(9)°, V = 286.611 Å^3

R_{wp} = 4.472, R_p = 3.491, R_e = 2.440, S = 1.8329

atom	site	g	x	y	z	B (Å)
Ti1	4i	1*	0.19816(17)	0*	0.28829(29)	0.525(65)
Ti2	4i	1*	0.09967(17)	0*	0.70272(27)	0.548(62)
O1	4i	1*	0.12513(41)	0*	0.99454(103)	1.092(147)
O2	4i	1*	0.27221(69)	0*	0.66142(80)	0.613(155)
O3	4i	1*	0.07131(58)	0*	0.37327(79)	1.010(163)
O4	4i	1*	0.37664(70)	0*	0.28138(87)	1.177(209)

*Fixed parameters

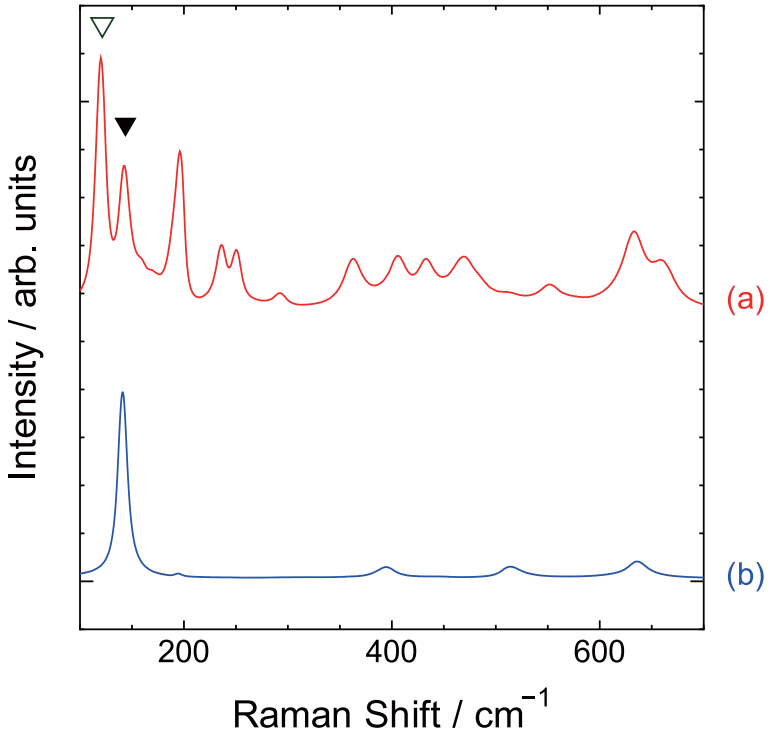

Figure 5-15 Raman spectra of the (a) obtained bulk TiO_2(B) and (b) anatase sample used as the precursor for TiO_2(B) synthesis. A 532.1 nm laser diode was used as the excitation source.

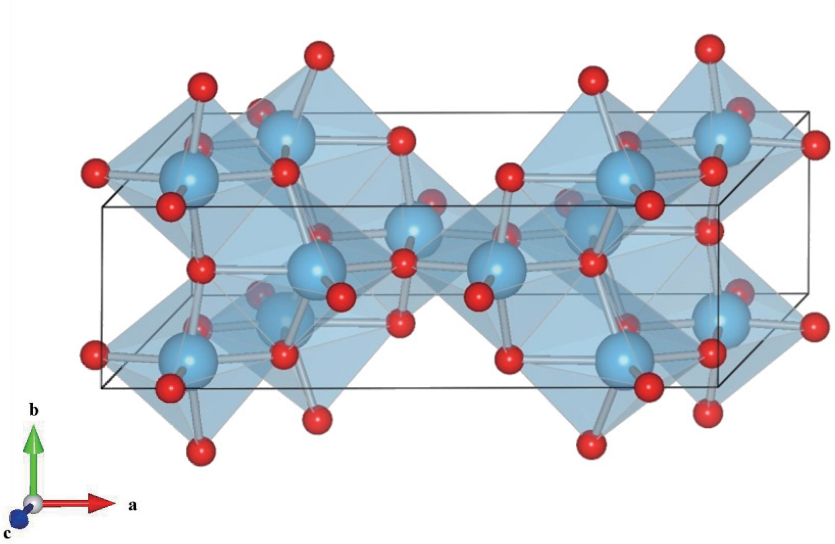

Figure 5-16 Crystal structure of TiO_2(B) determined by the Rietveld refinement of XRD pattern (Figure 5-14) obtained before lithium insertion. Oxygen and titanium atoms are shown in red and blue, respectively.

5.3.4 Structural Changes in TiO_2(B) Phase upon Lithium Insertion

Figure 5-19 shows the observed *in situ* XRD patterns of the TiO_2(B) electrode. Although unwanted diffraction peaks from the copper mesh and a complex background pattern caused by the electrolyte solution were also observed, clear diffraction patterns of TiO_2(B) were successfully obtained. As shown in Figure 5-19, the TiO_2(B) electrode exhibited reversible structural changes. The peak positions gradually shifted toward the small-angle side with lithium insertion and to the wide-angle side with lithium extraction. The small- and wide-angular shifts corresponded to the expansion and contraction of the crystal lattice, respectively. The peak positions observed after the first cycle (observed at 3.0 V vs. Li / Li^+, Li extracted state) were correctly matched with the position of a pristine electrode (observed at the open circuit potential before the cycles).

Until the electrode potential reached 1.6 V vs. Li / Li^+ in the discharge process, a

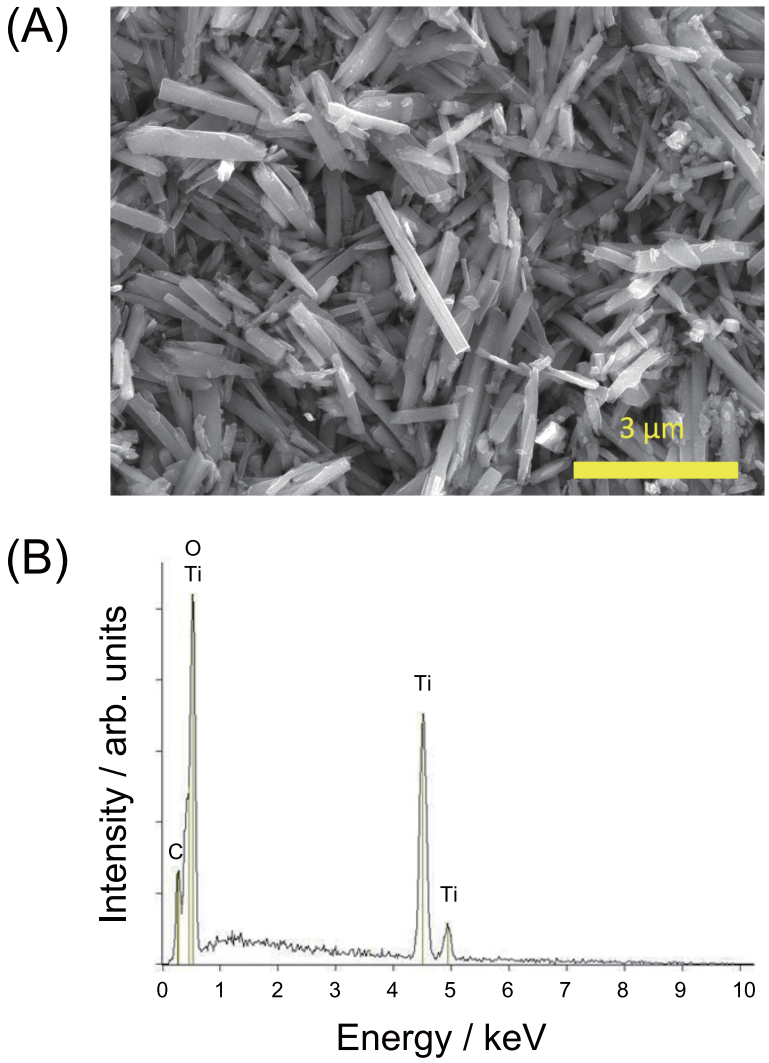

Figure 5-17 (A) SEM image and (B) EDX spectrum of the obtained bulk TiO_2(B) sample.

prominent peak shift was not observed. This indicates that TiO_2(B) can store Li ions without large structural changes at the primary state. Since remarkable structural changes were not observed around 1.75 V vs. Li / Li^+, the plateau observed at this voltage during the discharge seems to be independent with respect to the TiO_2(B) phase.

Clear peak shifts were observed mainly under 1.6 V vs. Li / Li^+. Interestingly, the number of peaks and their relative intensities were maintained even after reaching the fully lithiated state (observed at 1.3 V vs. Li / Li^+). This fact indicate that TiO_2(B) can store lithium ions with maintaining its initial monoclinic crystal structure This behavior of lithium storage is different from that of anatase, which requires a large structural change (tetragonal to orthorhombic) upon lithium insertion.[43, 165, 166] Table 5-3 show the lattice parameters and

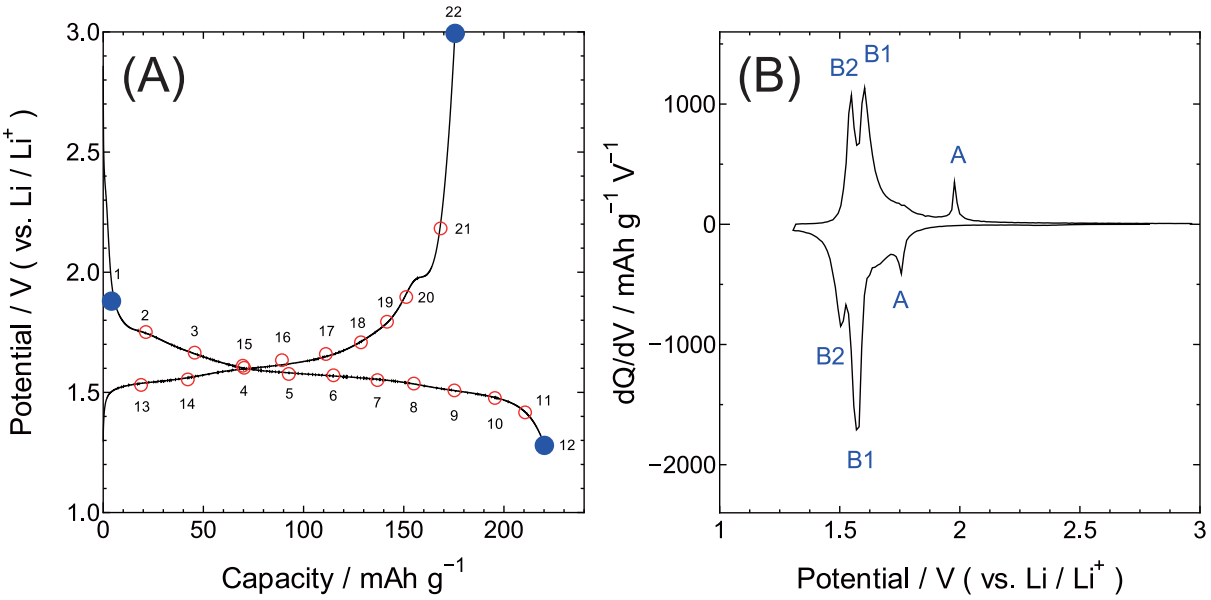

Figure 5-18 (A) Galvanostatic charge-discharge curves of the bulk TiO_2(B) electrode in the first cycle. The current density was set to 50 mA g^{-1}. (B) Derivation of the galvanostatic charge-discharge curve of the bulk TiO_2(B) electrode in the first cycle.

the crystal structure obtained by the Rietveld analysis of the XRD pattern observed at 1.3 V vs. Li / Li^+. Unfortunately, the detailed lithium positions and isotropic temperature factor (B) could not be refined because of the low scattering factor of lithium; however, a reasonable crystal structure was successively obtained. The obtained structure was in agreement with the previously reported $Li_{0.8}TiO_2$(B) structure determined by the *ex situ* neutron diffraction method.[176)]

As shown in Tables 5-2 and 5-3, the internal atomic coordinate in the fully lithiated state was very close to that in the pristine state. On the other hand, the outer shape of the crystal lattice (a, b, c, and β) changed anisotropically with lithium insertion. Figure 5-20 shows apparent changes of crystal parameters estimated from several types of major diffraction peaks. This figure shows each lattice parameter change as a function of lithium content. The length of the a-axis and b-axis gradually increased with lithium insertion, while that of the c-axis and angle-β were almost constant during lithium storage. Observing the figures carefully, we find that the changes in the cell parameters were not monotonous. In case of the a-axis, step-like changes were observed at around 120 mAh g^{-1} (~1.57 V vs. Li / Li^+) and

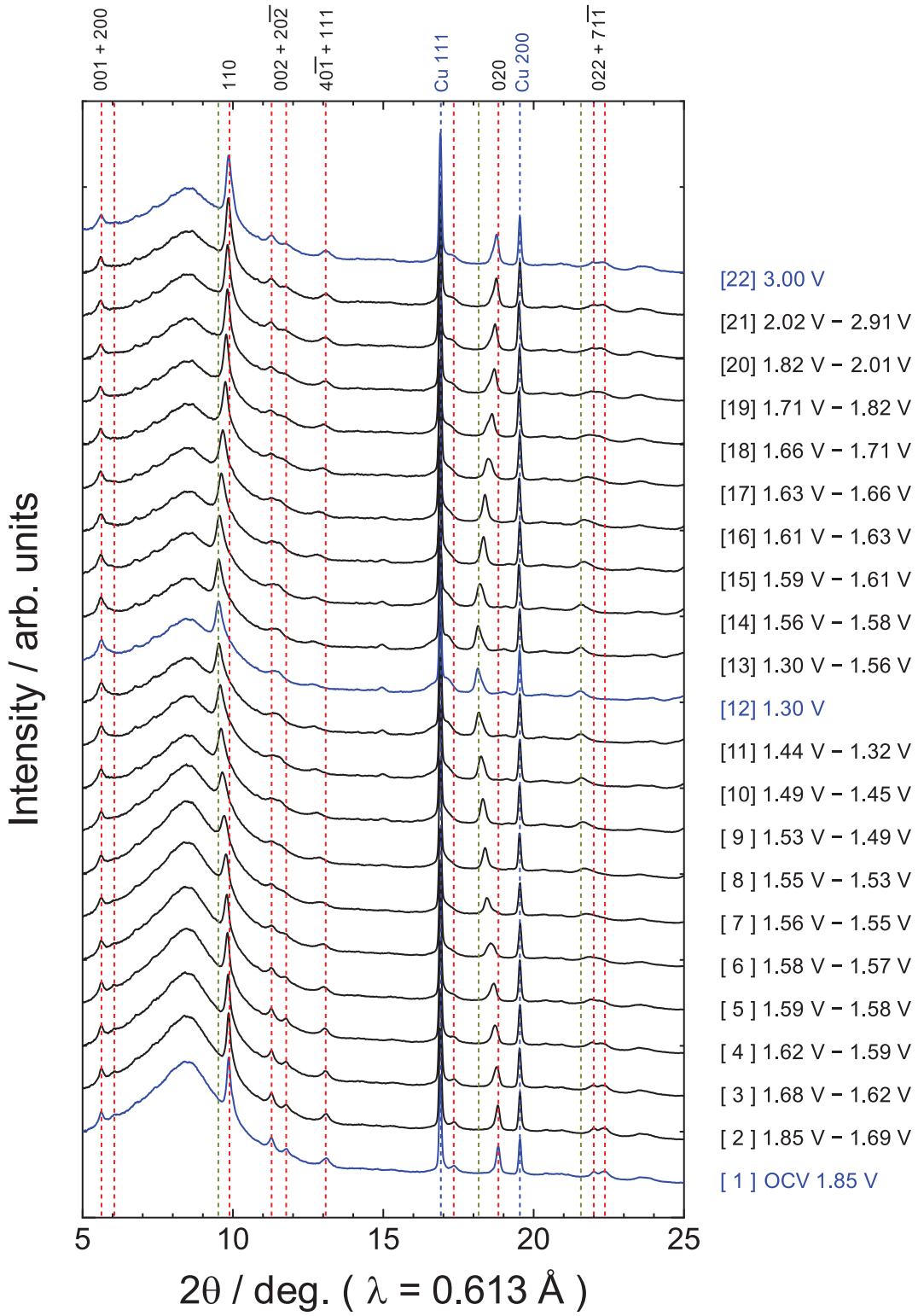

Figure 5-19 Observed *in situ* XRD patterns of the bulk TiO_2(B) electrode. The XRD patterns were sequentially collected with continuous galvanostatic charge-discharge cycles (30 mA g^{-1}). The potentials of the collected XRD patterns are indicated by circles in the charge-discharge curve in Figure 5-18(A).

Table 5-3 Structural parameters of the TiO_2(B) electrode observed at 1.3 V vs. Li / Li^+, determined by the Rietveld refinement.

Space group: $C2/m$ (No. 12, unique axis b, monoclinic)

a = 12.7404(92) Å, b = 3.9270(2) Å, c = 6.5872(25) Å, β = 109.081(58)°, V = 311.455 Å^3

R_{wp} = 7.266, R_p = 5.947, R_e = 4.154, S = 1.7492

atom	site	g	x	y	z	B (Å)
Ti1	4i	1*	0.30664(117)	0*	0.69622(117)	1.0*
Ti2	4i	1*	0.40177(117)	0*	0.32996(140)	1.0*
O1	4i	1*	0.36037(301)	0*	1.04376(472)	1.0*
O2	4i	1*	0.23610(334)	0*	0.33089(404)	1.0*
O3	4i	1*	0.12627(437)	0*	0.67115(304)	1.0*
O4	4i	1*	0.44971(455)	0*	0.69987(615)	1.0*

*Fixed parameters

160 mAh g^{-1} (~1.52 V vs. Li / Li^+). Similarly, in case of b-axis, the expansion slopes also changed at those points. These points were approximately matched with the peak potentials of differential capacity plot shown in Figure 5-18(B) (marked as B1 and B2). Plateaux observed in those potential regions seem to represent two-phase equilibrium reactions. In Figure 5-20, the error bars of volume (V) around the plateau potentials were significantly larger than those in the other regions. This indicates that single-phase fitting was not suitable for the plateau regions. In order to discuss the detailed lithium insertion process such as changes of internal atomic coordination, and composition of intermediate phases in each plateau region (B1 and B2), further assessment is required. One may think that, multiphase Rietveld pattern fitting is useful to discuss such two-phase reactions. However, we could not achieve a satisfying fit by using this method probably due to the small crystallite size of the TiO_2(B) sample (which causes broadening in the diffraction peaks), complicatedly overlapped peak feature, intricately-shaped background pattern, and low-scattering factor of Li atoms. Although pattern fitting with unnatural parameters can be done even in such a situation, we judged it is very hard

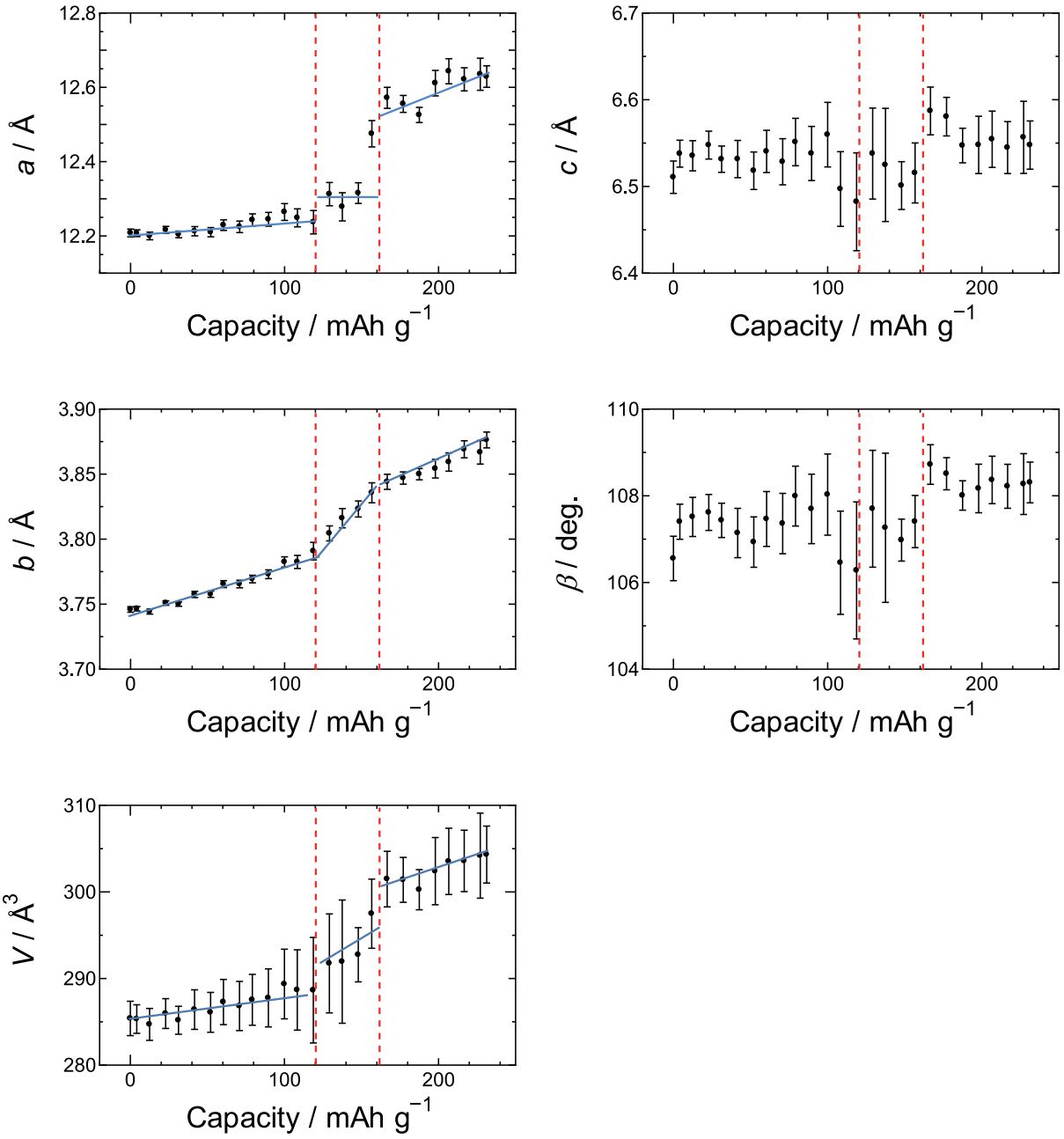

Figure 5-20 Changes in apparent crystal lattice parameters of TiO_2(B) upon lithium insertion.

to obtain reasonable parameters. Therefore, we did not perform farther multiphase Rietveld analysis.

In order to analyze the two-phase reactions in more safe and correct way, we focused on 020 diffraction peak observed at around 2θ=19°, because the peak intensity is quite high, and not overlapped with other diffraction peaks. In addition, the 020 peak is located between the peaks of copper current corrector that can be used as angular standards. A magnified view of the

020 peaks is shown in Figure 5-21. The peak shape of the pristine electrode was symmetrical, while their profiles observed at the plateau regions were asymmetrical. As seen in Figure 5-21, the asymmetric profiles at the plateau regions are well explained by the superposition of the two decomposed peaks. The intensity ratio of each decomposed peak changed gradually with lithium insertion, and finally their profile converged into a single component. This result is in good accordance with the typical feature of a two-phase equilibrium reaction. The first phase transition (noted as "two-phase equilibrium (1)" in Figure 5-21(A)) is located between 1.68 V vs. Li / Li^+ ($Li_{\sim 0.1}TiO_2$) and 1.57 V vs. Li / Li^+ ($Li_{\sim 0.25}TiO_2$). This potential region corresponds to the plateau region marked as B1 in Figure 5-21(B). In this phase transition, the length of *b*-axis is expanded from 3.75 Å to 3.77 Å. On the other hand, the second phase transition (noted as "two-phase equilibrium (2)" in Figure 5-21(A)) is located between 1.57 V vs. Li / Li^+ ($Li_{\sim 0.25}TiO_2$) and 1.52 V vs. Li / Li^+ ($Li_{\sim 0.5}TiO_2$). This potential corresponds to the plateau region marked as B2 in Figure 5-21(B). In this phase transition, the length of *b* is expanded from 3.77 Å to 3.83 Å. In the meantime, in the case of monoclinic system, *d* value of *hkl* diffraction line d_{hkl} is expressed as following equation:

$$\frac{1}{d_{hkl}^2} = \frac{1}{\sin^2\beta}\left(\frac{h^2}{a^2} + \frac{k^2\sin^2\beta}{b^2} + \frac{l^2}{c^2} - \frac{2hl\cos\beta}{ac}\right) \tag{5-3}$$

Therefore, the length of *a* can be estimated from *b*, β, and d_{110} as follow:

$$a = \frac{bd_{110}}{\sin\beta\sqrt{b^2 - d_{110}^2}} \tag{5-4}$$

Since the crystal cell parameter of β was almost constant during lithium insertion, it is meaningful to estimate the value of *a* in each intermediate state from the position of 110 diffraction peak with an assumption of a constant β value (β=108°). In the first phase transition (marked as B1 in Figure 5-21(B)), the length of *a* is expanded from 12.1 Å to 12.3 Å. On the other hand, in the second phase transition (marked as B2 in Figure 5-21(B)), the length of *a* is expanded from 12.3 Å to 12.7 Å. Therefore, the increments of both *a* and *b* in the second phase transition (marked as B2 in Figure 5-21(B)) were relatively larger than that in the first phase transition (marked as B1 in Figure 5-21(B)).

The phase transitions at the plateau regions can be explained by changing the lithium

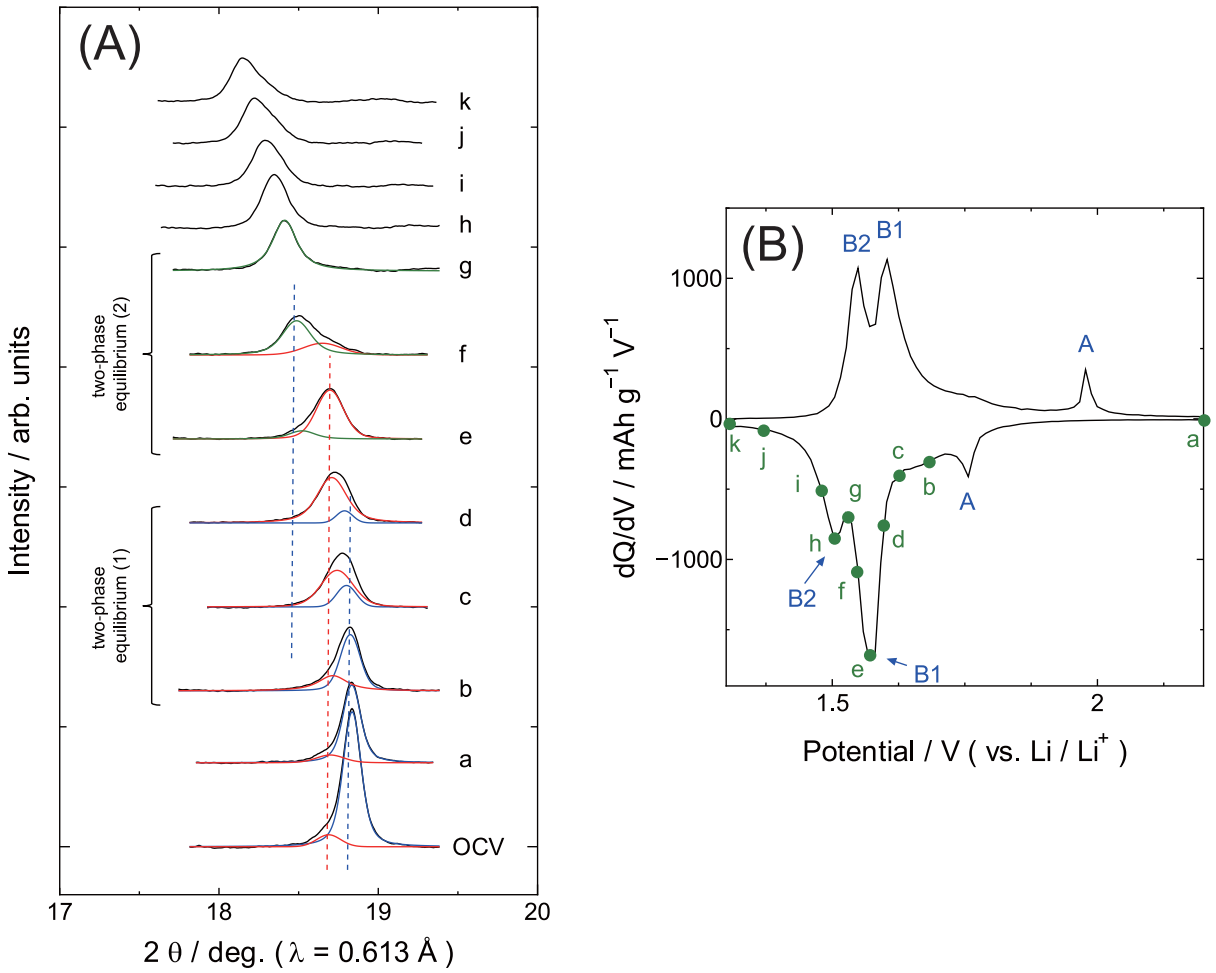

Figure 5-21 (A) Magnified view of the 020 peaks. The XRD patterns were sequentially collected with continuous galvanostatic charge-discharge cycles (25 mA g^{-1}). Each pattern was observed at the potential indicated by circles on the derivation of the galvanostatic charge-discharge curve of the TiO_2(B) electrode, shown in (B).

storage sites with a two-step transformation. Previous studies indicate that the TiO_2(B) crystals have at least three lithium storage sites located at vacancy spaces created by TiO_6 octahedral chains. The storage sites are named as A1, A2 and C (see Figure 5-22) in the previous reports.[174,176] Since the insertion energy is different for each type of site, lithium occupations should occur sequentially in a step-by-step manner.[173–176] Armstrong described that lithium ions are stored as a following manner: firstly C site is occupied at $x < 0.25$ for Li_xTiO_2(B), then A1 site is occupied at $0.25 < x < 0.5$, and finally A2 site is occupied at $x > 0.5$.[149] Since the C site is located at the center of large vacancy space of TiO_6 octahedral chains, the

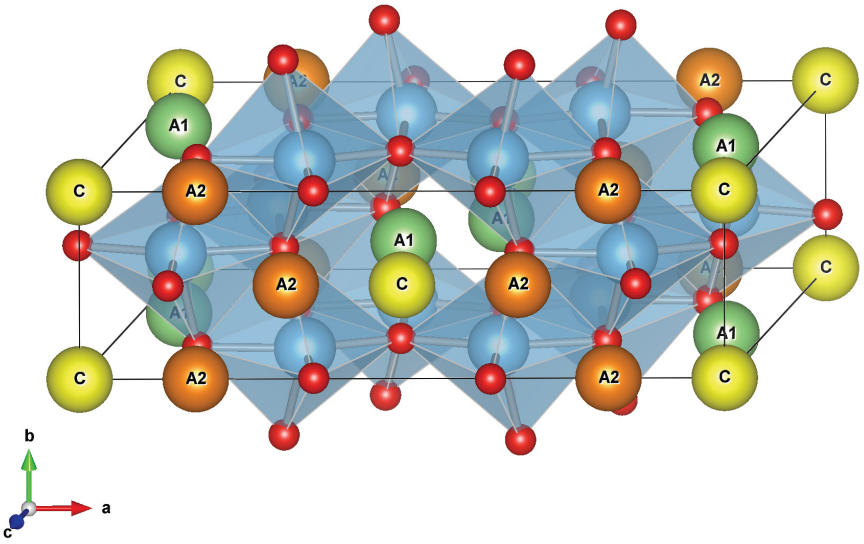

Figure 5-22 Lithium storage sites of TiO_2(B). Oxygen and titanium atoms are shown in red and blue, respectively.

degree of structural changes accompanied by the lithium insertion in $x < 0.25$ should become very small. This mechanism is reasonable to explain the observed small structural change at the first two-phase transition in this study (Li_0TiO_2(B) to $Li_{0.25}TiO_2$(B), marked as B1 in Figure 5-21(B)). The second two-phase transition ($Li_{0.25}TiO_2$(B) to $Li_{0.5}TiO_2$(B), marked as B2 in Figure 5-21(B)) also seems to be explained by the changing of storage site (C to A1 site).

However, it should be noted that the changing manner of cell parameters reported by Armstrong *et al.*[176] (*ex situ* neutron diffraction) differ from our *in situ* XRD results. Armstrong analyzed that, the cell parameter *a* was increased once with the first phase transition (Li_0TiO_2(B) to $Li_{0.25}TiO_2$(B); 12.2078(10) Å to 12.884(5) Å), and then decreased with the second phase transition ($Li_{0.25}TiO_2$(B) to $Li_{0.5}TiO_2$(B); 12.884(5) Å to 12.451(5) Å). In addition, the increment of *b* in the first phase transition (3.74878(13) Å to 3.8019(8) Å) was larger than that in the second phase transition (3.8019(8) Å to 3.8168(8) Å). Those results are completely different from our findings (i.e. the length *a* was continuously increased with lithium insertion, and the increment of *b* in the second phase transition was larger than that in the first phase transition.) Because of the advantage of large scattering factor of lithium ions, neutron diffraction analysis is useful to discuss the changing of atomic coordination in

lithium storage electrodes. However, since lithiated electrode is unstable, the *ex situ* method is accompanied with the risk of electrode degradation. In this respect, the *in situ* method used in this study has a great advantageous to analyze lithium storage process compared with *ex situ* method. Therefore, we think that the revision of $Li_{0.25}TiO_2$(B) structure is required to discuss detailed lithium storage process.

After the plateau region, the peak position shifted continuously and monotonically with lithium insertion. The increment of the lattice parameters under 1.5 V vs. Li / Li^+ can be understood by solid solution type lithium insertion into the TiO_2(B) lattice. From the number of Ti atoms and vacancy sites that can be stored by Li atoms, TiO_2(B) can store ions up to the $LiTiO_2$ composition, which corresponds to a capacity of 336 mAh g^{-1}. However, due to large ionic repulsions between neighboring lithium atoms, lithium storage in this region seems unstable. The crystal volume increased rapidly with lithium insertion in this region. Therefore, in general, the amount of lithium storage in the bulk TiO_2(B) samples is restricted to ~235 mAh g^{-1} ($Li_{0.7}TiO_2$).

To summarize the results this section, the following points were elucidated by the *in situ* XRD observations:

1. The monoclinic crystal structure of TiO_2(B) is maintained during lithium insertion.
2. TiO_2(B) can store lithium ions without large structural changes at the primary state ($E >$ 1.6 V vs. Li / Li^+, in discharge process).
3. Two types of two-phase equilibrium lithium storage were observed at 1.68 to 1.57 V vs. Li / Li^+, and 1.57 to 1.52 V vs. Li / Li^+. The potentials correspond to the plateau region marked as B1 and B2 in Figure 5-18(B), respectively.
4. The length of *c*-axis and angle-β were almost constant during lithium insertion. On the other hand, the length of *a*-axis and *b*-axis increased with phase transition. The increment of *a* and *b* in the second phase transition (marked as B2 in Figure 5-18(B)) was relatively larger than that in the first phase transition (marked as B1 in Figure 5-18(B)).
5. In the potential region of $E <$ 1.5 V vs. Li / Li^+, solid-solution-type lithium insertion occurs. The crystal volume was continuously increased with lithium insertion in this region.

6. Structural changes in TiO_2(B) are reversible: the peak positions observed after the first cycle (observed at 3.0 V vs. Li / Li^+, Li extracted state) returned to those original positions of the pristine electrode (observed at open circuit potential in the previous cycle).

5.3.5 Role of TiO_2(B) Phase in Mesoporous Carbon–TiO_2 Electrodes

As mentioned in Section 5.3.2, the MCT-600 electrode showed superior cycle stability and rate performance compared with the MCT-700 electrode. The difference in the performance seems to be related to the crystal phase of TiO_2. The reversible capacity, especially at the anatase storage region (region II), decreased rapidly with the cycles in the MCT-700 electrode. This result can be explained by the structural change in the anatase crystals. The framework structure of the composites is sensitive to the changes in crystal structure incorporated in the mesoporous framework. In case of anatase, drastic structural change (tetragonal to orthorhombic) occurs at the anatase plateau region (~1.75 V vs. Li / Li^+). Such structural change is detrimental to maintain the electrode structure. The deformation of the electrode structure would induce a decrease in capacity. On the other hand, TiO_2(B) crystals store lithium ions with maintaining its initial monoclinic structure. Therefore, its structural deformation seems to be relatively suppressed compared with that of anatase. As discussed in Section 5.3.2, the cycle performance of MCT electrodes were highly dependent on the the cut-off voltage: charge-discharge cycles under 1.3 V vs. Li / Li^+ are not suitable for stable cycle performance. This result may be explained by a volumetric expansion of TiO_2(B) phase. The *in situ* XRD investigation revealed that the lattice volume of TiO_2(B) increases continuously with lithium insertion under 1.5 V vs. Li / Li^+. Therefore, a lower cut-off voltage induces larger volume expansion of the TiO_2(B) crystal, which in turn induces structural deformation of the electrode analogous to that of anatase.

Because of the straight lithium conduction pass along *b*-axis, lithium storage at the monoclinic TiO_2(B) structure is suitable for high-power operations. Such a high-speed

lithium storage characteristic is known as pseudocapacitive behavior, previously reported by Zukalová *et al.*[179] Since TiO_2(B) electrodes show superior rate performance compared to anatase ones, the good rate capability of the MCT-600 electrode can be understood by the TiO_2(B) phase. In addition, it was found that the rate capability of region I (E > 1.6 V vs. Li / Li+) was superior to that of region III (E < 1.5 V vs. Li / Li^+) even though both the regions corresponded to the same TiO_2(B) structure. This fact may be related to the degree of structural change, since a large amount of this change is unlikely for high-speed lithium storage. As mentioned above, the structural change in region III was larger than that in region I.

5.4 Summary

In this study, lithium storage properties of the MCT-600 and MCT-700 electrodes were compared. It was found that the cycle stability and rate performance of the MCT-600 electrode was superior to that of the MCT-700. This result seemed to be related with the amount of TiO_2(B) phase. In order to discuss the detailed lithium storage process in the TiO_2(B) phase, *in situ* XRD measurements using a bulk TiO_2(B) sample was conducted. From these measurements, we have successfully obtained information about structural changes in the TiO_2(B) phase during Li insertion and extraction. It was revealed that the initial monoclinic structure of TiO_2(B) was almost maintained during lithium insertion. The unique crystal structure and the behavior of structural change seem to support the superior performance of electrodes containing the TiO_2(B) phase.

Chapter 6

Photoluminescence Properties of Ordered Mesoporous Carbon–SiO_2 Composites

6.1 Introduction

As mentioned in Section 1.3, photoluminescence materials having stable, efficient, and inexpensive phosphor materials that provide a high color rendering performance with less toxicity are desired. Recently the author found strong white-light emission from oxidized mesoporous carbon–SiO_2 composite systems (oxMCSs) under long-wavelength UV light (λ = 300–400 nm) irradiation. The photoluminescence (PL) spectra of the composites cover almost the entire visible range, and its shapes are similar to that of sunlight. The composites possessing ordered, cylindrical mesopores consist of a homogeneous matrix of silica nanoparticles and amorphous carbon. Furthermore, they are not comprised of expensive and toxic elements. These properties of the oxMCSs should be useful for the LED-phosphor application in terms of cost and color reproducibility. Therefore, photoluminescence properties of oxMCSs were studied in this chapter.

6.2 Experimental Methods

6.2.1 Sample Preparation

Mesoporous carbon–SiO_2 composites (MCSs) were synthesized by triconstituent co-assembly method as described in Section 2.2.1.4. Although, carbonization temperature was fixed to 900 °C in the previous section, the temperature was varied from 600 °C to 1200 °C in this chapter. For convenience, the obtained as-made MCSs were designated as MCS-x(AM),

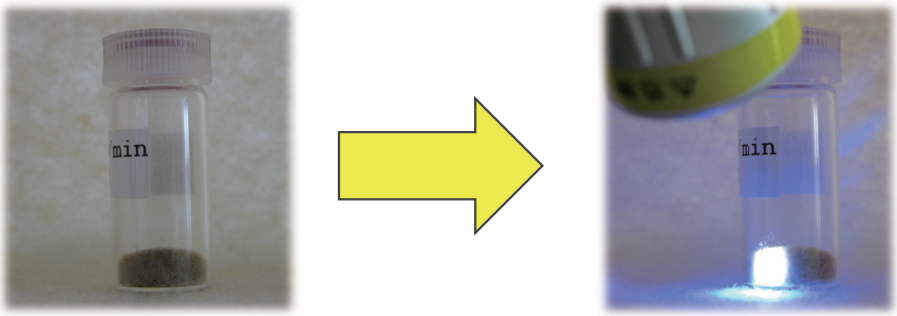

Figure 6-1 White-light emission from oxidized mesoporous carbon–SiO_2 composite. (MCS-900(ox500-2)). (Left) Under normal-light. (Right) Under 365 nm UV-light excitation.

where x represents carbonization temperature (°C). The as-made MCS-x(AM) samples are PL inactive, while they became activate after calcination in air (air-oxidation). Air-oxidation temperature of the as-made samples were varied in range from 400 °C to 700 °C in this study. In this chapter, the obtained oxidized MCS samples (oxMCSs) were designated as MCS-x(ox$y$-z), where y and z are oxidation temperature (°C) and oxidation-time (h), respectively. Furthermore, uncarbonized samples were also prepared for comparison. The uncarbonized samples were designated as MCS-UC(ox$y$-z), where y and z are oxidation temperature (°C) and oxidation-time (h), respectively.

6.2.2 Characterization

Nitrogen adsorption / desorption isotherms at 77 K were measured using a Shimadzu Gemini 2375 instrument. Prior to the isotherm measurements, the samples were heat treated at 200 °C under vacuum (< 3 Pa) for at least 1 h to remove adsorbed moisture. The specific surface areas (S_{BET}) were estimated using the Brunauer–Emmett–Teller (BET) method[32] and the adsorption data in the relative pressure (P / P_0) range from 0.05 to 0.16. The total pore volumes (V_{total}) were calculated using the Gurvich rule at P / P_0 = 0.97. Thermogravimetric (TG) measurements were performed using a Shimadzu TGA-50 instrument. Small-angle powder X-ray scattering (SAXS) measurements were carried out using

a Rigaku Nano-Viewer diffractometer, equipped with a two dimensional (2D) imaging plate detector (Rigaku R-AXIS IV^{++}), using Cu Kα radiation (λ = 1.54 Å) as an incident beam. X-ray photoelectron spectroscopy (XPS) analysis were performed using a ULVAC-PHI PHI 5000 spectrometer using monochromatic Al Kα radiation (1486.6 eV) as the excitation source. Fourier transform infrared absorption (FTIR) spectra were measured using a Perkin-Elmer System 2000 spectrometer or JASCO FT/IR-6300 spectrometer, using the conventional KBr pellet technique. Electron spin resonance (ESR) measurements were performed using JEOL RE-1X spectrometer. In the ESR measuremets, operating frequency, amplitude of magnetic field modulation, and modulation frequency were set to 9.15 GHz, 0.5 mT, and 100 kHz, respectively. Quartz tube was used as a sample container, and a Mn marker (MgO:Mn^{2+}) was used as a spin-density standard. ^{29}Si solid-state nuclear magnetic resonance (NMR) measurements were conducted using Varian INOVA-400 plus spectrometer. In the measurements, two types of method were used: one was magic angle spinning (MAS), and the other was cross-polarization/magic angle spinning (CP/MAS). In the both methods, the dipolar-decoupling (DD) technique was simultaneously used. ZrO_2 tube was used as a sample container, and rotating speed for the MAS was set to 6 kHz. In the obtained spectra, the peak position of tetramethylsilane ($Si(CH_3)_4$; TMS) was defined as 0 ppm. In addition, polydimethylsiloxane (PDMS) was used as external standard for chemical-shift calibration. Photoluminescence (PL) and PL excitation (PLE) spectral measurements were performed using a Horiba SPEX Fluorolog-3 spectrometer equipped with a 450 W Xe-lamp, or home-made PL microscope system equipped with 365 nm laser diode (Omicron-Laserage LEDMOD365; excitation source) and the Princeton Instrument Acton SP2300 charge-coupled device (CCD) detector. All measurements were performed at room temperature.

6.3 Results and Discussion

6.3.1 Structural Properties of Oxidized Mesoporous Carbon–SiO_2 Composites

Firstly, in order to investigate the effects of air-oxidation temperature, structural properties of MCS-900(ox$y$-2) series (y: oxidation temperature (°C)) were characterized. Structural peroperties of the un-oxidized sample, that is MCS-900(AM), was described in the Sections 2.4.1 and 2.4.2, as the "MCS" sample. The pore-size distribution curves and the SAXS patterns of the composite samples before and after the air-oxidation treatments are shown in Figures 6-2(B) and 6-3, respectively. As shown in these figures, with the air-oxidation temperature increases, the mean pore size of the composites increases and the crystallinity degrade. This is possible because the framework structure of MCS-900(AM), consisting of carbon–silica composite, is weakened by the removal of carbon during the air-oxidation treatment, and some channel pores may fuse together, thereby increasing the effective pore sizes of the materials. On the other hand, it was observed that the 10 diffraction peak position and its peak width are unaffected by the air-oxidation treatment, although its intensity decreases with increasing oxidation temperature. This implies that channel pore fusion occurs heterogeneously in the samples, and some parts of the samples maintain the ordered pore structure. The BET surface areas gradually decreased with increasing oxidation temperature. This decrease is attributed to two reasons. Firstly, the mass density of the sample could have increased by air-oxidation treatment because of the removal of carbon. Secondly, the possible fusion of the channel pores.

The elemental compositions of MCSs, which were estimated from XPS analysis, are summarized in Table 6-1. We confirmed the presence of Si, O, and C in all samples. As shown in the table, carbon concentration first gradually and then drastically decreased with increasing oxidation temperature. The critical burning temperature of the carbon component should be between 400 and 500 °C. However, a small amount of carbon was still present even after the

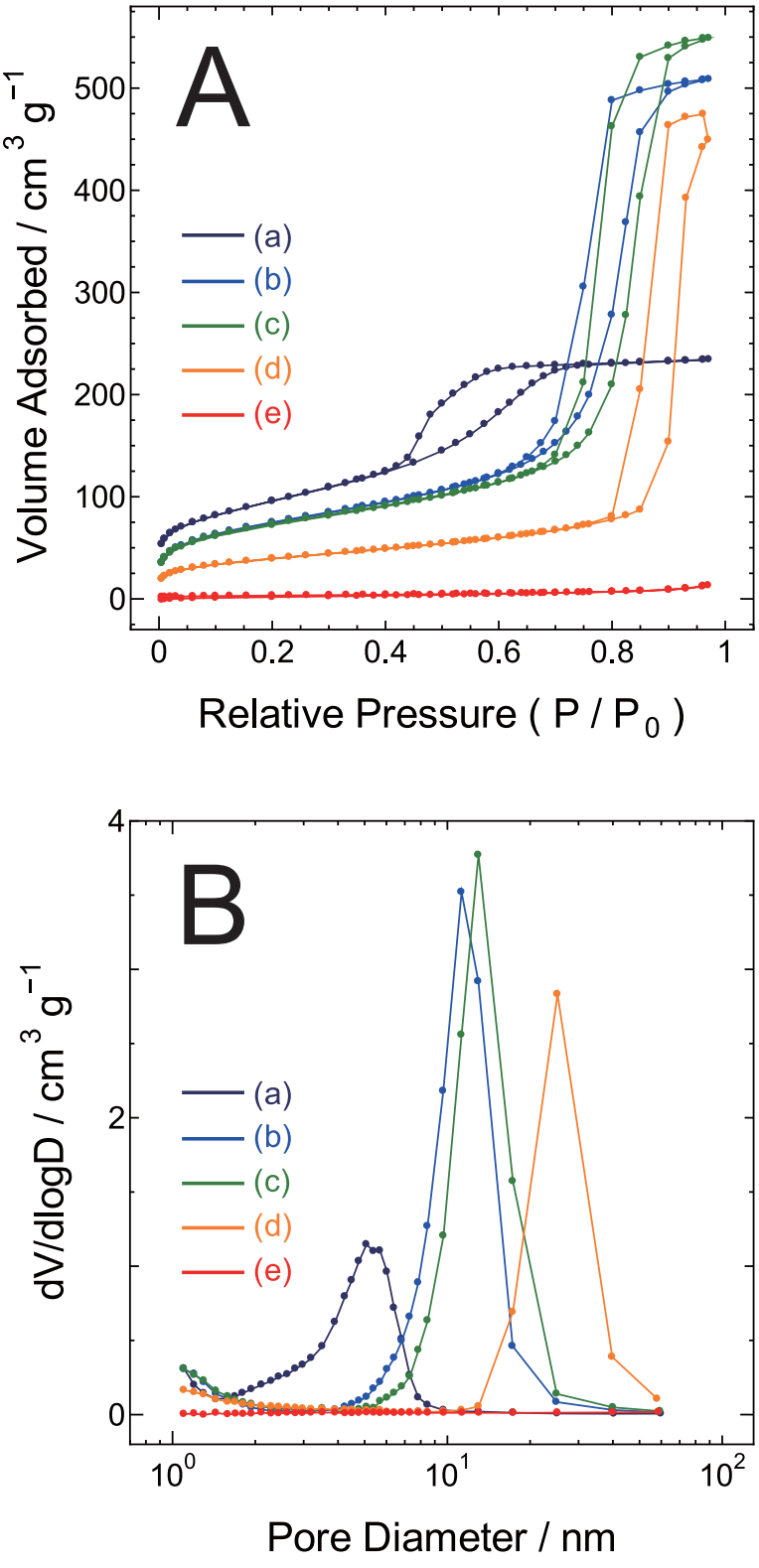

Figure 6-2 (A) N_2 adsorption / desorption isotherms and (B) BJH pore size distribution curves of (a) MCS-900(AM), (b) MCS-900(ox400-2), (c) MCS-900(ox500-2), (d) MCS-900(ox600-2),and (d) MCS-900(ox700-2).

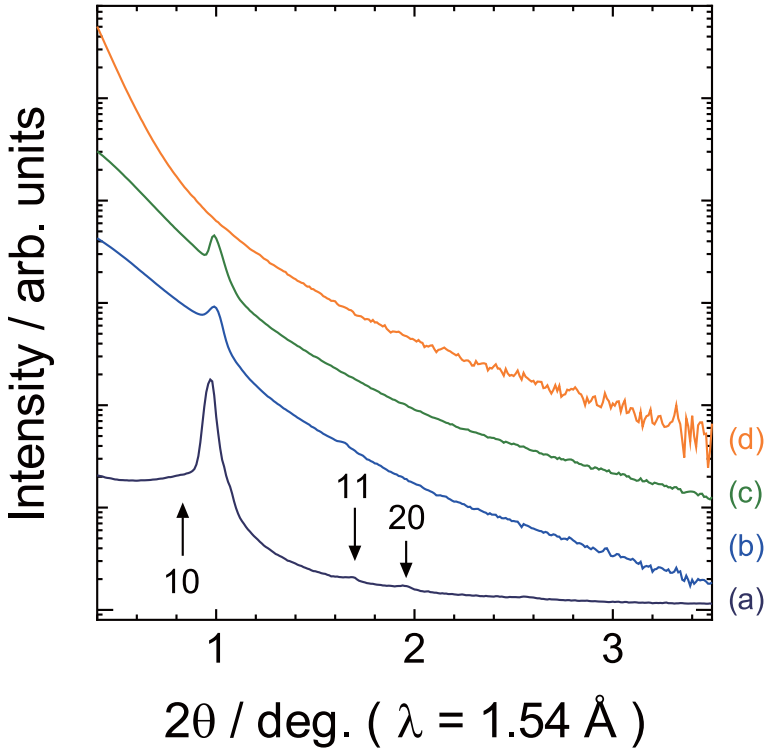

Figure 6-3 SAXS patterns of (a) MCS-900(AM), (b) MCS-900(ox400-2), (c) MCS-900(ox500-2), and (d) MCS-900(ox600-2). Cu Kα radiation (λ = 1.54 Å) was used as an incident beam.

highest oxidation temperature (700 °C) was attained (MCS-900(ox700-2)).

The FTIR spectra of MCSs are shown in Figure 6-4(A). The absorption bands at around 470 and 800 cm^{-1} are assigned to rocking (R) and symmetrical stretching (SS) vibration of the Si–O–Si group, respectively. These bands are commonly observed in bulk silica.[180, 181] The small peak at 950 cm^{-1} can be attributed to the stretching vibration of the Si–OH group (S_{OH}).[182] The broad band located between 980 and 1300 cm^{-1} can be assigned to the asymmetrical stretching vibrations of the Si–O–Si, C–O–C, and Si–O–C groups. The features in this area can be divided into several components. The most intense region in the band at approximately 980–1180 cm^{-1} appears to be dominated by three peaks centered at about 1060, 1100, and 1180 cm^{-1}, which are assigned to the Si–O–Si stretching in-phase transverse-optical mode (AS_1, TO), the Si–O–C or C–O–C stretching mode (AS_C), and the Si–O–Si stretching in-phase longitudinal-optical mode (AS_1, LO), respectively.[183–185] The band shoulder at

Table 6-1 Properties of the mesoporous carbon–SiO_2 composites as a function of air-oxdation temperature.[a]

	x	y	z	S_{BET}	V_{total}	Composition[b] (at.%)		
	(°C)	(°C)	(h)	(m^2 g^{-1})	(m^3 g^{-1})	C	Si	O
MCS-900(AM)	900	—	—	339	0.37	53.1	14.3	32.6
MCS-900(ox400-2)	900	400	2	265	0.82	32.4	20.0	47.6
MCS-900(ox500-2)	900	500	2	257	0.87	5.7	31.0	63.0
MCS-900(ox600-2)	900	600	2	138	0.70	2.5	30.4	67.0
MCS-900(ox700-2)	900	700	2	12	0.02	3.8	32.4	63.7

[a] x: carbonization temperature under inert atmosphere; y: air-oxidation temperature; z: duration of air-oxidation at T_{Ox}; S_{BET}: specific surface area estimated by the BET method; V_{total}: total pore volume.

[b] Chemical compositions of C, Si, and O were estimated using XPS C 1s, Si 2p, and O 1s, respectively.

approximately 1250 cm^{-1} can be assigned to the Si–O–Si stretching out-of-phase mode (AS_2).[181] Figure 6-4(B) shows the FTIR spectra of the air-oxidized MCSs normalized by the transmittance of the AS_2 mode (1250 cm^{-1}). As shown in the figure, the intensity ratios of AS_C to AS_2 gradually decrease with increasing oxidation temperature. This result indicates that the relative abundance of Si–O–C bonds to Si–O–Si bonds decreases with temperature. This behavior is considered reasonable if the decrease of carbon concentration accompanied by the increasing oxidation temperature is taken into account. Actually, carbon concentration esitimated by the XPS analysis was decreased with increasing oxidation temperature, as mentioned above.

Figure 6-5 shows ESR spectra of MCSs. Clear signal was observed at around 325 mT (g = 2.003). This signal can be assigned as dangling-bond of amorphous carbon. As shown in the figure, spin concentration was once increased until 400 °C, and subsequently decreased with increasing air-oxidation temperature. The initial increment of spin density seems to

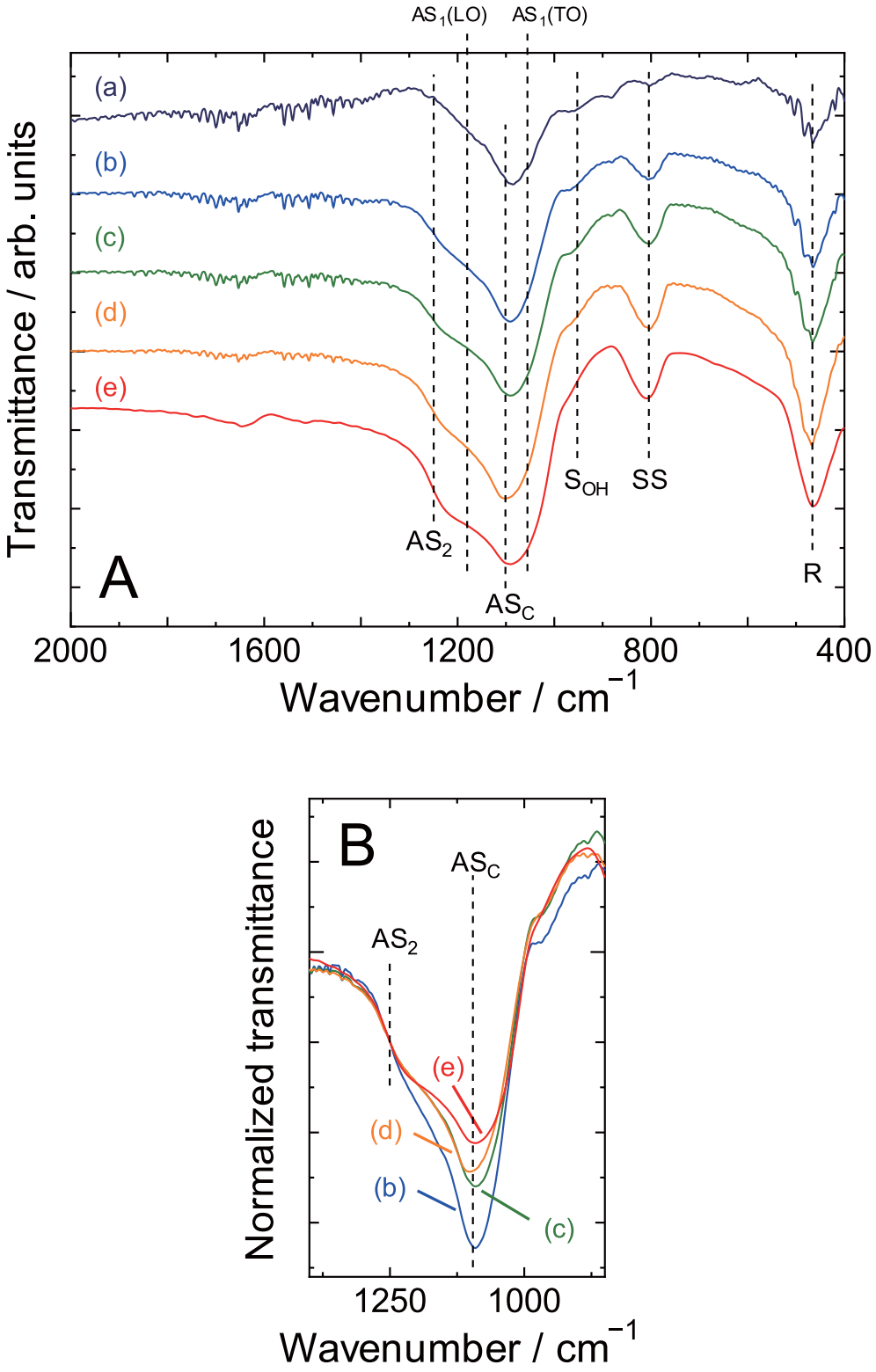

Figure 6-4 (A) FTIR spectra of (a) MCS-900(AM), (b) MCS-900(ox400-2), (c) MCS-900(ox500-2), and (d) MCS-900(ox600-2). FTIR spectra of airoxidized MCSs normalized with the transmittance values at 1250 cm^{-1} are shown in (B).

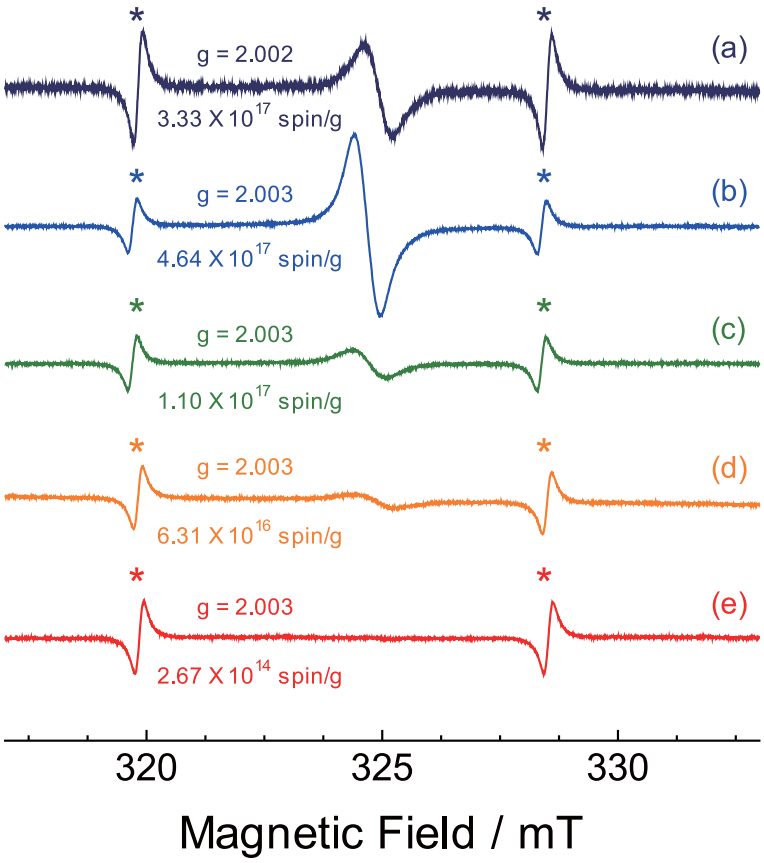

Figure 6-5 ESR spectra of (a) MCS-900(AM), (b) MCS-900(ox400-2), (c) MCS-900(ox500-2), (d) MCS-900(ox600-2), and (e) MCS-900(ox700-2). The peaks marked with asterisk (*) are signal of Mn marker ($MgO:Mn^{2+}$) used as a spin-density standard.

be explained by partial oxidation reaction of amorphous carbon in the pore-wall. Such a oxidation reaction should create dangling-bond at carbon-edge. The following decrement of spin density can be explained by the decrement of defective-carbon due to combustion reaction. As discussed above, concentration of amorphous carbon is rapidly decreased with oxidation treatment in > 400 °C temperature region. In the combustion reaction, defective carbons, which is probably the origin of the ESR signal observed at g = 2.003, should preferentially-removed compared to non-defective sp^2 carbon structure.

In order to analyze chemical character of SiO_2 component, ^{29}Si solid-state NMR measurements were performed. According to the previous reports, ^{29}Si NMR spectrum is sensitive to coordination number and coordination elements of silicon atoms. Figure 6-6(A) shows ^{29}Si MAS NMR spectra of MCSs. In the spectra, three peaks marked with Q_4 (ca.

−110 ppm), Q_3 (ca. −100 ppm), and T (ca. −45 ppm) were observed. Figure 6-6(B) shows ^{29}Si CP / MAS NMR spectra of MCSs. In the CP / MAS spectra, the T peaks were not observed, and the intensity of Q_3 peaks were relatively increased compare to the corresponding Q_4 peaks. By comparing MAS and CP / MAS spectra, the peaks of Q_4, Q_3 and T are assigned as $Si(OSi)_4$, $(HO)Si(OSi)_3$, and $(C)Si(OSi)_3$, respectively. As shown in Figure 6-6(A), the intensity of Q_3 peak was gradually decreased with increasing oxidation temperature. This result means that the concentration of silanol group (Si-OH) was decreased with increasing oxidation temperature. Such a decrement of Si-OH group was also confirmed in the FTIR spectra (see S_{OH} peaks in Figure 6-4). On the other hand, the concentration of Si–C bond (T peak) was increased with increasing oxidation temperature. These results (decrement of Si–OH, and increment of Si–C with increasing oxidation temperature) may be explained as following schemes. As mentioned above, combustion reaction of amorphous carbons occurs above 400 °C oxidation. In this reaction, reactive molecules such as carbon monoxide (CO) should be produced. The generated CO molecules would attack reactive defect-sites such as Si–OH. As a result Si–OH groups would be decreased, and Si–C bond can be created.

6.3.2 Photoluminescence Properties of Oxidized Mesoporous Carbon–SiO_2 Composites

Under UV light excitation, un-oxidized samples (i.e. MCS-600(AM), MCS-700(AM), MCS-800(AM), and MCS-900(AM)) did not exhibit luminescence, whereas air-oxidized MCSs (oxMCSs) exhibited strong white-light emission. The emission was strong white light, enough for the excitation by the very weak UV light of a portable pen-type 370-nm-LED lighting device, to be clearly observed even in daylight (not in the dark room) with naked eyes. Firstly, photoluminescence properties of MCS-900(ox*y*-2) series (*y*: oxidation temperature (°C)) were investigated.

By PLE measurement of the 550-nm emission, three intense peaks were observed at around 275, 310, and 370 nm, as shown in Figure 6-7. From the application perspective,

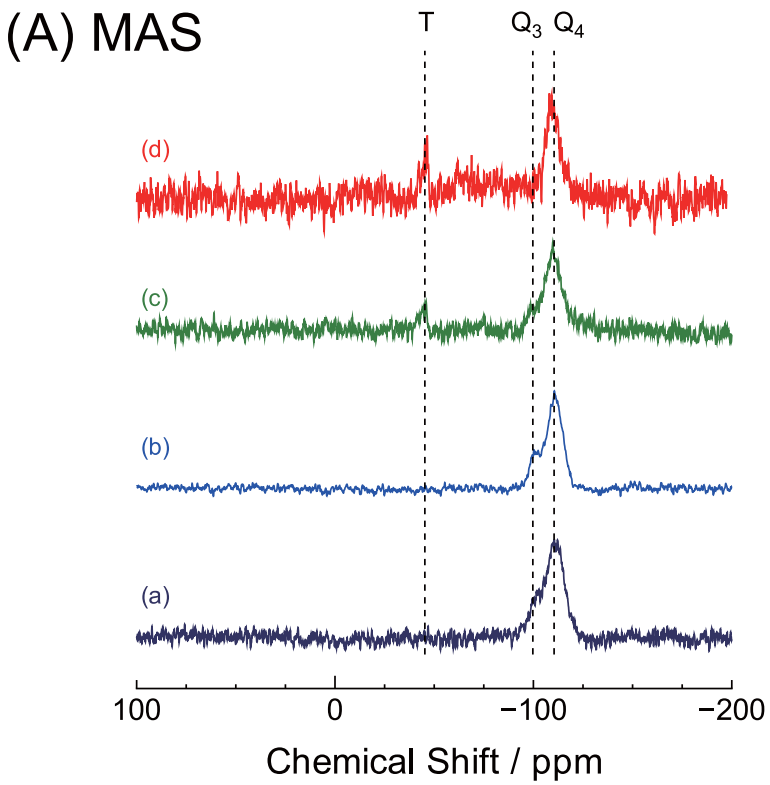

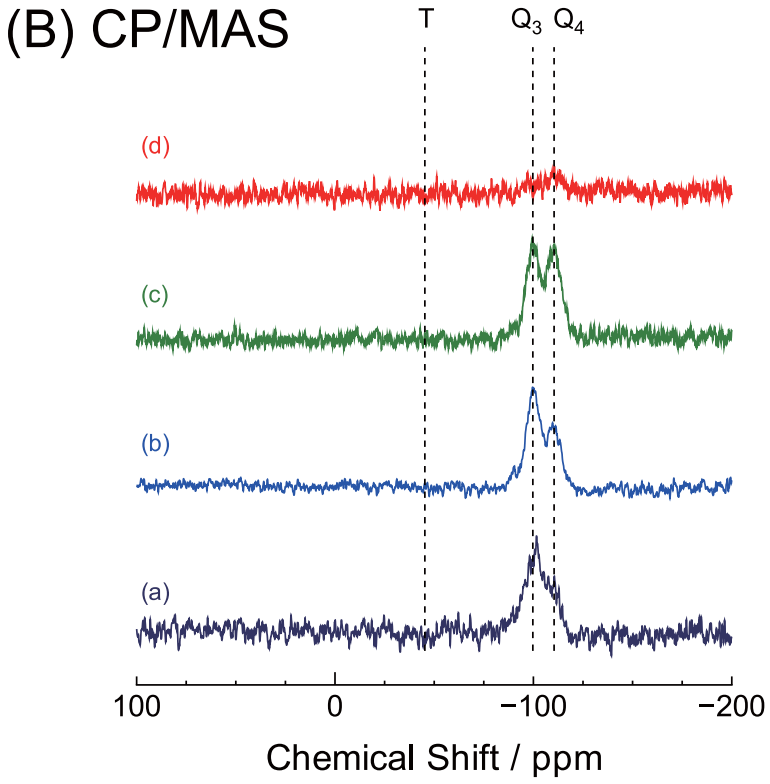

Figure 6-6 (A) MAS- and (B) CP / MAS- ^{29}Si solid-state NMR spectra of (a) MCS-900(AM), (b) MCS-900(ox400-2), (c) MCS-900(ox500-2), and (d) MCS-900(ox700-2).

excitation at 370 nm is favorable, because this wavelength can be easily generated by commercially available UV LEDs. Therefore, the author studied PL spectra at 370-nm excitation in more detail. The room-temperature PL spectra from the oxMCSs excited at 370 nm are shown in Figure 6-8(A). As shown in the figure, the spectra cover almost the entire visible light wavelength region. Figure 6-8(B) shows the black-body radiation spectrum at 6000 K, which is analogous to the effective spectrum of the sunlight.[186] Since the spectra of oxMCSs shown in Figure 6-8(A) are quite similar to the analogous sunlight spectrum, oxMCSs have potential to replace the widely used fluorescent lighting devices.

In the MCS-900(ox*y*-2) series, the most intense luminescence was observed in MCS-900(ox500-2), followed by MCS-900(ox600-2), and MCS-900(ox400-2) (see Figure 6-8(A)). In the case of MCS-900(ox700-2) sample, the luminescent intensity was very week and hard to confirm with naked eyes. Although it is very difficult to measure the absolute emission intensity for a solid powder sample, the relative intensities shown in Figure 6-8(A) are meaningful, because the measurements were performed under similar conditions. The luminescent intensity of MCS-900(ox400-2) was much weaker compared to that of bright samples (MCS-900(ox500-2) and MCS-900(ox600-2)). However, luminescent origin is essentially independent of the oxidation temperature, because the PL peak positions of each sample (peaks at about 413, 435, 462, 500, and 531 nm) remain unchanged with oxidation treatment. The difference in luminescent intensity is probably due to the differences in light transmittance of the samples, since the color of MCS-900(ox400-2) (dark-gray) is much darker (i.e., transmittance is much lower) compared to that of MCS-900(ox500-2) (light-brown) and MCS-900(ox600-2) (white) (see Figure 6-9). However, these differences fail to explain the reason for the PL intensity of MCS-900(ox500-2) being higher than that of MCS-900(ox600-2) and MCS-900(ox700-2). Therefore, in the following section, we discuss the population of the color centers of the three MCS samples.

The PL spectrum shapes of the samples were highly dependent on the oxidation temperature and oxidation time. The PL spectrum features can be divided into two large components, namely, a blue luminescent band and a green-yellow luminescent band, indicated

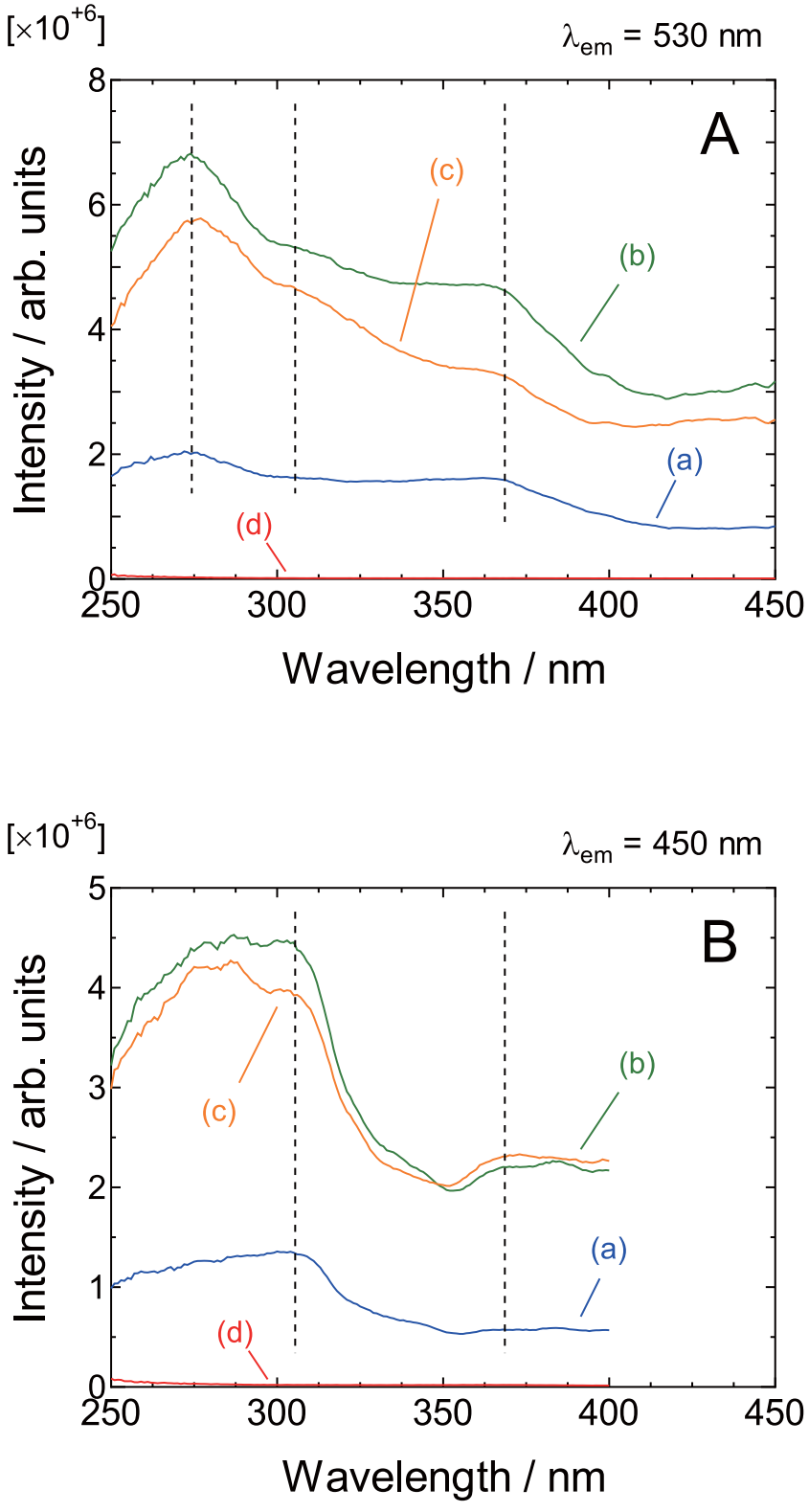

Figure 6-7 Photoluminescence excitation spectra of (a, blue line) MCS-900(ox400-2), (b, green line) MCS-900(ox500-2), (c, orange line) MCS-900(ox600-2), and (d, red line) MCS-900(ox700-2). Emission wavelength of (A) and (B) were set to 530 nm and 450 nm, respectively.

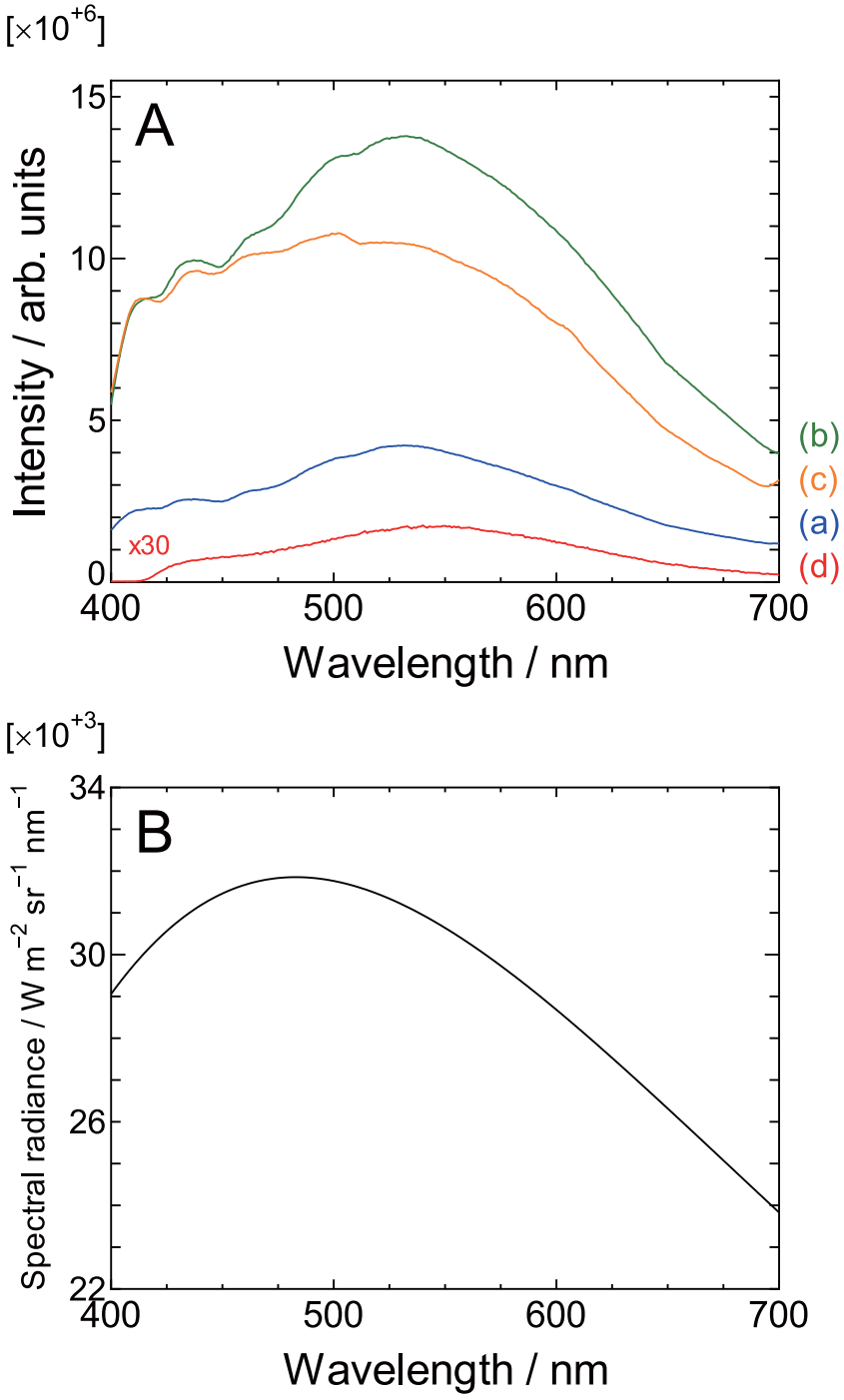

Figure 6-8 (A) Room temperature photoluminescence emission spectra of (a, blue line) MCS-900(ox400-2), (b, green line) MCS-900(ox500-2), (c, orange line) MCS-900(ox600-2), and (d, red line) MCS-900(ox700-2) excited at 370 nm. (B) Spectrum from black body radiation at 6000K.

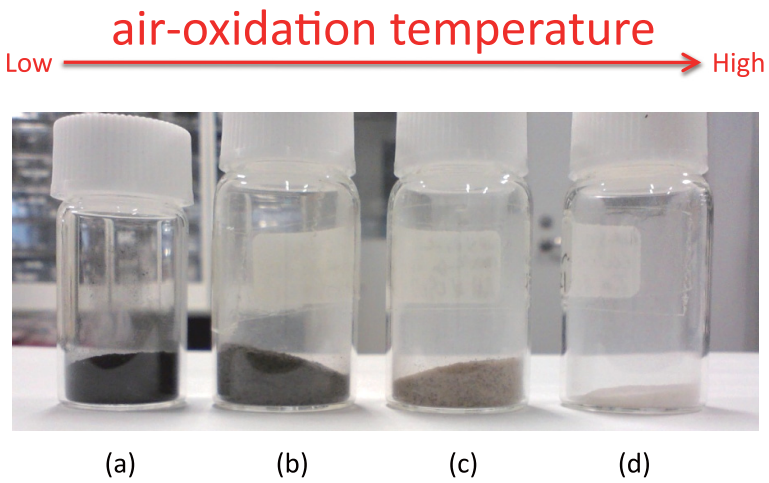

Figure 6-9 Photographs of (a) MCS-900(AM), (b) MCS-900(ox400-2), (c) MCS-900(ox500-2), and (d) MCS-900(ox600-2).

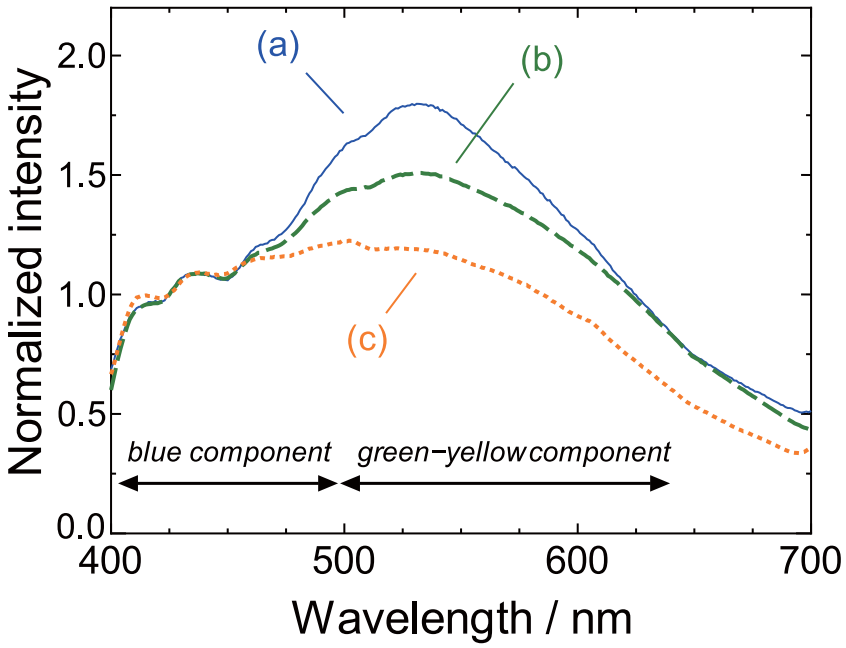

Figure 6-10 Photoluminescence emission spectra of (a, solid blue line) MCS-900(ox400-2), (b, dashed green line) MCS-900(ox500-2), and (c, dotted orange line) MCS-900(ox600-2) normalized with the emission intensity value at 425 nm. Excitation wavelength was set to 370 nm.

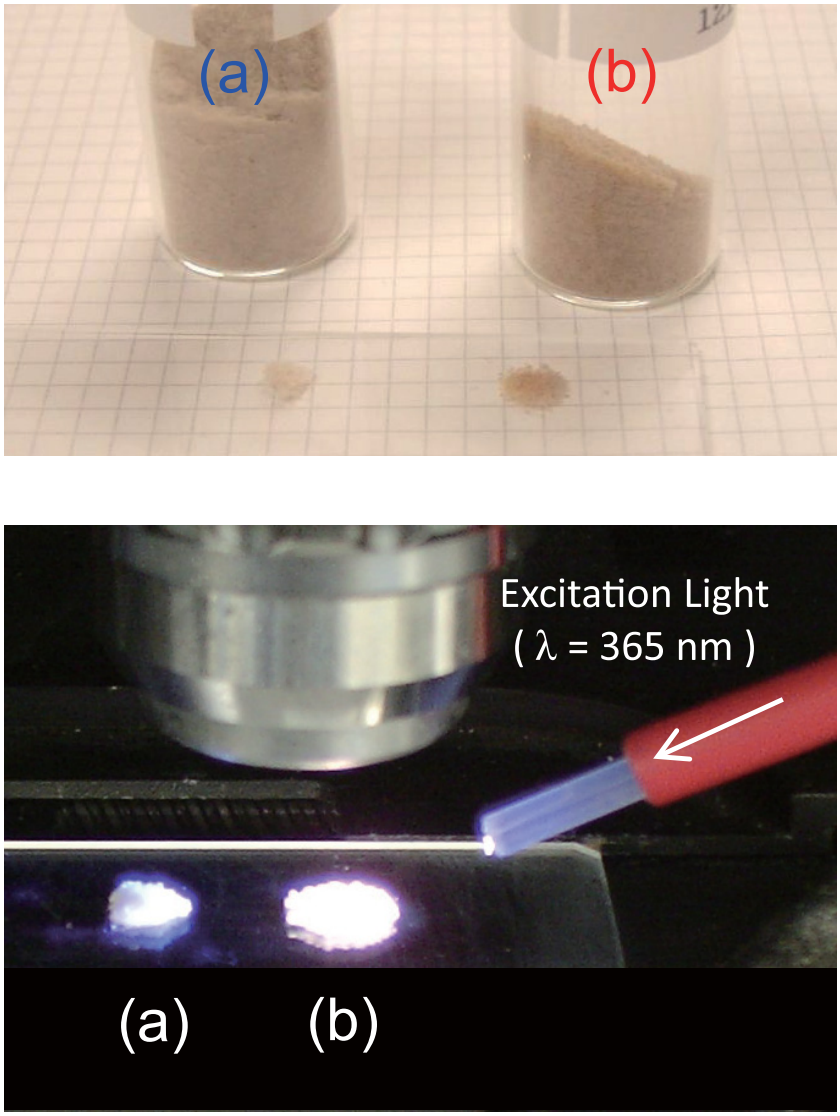

Figure 6-11 Photographs of (a) MCS-UC(ox500-2), and (b) MCS-600(ox500-2), taken under (Top) normal-light and (Bottom) 365 nm UV-light.

by the arrows in Figure 6-10(C). The former band structure is almost similar to the reported visible PL form defective silica materials such as silica gels,[187] sol-gel-delivered mesoporous silica,[188–191] amorphous silica nanoparticles,[192] and silica nanowires.[193] Although the detailed luminescent mechanisms of these materials are still unclear, several possible mechanisms stemming from SiO_2 structural defect sites were proposed to explain the PL phenomena. One may assume that the PL properties of the present samples originate from the same source. However, the luminescent of such defective silica samples is generally observed only in the blue-green region (peak center: 400–500 nm) and is much different from the spectra of our

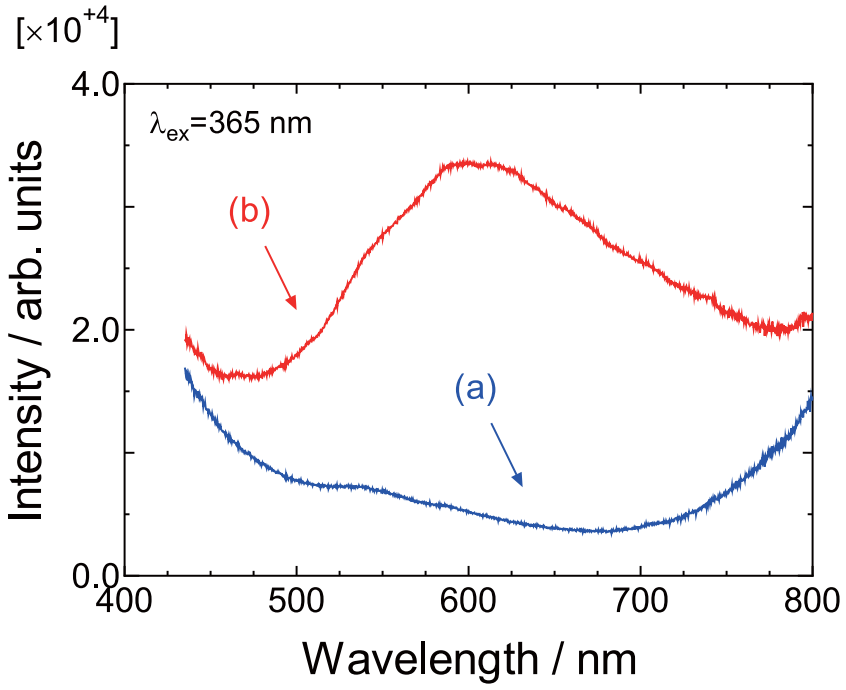

Figure 6-12 Room temperature photoluminescence emission spectra of (a) MCS-UC(ox500-2), and (b) MCS-600(ox500-2). The spectra were obtained using a PL microscope system equipped with 365 nm laser diode.

samples. Therefore, the PL properties of MCSs, especially the emission component of the green-yellow region, cannot be explained by the abovementioned SiO_2 defect mechanisms alone. However since all luminescent MCSs contain small amounts of carbon in their system, it is possible that the green-yellow luminescent center of MCSs is related to the presence of carbon atoms or carbon-fragment. The carbonization process seems to play an important role for making the PL centers of oxMCSs. Figures 6-11 and 6-12 shows a comparison between carbonized- and uncarbonized-sample. The PL intensity of the uncarbonized sample was much weaker than that of carbonized sample, especially at green-yellow region. Furthermore, it was found that PL color of oxMCSs were changed with their carbonization temperature (see Figures 6-13 and 6-14). The changes of PL color would be explained by the structural changes of carbon-fragments at the carbonization process. These experimental facts also support carbon-based PL center in oxMCSs.

To compare the intensities of the blue and green-yellow bands among the three MCSs,

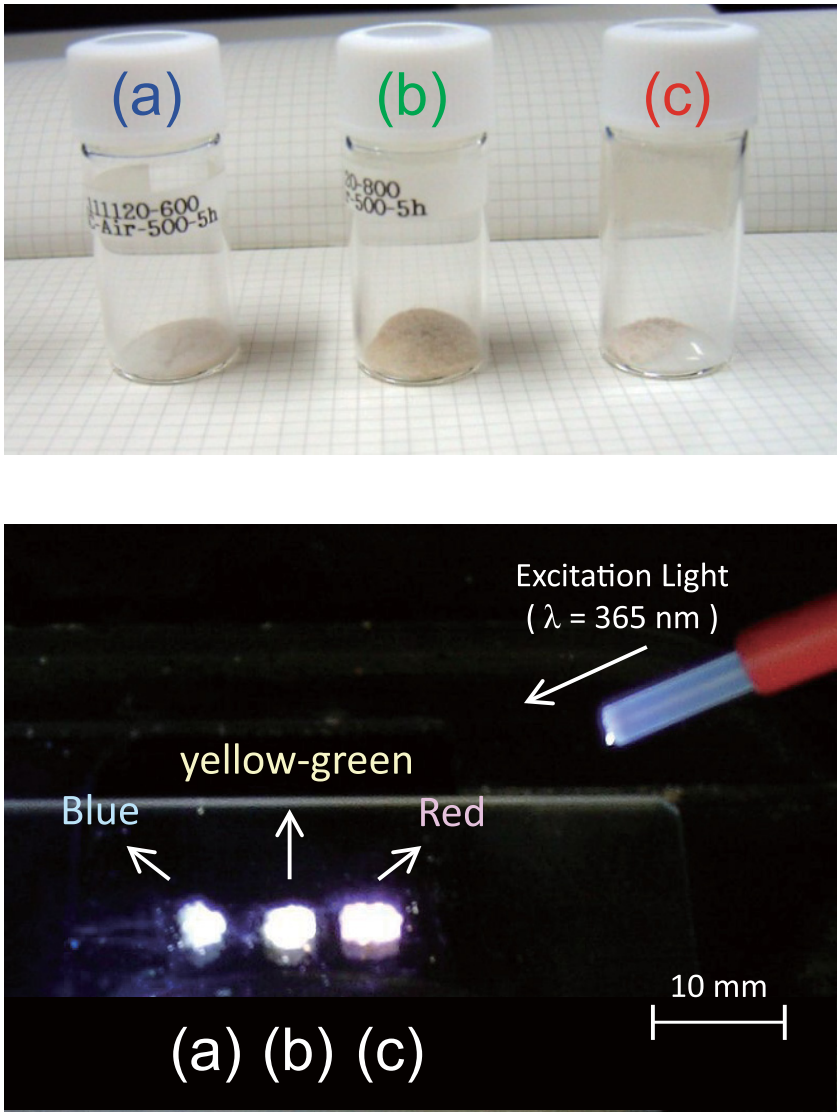

Figure 6-13 Photographs of (a) MCS-600(ox500-5), (b) MCS-800(ox500-5), and (c) MCS-1200(ox500-5), taken under (Top) normal-light and (Bottom) 365 nm UV-light.

the PL spectra of MCSs were rescaled by normalizing the emission intensity value at 425 nm, which correspond to the intensity of the blue component (Figure 6-10(C)). Figure 6-10(C) clearly shows that the intensity ratio of the green-yellow component to the blue component gradually decreases with increasing oxidation temperature. This indicates that the population of the color centers related to the presence of carbon atoms decreases with increasing temperature. In addition, the author found that the green-yellow PL component is also decreasing with increasing oxidation-time. On the other hand, the removal of carbon atoms increases the light transmittance of the samples. These two opposing temperature effects caused by the

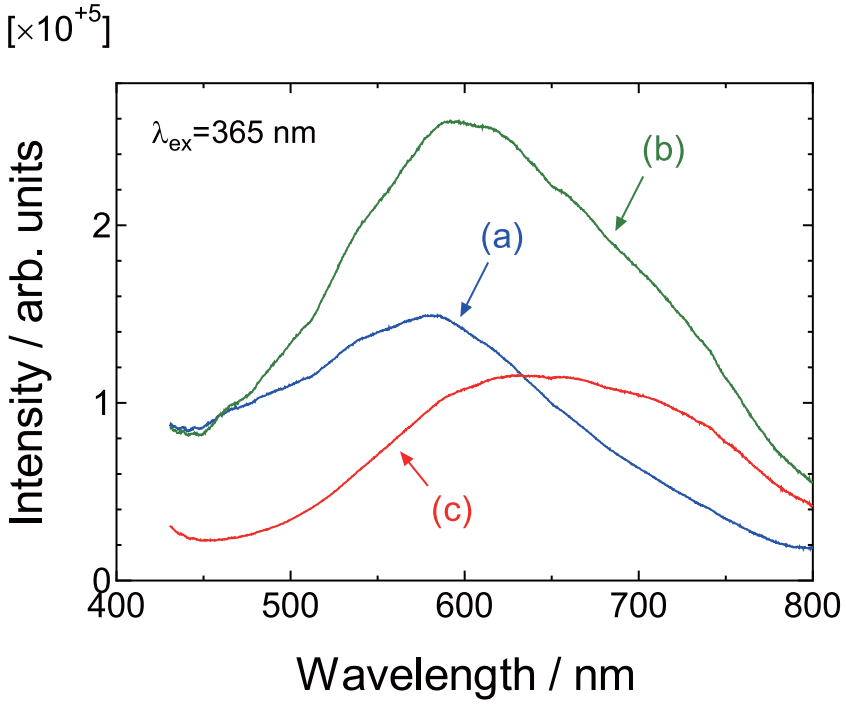

Figure 6-14 Room temperature photoluminescence emission spectra of (a) MCS-600(ox500-5), (b) MCS-800(ox500-5), and (c) MCS-1200(ox500-5). The spectra were obtained using a PL microscope system equipped with 365 nm laser diode.

air-oxidation treatment explain the reason for the PL intensity of MCS-900(ox500-2) being the highest among the three samples. Furthermore, we note that the FTIR intensity of the AS_C mode can be related to the green-yellow PL intensity, suggesting that the stretching of the C–O–C or Si–O–C bonds would be one candidate for the origin of the green-yellow PL emission.

However, the detailed chemical structure of the luminescent center and the luminescent mechanism is still unclear. To clarify the luminescence phenomenon, further studies (e.g., electron states calculation, fluorescence life time measurement) need to be conducted.

6.4 Summary

In this chapter, the author reported the generation of white PL from an air-oxidized mesoporous carbon–silica nanocomposite system under long-wavelength UV light irradiation. It was discovered that the PL spectra of these samples cover almost the entire visible wavelength range and that the shapes of the spectra are highly dependent on their oxidation condition. The PL band at the green-yellow region of the samples was not previously observed in the PL of defective SiO_2. It was indicated that carbon atoms in the composite samples play a key role in producing the photoluminescence phenomena.

Chapter 7

Synthesis and Characterization of Graphene Nanofragments

7.1 Introduction

In Chapter 6, photoluminescence properties of oxidized mesoporous carbon–SiO_2 composites (oxMCSs) were discussed. Although detailed luminescent mechanisms have not been elucidated yet, carbon-fragments in the composites seem to play an important role for luminescence. Since the carbon-fragments were existed even after 400 °C oxidation, their molecular structure should be consisted of aromatic-carbons with sp^2 planer network. In addition, the fragments should be nano-meter size, because the fragments are located on thin mesoporous-framework. Therefore, the author thinks that the carbon-fragments in oxMCSs could be treated as nanographene. In order to discuss the possibility of carbon-fragment based luminescence in oxMCSs, the author tried to synthesize graphene nano-fragments in this chapter.

As mentioned in Section 1.4, extensive researches have been performed for graphene synthesis, in recent-years. In order to prepare graphene nano-fragments, the author focused on a polycyclic aromatic hydrocarbon (PAH) based bottom-up synthesis method. Although, many PAH molecules can be considered as a candidate for graphene precursor, the author adopted pentacene ($C_{22}H_{14}$) in this study. It is because that pentacene is commercially available popular large PAH molecule, and the molecule have reactive sites at zig-zag edge. According to a previous report, by heating pentacenes under inert gas flow, a dehydrogenation condensation reaction occurs at the zigzag edge, and a mixture of a pentacene dimer (peripentacene) and trimer (trisperipentacene) can be obtained.[99] By optimizing reaction conditions, larger

graphene molecules may be obtained as shown in Figure 7-1. Therefore, the author tried to optimize the fusing conditions of pentacene to obtain currently unknown large-size graphene fragment, in this study.

7.2 Experimental and Computational Methods

7.2.1 Fusing Treatment of Pentacenes

The fusing treatments of pentacenes were performed as follows. First, 30 mg of commercially available pentacene powder (Kuroganekasei Co. Ltd., endothermic peak measured by a differential scanning calorimeter: 416 °C) was sealed in an evacuated quartz tube (< 2 Pa, inner volume ~20 cm^3). The tube was heated to the target temperature at a rate of 5 °C min^{-1} and maintained at the temperature for 10 h. The target temperature was varied at 275, 300, 310, 325, 340, 350, 375, 400, 425, 500, 600, 700, 800 and 900 °C. Here, vaporization of initial pentacene seemed to occur at around the target temperature and the fusing reaction should produce hydrogen gas. For the experiment at 325 °C, we varied initial pentacene weight (15, 30, and 100 mg) to check the effect of hydrogen gas pressure on the fusing reaction. To remove unreacted pentacene and byproducts, the samples recovered after the reactions were washed with toluene in an ultrasonic bath and filtered repeatedly until the solvent's color became clear and colorless. For convenience, the obtained insoluble products (fused pentacene, FP) were designated as FP-W-T, where W and T represent initial pentacene (**P**) weight (mg) and reaction target temperature (°C), respectively. In addition, to address the reaction mechanism, experiments using 6,13-dihydropentacene (**DHP**) mixed with initial pentacene (**P**) were also performed. In these experiments, the target temperature was fixed at 325 °C. The obtained materials were designated as PW_1-DHPW_2, where W_1 and W_2 represent initial **P** weight (mg) and initial **DHP** weight (mg), respectively.

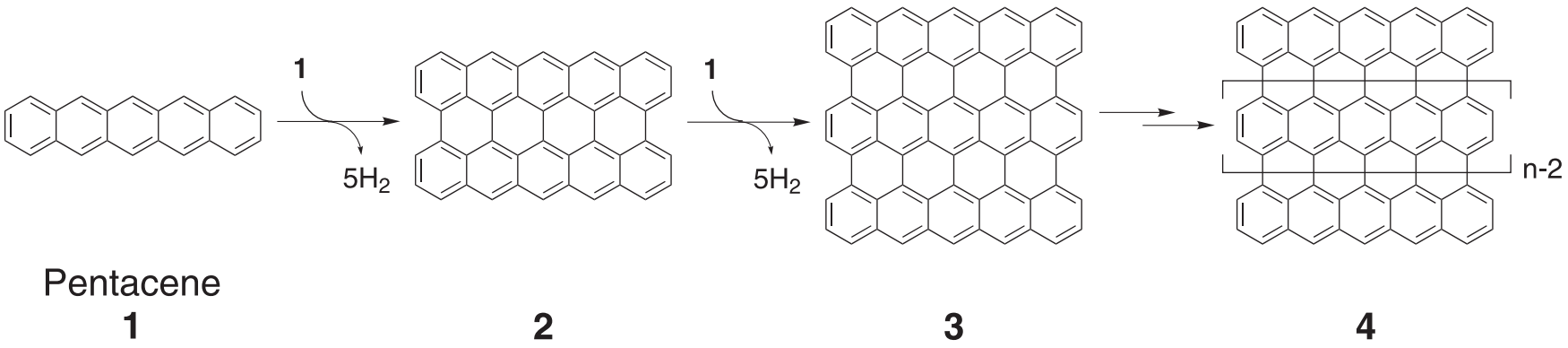

Figure 7-1 Bottom-up synthesis approach for graphene nanoribbons using pentacene as a precursor.

7.2.2 Characterization

Mass spectrum measurements of the obtained samples were conducted using a laser desorption / ionization time-of-flight (LDI-TOF) mass spectrometer (JEOL JMS-S3000) equipped with a 349-nm-wavelength UV laser as ionization source. The mass spectrometer was operated in positive-ion detection mode. The Measurements were performed without using any matrix. The m / z scales of obtained spectra were externally calibrated with the decomposition peak positions of polyethylene glycol (PEG). Metallic impurity of the initial pentacene sample was checked by elemental analysis data obtained by an energy dispersive X-ray (EDX) spectrometer equipped with a JEOL JSM-7001F scanning electron microscope (SEM). Raman scattering spectra excited by 514.5 nm Ar laser were collected using a Raman microscope system equipped with the Princeton Instrument Acton SP2300 charge-coupled device (CCD) detector. Powder X-ray diffraction (XRD) patterns of the obtained materials were collected using a Rigaku MiniFlex diffractometer using Cu Kα radiation (λ = 1.54 Å) as an incident beam. Photoluminescence spectra were obtained using JASCO FP8600 spectrometer. All measurements were performed at room-temperature.

7.2.3 Theoretical Method

To examine the electronic structure of polymerized pentacenes, first-principles calculations were performed. Structural optimizations and energy calculations of fused pentacene molecules were performed by density functional theory (DFT) calculations using Gaussian 03 software.[194] Here, we used the B3LYP exchange-correlation hybrid functional[195] with Dunning's double-zeta correlation consistent basis sets (cc-pVDZ).[196] The electronic structures of a graphene nanoribbon having infinite length and the pentacene monomer units were calculated with the ABINIT code.[197,198] Here, the Perdew–Wang 92 exchange-correlation functional[199] within the local density approximation with the projected augmented wave method[200,201] was employed for the calculation. The unit cell structure (slab

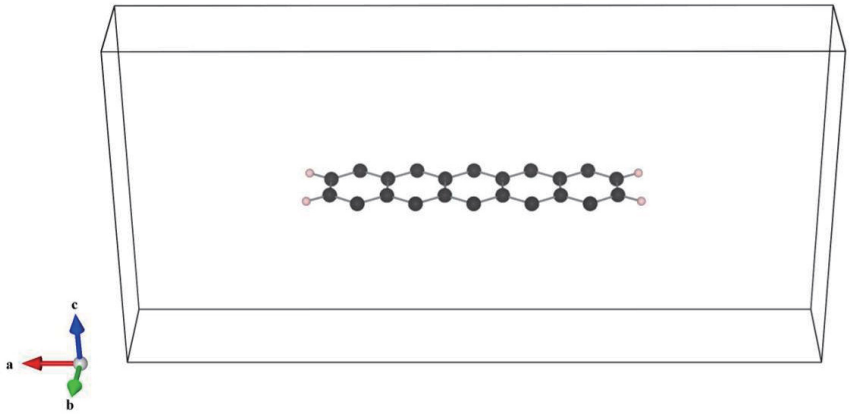

Figure 7-2 Unit cell structure of the pentacene-based GNR used for the calculation. (a = 30.0 Å, b = 4.26 Å, c = 15.0 Å, $\alpha = \beta = \gamma = 90.0°$).

model) of the graphene nanoribbon that was used for the calculation is shown in Figure 7-2. We employed a tetragonal unit cell and the direction of the nanoribbon's axis was set to b. Each nanoribbon was separated by a ~1.5 nm vacuum layer in the a- and c-axes directions to suppress the interaction between the layers. A 2 × 16 × 4 Monkhorst–Pack k-point mesh sampling was used for Brillouin zone integration. Moreover, the plane wave cutoff was set to 30 Ha (816 eV).

7.3 Results and Discussion

7.3.1 Characterization of Obtained Materials

Figure 7-3 shows the laser desorption / ionization time-of-flight (LDI-TOF) mass spectra of the obtained materials as a function of heat treatment temperature. Except in the case of 310 °C, well-separated strong peak bands (marked with down-pointing triangles in Figure 7-3) were clearly observed at around m/z = 550, 810, 1090, 1360, 1630, 1900, and 2160. These positions are in agreement with the molecular weights of polymerized pentacenes. Some readers may think that these bands originated from noncovalently bonded pentacene clusters

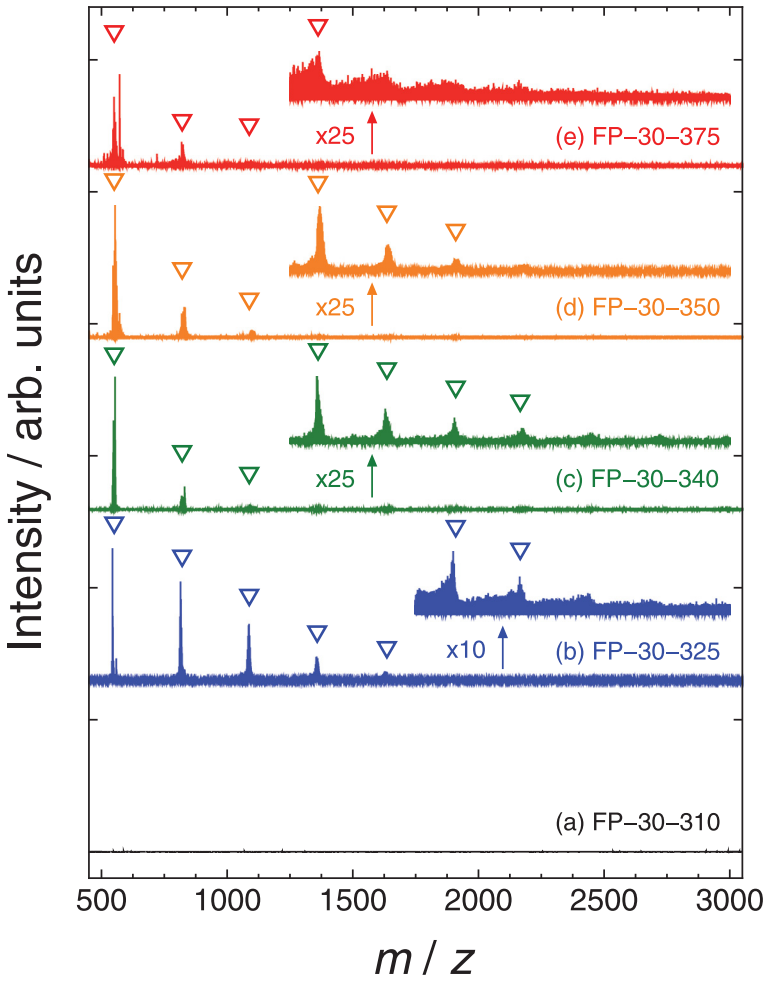

Figure 7-3 LDI-TOF mass spectra of the samples (a) FP-30-310, (b) FP-30-325, (c) FP-30-340, (d) FP-30-350, and (e) FP-30-375.

generated in the ionization process of mass spectroscopic measurements. However, this idea should be dismissed because the specific peak positions of the observed spectra (Figure 7-4) are quite different from those of the cluster ions. The observed peak positions cannot be explained without the existence of covalently bonded pentacenes.

The detailed mass spectra of each band are shown in Figure 7-4. In the case of the pentacene dimer region shown in Figure 7-4A(a), the most intense peak position ($m\,/\,z$ = 546.13) shows good agreement with the monoisotopic mass of peripentacene (**2**; $C_{44}H_{18}$; m = 546.14). Although peak intensities were not always highest in each band region, straightly grown pentacene polymers (**4**; $C_{22n}H_{4n+10}$, n = 1, 2, 3 $\cdots$) were detected at least until octamer (n = 8) in this study. This degree of polymerization was much higher than that in the previous

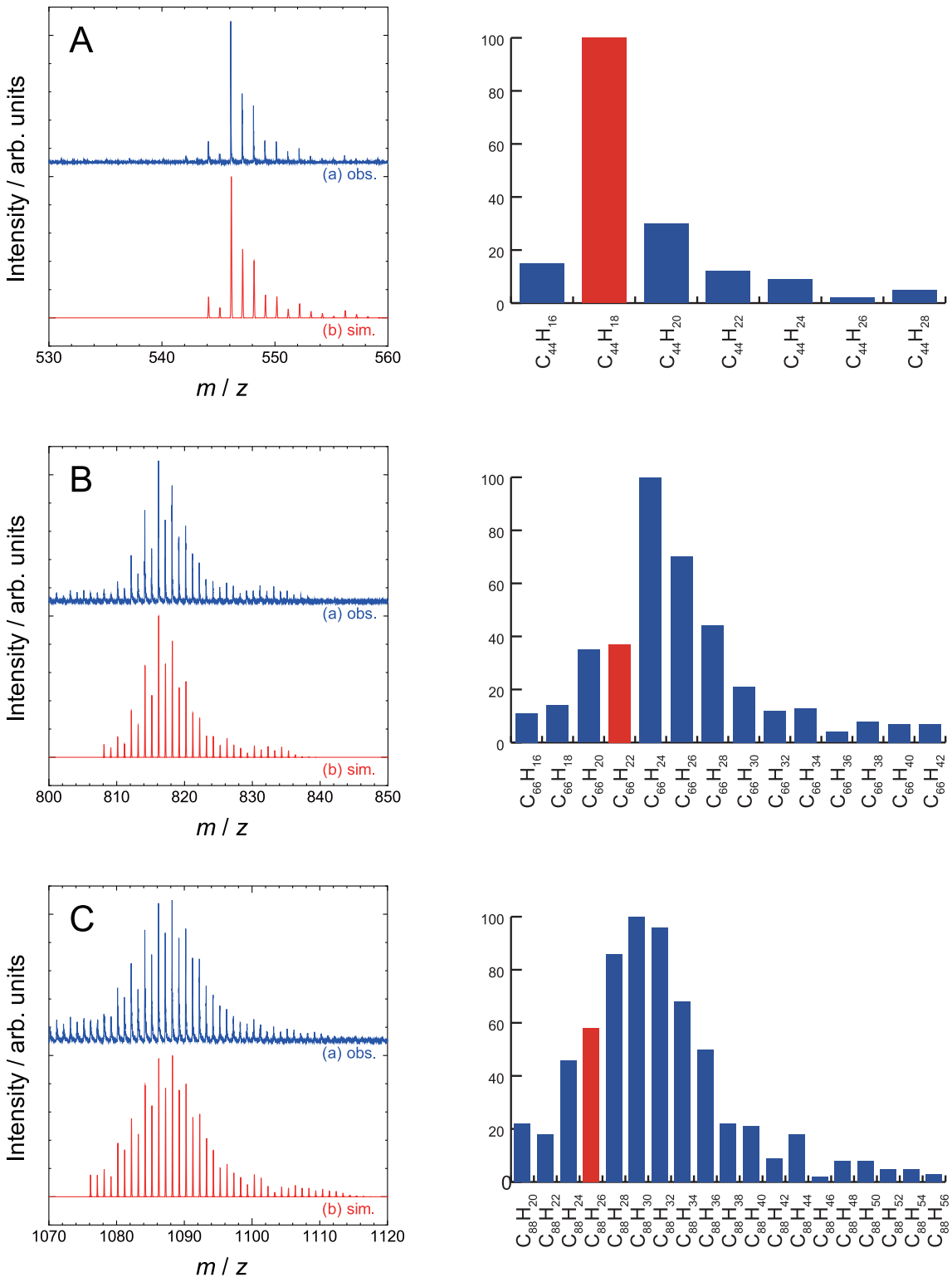

Figure 7-4 Detailed LDI-TOF mass spectra of the FP-30-325 sample in (A) dimer, (B) trimer, and (C) tetramer regions. In addition to the (a) observed spectra, (b) simulated patterns that considered isotope distribution are also shown in the graph. Molecular compositions used in the spectrum simulation are shown in the right panels.

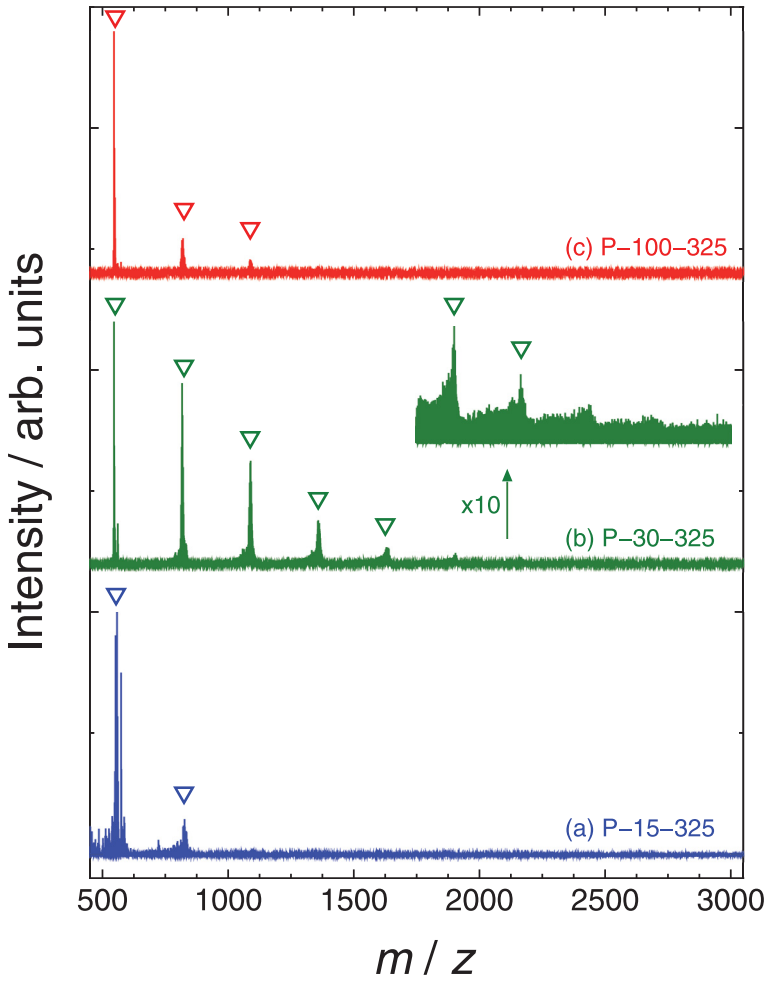

Figure 7-5 LDI-TOF mass spectra of the (a) FP-15-325, (b) FP-30-325, and (c) FP-100-325 samples.

report (n = 2, 3).[99] LDI-TOF mass spectra of the obtained materials as a function of initial pentacene weight are shown in Figure 7-5. As shown in Figures 7-3 and 7-5, the most suitable reaction temperature and initial pentacene weight for obtaining large fused products were found to be 325 °C and 30 mg, respectively, for a 20 cm^3 vacuum tube. Under these conditions, about 9 mg of the fused product was recovered after the purification process. The relation between the size of polymerized molecules and above mentioned experimental parameters (i.e. reaction temperature, and initial pentacene weight) will be discussed later in this chapter.

To characterize the structural properties of the obtained materials, Raman spectroscopy and powder X-ray diffraction (XRD) measurements were performed. In addition to the well-known G-band (in-plane carbon atom vibration mode of the graphene layer)

located at around 1600 cm^{-1}, a fused pentacene system should show unique Raman peak features due to hydrogen atom vibrations at the molecular edge. The Raman spectrum of the FP-30-325 sample is shown in Figure 7-6(a). In the spectrum, small peaks were observed at 1239, 1346, and 1460 cm^{-1} in addition to a large peak at ~1600 cm^{-1}. The positions of these small peaks agree well with those of theoretically predicted pentacene-based GNFs (see Figures 7-6(b)–(d)). A typical XRD pattern of fused pentacene (FP-30-325) is shown in Figure 7-7. We found that the XRD patterns of the fused pentacene samples were completely different from that of initial pentacene. As shown in Figure 7-7, only some broad peak features (halo pattern) were observed in the FP-30-325 sample. This result means that the fused pentacenes existed in an amorphous state. The largest halo peak was observed at $2\theta = 25.6°$. This peak probably represents the π-π stacking feature of graphene layers, and we evaluated the average layer distance as 0.348 nm. Interestingly, the estimated layer distance is considerably larger than that of the well-known graphite crystal (3.35 Å). Having a larger interlayer distance is favourable for suppressing interactions between adjacent layers.

Because of the existence of various molecules and isotope ions, the observed mass spectra were highly complicated. To evaluate the detailed molecular distributions of the mass spectra, we performed spectrum analysis that considered isotope distribution. Strictly speaking, we cannot discuss the exact quantitative distributions in the entire range of the spectra owing to differences in the ionization efficiency of molecules. However, the discussion of individual band regions should be meaningful. This is because the ionization efficiencies of molecules in the same region should be similar owing to their similar elemental composition, structure, and molecular weight. The simulation patterns were calculated as the sum of isotope patterns of various hydrocarbon molecules (C_aH_b; a, b = 1, 2, 3 $\cdots$). The peak intensities of the isotope patterns were sequentially fitted to those of the observed patterns in the order of increasing molecular weight. Here, we did not consider the existence of multivalent ions because every observed mass peak was separated at constant intervals of 1 mass unit. Here, to allow comparison with experimental spectra, the calculated patterns were broadened by a Gaussian function with 0.07 mass unit of a full width at half maximum. The simulated patterns

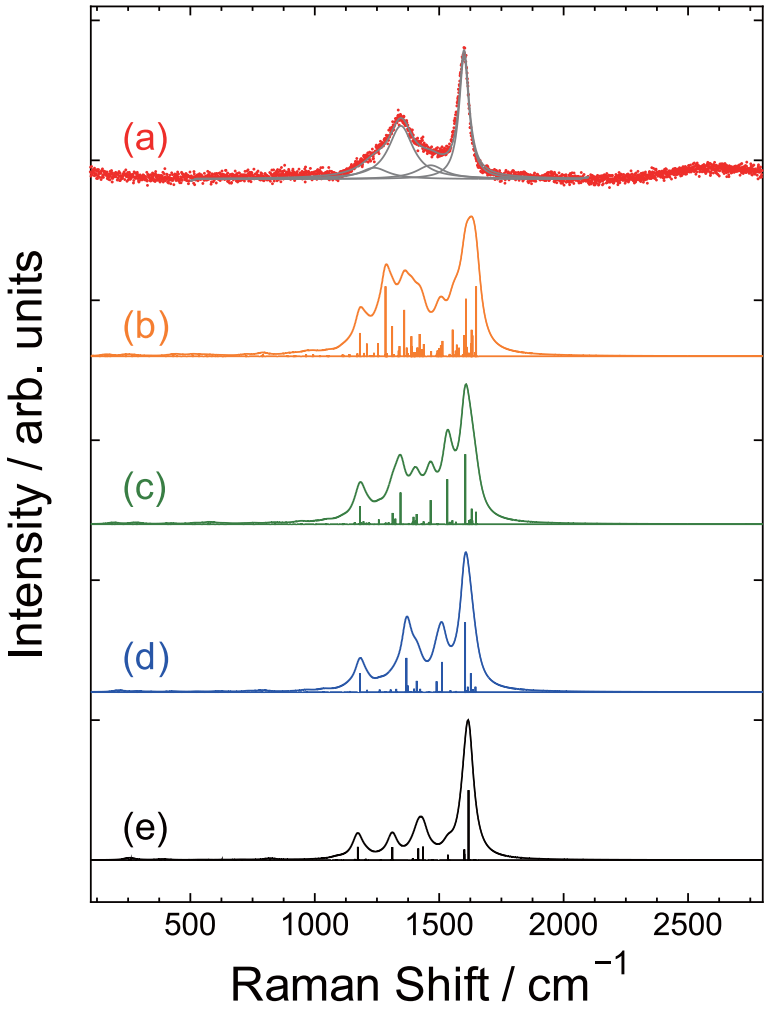

Figure 7-6 (a) Raman spectrum of the FP-30-325 sample. Simulation pattern of (b) pentacene pentamer (**4**, $n = 5$), (c) pentacene tetramer (**4**, $n = 4$), (d) pentacene trimer (**3**), and (e) pentacene dimer (**2**), that calculated by DFT B3LYP / cc-pVDZ method, are also shown in the figure.

of each region are shown in Figure 7-4(b). It can be seen that the simulated patterns reproduced the observed spectra well only by assuming $C_{22n}H_{14n-2x}$ ($x = 0, 1, 2, 3\cdots$) type molecules. This result indicates that pentacene (**1**; $C_{22}H_{14}$) molecules were polymerized with a stepwise elimination reaction of H_2 molecules.

As mentioned before, straightly grown products (**4**) are expressed as $C_{22n}H_{4n+10}$. Other observed peaks having a larger number of hydrogen atoms ($C_{22n}H_{4n+12}$, $C_{22n}H_{4n+14}$, $C_{22n}H_{4n+16}\cdots$) can be explained by the relative positioning of the two pentacene units (i.e.,

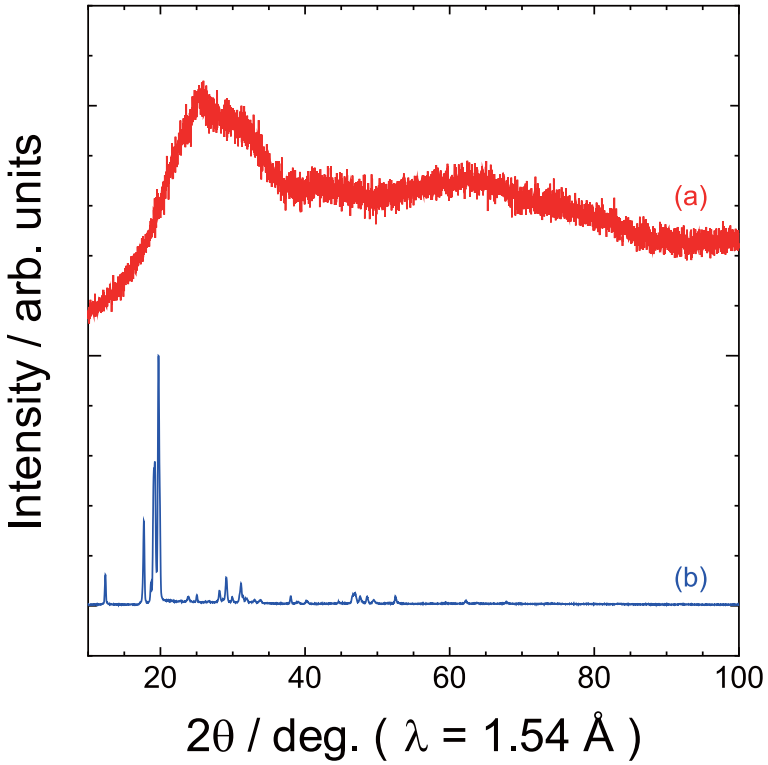

Figure 7-7 XRD pattern of the (a) FP-30-325 and (b) initial pentacene. Cu Kα radiation (λ = 1.54 Å) was used as an incident beam.

shift) and/or unconnected sites as in structures **5**, **6**, and **7** shown in Figure 7-8. In addition, molecules having smaller number of hydrogen atoms than that of the straightly grown products (**4**), such as $C_{22n}H_{4n+8}$, and $C_{22n}H_{4n+6}$, were also detected in this study. These hydrogen-poor molecules were not mentioned in the previous reports, but the structure of these molecules might be explained by the five-member ring structure included at shifted sites such as **8**. By introducing the five-member ring, steric repulsions between hydrogen atoms placed at the shifted sites (marked with circles in Figure 7-9) should be weakened.

7.3.2 Electronic Structure of Fused Pentacenes

Regarding the size of the conjugated carbon system, the width of a pentacene monomer unit is about 1.2 nm. On the other hand, the length of a fused pentacene is expressed as 0.43n (nm). Therefore, the obtained materials are considered to be nanosize graphene fragments. Here, note that such small-width GNRs or GNFs cannot be prepared by well-known top-down

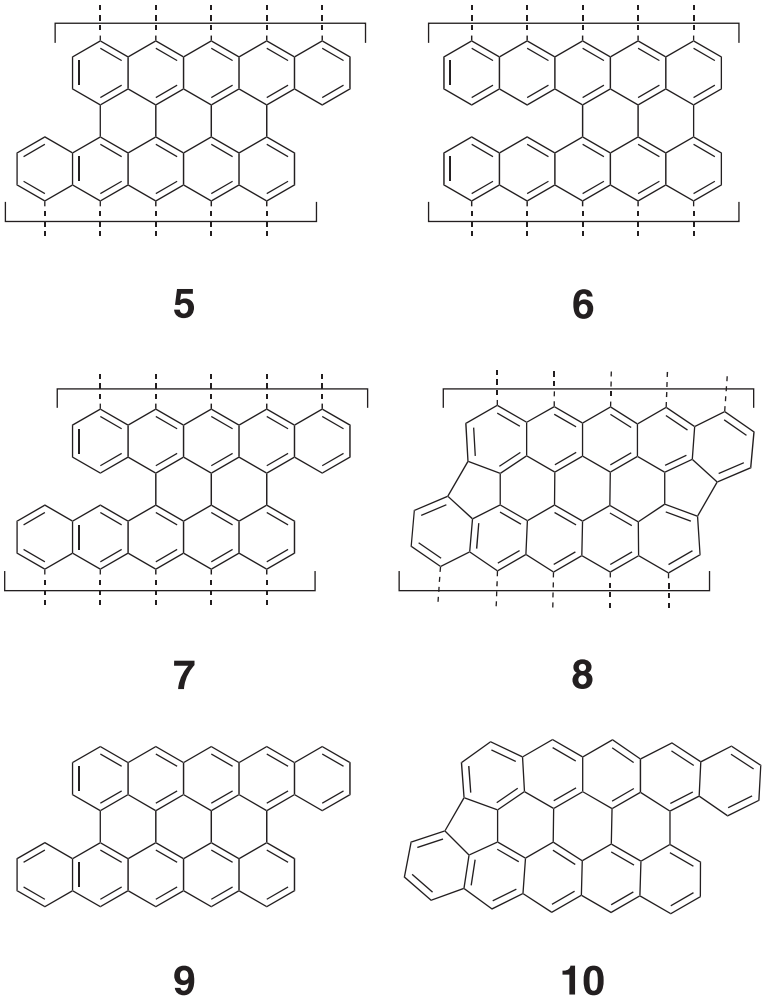

Figure 7-8 Possible structure of byproducts included in the obtained materials.

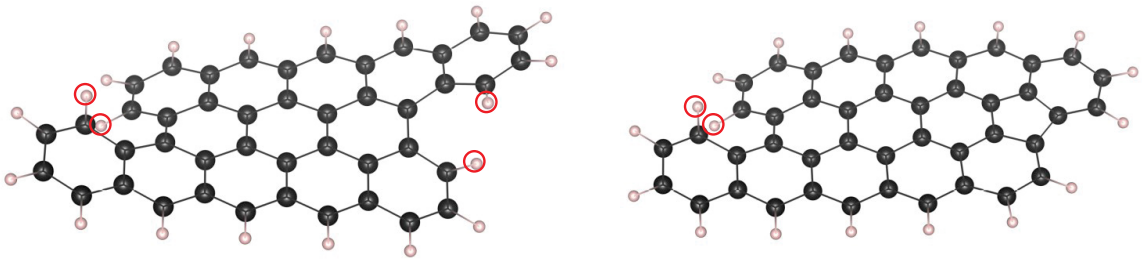

Figure 7-9 Three-dimensional molecular structure of $C_{44}H_{20}$ (**9**, left) and $C_{44}H_{18}$ (**10**, right). Steric repulsions between hydrogen atoms placed at the shifted site were marked with circles.

techniques such as electron beam lithography.[202] Such small-size molecules should show unique electronic and magnetic structures due to the so-called quantum confinement or edge effect.[89–93]

To understand the electronic and magnetic structures of the fused pentacene system, we performed theoretical calculations. The electronic densities of states (DOSs) and spin densities of the straightly grown fused pentacenes (**4**; n = 1, 2, 3, 4, and 5) are summarized in Figure 7-10. As is well known, the electronic structure of bulk graphene is described as a zero-gap semiconductor (semi-metal); the unique electronic structure of graphene is represented by so-called Dirac cones, and its valence and conduction bands are crossed at the Fermi level (E_F).[203] Therefore, the DOSs of bulk graphene sheets linearly increase with distance from E_F. As can be seen in Figure 7-10, the DOSs of the fused pentacene system (n > 2) were symmetrically dispersed from E_F just like the above-mentioned graphene's DOS feature (see dashed red lines in Figure 7-10(e)). However, the fused pentacenes have an additional DOS feature that can be observed in bulk graphene; some discrete energy levels (marked with red arrows in Figure 7-10(e)) just like the van Hove singularities in SWCNTs are also observed in the fused pentacene system. Interestingly, the positions of the discrete energy levels were almost independent of the polymerized length (n) of pentacenes (see Figure 7-10). These discrete energy levels were maintained even in the pentacene-based GNR having infinite length (see Figure 7-11). From the DFT calculation of the fused oligomers, we found that the fused pentacene molecules have some band gap. For example, the HOMO-LUMO gap of the pentakisperipentacene (**4**; n = 5) was estimated to be 1.45 eV. Having such a band gap feature is a great advantage for semiconductor applications. Because the band gap of an ideal graphene sheet is zero, logic devices composed of ideal large-area graphene cannot be switched off; therefore, bulk graphene sheets are unsuitable for such applications.[204, 205] Furthermore, because the obtained fused molecules were of nanoscale, the molecules may be used for extremely small-size electronic circuit systems. Thus, fused pentacenes should be promising candidates for next-generation nanoelectronic materials.

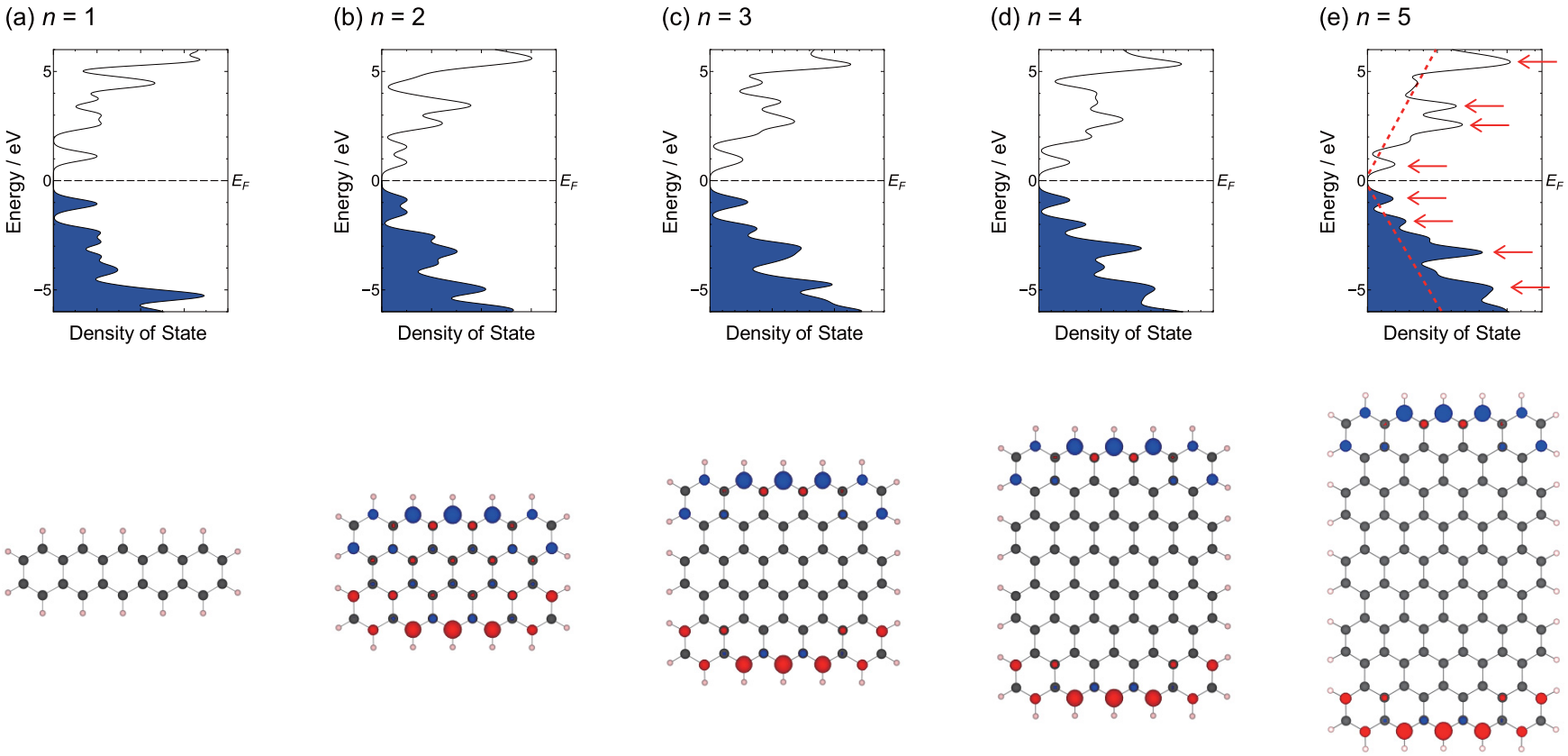

Figure 7-10 Electronic density of states plots (DOS, upper) and graphical representation of net spin densities (lower) of (a) pentacene, (b) peripentacene, (c) trisperipentacene, (d) tetrakisperipentacene, and (e) pentakisperipentacene calculated by the spin-unrestricted B3LYP/cc-pVDZ method. The DOS plots were obtained as the sum of Gaussian functions centered at molecular orbital energies with a full width at half maximum of 0.5 eV. In these figures, the positions of Fermi energies (E_F) are set as 0 eV and valence levels are filled with blue. In the spin density plots, red and blue regions represent excess α-spin density and excess β-spin density, respectively.

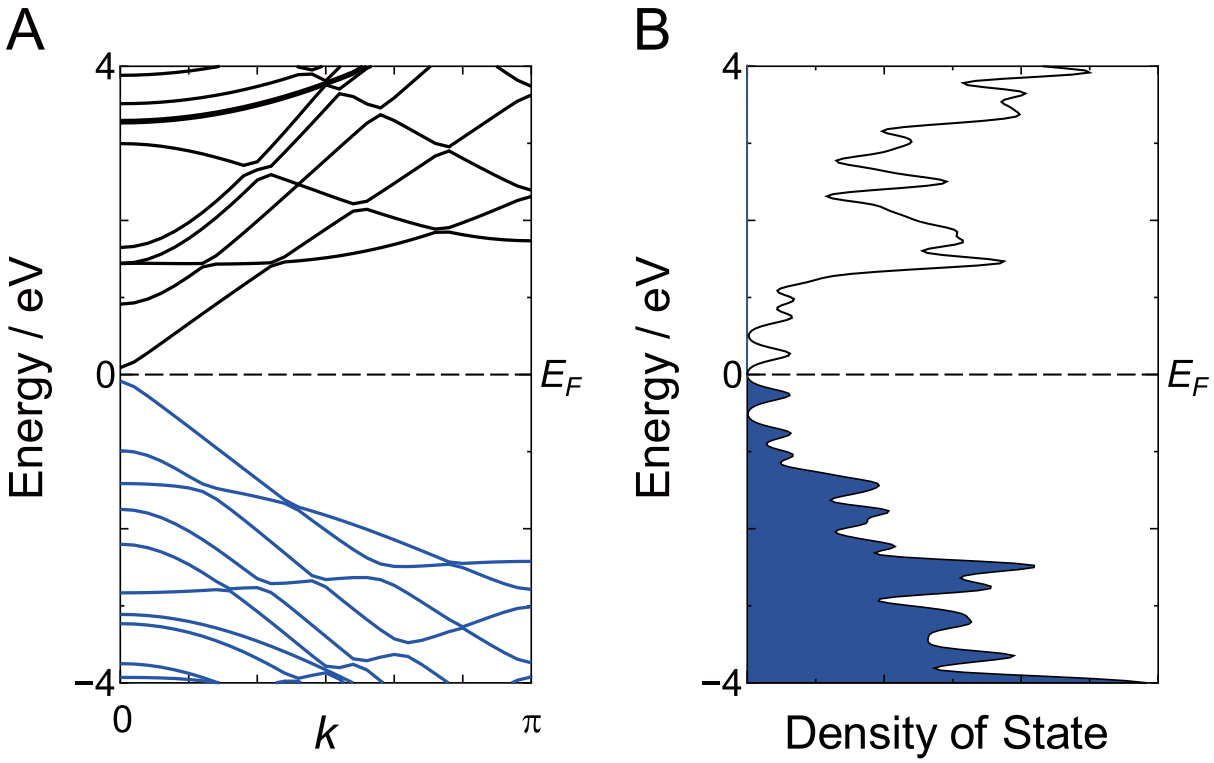

Figure 7-11 Calculated band structure (A) and DOS (B) of the pentacene-based GNR. In the DOS plot, the positions of Fermi energies (E_F) were set as 0 eV, and valence levels were filled with blue.

The fused pentacenes ($n > 2$) also seem to have unique magnetic properties. Although the net electronic structures of the fused pentacenes have been described as a singlet, their α- and β-spin densities were asymmetrically located at two opposing zigzag edges (see Figure 7-10). Similar asymmetrical spin features have been theoretically predicted for GNRs and SWCNTs having a zigzag edge structure,[89–91,93,206] but such a unique feature was not observed in the initial pentacene precursor ($n = 1$). Interestingly, the unique spin feature also seems to exist in other GNFs having acene monomer units larger than anthracene (see Figure 7-12). Such a localized spin feature should be favourable for magnetic applications. The obtained fused pentacenes may be used as a model material for studying the electromagnetic properties of spin-localized GNFs.

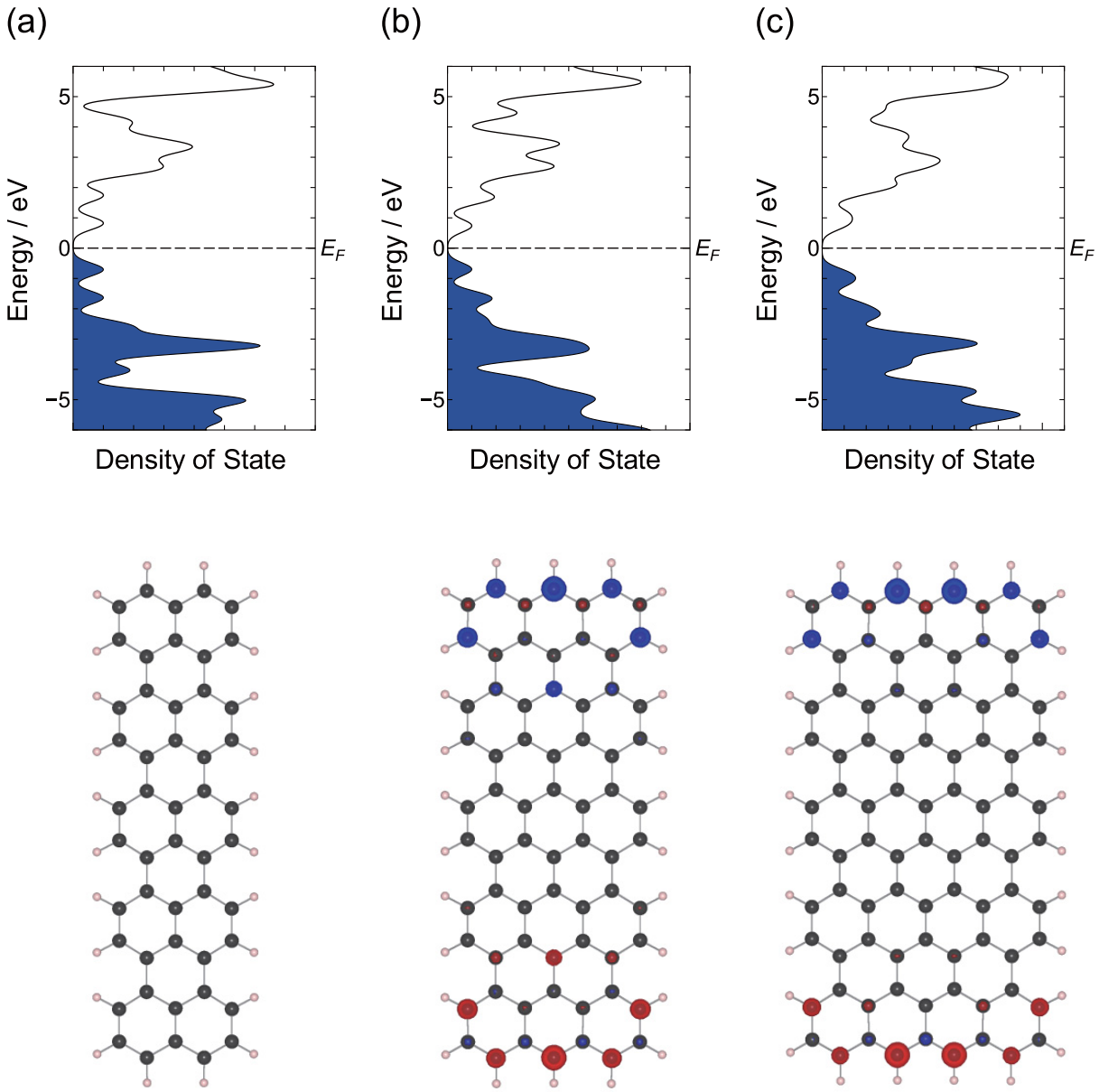

Figure 7-12 Electronic density of states plots (DOS, upper) and graphical representation of net spin-densities (lower) of (a) naphthalene pentamer, (b) anthracene pentamer, and (c) tetracene pentamer calculated by spin-unrestricted B3LYP/cc-pVDZ method. The DOS plots were obtained as the sum of Gaussian functions centered at molecular orbital energies with a full-width at half-maximum of 0.5 eV. In these figures, the positions of Fermi energies (E_F) were set as 0 eV, and valence levels were filled with blue. In the spin-density plots, red and blue regions represent excess α-spin density and excess β-spin density, respectively.

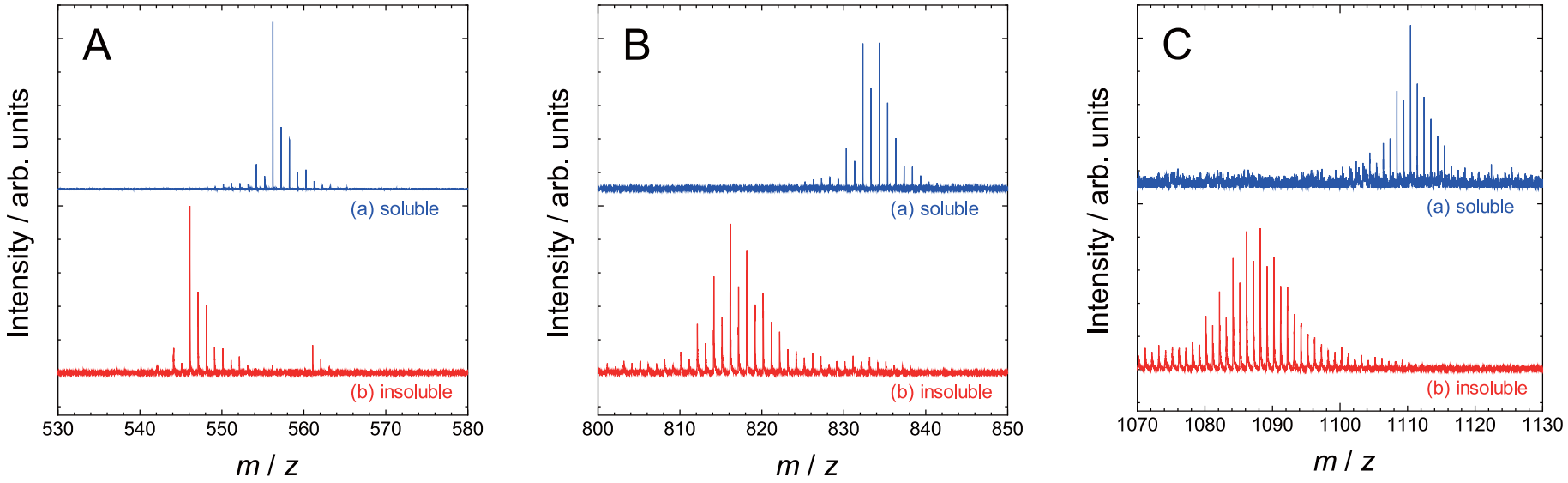

Figure 7-13 LDI-TOF mass spectra of the FP-30-325 sample. The soluble components that were removed in the purification process (a) and the purified component that was insoluble in toluene (b) are compared. Magnified views of the dimer (n = 2), trimer (n = 3), and tetramer (n = 4) regions are separately shown in A, B, and C, respectively.

7.3.3 Photoluminescence Properties

As shown in Figures 7-14–7-17, fused pentacenes showed intense visible photoluminescence, under 600 °C treatment. The luminescent color was changed blue to yellow; depend on the fusing-temperature. This results means that graphene-nanofragments have a potential as a photoluminescence center, and their luminescence wavelength are changed with their structure and size of fragments. The observed luminescence phenomenon may reflect the unique electronic structure of fused pentacene molecules. In the meantime, FP samples processed above 700 °C treatment, did not show any visible-luminescence. This is probably due to excess polymerization (graphitization). As is well known, bulk graphene or graphite do not show such photoluminescence phenomena because of its simple semi-metallic energy structure. On the other hand, fused pentacenes are expected to have some band gap and discrete energy levels probably caused by the quantum-size or edge effect as discussed in Section 7.3.2. The unique energy structure of the fused pentacene system might work as a luminescent center. However, in order to discuss more detailed relationship between structure of nano-fragments and photoluminescence properties, more advanced separation and purification process should be required for the fragments in the next step.

7.3.4 Polymerization Mechanism

In Sections 7.3.1 and 7.3.2, the author have focused on purified samples (i.e., fused components that are insoluble in toluene). Let us broaden our scope to soluble byproducts that were removed in the purification process. A typical LDI-TOF mass spectrum of a soluble component recovered in the purification process is shown in Figure 7-13. As shown in the figure, the molecules in the soluble component have greater molecular weight than those in the insoluble component. Through a detailed spectrum analysis, we found that this difference in molecular weight is explained by the different number of hydrogen atoms in the structures; although the number of carbon atoms in each component was the same, the molecules in the soluble

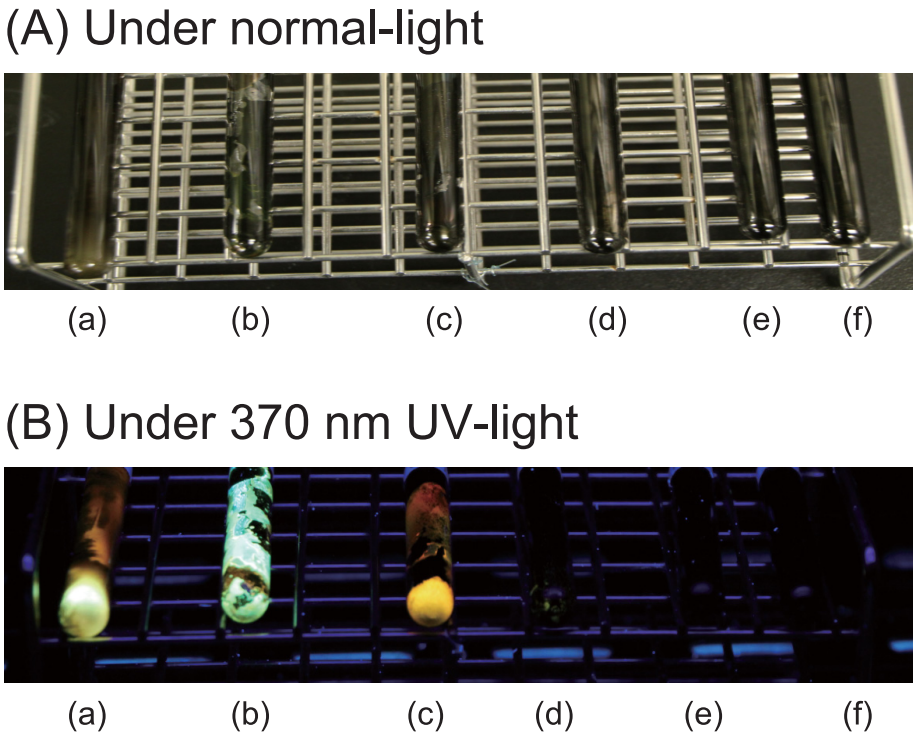

Figure 7-14 Photographs of (a) FP-30-400, (b) FP-30-500, (c) FP-30-600, (d) FP-30-700, (e) FP-30-800, and (f) FP-30-900 samples before purification (washing with toluene) process. (A) Under normal-light. (B) Under 370 nm UV-light excitation.

component contained more hydrogen atoms than the insoluble component. As clearly shown in Figure 7-13, such hydrogen-rich molecules were well removed in the purification process. We found that except for toluene, the hydrogen-rich molecules showed higher solubility in commonly used organic solvents (such as cyclohexane and tetrahydrofuran) compared with the hydrogen-poor products. This is probably owing to the electric dipole moments of the hydrogen-rich molecules originating from the intricate three-dimensional structure in contrast to the planer structure of well-dehydrogenated graphene-like fragments. Toluene liquids containing hydrogen-rich molecules (soluble components removed in the purification process) were yellow or red; on the other hand, the recovered hydrogen-poor insoluble components (purified FPs) were black. These results indicate that conjugated carbon systems of the hydrogen-rich molecules were not well developed in contrast to the hydrogen-poor molecules. Note that as far as we tested, the hydrogen-poor molecules (purified FPs) did not dissolve in any solvent except 1-methyl-2-pyrrolidinone (NMP).

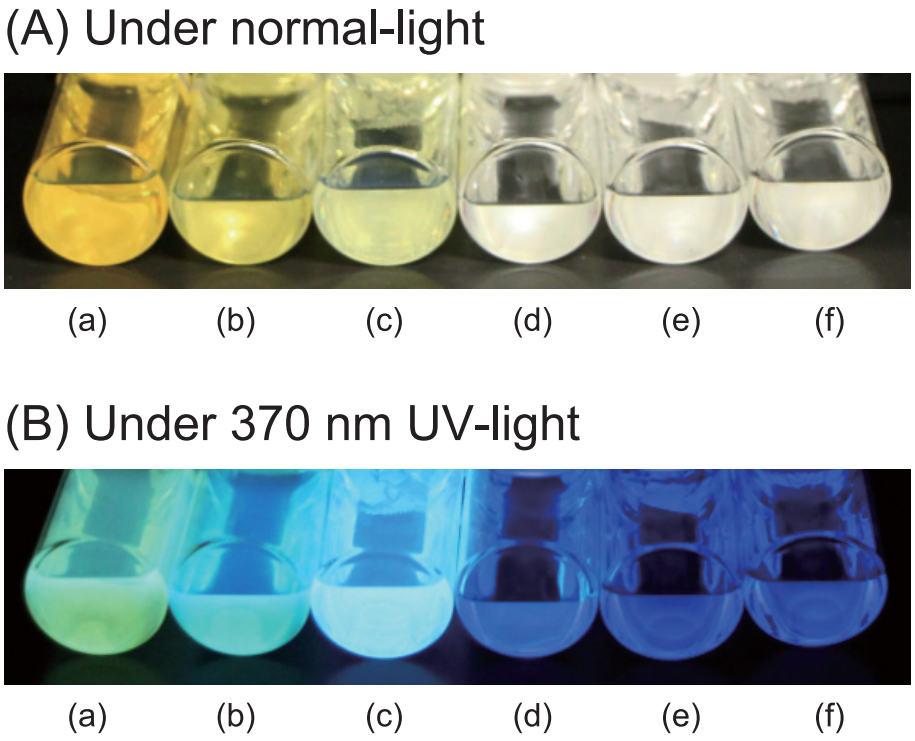

Figure 7-15 Photographs of filtrates recovered at purification (washing with toluene) process of (a) FP-30-400, (b) FP-30-500, (c) FP-30-600, (d) FP-30-700, (e) FP-30-800, (f) FP-30-900. (A) Under normal-light. (B) Under 370 nm UV-light excitation.

Although the hydrogen-rich molecules observed in the soluble components are undesirable byproducts for the synthesis of nanosize graphene-like molecules, we can acquire useful information about the reaction mechanism from these molecules. Here, we would like to address the fusing mechanism of pentacene molecules. In a previous report, Northrop *et al.* discussed the formation mechanism of peripentacene (**2**) from a theoretical point of view.[207] However, to the best of our knowledge, no experimental verification was performed after Northrop's report. Therefore, we attempt to discuss it here on the basis of mass spectroscopic analysis.

In the LDI-TOF mass spectra of the soluble components (Figure 7-13), some molecules having hydrogen atoms larger than $14n$ at the n'th-mer region (such as $C_{22n}H_{14n}$, $C_{22n}H_{14n+2}$, and $C_{22n}H_{14n+4}$) were observed. These hydrogen-rich molecules cannot be explained by the fused products generated only by the dehydrogenation reactions. This is because such dehydrogenated products should be expressed as $C_{22n}H_{14n-2x}$, where

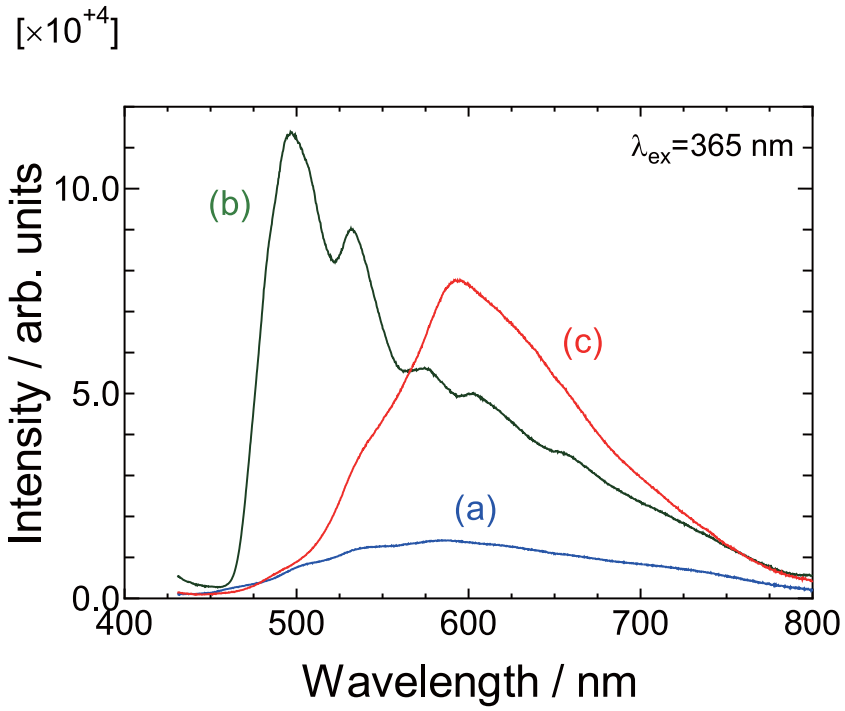

Figure 7-16 Room temperature photoluminescence emission spectra of (a) FP-30-400, (b) FP-30-500, and (c) FP-30-600. The spectra were obtained using a PL microscope system equipped with 365 nm laser diode.

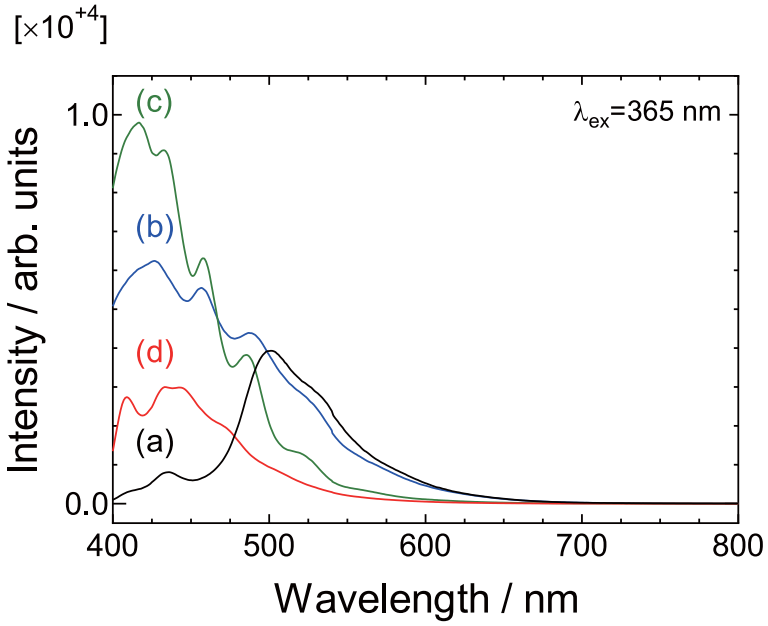

Figure 7-17 Room temperature photoluminescence emission spectra of filtrates recovered at purification (washing with toluene) process of (a) FP-30-325, (b) FP-30-400, (c) FP-30-500, (d) FP-30-600.

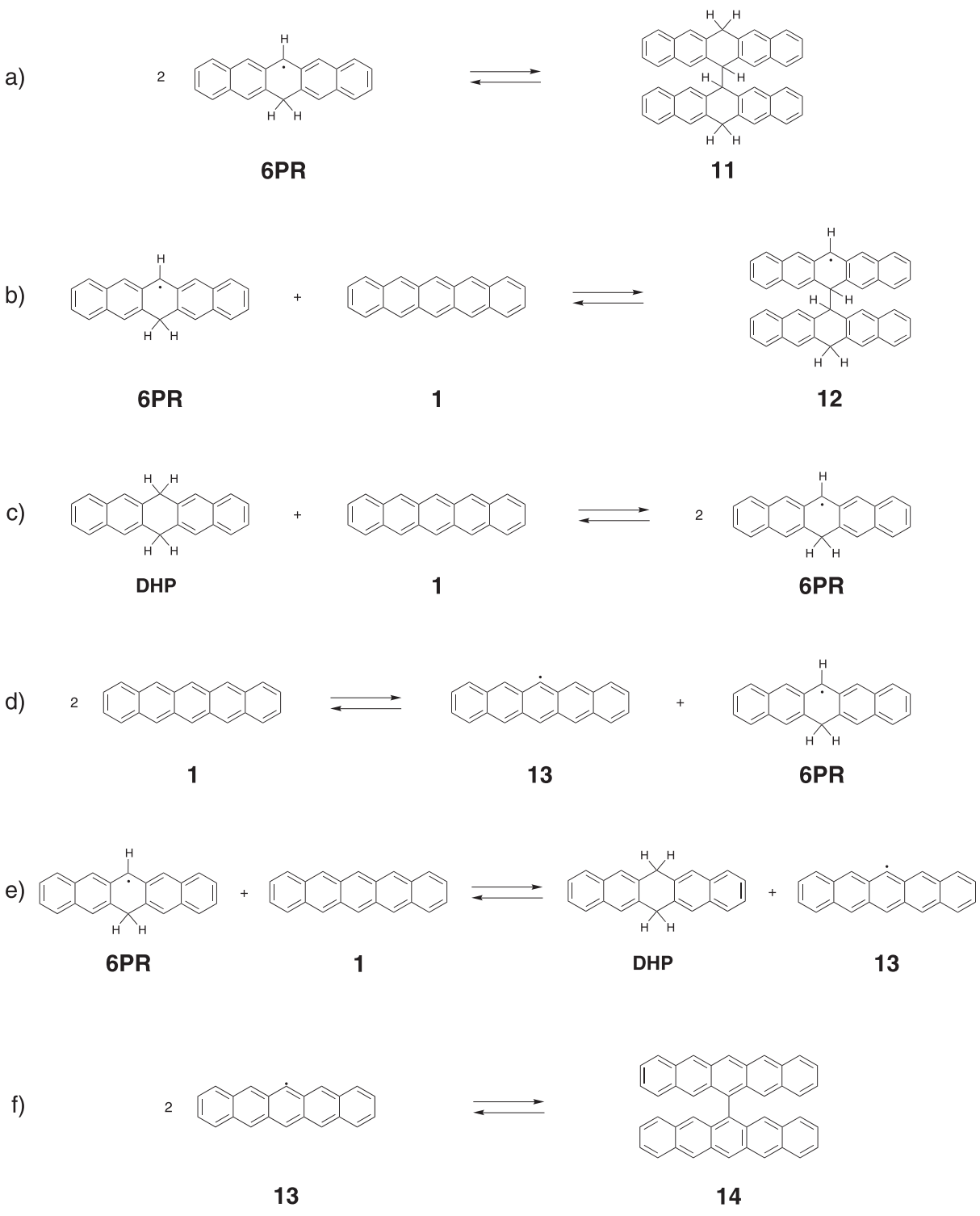

Figure 7-18 Possible dimerization process of pentacene and related molecules.

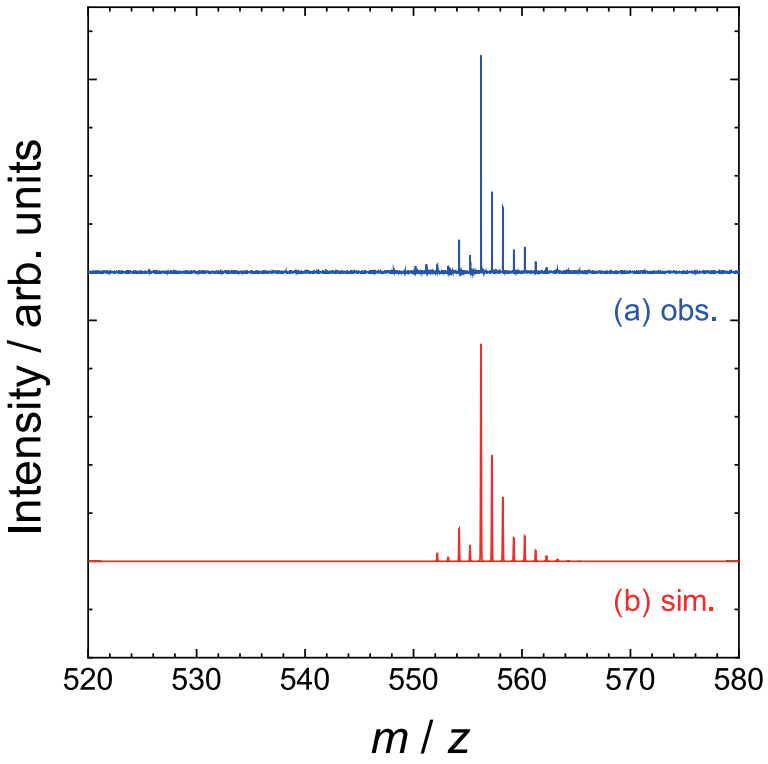

Figure 7-19 Magnified view of (a) observed and (b) simulated LDI-TOF mass spectra of soluble component of the FP-30-325 sample. In the spectrum simulation, the molecular composition was set to $C_{44}H_{24} : C_{44}H_{26} : C_{44}H_{28} : C_{44}H_{30} : C_{44}H_{32} : C_{44}H_{34}$ = 4 : 15 : 100 : 19 : 10 : 1.

x is the number of sublimated hydrogen molecules. This means that some types of hydrogen-atom-addition or hydrogen-atom-transfer reactions also occurred in the reaction tubes. According to the previous report, these hydrogen-rich molecules seem to be attributed to the reaction intermediates produced within the fusion process. In the reaction pathway proposed by Northrop *et al.*, the 6-hydropentacenyl radical ($C_{22}H_{15}^{\cdot}$; **6PR**) was treated as a requisite intermediate.[207] They claimed that once **6PR** was generated, $C_{44}H_{30}$ (**11**) and the radical $C_{44}H_{29}^{\cdot}$ (**12**) were easily produced by the dimerization reaction of **6PR**s (Figure 7-18(a)) and the addition reaction of **6PR** and **1** (Figure 7-18(b)), respectively. Then, **11** and **12** are gradually converted to a peripentacene (**2**) through a dehydrogenation process. Based on this mechanism, the peak observed at m / z = 558.24 in Figure 7-13 seems to be attributed to **11** (m = 558.23). Except for $C_{44}H_{30}$ (**11**), the existence of $C_{44}H_{24}$, $C_{44}H_{26}$,

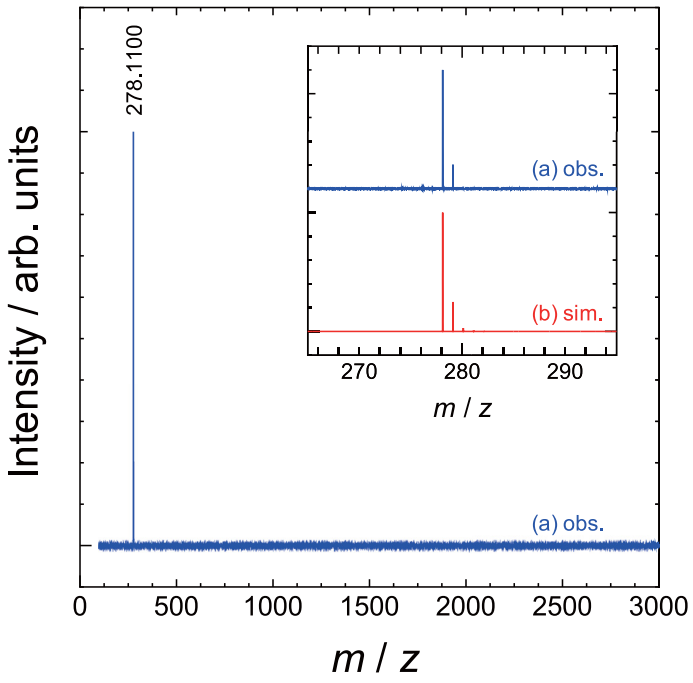

Figure 7-20 LDI-TOF mass spectrum of pentacene sample that used for the fusing reaction. The observed spectrum (a) was completely-consistent with the simulated isotope pattern of $C_{22}H_{14}$ (b).

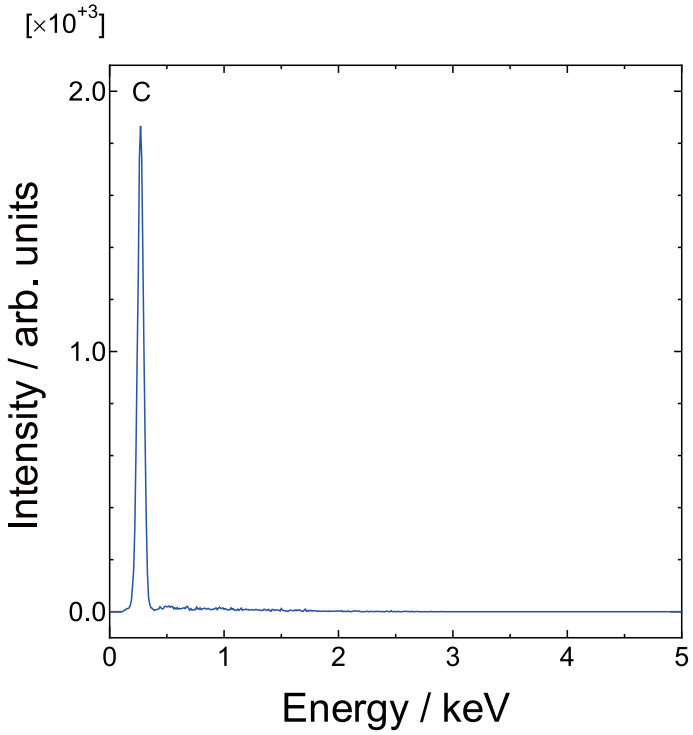

Figure 7-21 EDX spectrum of the pentacene sample that used for the fusing reaction.

$C_{44}H_{28}$, $C_{44}H_{32}$, and $C_{44}H_{34}$ was also confirmed in the soluble component (Figure 7-19). The observed $C_{44}H_{24}$, $C_{44}H_{26}$, and $C_{44}H_{28}$ molecule can be explained by dehydrogenated product **11**. The other molecules were not fully discussed in the previous report, but we think that the molecules can also be explained by the additional hydrogen-atom addition / transfer reaction of **11** and **12**. Because the radical species generated in the dimerization process (such as **12**, **6PR**, and **13**) are expected to have high reactivity, various types of side reactions (e.g., hydrogen-atom abstraction, hydrogen-atom transfer) are conceivable.

An important issue is the origin of **6PR**. Although the de-tailed reaction pathway was somewhat different from that in Northrop's report, the formation of **6PR** was also predicted in the Roberson's report.[99] In both reports, the assumption was that **6PR** was generated from the radical-type hydrogen-atom transfer from **DHP** to pentacene (**1**) at the initial reaction step (Figure 7-18(c)).[99,207] Here, **DHP** was treated as a trace amount of impurity that is often contained in commercially available pentacenes. However, we found that the precursor used in this study did not contain any **DHP** impurity (see Figure 7-20). In addition, **DHP** (m = 280.13) was not observed in treatment below 325 °C as shown in Figure 7-22. This indicates that the initial polymerization reaction should occur without a **DHP** molecule. Because the initial pentacene sample used in this study did not contain any organic and metallic impurity (see Figures 7-20 and 7-21), we believe that a disproportional reaction of two pentacene molecules (Figure 7-18(d)) should have occurred without a catalyst at the first step. Even through a scheme shown in Figure 7-18(d), **6PR** can be produced from the reaction route of **DHP** and pentacene (Figure 7-18(c)). In addition, by considering a scheme shown in Figure 7-18(d), additional simple dimerization routes, such as Figure 7-18(f), can also be considered in addition to previously discussed schemes shown in Figures 7-18(a) and 7-18(c). The reaction root shown in Figure 7-18(d) is probably high-energy unfavourable process compared to the reaction shown in Figure 7-18(c). However, once **6PR** is generated through a scheme shown in Figure 7-18(d), **DHP** can be produced from **6PR** through a backward reaction shown in Figure 7-18(c) and a hydrogen-atom abstraction reaction shown in Figure 7-18(e). Thus, the difference between schemes shown in Figures 7-18(c) and 7-18(d) becomes unclear after initial radical formation.

To check the role of the **DHP** molecule more actively, experiments using **DHP** mixed with the initial pentacene precursor were performed. The obtained LDI-TOF mass spectra are summarized in Figure 7-23. As shown in the figure, the addition of **DHP** molecules did not promote fusing reactions. This result also supports our initial **DHP**-free reaction mechanism.

As mentioned above, the electronic structure of fused pentacene molecules is almost independent of the polymerization degree (see Figure 7-10). Because reactive zigzag edge structures remain even through fusing reactions, additional fusion can occur. Therefore, the formation mechanism of large fused pentacenes (trimer, tetramer, pentamer$\cdots$) might also be explained by the further addition reaction of radical-activated pentacene (**6PR**, **13**) molecules.

Finally, we would like to discuss the suitable reaction conditions for obtaining large fused pentacenes based on the above-mentioned reaction mechanism. We investigated the effect of reaction temperature and initial precursor weight in this study. As a result, the lowest reaction temperature (T_{low}) required for the fusing reaction was found to be 310 °C $< T_{\mathrm{low}} <$ 325 °C. Above 325 °C, the relative abundances of highly polymerized products gradually decreased with increasing reaction temperature (see Figure 7-3). In addition, we found that the molecular distributions of fused products broadened with increasing reaction temperature (see Figure 7-22). These results probably came from the low selectivity of the fusing reaction. The regioselectivity of the pentacene dimerization process was discussed in the previous theoretical study.[207] Although formation of straightly grown pentacene (such as **2**) is energetically the most preferable process compared with shifted ones (such as **9**), the energy difference does not seem to be very large in some cases. Because the fusing reaction of pentacenes can be explained by radical reactions via unstable intermediates such as **6PR** and **13**, various types of side reactions can be considered and the final byproducts became ignorable especially at high temperature conditions. The observed large distribution of fused molecules at high temperature might have occurred because the emergence of side-reaction pathways and byproducts is unfavourable for obtaining large fused pentacenes. This is because the relative formation probability of valid fused products should be decreased in a statistical sense. Moreover, initial precursor weight also affected the efficiency of the fusing reaction. As

far as we tested, the most suitable initial pentacene weight was found to be about 30 mg for a 20 cm^3 quartz tube (see Figure 7-5). We think that this result can be explained by the inner gas pressure of the reaction tube. As the important intermediates for the fusing reaction (such as **6PR** and **13**) are generated by gas-phase bimolecular reactions, as shown in Figure 7-18(d), a certain amount of vapour pressure in initial pentacene is required for bimolecular collision. In this sense, a larger amount of initial pentacene is more suitable for promoting the fusing reaction. On the other hand, excess gas pressure accompanied by an excessive amount of initial pentacene in the reaction tube is also unfavourable because hydrogen-gas eliminations accompanied by the fusing reactions should be suppressed. Based on the balance of these conflicting factors, the optimal precursor value seemed to be 30 mg.

7.4 Summary

We investigated the synthesis condition and products of a polymerized pentacene system. By optimizing the fusing condition, we have successfully obtained large fused pentacene molecules up to at least octamer ($n = 8$). First-principles calculations revealed that the fused pentacenes have a unique electronic structure that does not exist in bulk graphene samples. The obtained materials show strong visible luminescence in blue to yellow region under 365 nm UV-light exposure. To evaluate the reaction mechanism, detailed mass spectroscopical analysis was performed. The fusing mechanism of pentacene molecules seems to be explained by a complex radical reaction pathway via the **6PR** intermediate as mentioned in previous studies. However, our perspective of the **6PR** formation scheme was somewhat different from the previous report; we think that **6PR** was formed without the **DHP** impurity at the initial step.

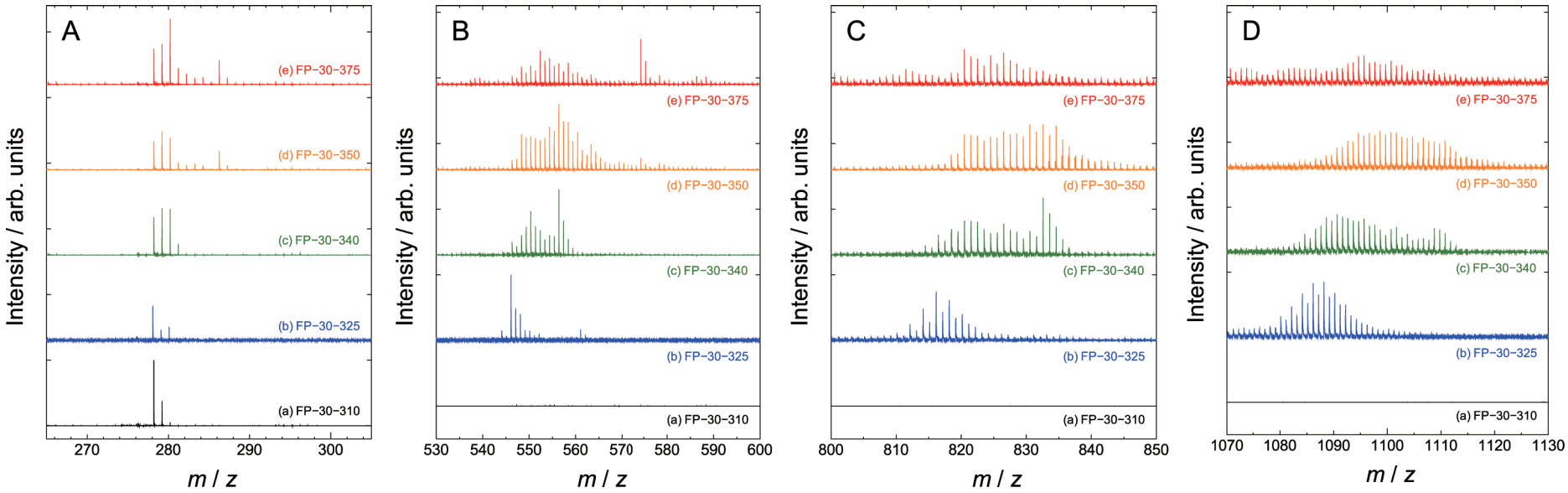

Figure 7-22 Detailed LDI-TOF mass spectra (magnified view of Figure 7-3) of the (a) FP-30-310, (b) FP-30-325, (c) FP-30-340, (d) FP-30-350, and (e) FP-30-375 samples. The pentacene monomer (n = 1), dimer (n = 2), trimer (n = 3), and tetramer (n = 4) regions are separately shown in A, B, C, and D, respectively.

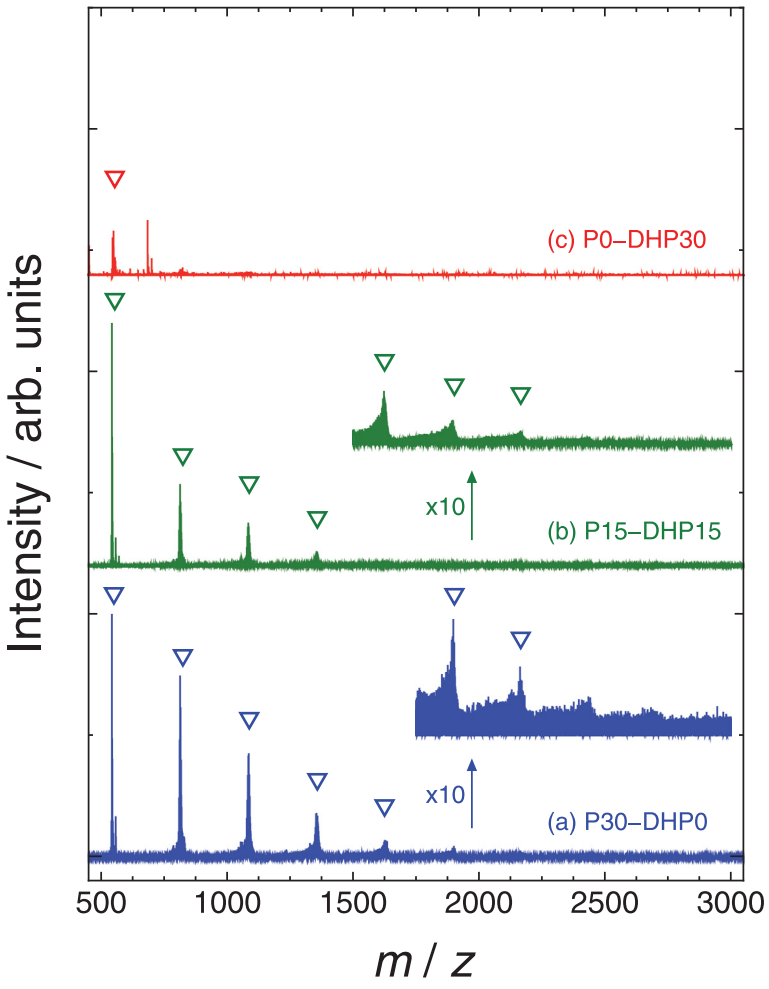

Figure 7-23 LDI-TOF mass spectra of the (a) P30-DHP0, (b) P15-DHP15, and (c) P0-DHP30 samples.

Chapter 8

Conclusion and Perspectives

In this dissertation, a novel XRD-based structural characterization method was proposed for ordered mesoporous materials. Furthermore electrochemical energy storage and photo-energy conversion properties of mesoporous carbons (MCs), mesoporous carbon–TiO_2 composites (MCTs), and mesoporous carbon–SiO_2 composites (MCSs) were investigated.

The XRD-based structural characterization method developed in the present study was described in Chapter 2. The structure factor, which is required for calculate the intensity of diffraction peaks, was analytically deduced. The theoretically calculated XRD profiles were in good agreement with real mesoporous materials. In addition to the previously determined structural symmetry and pore-to-pore distance (i.e. unit-cell constant a), mesopore-diameter and density of frame-work structure can also be determined by using this method. In this study, it was demonstrated that the XRD analysis can be performed even for samples immersed in water. The author believe that this XRD-based method has great potential for *in situ* experiments that cannot be performed by electron microscopy or gas-adsorption methods, because the XRD method does not require any special measurement environments or pretreatments. Therefore, the author expect that the XRD analysis proposed in this study would be used to reveal poorly understood structural properties of mesoporous materials in various environments (such as high pressures and high temperatures) in the near future.

By analyzing N_2 adsorption / desorption isotherms and XRD data, structural changes of various types of mesoporous materials associated with heat-treatments were discussed in Chapter 3. It was found that the mesoporous carbon has superior thermal stability compared to the mesoporous SiO_2 samples and mesoporous carbon–SiO_2 composite. Although ordered pore structure of mesoporous SiO_2 samples were collapsed below 1000 °C treatment, the structure

of mesoporous carbon was maintained even after the 2000 °C treatment.

In Chapter 4, electrochemical energy storage properties of heat-treated mesoporous carbons were studied. The mesoporous carbon electrode processed at 1200 °C showed good electrode properties for EDLC and LIB application. It was expected that micropores in the carbon-framework seems to be used as effective ion-storage sites. Therefore, development of micropore-modification methods should be required for increasing the electrode performance of mesoporous carbons in the future study.

In Chapter 5, lithium-ion storage properties of mesoporous carbon–TiO_2 composites (MCTs) were investigated. The MCT electrode synthesized at 600 °C showed good electrode performance even at high current-density conditions. This superior electrode performance seems to come from TiO_2(B) crystals in the composites. In order to elucidate lithium-ion storage mechanisms of the TiO_2(B) phase, an *in situ* XRD observation during galvanostatic charge / discharge cycling was performed. Reversible structural changes of TiO_2(B) during lithium-ion insertion / extraction were successfully observed in the present investigation. Although two-steps of two-phase equilibrium reactions and a following solid-solution-type lithium insertion reaction occurs at charge / discharge cycling, its crystal structure was almost maintained in contrast to well-known anatase-type TiO_2 electrodes. The manner of unique structural changes, and ideal ion-diffusion pathway of TiO_2(B) crystals seem to play an important role for the good rate-performance and cyclability of the MCT electrodes.

In Chapter 6, photoluminescence properties of oxidized mesoporous carbon–SiO_2 composites (oxMCSs) were investigated. Even though the oxMCSs do not contains any transition-metal or rare-earth elements, the composites showed strong visible-white-light under 365 nm UV-light exposure. The shapes of photoluminescence spectra were close to the spectrum of sun-light, and the spectra of oxMCSs covered almost entire visible-range (400–800 nm). It was found that the color of luminescence can be varied with changing preparation conditions such as carbonization temperature, oxidation temperature, and duration of oxidation-treatment. Although detailed luminescence mechanisms have not been elucidated yet, carbon-fragments in the composites seem to play an important role for luminescence.

In order to discuss a possibility of carbon-fragment based luminescence in the oxMCSs, nano-sized graphene (graphene nano-fragments) were prepared by using pentacenes as a precursor (Chapter 7). By optimizing preparation methods, polymerized pentacene molecules, which would be regard as graphene nano-fragment, were obtained up to octamer. First principle calculations revealed that such polymerized pentacene molecules have a unique electronic-structure. The obtained nano-fragments showed strong visible-luminescence under UV-irradiation, and the luminescence color was changed with synthetic condition. Although various lengths of fused pentacenes were confirmed through mass spectra, the synthesized materials were obtained as a "mixture". In order to clarify more detailed luminescent properties of the fused systems, a separation method should be developed as the next step. Fortunately, various separation methods have been proposed for nanocarbon systems (especially for SWCNTs) and the technique is still being developed. The author expects that separation of pentacene-polymer will be possible in the near future.

List of Publications

Publications Related to This Study

1. Yosuke Ishii, Yoshiki Nishiwaki, Ayar Al-zubaidi, and Shinji Kawasaki. Pore size determination in ordered mesoporous materials using powder X-ray diffraction. *J. Phys. Chem. C* **117**, 18120–18130 (2013). DOI: 10.1021/jp4057362.
2. Yosuke Ishii, Koki Okamura, Tomohiro Matsushita, and Shinji Kawasaki. Origin of high power performance of mesoporous carbon–TiO_2(B) nanocomposite electrodes: An *in situ* synchrotron X-ray diffraction study of TiO_2(B) electrode upon lithium insertion. *Mater. Express* **2**, 23–36 (2012). DOI: 10.1166/mex.2012.1050.
3. Yosuke Ishii, Akihiro Matsumura, Yukari Ishikawa, and Shinji Kawasaki. White light emission from mesoporous carbon–silica nanocomposites. *Jpn. J. Appl. Phys.* **50**, 01AF06 (2011). DOI: 10.1143/JJAP.50.01AF06.
4. Yosuke Ishii, Tomohiro Sakashita, Shinji Kawasaki, Hidenori Kato, and Masashige Takatori. Fusing treatment of pentacenes: toward giant graphene-like molecule. *Mater. Express* **1**, 36–42 (2011). DOI: 10.1166/mex.2011.1005.
5. Yosuke Ishii, Hayong Song, Hidenori Kato, Masashige Takatori, and Shinji Kawasaki. Facile bottom-up synthesis of graphene nanofragments and nanoribbons by thermal polymerization of pentacenes. *Nanoscale* **4**, 6553–6561 (2012). DOI: 10.1039/C2NR31893H.

Other Publications

1. Yosuke Ishii, Saki Yamada, Tomohiro Matsushita, Ayar Al-zubaidi, and Shinji Kawasaki. Halogen ion adsorption properties of carbon nanotube electrodes. *TANSO* **250**, 253–262 (2011). DOI: 10.7209/tanso.2011.253. (written in Japanese with English abstract).

2. Yosuke Ishii, Yusuke Kanamori, Takehiro Kawashita, Indrajit Mukhopadhyay, and Shinji Kawasaki. Mesoporous carbon–titania nanocomposites for high-power Li-ion battery anode material. *J. Phys. Chem. Solids* **71**, 511–514 (2010). DOI: 10.1016/j.jpcs.2009.12.024.
3. Ayar Al-zubaidi, Yosuke Ishii, Saki Yamada, Tomohiro Matsushita, and Shinji Kawasaki. Spectroscopic evidence of the origin the dumbbell cyclic voltammogram of single-walled carbon nanotubes. *Phys. Chem. Chem. Phys.* **15**, 20672–20678 (2013). DOI: 10.1039/C3CP53898B.
4. Hayong Song, Yosuke Ishii, Ayar Al-zubaidi, Takenobu Sakai, and Shinji Kawasaki. Temperature-dependent water solubility of iodine-doped single-walled carbon nanotubes prepared using an electrochemical method. *Phys. Chem. Chem. Phys.* **15**, 5767–5770 (2013). DOI: 10.1039/C3CP50506E.
5. Tomohiro Matsushita, Yosuke Ishii, and Shinji Kawasaki. Sodium ion battery anode properties of empty and C_{60}-inserted single-walled carbon nanotubes. *Mater. Express* **3**, 30–36 (2013). DOI: 10.1166/mex.2013.1095.
6. Ayar Al-zubaidi, Yosuke Ishii, Tomohiro Matsushita, and Shinji Kawasaki. Diameter dependent doping of single-walled carbon nanotube used as electrical double layer capacitor electrode. *ECS Trans.* **50**, 13–18 (2013). DOI: 10.1149/05043.0013ecst.
7. Tomohiro Matsushita, Yosuke Ishii, and Shinji Kawasaki. Electrochemical insertion of sodium ion into nanocarbon materials for sodium ion batteries. *ECS Trans.* **50**, 1–6 (2013). DOI: 10.1149/05015.0001ecst.
8. Ayar Al-zubaidi, Tsuyoshi Inoue, Tomohiro Matsushita, Yosuke Ishii, and Shinji Kawasaki. Ion adsorption on the inner surface of single-walled carbon nanotubes used as electrodes for electric double-layer capacitors. *Phys. Chem. Chem. Phys.* **14**, 16055–16061 (2012). DOI: 10.1039/C2CP43011H.
9. Ayar Al-zubaidi, Tsuyoshi Inoue, Tomohiro Matsushita, Yosuke Ishii, Takeshi Hashimoto, and Shinji Kawasaki. Cyclic voltammogram profile of single-walled carbon nanotube electric double-layer capacitor electrode reveals dumbbell shape. *J. Phys. Chem. C* **116**, 7681–7686 (2012). DOI: 10.1021/jp300802z.

10. Yukari Ishikawa, Koji Sato, Shinji Kawasaki, Yosuke Ishii, Akihiro Matsumura, and Shunsuke Muto. White light emission from amorphous silicon-oxycarbide materials. *Physica Status Solidi A* **209**, 1022–1025 (2012). DOI: 10.1002/pssa.201100816.
11. Yukari Ishikawa, Shinji Kawasaki, Yosuke Ishii, Koji Sato, and Akihiro Matsumura. White photoluminescence from carbon-incorporated silica fabricated from rice husk. *Jpn. J. Appl. Phys.* **51**, 01AK02 (2012). DOI: 10.1143/JJAP.51.01AK02.
12. Koji Sato, Yukari Ishikawa, Yosuke Ishii, Shinji Kawasaki, Shunsuke Muto, and Yuta Yamamoto. Effects of synthesis process on luminescence properties and structure of mesoporous carbon-silica nanocomposite. *Jpn. J. Appl. Phys.* **51**, 082402 (2012). DOI: 10.1143/JJAP.51.082402.
13. Koji Sato, Yukari Ishikawa, Akihiro Matsumura, Yosuke Ishii, and Shinji Kawasaki. Synthesis of white light emitting mesoporous carbon-silica nanocomposite. *IOP Conf. Ser.: Mater. Sci. Eng.* **18**, 102022 (2011). DOI: 10.1088/1757-899X/18/10/102022.
14. Akihiro Matsumura, Yosuke Ishii, Koji Sato, Yukari Ishikawa, and Shinji Kawasaki. White light emitting mesoporous carbon-silica nanocomposite. *IOP Conf. Ser.: Mater. Sci. Eng.* **18**, 102019 (2011). DOI: 10.1088/1757-899X/18/10/102019.
15. Yukari Ishikawa, Yosuke Ishii, Koji Satoh, Akihiro Matsumura, and Shinji Kawasaki. Preparation of light emitting material by thermal treatment of rice husks. *IOP Conf. Ser.: Mater. Sci. Eng.* **18**, 102015 (2011). DOI: 10.1088/1757-899X/18/10/102015.

Presentations (International Conferences)

1. Yosuke Ishii, Koji Sato, Yukari Ishikawa, and Shinji Kawasaki. Effects of preparation condition for photoluminescent properties of white light emitting mesoporous carbon–silica nanocomposites. *Pacific Rim Meeting on Electrochemical and Solid-State Science (PRiME 2012)*, oral presentation #3900. October 9, 2012 (Honolulu, Hawaii, USA).
2. Yosuke Ishii, Koki Okamura, Tomohiro Matsushita, and Shinji Kawasaki. *In situ* X-ray diffraction investigation of lithium intercalation process on TiO_2(B) electrode. *62nd*

Annual Meeting of the International Society of Electrochemistry (ISE62), oral presentation. September 16, 2011 (Nigata, Japan).

3. Yosuke Ishii, Koji Sato, Yukari Ishikawa, and Shinji Kawasaki. Photoluminescence properties of mesoporous Carbon–Silica nanocomposites. *International Synposium Nanoporous Materials-VI (NANO-VI)*, oral presentation. August 22, 2011 (Banff, Alberta, Canada).
4. Yosuke Ishii, Koki Okamura, Tomohiro Matsushita, and Shinji Kawasaki. Mesoporous carbon–titania composite as a lithium ion battery electrode. *4th International Workshop on Advanced Ceramics (IWAC04)*, oral presentation. December 12, 2010 (Nagoya Japan).
5. Yosuke Ishii, Tomohiro Matsushita, and Shinji Kawasaki. Electrochemical sodium ion storage properties of nanocarbon materials. *5th International Symposium on Advanced Plasma Science and its Applications for Nitrides and Nanomaterials (ISPlasma2013)*, poster presentation P1116C-LN. January 29, 2013 (Nagoya, Japan).
6. Yosuke Ishii, Koki Okamura, Tomohiro Matsushita, and Shinji Kawasaki. Lithium storage properties of mesoporous carbon–TiO_2(B) electrodes. *International Synposium Nanoporous Materials-VI (NANO-VI)*, poster presentation PII-36. August 22, 2011 (Banff, Alberta, Canada).
7. Yosuke Ishii, and Shinji Kawasaki. Synthesis of peripentacene by fusing pentacenes and its electronic structure. *6th International Conference on DV-Xα Method (DV-Xα 2010)*, poster presentation. August 5, 2010 (Daejeon, Korea).
8. Yosuke Ishii, Akihiro Matsumura, Yukari Ishikawa, and Shinji Kawasaki. White light photoluminescence from mesoporous carbon–silica nanocomposite. *2nd International Symposium on Advanced Plasma Science and its Applications for Nitrides and Nanomaterials (ISPlasma2010)*, poster presentation PA058C. March 8, 2010 (Nagoya, Japan).
9. Yosuke Ishii, Yusuke Kanamori, Takehiro Kawashita, and Shinji Kawasaki. Mesoporous carbon–titania nanocomposites for high-power Li-ion battery anode material. *15th International Symposium on Intercalation Compounds (ISIC15)*, poster presentation P175.

May 13, 2009 (Beijing, China).

Presentations (Domestic Conferences)

1. 石井陽祐. 放射光 X 線回折を利用した規則性ナノカーボン材料の構造解析. 第 51 回炭素材料夏季セミナー, 口頭発表（招待講演）. 2013 年 8 月 27 日（千葉）.
2. 石井陽祐, Ayar Al-zubaidi, 筒井誠人, 川崎晋司. 単層カーボンナノチューブ電極のイオン吸着時のラマンスペクトル変化. 電気化学会第 80 回大会, 口頭発表 2E09. 2013 年 3 月 30 日（仙台）.
3. 石井陽祐, 川崎晋司, 石川由加里, 佐藤功二. X 線回折を用いた規則性多孔質材料の構造評価法. 第 12 回日本表面科学会中部支部学術講演会, 口頭発表. 2012 年 12 月 22 日（名古屋）.
4. 石井陽祐, 松下知弘, 川崎晋司. ナノカーボン電極のナトリウムイオン貯蔵特性. 第 43 回中部化学関係学協会支部連合秋季大会, 口頭発表 2E10. 2012 年 11 月 11 日（名古屋）.
5. 石井陽祐, Ayar Al-zubaidi, 山田早紀, 松下知弘, 川崎晋司. 特異な電子構造に由来した単層カーボンナノチューブ電極のイオン吸着特性. 電気化学会第 79 回大会, 口頭発表 1E07. 2012 年 3 月 29 日（浜松）.
6. 石井陽祐, 石川由加理, 佐藤功二, 松村明浩, 川崎晋司. メソポーラスカーボン–シリカ複合体の白色蛍光特性. 第 37 回炭素材料学会年会, 口頭発表 1C11. 2010 年 12 月 1 日（姫路）.
7. 石井陽祐, 岡村光起, 川崎晋司. メソポーラスカーボン–TiO_2 複合体のリチウムイオン貯蔵特性. 第 41 回中部化学関係学協会支部連合秋季大会, 口頭発表 2B13. 2010 年 11 月 7 日（豊橋）.
8. 石井陽祐, 西脇義記, Hayong Song, Ayar Al-zubaidi, 川崎晋司. 規則性多孔質炭素内に閉じ込められた硫黄分子の分析. 第 40 回炭素材料学会年会, ポスター発表 PI09. 2013 年 12 月 3 日（京都）.
9. 石井陽祐, 西脇義記, 川崎晋司. 規則性細孔構造を有する多孔体の X 線回折図形の解析法. 第 39 回炭素材料学会年会, ポスター発表 PII02. 2012 年 11 月 28 日（長野）.
10. 石井陽祐, 岡井悠祐, 加藤秀典, 高鳥正重, 川崎晋司. ペンタセン重合体の合成とその電池

電極への応用. 第 38 回 炭素材料学会年会, ポスター発表 1P12. 2011 年 11 月 29 日（名古屋）.

11. Yosuke Ishii, Shinji Kawasaki, and Yusuke Okai. Visible light emissions from nanocarbon fragments. 第 41 回フラーレン・ナノチューブ・グラフェン総合シンポジウム, ポスター発表 3P-28. 2011 年 9 月 7 日（東京）.
12. 石井陽祐, 川崎晋司. 多孔質炭素に組み込んだ TiO_2(B) 相の Li イオン挿入過程の X 線回折実験. 第 28 回 PF シンポジウム, ポスター発表 P-UG7-09. 2011 年 7 月 12 日（つくば）.
13. Yosuke Ishii, Tomohiro Sakashita, Hidenori Kato, Masashige Takatori, and Shinji Kawasaki. Synthesis and Spectroscopical Characterization of Peripentacene. 第 40 回フラーレン・ナノチューブ総合シンポジウム, ポスター発表 1P-35. 2011 年 3 月 8 日（名古屋）.
14. 石井陽祐, 金森佑輔, 川下雄大, 廣瀬雅一, 川崎晋司. カーボン–チタニア複合多孔体の合成と電気化学特性の評価. 第 11 回 東海地区ヤングエレクトロケミスト研究会, ポスター発表. 2008 年 9 月（浜松）.

Awards

1. 第 12 回 日本表面科学会中部支部学術講演会 講演奨励賞「X 線回折を用いた規則性多孔質材料の構造評価法」（2012 年 12 月 22 日）.
2. 愛知県若手研究者奨励事業 第 6 回わかしゃち奨励賞 優秀提案賞「キャパシタを高容量化するための電極構造最適化～放射光を利用した細孔内イオン吸着のその場観察実験～」（2012 年 2 月 16 日）.
3. 平成 24 年度 名古屋工業大学・学長表彰（2013 年 3 月）.
4. 平成 23 年度 名古屋工業大学・学長表彰（2012 年 3 月）.
5. 平成 22 年度 名古屋工業大学・副学長表彰（2011 年 3 月）.
6. 日本化学会東海支部長賞（2011 年 3 月）.
7. 名古屋工業会賞（2009 年 3 月）

References

1) M. E. Davis. Ordered porous materials for emerging applications. *Nature* **417**, 813–821 (2002). DOI: 10.1038/nature00785.

2) A. Corma. From microporous to mesoporous molecular sieve materials and their use in catalysis. *Chem. Rev.* **97**, 2373–2419 (1997). DOI: 10.1021/cr960406n.

3) D. E. De, Vos, M. Dams, B. F. Sels, and P. A. Jacobs. Ordered mesoporous and microporous molecular sieves functionalized with transition metal complexes as catalysts for selective organic transformations. *Chem. Rev.* **102**, 3615–3640 (2002). DOI: 10.1021/cr010368u.

4) A. Taguchi and F. Schüeth. Ordered mesoporous materials in catalysis. *Microporous Mesoporous Mater.* **77**, 1–45 (2004). DOI: 10.1016/j.micromeso.2004.06.030.

5) M. Hartmann. Ordered mesoporous materials for bioadsorption and biocatalysis. *Chem. Mater.* **17**, 4577–4593 (2005). DOI: 10.1021/cm0485658.

6) D. M. D'Alessandro, B. Smit, and J. R. Long. Carbon dioxide capture: Prospects for new materials. *Angew. Chem. Int. Ed.* **49**, 6058–6082 (2010). DOI: 10.1002/anie.201000431.

7) M. Vallet-Regi, F. Balas, and D. Arcos. Mesoporous materials for drug delivery. *Angew. Chem. Int. Ed.* **46**, 7548–7558 (2007). DOI: 10.1002/anie.200604488.

8) I. I. Slowing, B. G. Trewyn, S. Giri, and V. S.-Y. Lin. Mesoporous silica nanoparticles for drug delivery and biosensing applications. *Adv. Funct. Mater.* **17**, 1225–1236 (2007). DOI: 10.1002/adfm.200601191.

9) J. C. Ndamanisha and L.-p. Guo. Ordered mesoporous carbon for electrochemical sensing: A review. *Anal. Chim. Acta* **747**, 19–28 (2012). DOI: 10.1016/j.aca.2012.08.032.

10) M. Shalom, S. Dor, S. Rühle, L. Grinis, and A. Zaban. Core/CdS quantum dot/shell mesoporous solar cells with improved stability and efficiency using an amorphous TiO_2 coating. *J. Phys. Chem. C* **113**, 3895–3898 (2009). DOI: 10.1021/jp8108682.

11) X. Ji, K. T. Lee, and L. F. Nazar. A highly ordered nanostructured carbon–sulphur cathode for lithium–sulphur batteries. *Nat. Mater.* **8**, 500–506 (2009). DOI: 10.1038/nmat2460.

12) T. Brezesinski, J. Wang, S. H. Tolbert, and B. Dunn. Ordered mesoporous α-MoO_3 with iso-oriented nanocrystalline walls for thin-film pseudocapacitors. *Nat. Mater.* **9**, 146–151 (2010). DOI: 10.1038/nmat2612.

13) C. T. Kresge, M. E. Leonowicz, W. J. Roth, J. C. Vartuli, and J. S. Beck. Ordered mesoporous molecular sieves synthesized by a liquid-crystal template mechanism. *Nature* **359**, 710–712 (1992). DOI: 10.1038/359710a0.

14) Y. Sakamoto, M. Kaneda, O. Terasaki, D. Y. Zhao, J. M. Kim, G. Stucky, H. J. Shin, and R. Ryoo. Direct imaging of the pores and cages of three-dimensional mesoporous materials. *Nature* **408**, 449–453 (2000). DOI: 10.1038/35044040.

15) M. Kaneda, T. Tsubakiyama, A. Carlsson, Y. Sakamoto, T. Ohsuna, O. Terasaki, S. H. Joo, and R. Ryoo. Structural study of mesoporous MCM-48 and carbon networks synthesized in the spaces of MCM-48 by electron crystallography. *J. Phys. Chem. B* **106**, 1256–1266 (2002). DOI: 10.1021/jp0131875.

16) Y. Sakamoto, I. Diaz, O. Terasaki, D. Zhao, J. Perez-Pariente, J. M. Kim, and G. D. Stucky. Three-dimensional cubic mesoporous structures of SBA-12 and related materials by electron crystallography. *J. Phys. Chem. B* **106**, 3118–3123 (2002). DOI: 10.1021/jp014094q.

17) A. E. Garcia-Bennett, K. Miyasaka, O. Terasaki, and S. Che. Structural solution of mesocaged material AMS-8. *Chem. Mater.* **16**, 3597–3605 (2004). DOI: 10.1021/cm049398e.

18) Y. Sakamoto, T.-W. Kim, R. Ryoo, and O. Terasaki. Three-dimensional structure of large-pore mesoporous cubic $ia\bar{3}d$ silica with complementary pores and its carbon replica by electron crystallography. *Angew. Chem. Int. Ed.* **43**, 5231–5234 (2004). DOI: 10.1002/anie.200460449.

19) A. E. Garcia-Bennett, N. Kupferschmidt, Y. Sakamoto, S. Che, and O. Terasaki. Synthesis of mesocage structures by kinetic control of self-assembly in anionic surfactants. *Angew.*

Chem. Int. Ed. **44**, 5317–5322 (2005). DOI: 10.1002/anie.200500113.

20) C. Gao, Y. Sakamoto, K. Sakamoto, O. Terasaki, and S. Che. Synthesis and characterization of mesoporous silica AMS-10 with bicontinuous cubic $pn\bar{3}m$ symmetry. *Angew. Chem. Int. Ed.* **45**, 4295–4298 (2006). DOI: 10.1002/ange.200504114.

21) Y. Han, D. Zhang, L. L. Chng, J. Sun, L. Zhao, X. Zou, and J. Y. Ying. A tri-continuous mesoporous material with a silica pore wall following a hexagonal minimal surface. *Nat. Chem.* **1**, 123–127 (2009). DOI: 10.1038/nchem.166.

22) S. Che, Z. Liu, T. Ohsuna, K. Sakamoto, O. Terasaki, and T. Tatsumi. Synthesis and characterization of chiral mesoporous silica. *Nature* **429**, 281–284 (2004). DOI: 10.1038/nature02529.

23) P. Yang, D. Zhao, D. I. Margolese, B. F. Chmelka, and G. D. Stucky. Generalized syntheses of large-pore mesoporous metal oxides with semicrystalline frameworks. *Nature* **396**, 152–155 (1998). DOI: 10.1038/24132.

24) S. Inagaki, S. Guan, T. Ohsuna, and O. Terasaki. An ordered mesoporous organosilica hybrid material with a crystal-like wall structure. *Nature* **416**, 304–307 (2002). DOI: 10.1038/416304a.

25) S. Tanaka, N. Nishiyama, Y. Egashira, and K. Ueyama. Synthesis of ordered mesoporous carbons with channel structure from an organic-organic nanocomposite. *Chem. Commun.* 2125–2127 (2005). DOI: 10.1039/B501259G.

26) F. Zhang, Y. Meng, D. Gu, Y. Yan, C. Yu, B. Tu, and D. Zhao. A facile aqueous route to synthesize highly ordered mesoporous polymers and carbon frameworks with $ia\bar{3}d$ bicontinuous cubic structure. *J. Am. Chem. Soc.* **127**, 13508–13509 (2005). DOI: 10.1021/ja0545721.

27) D. Sun, A. E. Riley, A. J. Cadby, E. K. Richman, S. D. Korlann, and S. H. Tolbert. Hexagonal nanoporous germanium through surfactant-driven self-assembly of Zintl clusters. *Nature* **441**, 1126–1130 (2006). DOI: 10.1038/nature04891.

28) E. K. Richman, C. B. Kang, T. Brezesinski, and S. H. Tolbert. Ordered mesoporous silicon through magnesium reduction of polymer templated silica thin films. *Nano Lett.* **8**,

3075–3079 (2008). DOI: 10.1021/nl801759x.

29) Y. Yamauchi, A. Takai, M. Komatsu, M. Sawada, T. Ohsuna, and K. Kuroda. Vapor infiltration of a reducing agent for facile synthesis of mesoporous Pt and Pt-based alloys and its application for the preparation of mesoporous Pt microrods in anodic porous membranes. *Chem. Mater.* **20**, 1004–1011 (2008). DOI: 10.1021/cm701985f.

30) R. Liu, Y. Shi, Y. Wan, Y. Meng, F. Zhang, D. Gu, Z. Chen, B. Tu, and D. Zhao. Triconstituent co-assembly to ordered mesostructured polymer–silica and carbon–silica nanocomposites and large-pore mesoporous carbons with high surface areas. *J. Am. Chem. Soc.* **128**, 11652–11662 (2006). DOI: 10.1021/ja0633518.

31) J. M. Cowley and A. F. Moodie. The scattering of electrons by atoms and crystals I. A new theoretical approach. *Acta Crystallogr.* **10**, 609–19 (1957). DOI: 10.1107/S0365110X57002194.

32) S. Brunauer, P. H. Emmett, and E. Teller. Adsorption of gases in multimolecular layers. *J. Am. Chem. Soc.* **60**, 309–319 (1938). DOI: 10.1021/ja01269a023.

33) E. P. Barrett, L. G. Joyner, and P. P. Halenda. The determination of pore volume and area distributions in porous substances. I. Computations from nitrogen isotherms. *J. Am. Chem. Soc.* **73**, 373–380 (1951). DOI: 10.1021/ja01145a126.

34) C. Lastoskie, K. E. Gubbins, and N. Quirke. Pore size distribution analysis of microporous carbons: A density functional theory approach. *J. Phys. Chem.* **97**, 4786–4796 (1993). DOI: 10.1021/j100120a035.

35) A. V. Neimark, P. I. Ravikovitch, M. Grün, F. Schüth, and K. K. Unger. Pore size analysis of MCM-41 type adsorbents by means of nitrogen and argon adsorption. *J. Colloid Interface Sci.* **207**, 159–169 (1998). DOI: 10.1006/jcis.1998.5748.

36) P. I. Ravikovitch and A. V. Neimark. Characterization of micro- and mesoporosity in SBA-15 materials from adsorption data by the NLDFT method. *J. Phys. Chem. B* **105**, 6817–6823 (2001). DOI: 10.1021/jp010621u.

37) P. I. Ravikovitch and A. V. Neimark. Density functional theory of adsorption in spherical cavities and pore size characterization of templated nanoporous silicas with

cubic and three-dimensional hexagonal structures. *Langmuir* **18**, 1550–1560 (2002). DOI: 10.1021/la0107594.

38) R. J.-M. Pellenq, B. Rousseau, and P. E. Levitz. A grand canonical Monte Carlo study of argon adsorption/condensation in mesoporous silica glasses. *Phys. Chem. Chem. Phys.* **3**, 1207–1212 (2001). DOI: 10.1039/B008961N.

39) T. Ohkubo, J. Miyawaki, K. Kaneko, R. Ryoo, and N. A. Seaton. Adsorption properties of templated mesoporous carbon (CMK-1) for nitrogen and supercritical methane-experiment and GCMC simulation. *J. Phys. Chem. B* **106**, 6523–6528 (2002). DOI: 10.1021/jp0200369.

40) C. Herdes, M. A. Santos, F. Medina, and L. F. Vega. Pore size distribution analysis of selected hexagonal mesoporous silicas by grand canonical Monte Carlo simulations. *Langmuir* **21**, 8733–8742 (2005). DOI: 10.1021/la050977n.

41) S. Migge, G. Sandmann, D. Rahner, H. Dietz, and W. Plieth. Studying lithium intercalation into graphite particles via *in situ* Raman spectroscopy and confocal microscopy. *J. Solid State Electrochem.* **9**, 132–137 (2005). DOI: 10.1007/s10008-004-0563-4.

42) H. Asahina, M. Kurotaki, A. Yonei, S. Yamaguchi, and S. Mori. Real-time X-ray diffraction measurement of carbon structure during lithium-ion intercalation. *J. Power Sources* **68**, 249–252 (1997). DOI: 10.1016/S0378-7753(97)02585-8.

43) U. Lafont, D. Carta, G. Mountjoy, A. V. Chadwick, and E. M. Kelder. *In situ* structural changes upon electrochemical lithium insertion in nanosized anatase TiO_2. *J. Phys. Chem. C* **114**, 1372–1378 (2010). DOI: 10.1021/jp908786t.

44) R. Baddour-Hadjean and J.-P. Pereira-Ramos. Raman microspectrometry applied to the study of electrode materials for lithium batteries. *Chem. Rev.* **110**, 1278–1319 (2010). DOI: 10.1021/cr800344k.

45) C. Jiang, I. Honma, T. Kudo, and H. Zhou. Nanocrystalline rutile TiO_2 electrode for high-capacity and high-rate lithium storage. *Electrochem. Solid-State Lett.* **10**, 127–129 (2007). DOI: 10.1149/1.2712041.

46) D. Wang, D. Choi, Z. Yang, V. V. Viswanathan, Z. Nie, C. Wang, Y. Song, J. G. Zhang, and J. Liu. Synthesis and Li-ion insertion properties of highly crystalline mesoporous rutile TiO_2. *Chem. Mater.* **20**, 3435–3442 (2008). DOI: 10.1021/cm8002589.

47) R. Marchand, L. Brohan, and M. Tournoux. TiO_2(B) a new form of titanium dioxide and the potassium octatitanate $K_2Ti_8O_{17}$. *Mater. Res. Bull.* **15**, 1129–1133 (1980). DOI: 10.1016/0025-5408(80)90076-8.

48) Y. Wang, M. Wu, and W. F. Zhang. Preparation and electrochemical characterization of TiO_2 nanowires as an electrode material for lithium-ion batteries. *Electrochim. Acta* **53**, 7863–7868 (2008). DOI: 10.1016/j.electacta.2008.05.068.

49) T. Beuvier, M. Richard-Plouet, M. Mancini-Le Granvalet, T. Brousse, O. Crosnier, and L. Brohan. TiO_2(B) nanoribbons as negative electrode material for lithium ion batteries with high rate performance. *Inorg. Chem.* **49**, 8457–8464 (2010). DOI: 10.1021/ic1010192.

50) J. Li, W. Wan, H. Zhou, J. Li, and D. Xu. Hydrothermal synthesis of TiO_2(B) nanowires with ultrahigh surface area and their fast charging and discharging properties in Li-ion batteries. *Chem. Commun.* **47**, 3439–3441 (2011). DOI: 10.1039/c0cc04634e.

51) J.-Y. Shin, D. Samuelis, and J. Maier. Sustained lithium-storage performance of hierarchical, nanoporous anatase TiO_2 at high rates: Emphasis on interfacial storage phenomena. *Adv. Funct. Mater.* **21**, 3464–3472 (2011). DOI: 10.1002/adfm.201002527.

52) Z. Yang, G. Du, Z. Guo, X. Yu, Z. Chen, T. Guo, and H. Liu. TiO_2(B)@carbon composite nanowires as anode for lithium ion batteries with enhanced reversible capacity and cyclic performance. *J. Mater. Chem.* **21**, 8591–8596 (2011). DOI: 10.1039/c0jm03873c.

53) Z. Yang, G. Du, Z. Guo, X. Yu, Z. Chen, T. Guo, N. Sharma, and H. Liu. TiO_2(B)@anatase hybrid nanowires with highly reversible electrochemical performance. *Electrochem. Commun.* **13**, 46–49 (2011). DOI: 10.1016/j.elecom.2010.11.009.

54) M. D. Slater, D. Kim, E. Lee, and C. S. Johnson. Sodium-ion batteries. *Adv. Funct. Mater.* **23**, 947–958 (2013). DOI: 10.1002/adfm.201200691.

55) S. Komaba, W. Murata, T. Ishikawa, N. Yabuuchi, T. Ozeki, T. Nakayama, A. Ogata,

K. Gotoh, and K. Fujiwara. Electrochemical na insertion and solid electrolyte interphase for hard-carbon electrodes and application to na-ion batteries. *Adv. Funct. Mater.* **21**, 3859–3867 (2011). DOI: 10.1002/adfm.201100854.

56) B. E. Conway. *Electrochemical Supercapacitors: Scientific Fundamentals and Technological Applications*. Kluwer Academic / Plenum Publishers (1999).

57) C. Feldmann, T. Jüstel, C. R. Ronda, and P. J. Schmidt. Inorganic luminescent materials: 100 years of research and application. *Adv. Funct. Mater.* **13**, 511–516 (2003). DOI: 10.1002/adfm.200301005.

58) T. Taguchi. Developing white LED lighting systems and its technological roadmap in japan. *J. Light Vis. Environ.* **30**, 177–182 (2007). DOI: 10.2150/jlve.30.177.

59) T. Fukui, K. Kamon, J. Takeshita, H. Hayashi, T. Miyachi, Y. Uchida, S. Kurai, and T. Taguchi. Superior illuminant characteristics of color rendering and luminous efficacy in multilayered phosphor conversion white light sources excited by near-ultraviolet light-emitting diodes. *Jpn. J. Appl. Phys.* **48**, 112101 (2009). DOI: 10.1143/JJAP.48.112101.

60) Y. Narukawa, J. Narita, T. Sakamoto, K. Deguchi, T. Yamada, and T. Mukai. Ultra-high efficiency white light emitting diodes. *Jpn. J. Appl. Phys.* **45**, L1084–L1086 (2006). DOI: 10.1143/JJAP.45.L1084.

61) W. H. Green, K. P. Le, J. Grey, T. T. Au, and M. J. Sailor. White phosphors from a silicate-carboxylate sol-gel precursor that lack metal activator ions. *Science* **276**, 1826–1828 (1997). DOI: 10.1126/science.276.5320.1826.

62) T. Hayakawa, A. Hiramitsu, and M. Nogami. White light emission from radical carbonyl-terminations in Al_2O_3-SiO_2 porous glasses with high luminescence quantum efficiencies. *Appl. Phys. Lett.* **82**, 2975–2977 (2003). DOI: 10.1063/1.1569038.

63) K. S. Novoselov, A. K. Geim, S. V. Morozov, D. Jiang, Y. Zhang, S. V. Dubonos, I. V. Grigorieva, and A. A. Firsov. Electric field in atomically thin carbon films. *Science* **306**, 666–669 (2004). DOI: 10.1126/science.1102896.

64) A. K. Geim and K. S. Novoselov. The rise of graphene. *Nat. Mater.* **6**, 183–191 (2007).

DOI: 10.1038/nmat1849.

65) M. I. Katsnelson. Graphene: Carbon in two dimensions. *Mater. Today* **10**, 20–27 (2007). DOI: 10.1016/S1369-7021(06)71788-6.

66) A. K. Geim. Graphene: Status and prospects. *Science* **324**, 1530–1534 (2009). DOI: 10.1126/science.1158877.

67) C. N. R. Rao, A. K. Sood, K. S. Subrahmanyam, and A. Govindaraj. Graphene: The new two-dimensional nanomaterial. *Angew. Chem. Int. Ed.* **48**, 7752–7777 (2009). DOI: 10.1002/anie.200901678.

68) F. Schwierz. Graphene transistors. *Nat. Nanotechnol.* **5**, 487–496 (2010). DOI: 10.1038/nnano.2010.89.

69) F. Schedin, A. K. Geim, S. V. Morozov, E. W. Hill, P. Blake, M. I. Katsnelson, and K. S. Novoselov. Detection of individual gas molecules adsorbed on graphene. *Nat. Mater.* **6**, 652–655 (2007). DOI: 10.1038/nmat1967.

70) R. K. Joshi, H. Gomez, F. Alvi, and A. Kumar. Graphene films and ribbons for sensing of o_2, and 100 ppm of CO and NO_2 in practical conditions. *J. Phys. Chem. C* **114**, 6610–6613 (2010). DOI: 10.1021/jp100343d.

71) Y. Shao, J. Wang, H. Wu, J. Liu, I. A. Aksay, and Y. Lin. Graphene based electrochemical sensors and biosensors: A review. *Electroanalysis* **22**, 1027–1036 (2010). DOI: 10.1002/elan.200900571.

72) W. Yang, K. R. Ratinac, S. R. Ringer, P. Thordarson, J. J. Gooding, and F. Braet. Carbon nanomaterials in biosensors: Should you use nanotubes or graphene? *Angew. Chem. Int. Ed.* **49**, 2114–2138 (2010). DOI: 10.1002/anie.200903463.

73) K. S. Kim, Y. Zhao, H. Jang, S. Y. Lee, J. M. Kim, K. S. Kim, J.-H. Ahn, P. Kim, J.-Y. Choi, and B. H. Hong. Large-scale pattern growth of graphene films for stretchable transparent electrodes. *Nature* **457**, 706–710 (2009). DOI: 10.1038/nature07719.

74) G. Kalita, M. Matsushima, H. Uchida, K. Wakita, and M. Umeno. Graphene constructed carbon thin films as transparent electrodes for solar cell applications. *J. Mater. Chem.* **20**, 9713–9717 (2010). DOI: 10.1039/c0jm01352h.

75) E. J. Yoo, J. Kim, E. Hosono, H.-S. Zhou, T. Kudo, and I. Honma. Large reversible Li storage of graphene nanosheet families for use in rechargeable lithium ion batteries. *Nano Lett.* **8**, 2277–2282 (2008). DOI: 10.1021/nl800957b.

76) M. D. Stoller, S. Park, Z. Yanwu, J. An, and R. S. Ruoff. Graphene-based ultracapacitors. *Nano Lett.* **8**, 3498–3502 (2008). DOI: 10.1021/nl802558y.

77) C. Wang, D. Li, C. O. Too, and G. G. Wallace. Electrochemical properties of graphene paper electrodes used in lithium batteries. *Chem. Mater.* **21**, 2604–2606 (2009). DOI: 10.1021/cm900764n.

78) D. Pan, S. Wang, B. Zhao, M. Wu, H. Zhang, Y. Wang, and Z. Jiao. Li storage properties of disordered graphene nanosheets. *Chem. Mater.* **21**, 3136–3142 (2009). DOI: 10.1021/cm900395k.

79) C. Berger, Z. Song, T. Li, X. Li, A. Y. Ogbazghi, R. Feng, Z. Dai, N. Alexei, M. E. H. Conrad, P. N. First, and W. A. De Heer. Ultrathin epitaxial graphite: 2D electron gas properties and a route toward graphene-based nanoelectronics. *J. Phys. Chem. B* **108**, 19912–19916 (2004). DOI: 10.1021/jp040650f.

80) C. Berger, Z. Song, X. Li, X. Wu, N. Brown, C. Naud, D. Mayou, T. Li, J. Hass, A. N. Marchenkov, E. H. Conrad, P. N. First, and W. A. De Heer. Electronic confinement and coherence in patterned epitaxial graphene. *Science* **312**, 1191–1196 (2006). DOI: 10.1126/science.1125925.

81) H. Huang, W. Chen, S. Chen, and A. T. S. Wee. Bottom-up growth of epitaxial graphene on 6H-SiC(0001). *ACS Nano* **2**, 2513–2518 (2008). DOI: 10.1021/nn800711v.

82) K. V. Emtsev, A. Bostwick, K. Horn, J. Jobst, G. L. Kellogg, L. Ley, J. L. McChesney, T. Ohta, S. A. Reshanov, J. Röhrl, E. Rotenberg, A. K. Schmid, D. Waldmann, H. B. Weber, and T. Seyller. Towards wafer-size graphene layers by atmospheric pressure graphitization of silicon carbide. *Nat. Mater.* **8**, 203–207 (2009). DOI: 10.1038/nmat2382.

83) P. W. Sutter, J.-I. Flege, and E. A. Sutter. Epitaxial graphene on ruthenium. *Nat. Mater.* **7**, 406–411 (2008). DOI: 10.1038/nmat2166.

84) X. Li, W. Cai, L. Colombo, and R. S. Ruoff. Evolution of graphene growth on Ni and Cu by carbon isotope labeling. *Nano Lett.* **9**, 4268–4272 (2009). DOI: 10.1021/nl902515k.

85) H. Zhang and P. X. Feng. Fabrication and characterization of few-layer graphene. *Carbon* **48**, 359–364 (2010). DOI: 10.1016/j.carbon.2009.09.037.

86) A. T. T. Koh, Y. M. Foong, and D. H. C. Chua. Comparison of the mechanism of low defect few-layer graphene fabricated on different metals by pulsed laser deposition. *Diamond Relat. Mater.* **25**, 98–102 (2012). DOI: 10.1016/j.diamond.2012.02.014.

87) K. Nakada, M. Fujita, G. Dresselhaus, and M. S. Dresselhaus. Edge state in graphene ribbons: Nanometer size effect and edge shape dependence. *Phys. Rev. B* **54**, 17954–17961 (1996). DOI: 10.1103/PhysRevB.54.17954.

88) Y.-W. Son, M. L. Cohen, and S. G. Louie. Energy gaps in graphene nanoribbons. *Phys. Rev. Lett.* **97**, 216803 (2006). DOI: 10.1103/PhysRevLett.97.216803.

89) Y.-W. Son, M. L. Cohen, and S. G. Louie. Half-metallic graphene nanoribbons. *Nature* **444**, 347–349 (2006). DOI: 10.1038/nature05180.

90) V. Barone, O. Hod, and G. E. Scuseria. Electronic structure and stability of semiconducting graphene nanoribbons. *Nano Lett.* **6**, 2748–2754 (2006). DOI: 10.1021/nl0617033.

91) L. Pisani, J. A. Chan, B. Montanari, and N. M. Harrison. Electronic structure and magnetic properties of graphitic ribbons. *Phys. Rev. B* **75**, 064418 (2007). DOI: 10.1103/PhysRevB.75.064418.

92) C. D. Simpson, J. D. Brand, A. J. Berresheim, L. Przybilla, H. J. Räder, and K. Müllen. Synthesis of a giant 222 carbon graphite sheet. *Chem. Eur. J.* **8**, 1424–1429 (2002). DOI: 10.1002/1521-3765(20020315)8:6<1424::AID-CHEM1424>3.0.CO;2-Z.

93) A. V. Talyzin, S. M. Luzan, K. Leifer, S. Akhtar, J. Fetzer, F. Cataldo, Y. O. Tsybin, C. W. Tai, A. Dzwilewski, and E. Moons. Coronene fusion by heat treatment: Road to nanographenes. *J. Phys. Chem. C* **115**, 13207–13214 (2011). DOI: 10.1021/jp2028627.

94) A. Chuvilin, E. Bichoutskaia, M. C. Gimenez-Lopez, T. W. Chamberlain, G. A. Rance, N. Kuganathan, J. Biskupek, U. Kaiser, and A. N. Khlobystov. Self-assembly of a

sulphur-terminated graphene nanoribbon within a single-walled carbon nanotube. *Nat. Mater.* **10**, 687–692 (2011). DOI: 10.1038/nmat3082.

95) T. Chamberlain, J. Biskupek, G. Rance, A. Chuvilin, T. Alexander, E. Bichoutskaia, U. Kaiser, and A. Khlobystov. Size, structure, and helical twist of graphene nanoribbons controlled by confinement in carbon nanotubes. *ACS Nano* **6**, 3943–3953 (2012). DOI: 10.1021/nn300137j.

96) A. V. Talyzin, I. V. Anoshkin, A. V. Krasheninnikov, R. M. Nieminen, A. G. Nasibulin, H. Jiang, and E. I. Kauppinen. Synthesis of graphene nanoribbons encapsulated in single-walled carbon nanotubes. *Nano Lett.* **11**, 4352–4356 (2011). DOI: 10.1021/nl2024678.

97) A. N. Khlobystov. Carbon nanotubes: From nano test tube to nano-reactor. *ACS Nano* **5**, 9306–9312 (2011). DOI: 10.1021/nn204596p.

98) J. Cai, P. Ruffieux, R. Jaafar, M. Bieri, T. Braun, S. Blankenburg, M. Muoth, A. P. Seitsonen, M. Saleh, X. Feng, K. Müllen, and R. Fasel. Atomically precise bottom-up fabrication of graphene nanoribbons. *Nature* **466**, 470–473 (2010). DOI: 10.1038/nature09211.

99) L. B. Roberson, J. Kowalik, L. M. Tolbert, C. Kloc, R. Zeis, X. Chi, R. Fleming, and C. Wilkins. Pentacene disproportionation during sublimation for field-effect transistors. *J. Am. Chem. Soc.* **127**, 3069–3075 (2005). DOI: 10.1021/ja044586r.

100) B. P. Feuston and J. B. Higgins. Model structures for MCM-41 materials: A molecular dynamics simulation. *J. Phys. Chem.* **98**, 4459–62 (1994). DOI: 10.1021/j100067a037.

101) M. Impéror-Clerc, P. Davidson, and A. Davidson. Existence of a microporous corona around the mesopores of silica-based SBA-15 materials templated by triblock copolymers. *J. Am. Chem. Soc.* **122**, 11925–11933 (2000). DOI: 10.1021/ja002245h.

102) L. A. Solovyov, S. D. Kirik, A. N. Shmakov, and V. N. Romannikov. X-ray structural modeling of silicate mesoporous mesophase material. *Microporous Mesoporous Mater.* **44-45**, 17–23 (2001). DOI: 10.1016/S1387-1811(01)00164-0.

103) W. Schmidt. Calculation of XRD patterns of simulated FDU-15, CMK-5, and CMK-3

carbon structures. *Microporous Mesoporous Mater.* **117**, 372–379 (2008). DOI: 10.1016/j.micromeso.2008.07.020.

104) M. Kruk, M. Jaroniec, C. H. Ko, and R. Ryoo. Characterization of the porous structure of SBA-15. *Chem. Mater.* **12**, 1961–1968 (2000). DOI: 10.1021/cm000164e.

105) Q. Huo, D. Zhao, J. Feng, K. Weston, S. K. Buratto, G. D. Stucky, S. Schacht, and F. Schüth. Room-temperature growth of mesoporous silica fibers: A new high-surface-area optical waveguide. *Adv. Mater.* **9**, 974–978 (1997). DOI: 10.1002/adma.19970091210.

106) M. Jaroniec, M. Kruk, and J. P. Olivier. Standard nitrogen adsorption data for characterization of nanoporous silicas. *Langmuir* **15**, 5410–5413 (1999). DOI: 10.1021/la990136e.

107) M. Kruk, M. Jaroniec, and A. Sayari. Application of large pore MCM-41 molecular sieves to improve pore size analysis using nitrogen adsorption measurements. *Langmuir* **13**, 6267–6273 (1997). DOI: 10.1021/la970776m.

108) Y. Seto, D. Nishio-Hamane, T. Nagai, and N. Sata. Development of a software suite on X-ray diffraction experiments. *Rev. High Press. Sci. Technol.* **20**, 269–276 (2010). DOI: 10.4131/jshpreview.20.269.

109) L. B. Skinner, C. J. Benmore, and J. B. Parise. Area detector corrections for high quality synchrotron X-ray structure factor measurements. *Nucl. Instrum. Methods Phys. Res., Sect. A* **662**, 61–70 (2012). DOI: 10.1016/j.nima.2011.09.031.

110) P. J. Brown, A. G. Fox, E. N. Maslen, M. A. O'Keefe, and B. T. M. Willis. Intensity of diffracted intensities. *International Tables for Crystallography*, Vol. C, Chapter 6.1, 554–595. John Wiley and Sons, Inc. (2006). DOI: 10.1107/97809553602060000600.

111) K. S. W. Sing. Reporting physisorption data for gas/solid systems with special reference to the determination of surface area and porosity. *Pure Appl. Chem.* **54**, 2201–2218 (1982). DOI: 10.1351/pac198254112201.

112) P. J. Branton, P. G. Hall, and K. S. W. Sing. Physisorption of nitrogen and oxygen by MCM-41, a model mesoporous adsorbent. *J. Chem. Soc., Chem. Commun.* 1257–1258

(1993). DOI: 10.1039/C39930001257.

113) M. Kruk, M. Jaroniec, and A. Sayari. Adsorption study of surface and structural properties of MCM-41 materials of different pore sizes. *J. Phys. Chem. B* **101**, 583–589 (1997). DOI: 10.1021/jp962000k.

114) M. Kruk and M. Jaroniec. Argon adsorption at 77 K as a useful tool for the elucidation of pore connectivity in ordered materials with large cagelike mesopores. *Chem. Mater.* **15**, 2942–2949 (2003). DOI: 10.1021/cm021774c.

115) T. Dabadie, A. Ayral, C. Guizard, L. Cot, and P. Lacan. Synthesis and characterization of inorganic gels in a lyotropic liquid crystal medium. Part 2. –synthesis of silica gels in lyotropic crystal phases obtained from cationic surfactants. *J. Mater. Chem.* **6**, 1789–1794 (1996). DOI: 10.1039/JM9960601789.

116) M. Kruk, M. Jaroniec, and A. Sayari. Structural and surface properties of siliceous and titanium-modified HMS molecular sieves. *Microporous Mater.* **9**, 173–182 (1997). DOI: 10.1016/S0927-6513(96)00099-5.

117) M. Kruk, M. Jaroniec, and A. Sayari. Relations between pore structure parameters and their implications for characterization of MCM-41 using gas adsorption and X-ray diffraction. *Chem. Mater.* **11**, 492–500 (1999). DOI: 10.1021/cm981006e.

118) A. Thess, R. Lee, P. Nikolaev, H. Dai, P. Petit, J. Robert, C. Xu, Y. H. Lee, S. G. Kim, A. G. Rinzler, D. T. Colbert, G. E. Scuseria, D. Tománek, J. E. Fischer, and R. E. Smalley. Crystalline ropes of metallic carbon nanotubes. *Science* **273**, 483–487 (1996). DOI: 10.1126/science.273.5274.483.

119) Y. Maniwa, Y. Kumazawa, Y. Saito, H. Tou, H. Kataura, H. Ishii, S. Suzuki, Y. Achiba, A. Fujiwara, and H. Suematsu. Anomaly of X-ray diffraction profile in single-walled carbon nanotubes. *Jpn. J. Appl. Phys.* **38**, L668–L670 (1999). DOI: 10.1143/JJAP.38.L668.

120) C. G. Sonwane, S. K. Bhatia, and N. Calos. Experimental and theoretical investigations of adsorption hysteresis and criticality in MCM-41: Studies with O_2, Ar, and CO_2. *Ind. Eng. Chem. Res.* **37**, 2271–2283 (1998). DOI: 10.1021/ie970883b.

121) K. Koga, G. T. Gao, H. Tanaka, and X. C. Zeng. Formation of ordered ice nanotubes inside carbon nanotubes. *Nature* **412**, 802–805 (2001). DOI: 10.1038/35090532.

122) Y. Maniwa, H. Kataura, M. Abe, S. Suzuki, Y. Achiba, H. Kira, and K. Matsuda. Phase transition in confined water inside carbon nanotubes. *J. Phys. Soc. Jpn.* **71**, 2863–2866 (2002). DOI: 10.1143/JPSJ.71.2863.

123) O. Byl, J.-C. Liu, Y. Wang, W.-L. Yim, J. K. Johnson, and J. T. Yates. Unusual hydrogen bonding in water-filled carbon nanotubes. *J. Am. Chem. Soc.* **128**, 12090–12097 (2006). DOI: 10.1021/ja057856u.

124) S. Kittaka, S. Ishimaru, M. Kuranishi, T. Matsuda, and T. Yamaguchi. Enthalpy and interfacial free energy changes of water capillary condensed in mesoporous silica, MCM-41 and SBA-15. *Phys. Chem. Chem. Phys.* **8**, 3223–3231 (2006). DOI: 10.1039/B518365K.

125) W. Sekhaneh, M. Kotecha, U. Dettlaff-Weglikowska, and W. S. Veeman. High resolution NMR of water absorbed in single-wall carbon nanotubes. *Chem. Phys. Lett.* **428**, 143–147 (2006). DOI: 10.1016/j.cplett.2006.06.105.

126) Y. Maniwa, K. Matsuda, H. Kyakuno, S. Ogasawara, T. Hibi, H. Kadowaki, S. Suzuki, Y. Achiba, and H. Kataura. Water-filled single-wall carbon nanotubes as molecular nanovalves. *Nat. Mater.* **6**, 135–141 (2007). DOI: 10.1038/nmat1823.

127) A. Endo, T. Yamamoto, Y. Inagi, and T. Iwakabe, Koichiand Ohmori. Characterization of nonfreezable pore water in mesoporous silica by thermoporometry. *J. Phys. Chem. C* **112**, 9034–9039 (2008). DOI: 10.1021/jp8016248.

128) H.-J. Wang, X.-K. Xi, A. Kleinhammes, and Y. Wu. Temperature-induced hydrophobic-hydrophilic transition observed by water adsorption. *Science* **322**, 80–83 (2008). DOI: 10.1126/science.1162412.

129) K. Urita, Y. Shiga, T. Fujimori, T. Iiyama, Y. Hattori, H. Kanoh, T. Ohba, H. Tanaka, M. Yudasaka, S. Iijima, M. Isamu, F. Okino, M. Endo, and K. Kaneko. Confinement in carbon nanospace-induced production of KI nanocrystal of high-pressure phase. *J. Am. Chem. Soc.* **133**, 10344–10347 (2011). DOI: 10.1021/ja202565r.

130) S. Oh, S.-H. Park, and Y.-K. Sun. Hydrothermal synthesis of nano-sized anatase TiO_2 powders for lithium secondary anode materials. *J. Power Sources* **161**, 1314–1318 (2006). DOI: 10.1016/j.jpowsour.2006.05.050.

131) M. Wagemaker, W. Borghols, E. R. H. Van Eck, A. P. M. Kentgens, G. J. Kearley, and F. M. Mulder. The influence of size on phase morphology and Li-ion mobility in nanosized lithiated anatase TiO_2. *Chem. Eur. J.* **13**, 2023–2028 (2007). DOI: 10.1002/chem.200600803.

132) J. Chen, L. Yang, and Y. Tang. Electrochemical lithium storage of TiO_2 hollow microspheres assembled by nanotubes. *J. Power Sources* **195**, 6893–6896 (2010). DOI: 10.1016/j.jpowsour.2010.04.005.

133) S. Yoon and A. Manthiram. Hollow core-shell mesoporous TiO_2 spheres for lithium ion storage. *J. Phys. Chem. C* **115**, 9410–9416 (2011). DOI: 10.1021/jp1123184.

134) F. Zhang, Y. Zhang, S. Song, and H. Zhang. Superior electrode performance of mesoporous hollow TiO_2 microspheres through efficient hierarchical nanostructures. *J. Power Sources* **196**, 8618–8624 (2011). DOI: 10.1016/j.jpowsour.2011.06.006.

135) J. Li, Z. Tang, and Z. Zhang. Preparation and novel lithium intercalation properties of titanium oxide nanotubes. *Electrochem. Solid-State Lett.* **8**, A316–A319 (2005). DOI: 10.1149/1.1904465.

136) J. Xu, C. Jia, B. Cao, and W. F. Zhang. Electrochemical properties of anatase TiO_2 nanotubes as an anode material for lithium-ion batteries. *Electrochim. Acta* **52**, 8044–8047 (2007). DOI: 10.1016/j.electacta.2007.06.077.

137) M. G. Choi, Y.-G. Lee, S.-W. Song, and K. M. Kim. Lithium-ion battery anode properties of TiO_2 nanotubes prepared by the hydrothermal synthesis of mixed (anatase and rutile) particles. *Electrochim. Acta* **55**, 5975–5983 (2010). DOI: 10.1016/j.electacta.2010.05.052.

138) G. Du, B. Wan, Z. Guo, J. Shen, Y. Li, and H. Liu. Effect of annealing on electrochemical performance of anodized TiO_2 nanotubes for lithium ion batteries. *Adv. Sci. Lett.* **4**, 469–473 (2011). DOI: 10.1166/asl.2011.1237.

139) T. Yuan, B. Zhao, R. Cai, Y. Zhou, and Z. Shao. Electrospinning based fabrication and performance improvement of film electrodes for lithium-ion batteries composed of TiO_2 hollow fibers. *J. Mater. Chem.* **21**, 15041–15048 (2011). DOI: 10.1039/c1jm11483b.

140) Y. Wang, S. Liu, K. Huang, D. Fang, and S. Zhuang. Electrochemical properties of freestanding TiO_2 nanotube membranes annealed in Ar for lithium anode material. *J. Solid State Electrochem.* **16**, 723–729 (2012). DOI: 10.1007/s10008-011-1417-5.

141) J. Kim and J. Cho. Rate characteristics of anatase TiO_2 nanotubes and nanorods for lithium battery anode materials at room temperature. *J. Electrochem. Soc.* **154**, A542–A546 (2007). DOI: 10.1149/1.2724756.

142) S. Dong, H. Wang, L. Gu, X. Zhou, Z. Liu, P. Han, Y. Wang, X. Chen, G. Cui, and L. Chen. Rutile TiO_2 nanorod arrays directly grown on Ti foil substrates towards lithium-ion micro-batteries. *Thin Solid Films* **519**, 5978–5982 (2011). DOI: 10.1016/j.tsf.2011.03.048.

143) F. Wu, X. Li, Z. Wang, H. Guo, L. Wu, X. Xiong, and X. Wang. A novel method to synthesize anatase TiO_2 nanowires as an anode material for lithium-ion batteries. *J. Alloys Compd.* **509**, 3711–3715 (2011). DOI: 10.1016/j.jallcom.2010.12.182.

144) L. Kavan, J. Rathouský, M. Grätzel, V. Shklover, and A. Zukal. Mesoporous thin film TiO_2 electrodes. *Microporous Mesoporous Mater.* **44-45**, 653–659 (2001). DOI: 10.1016/S1387-1811(01)00246-3.

145) H. Yamada, T. Yamato, I. Moriguchi, and T. Kudo. Interconnected macroporous TiO_2(anatase) as a lithium insertion electrode material. *Solid State Ionics* **175**, 195–198 (2004). DOI: 10.1016/j.ssi.2003.11.031.

146) D. Fattakhova-Rohlfing, M. Wark, T. Brezesinski, B. Smarsly, and J. Rathouský. Highly organized mesoporous TiO_2 films with controlled crystallinity: A Li-insertion study. *Adv. Funct. Mater.* **17**, 123–132 (2007). DOI: 10.1002/adfm.200600425.

147) Z. Wang, S. Liu, G. Chen, and D. Xia. Preparation and Li-intercalation properties of mesoporous anatase-TiO_2 spheres. *Electrochem. Solid-State Lett.* **10**, A77–A80 (2007). DOI: 10.1149/1.2430567.

148) P. Kubiak, J. Geserick, N. Hüsing, and M. Wohlfahrt-Mehrens. Electrochemical performance of mesoporous TiO_2 anatase. *J. Power Sources* **175**, 510–516 (2008). DOI: 10.1016/j.jpowsour.2007.09.044.

149) J. Lee, Y. S. Jung, S. C. Warren, M. Kamperman, S. M. Oh, F. J. Disalvo, and U. Wiesner. Direct access to mesoporous crystalline TiO_2/carbon composites with large and uniform pores for use as anode materials in lithium ion batteries. *Macromol. Chem. Phys.* **212**, 383–390 (2011). DOI: 10.1002/macp.201000687.

150) H. Liu, Z. Bi, X.-G. Sun, R. R. Unocic, M. P. Paranthaman, S. Dai, and G. M. Brown. Mesoporous TiO_2-B microspheres with superior rate performance for lithium ion batteries. *Adv. Mater.* **23**, 3450–3454 (2011). DOI: 10.1002/adma.201100599.

151) J. Wang, Y. Zhou, Y. Hu, R. O'hayre, and Z. Shao. Facile synthesis of nanocrystalline TiO_2 mesoporous microspheres for lithium-ion batteries. *J. Phys. Chem. C* **115**, 2529–2536 (2011). DOI: 10.1021/jp1087509.

152) J. Ye, W. Liu, J. Cai, S. Chen, X. Zhao, H. Zhou, and L. Qi. Nanoporous anatase TiO_2 mesocrystals: Additive-free synthesis, remarkable crystalline-phase stability, and improved lithium insertion behavior. *J. Am. Chem. Soc.* **133**, 933–940 (2011). DOI: 10.1021/ja108205q.

153) Y. Zhou, Y. Kim, C. Jo, J. Lee, C. W. Lee, and S. Yoon. A novel mesoporous carbon-silica-titania nanocomposite as a high performance anode material in lithium ion batteries. *Chem. Commun.* **47**, 4944–4946 (2011). DOI: 10.1039/c1cc10539f.

154) H. Zhou, D. Li, M. Hibino, and I. Honma. A self-ordered, crystalline-glass, mesoporous nanocomposite for use as a lithium-based storage device with both high power and high energy densities. *Angew. Chem. Int. Ed.* **44**, 797–802 (2005). DOI: 10.1002/anie.200460937.

155) I. Moriguchl, R. Hidaka, H. Yamada, T. Kudo, H. Murakami, and N. Nakashima. A mesoporous nanocomposite of TiO_2 and carbon nanotubes as a high-rate Li-intercalation electrode material. *Adv. Mater.* **18**, 69–73 (2006). DOI: 10.1002/adma.200501366.

156) Y.-G. Guo, Y.-S. Hu, W. Sigle, and J. Maier. Superior electrode performance

of nanostructured mesoporous TiO_2(anatase) through efficient hierarchical mixed conducting networks. *Adv. Mater.* **19**, 2087–2091 (2007). DOI: 10.1002/adma.200602828.

157) J. S. Chen, H. Liu, S. Z. Qiao, and X. W. Lou. Carbon-supported ultra-thin anatase TiO_2 nanosheets for fast reversible lithium storage. *J. Mater. Chem.* **21**, 5687–5692 (2011). DOI: 10.1039/c0jm04412a.

158) S.-J. Park, H. Kim, Y.-J. Kim, and H. Lee. Preparation of carbon-coated TiO_2 nanostructures for lithium-ion batteries. *Electrochim. Acta* **56**, 5355–5362 (2011). DOI: 10.1016/j.electacta.2011.03.119.

159) S.-J. Park, Y.-J. Kim, and H. Lee. Synthesis of carbon-coated TiO_2 nanotubes for high-power lithium-ion batteries. *J. Power Sources* **196**, 5133–5137 (2011). DOI: 10.1016/j.jpowsour.2011.01.105.

160) H. Huang, W. K. Zhang, X. P. Gan, C. Wang, and L. Zhang. Electrochemical investigation of TiO_2/carbon nanotubes nanocomposite as anode materials for lithium-ion batteries. *Mater. Lett.* **61**, 296–299 (2007). DOI: 10.1016/j.matlet.2006.04.053.

161) D. Wang, D. Choi, J. Li, Z. Yang, Z. Nie, R. Kou, D. Hu, C. Wang, L. V. Saraf, J. Zhang, I. A. Aksay, and J. Liu. Self-assembled TiO_2-graphene hybrid nanostructures for enhanced Li-ion insertion. *ACS Nano* **3**, 907–914 (2009). DOI: 10.1021/nn900150y.

162) J. S. Chen, Z. Wang, X. C. Dong, P. Chen, and X. W. Lou. Graphene-wrapped TiO_2 hollow structures with enhanced lithium storage capabilities. *Nanoscale* **3**, 2158–2161 (2011). DOI: 10.1039/c1nr10162e.

163) S. Ding, J. S. Chen, D. Luan, F. Y. C. Boey, S. Madhavi, and X. W. Lou. Graphene-supported anatase TiO_2 nanosheets for fast lithium storage. *Chem. Commun.* **47**, 5780–5782 (2011). DOI: 10.1039/c1cc10687b.

164) N. Li, G. Liu, C. Zhen, F. Li, L. Zhang, and H.-M. Cheng. Battery performance and photocatalytic activity of mesoporous anatase TiO_2 nanospheres/graphene composites by template-free self-assembly. *Adv. Funct. Mater.* **21**, 1717–1722 (2011). DOI: 10.1002/adfm.201002295.

165) R. Van De Krol, A. Goossens, and E. A. Meulenkamp. *In situ* X-ray diffraction of lithium intercalation in nanostructured and thin film anatase TiO_2. *J. Electrochem. Soc.* **146**, 3150–3154 (1999). DOI: 10.1149/1.1392447.

166) L. J. Hardwick, M. Holzapfel, P. Novák, L. Dupont, and E. Baudrin. Electrochemical lithium insertion into anatase-type TiO_2: An *in situ* Raman microscopy investigation. *Electrochim. Acta* **52**, 5357–5367 (2007). DOI: 10.1016/j.electacta.2007.02.050.

167) R. Liu, Y. Ren, Y. Shi, F. Zhang, L. Zhang, B. Tu, and D. Zhao. Controlled synthesis of ordered mesoporous C-TiO_2 nanocomposites with crystalline titania frameworks from organic-inorganic-amphiphilic coassembly. *Chem. Mater.* **20**, 1140–1145 (2008). DOI: 10.1021/cm071470w.

168) F. Izumi and K. Momma. Three-dimensional visualization in powder diffraction. *Solid State Phenom.* **130**, 15–20 (2007). DOI: 10.4028/www.scientific.net/SSP.130.15.

169) A. R. Armstrong, G. Armstrong, J. Canales, and P. G. Bruce. TiO_2-B nanowires. *Angew. Chem. Int. Ed.* **43**, 2286–2288 (2004). DOI: 10.1002/anie.200353571.

170) H. Kaper, S. Sallard, I. Djerdj, M. Antonietti, and B. M. Smarsly. Toward a low-temperature sol-gel synthesis of TiO_2(B) using mixtures of surfactants and ionic liquids. *Chem. Mater.* **22**, 3502–3510 (2010). DOI: 10.1021/cm100627g.

171) C. Wessel, L. Zhao, S. Urban, R. Ostermann, I. Djerdj, B. M. Smarsly, L. Chen, Y.-S. Hu, and S. Sallard. Ionic-liquid synthesis route of TiO_2(B) nanoparticles for functionalized materials. *Chem. Eur. J.* **17**, 775–779 (2011). DOI: 10.1002/chem.201002791.

172) J. Procházka, L. Kavan, M. Zukalova, O. Frank, M. Kalbác, A. Zukal, M. Klementova, D. Carbone, and M. Graetzel. Novel synthesis of the TiO_2(B) multilayer templated films. *Chem. Mater.* **21**, 1457–1464 (2009). DOI: 10.1021/cm801819q.

173) G. Nuspl, K. Yoshizawa, and T. Yamabe. Lithium intercalation in TiO_2 modifications. *J. Mater. Chem.* **7**, 2529–2536 (1997). DOI: 10.1039/A703935B.

174) C. Arrouvel, S. C. Parker, and M. Saiful Islam. Lithium insertion and transport in the TiO_2-B anode material: A computational study. *Chem. Mater.* **21**, 4778–4783 (2009). DOI: 10.1021/cm900373u.

175) D. Panduwinata and J. D. Gale. A first principles investigation of lithium intercalation in TiO_2-B. *J. Mater. Chem.* **19**, 3931–3940 (2009). DOI: 10.1039/b902683e.

176) A. Armstrong, C. Arrouvel, V. Gentili, S. Parker, M. Islam, and P. Bruce. Lithium coordination sites in Li_xTiO_2(B): A structural and computational study. *Chem. Mater.* **22**, 6426–6432 (2010). DOI: 10.1021/cm102589x.

177) T. Okumura, T. Fukutsuka, A. Yanagihara, Y. Orikasa, H. Arai, Z. Ogumi, and Y. Uchimoto. Electronic and local structural changes with lithium-ion insertion in TiO_2-b: X-ray absorption spectroscopy study. *J. Mater. Chem.* **21**, 15369–15377 (2011). DOI: 10.1039/c1jm11335f.

178) T. Beuvier, M. Richard-Plouet, and L. Brohan. Accurate methods for quantifying the relative ratio of anatase and TiO_2(*b*) nanoparticles. *J. Phys. Chem. C* **113**, 13703–13706 (2009). DOI: 10.1021/jp903755p.

179) M. Zukalová, M. Kalbáĉ, L. Kavan, I. Exnar, and M. Graetzel. Pseudocapacitive lithium storage in TiO_2(B). *Chem. Mater.* **17**, 1248–1255 (2005). DOI: 10.1021/cm048249t.

180) P. Lange. Evidence for disorder-induced vibrational mode coupling in thin amorphous SiO_2 films. *J. Appl. Phys.* **66**, 201–204 (1989). DOI: 10.1063/1.344472.

181) M. K. Gunde. Vibrational modes in amorphous silicon dioxide. *Physica B: Condensed Matter.* **292**, 286–295 (2000). DOI: 10.1016/S0921-4526(00)00475-0.

182) T. Maruyama and S. Ohtani. Silicon dioxide thin films prepared by chemical vapor deposition from tetrakis(diethylamino)silane and ozone. *Appl. Phys. Lett.* **64**, 2800–2802 (1994). DOI: 10.1063/1.111429.

183) R. Peña Alonso, F. Rubio, J. Rubio, and J. L. Oteo. Study of the hydrolysis and condensation of γ- aminopropyltriethoxysilane by FT-IR spectroscopy. *J. Mater. Sci.* **42**, 595–603 (2007). DOI: 10.1007/s10853-006-1138-9.

184) G. Katumba, B. W. Mwakikunga, and T. R. Mothibinyane. FTIR and Raman spectroscopy of carbon nanoparticles in SiO_2, ZnO and NiO matrices. *Nanoscale Res. Lett.* **3**, 421–426 (2008). DOI: 10.1007/s11671-008-9172-y.

185) R. M. Pasternack, S. R. Amy, and Y. J. Chabal. Attachment of

3-(aminopropyl)triethoxysilane on silicon oxide surfaces: Dependence on solution temperature. *Langmuir* **24**, 12963–12971 (2008). DOI: 10.1021/la8024827.

186) Y. Ishikawa, A. V. Vasin, J. Salonen, S. Muto, V. S. Lysenko, A. N. Nazarov, N. Shibata, and V.-P. Lehto. Color control of white photoluminescence from carbon-incorporated silicon oxide. *J. Appl. Phys.* **104**, 083522 (2008). DOI: 10.1063/1.3003079.

187) Y. Nakazaki, K. Fujita, K. Tanaka, and T. Uchino. Effect of microscopic structure and porosity on the photoluminescence properties of silica gels. *J. Phys. Chem. C* **112**, 10878–10882 (2008). DOI: 10.1021/jp8025368.

188) M. E. Gimon-Kinsel, K. Groothuis, and K. J. Balkus Jr. Photoluminescent properties of MCM-41 molecular sieves. *Microporous Mesoporous Mater.* **20**, 67–76 (1998). DOI: 10.1016/S1387-1811(97)00004-8.

189) Y. C. Lee, Y. L. Liu, J.-L. Shen, I. J. Hsu, P. W. Cheng, C. F. Cheng, and C.-H. Ko. Blue-green luminescence from mesoporous MCM-48 molecular sieves. *J. Non-Cryst. Solids* **341**, 16–20 (2004). DOI: 10.1016/j.jnoncrysol.2004.05.005.

190) T. Y. Lin, J. Chang, G. Z. Huang, H. M. Lin, Y. J. Yeah, and J. L. Shen. Effect of laser illumination on the blue-green luminescence from MCM-41 at room temperature. *J. Phys.: Condens. Matter.* **20**, 255217 (2008). DOI: 10.1088/0953-8984/20/25/255217.

191) L. Gai, H. Jiang, D. Cui, and Q. Wang. Room temperature blue-green photoluminescence of MCM-41, MCM-48 and SBA-15 mesoporous silicas in different conditions. *Microporous Mesoporous Mater.* **120**, 410–413 (2009). DOI: 10.1016/j.micromeso.2008.12.008.

192) A. Aboshi, N. Kurumoto, T. Yamada, and T. Uchino. Influence of thermal treatments on the photoluminescence characteristics of nanometer-sized amorphous silica particles. *J. Phys. Chem. C* **111**, 8483–8488 (2007). DOI: 10.1021/jp0718505.

193) D. P. Yu, Q. L. Hang, Y. Ding, H. Z. Zhang, Z. G. Bai, J. J. Wang, Y. H. Zou, W. Qian, G. C. Xiong, and S. Q. Feng. Amorphous silica nanowires: Intensive blue light emitters. *Appl. Phys. Lett.* **73**, 3076–3078 (1998). DOI: doi: 10.1063/1.122677.

194) M. J. Frisch, G. W. Trucks, H. B. Schlegel, G. E. Scuseria, M. A. Rob, J. R. Cheeseman,

J. A. M. Jr., T. Vreven, K. N. Kudin, J. C. Burant, J. M. Millam, S. S. Iyengar, J. Tomasi, V. Barone, B. Mennucci, M. Cossi, G. Scalmani, N. Rega, G. A. Petersson, H. Nakatsuji, M. Hada, M. Ehara, K. Toyota, R. Fukuda, J. Hasegawa, M. Ishida, T. Nakajima, Y. Honda, O. Kitao, H. Nakai, M. Klene, X. Li, J. E. Knox, H. P. Hratchian, J. B. Cross, V. Bakken, C. Adamo, J. Jaramillo, R. Gomperts, R. E. Stratmann, O. Yazyev, A. J. Austin, R. Cammi, C. Pomelli, J. W. Ochterski, P. Y. Ayala, K. Morokuma, G. A. Voth, P. Salvador, J. J. Dannenberg, V. G. Zakrzewski, S. Dapprich, A. D. Daniels, M. C. Strain, O. Farkas, D. K. Malick, A. D. Rabuck, K. Raghavachari, J. B. Foresman, J. V. Ortiz, Q. Cui, A. G. Baboul, S. Clifford, J. Cioslowski, B. B. Stefanov, G. Liu, A. Liashenko, P. Piskorz, I. Komaromi, R. L. Martin, D. J. Fox, T. Keith, M. A. Al-Laham, C. Y. Peng, A. Nanayakkara, M. Challacombe, P. M. W. Gill, B. Johnson, W. Chen, M. W. Wong, C. Gonzalez, , and J. A. Pople. Gaussian 03 Revision D.02. Gaussian Inc. Wallingford CT. (2003).

195) A. D. Becke. Density-functional thermochemistry. III. The role of exact exchange. *J. Chem. Phys.* **98**, 5648–5652 (1993). DOI: 10.1063/1.464913.

196) T. H. Dunning. Gaussian basis sets for use in correlated molecular calculations. I. the atoms boron through neon and hydrogen. *J. Chem. Phys.* **90**, 1007–1023 (1989). DOI: 10.1063/1.456153.

197) X. Gonze, G.-M. Rignanese, M. Verstraete, J.-M. Beuken, Y. Pouillon, R. Caracas, F. Jollet, M. Torrent, G. Zerah, M. Mikami, P. Ghosez, M. Veithen, J.-Y. Raty, V. Olevano, F. Bruneval, L. Reining, R. Godby, G. Onida, D. R. Hamann, and D. C. Allan. A brief introduction to the ABINIT software package. *Z. Kristallogr.* **220**, 558–562 (2005). DOI: 10.1524/zkri.220.5.558.65066.

198) X. Gonze, B. Amadon, P.-M. Anglade, J.-M. Beuken, F. Bottin, P. Boulanger, F. Bruneval, D. Caliste, R. Caracas, M. Côté, T. Deutsch, L. Genovese, P. Ghosez, M. Giantomassi, S. Goedecker, D. R. Hamann, P. Hermet, F. Jollet, G. Jomard, S. Leroux, M. Mancini, S. Mazevet, M. J. T. Oliveira, G. Onida, Y. Pouillon, T. Rangel, G.-M. Rignanese, D. Sangalli, R. Shaltaf, M. Torrent, M. J. Verstraete, G. Zerah, and J. W. Zwanziger.

ABINIT: First-principles approach to material and nanosystem properties. *Comput. Phys. Commun.* **180**, 2582–2615 (2009). DOI: 10.1016/j.cpc.2009.07.007.

199) J. P. Perdew and Y. Wang. Accurate and simple analytic representation of the electron-gas correlation energy. *Phys. Rev. B* **45**, 13244–13249 (1992). DOI: 10.1103/PhysRevB.45.13244.

200) P. E. Blöchl. Projector augmented-wave method. *Phys. Rev. B* **50**, 17953–17979 (1994). DOI: 10.1103/PhysRevB.50.17953.

201) G. Kresse and D. Joubert. From ultrasoft pseudopotentials to the projector augmented-wave method. *Phys. Rev. B* **59**, 1758–1775 (1999). DOI: 10.1103/PhysRevB.59.1758.

202) R. Juhasz, N. Elfström, and J. Linnros. Controlled fabrication of silicon nanowires by electron beam lithography and electrochemical size reduction. *Nano Lett.* **5**, 275–280 (2004). DOI: 10.1021/nl0481573.

203) A. H. Castro, Neto, F. Guinea, N. M. R. Peres, K. S. Novoselov, and A. K. Geim. The electronic properties of graphene. *Rev. Mod. Phys.* **81**, 109–162 (2009). DOI: 10.1103/RevModPhys.81.109.

204) S.-L. Li, H. Miyazaki, H. Hiura, C. Liu, and K. Tsukagoshi. Enhanced logic performance with semiconducting bilayer graphene channels. *ACS Nano* **5**, 500–506 (2011). DOI: 10.1021/nn102346b.

205) R. Lv and M. Terrones. Towards new graphene materials: Doped graphene sheets and nanoribbons. *Mater. Lett.* **78**, 209–218 (2012). DOI: 10.1016/j.matlet.2012.04.033.

206) A. J. Du, Y. Chen, G. Q. Lu, and S. C. Smith. Half metallicty in finite-length zigzag single walled carbon nanotube: A first-principle prediction. *Appl. Phys. Lett.* **93**, 073101 (2008). DOI: 10.1063/1.2970055.

207) B. H. Northrop, J. E. Norton, and K. N. Houk. On the mechanism of peripentacene formation from pentacene: Computational studies of a prototype for graphene formation from smaller acenes. *J. Am. Chem. Soc.* **129**, 6536–6546 (2007). DOI: 10.1021/ja070392a.